44 93

SMALL BODIES IN THE OUTER SOLAR SYSTEM: FROM KUIPER BELT OBJECTS TO CENTAURS TO SATELLITES

A DISSERTATION SUBMITTED TO THE GRADUATE DIVISION OF THE UNIVERSITY OF HAWAI'I IN PARTIAL FULFILLMENT OF THE REQUIREMENTS FOR THE DEGREE OF

DOCTOR OF PHILOSOPHY

IN

ASTRONOMY

August 2004

By
Scott S. Sheppard

Dissertation Committee:

D. Jewitt, Chairperson
P. Lucey
T. Owen
J. Rayner
D. Tholen

© Copyright 2004
by
Scott S. Sheppard
All Rights Reserved

To My Parents

Acknowledgements

I am highly indebted to my advisor David Clifford Jewitt. Without his vast knowledge, insightful comments, grant writing and just plain hard work this thesis would not have been accomplished. I also thank Paul Lucey, Eduardo Martin, Tobias Owen, John Rayner and Dave Tholen for agreeing to be on my thesis committee and giving valuable ideas for the project.

My Cold and Calculating (C&C) office mates, Chad Trujillo, Bob Thornton, Mike "The Dark Lord" Cushing, Dan Potter, David Donovan, Dale Kocevski, Henry Hsieh and Brian Stalder kept me from insanity with tangram challenge, around the world basketball, common area bowling, super bouncy balls, penny wars, key golf, coin ceiling toss, Half-Life, Quake, and of course speed hall football. I thank John Tonry for being an excellent neighbor to C&C. I could think of no one better to have as a neighbor at the IFA.

This work would not have been accomplished without the help of Peter Capak, David Donovan, Dale Kocevski and Nick Kaiser on how to work with the Cronus cluster of 21 computers and write Pearl code. I'm also grateful for the help Mike Cushing gave me with IDL programming. I would also like to thank Yanga Fernandez and Jan Kleyna for their observational and data analysis help throughout my time at the University of Hawaii.

No animals were harmed during this work.

Abstract

This thesis is split into two parts. Part one describes Kuiper Belt and Centaur work and part two describes outer satellite surveys of the planets.

A wide-field survey was conducted near the ecliptic in search of bright Kuiper Belt objects and Centaurs. It was determined that the Centaur population is of order 1×10^7 (radius $\geq$1 km) assuming a geometric albedo of 0.04. The Centaur population taken along with their average dynamical lifetime is consistent with the Kuiper Belt as the source of the Centaurs. The current total mass of the Centaurs is 10^{-4} $M_{\oplus}$.

In the Hawaii Kuiper Belt Variability Project nearly 40 bright Kuiper Belt objects and Centaurs were observed to systematically monitor them for possible short and long term light variations due to rotational, phase angle, binary and cometary effects. About 29% display significant ($\geq$ 0.15 magnitude range) lightcurves. Statistically, the trans-Neptunian objects are less spherical than their main-belt asteroid counterparts, indicating structural differences or a higher specific angular momentum perhaps resulting from the formation epoch. Short-term lightcurves of KBOs were observed to resemble rotationally distorted, low density rubble piles, contact binaries and albedo effects. By correcting for the effects of projection, it is estimated that the fraction of contact binaries in the Kuiper Belt is at least $\sim$10% to 20%.

Phase darkening for 13 Kuiper Belt objects in the 0 to 2 degree phase angle range were measured. Unlike Pluto, the measured values show steep linear slopes indicating backscatter from low albedo porous surface materials.

Deep wide-field surveys of Mars, Jupiter, Saturn, Uranus and Neptune have discovered 46 new outer satellites of Jupiter, 1 of Saturn, 2 of Uranus and 1 of Neptune. Through these surveys it is shown that the giant planets all have statistically similar irregular satellite population densities, size distributions and orbital structures independent of their mass or formation scenario.

Table of Contents

Acknowledgements v

Abstract vi

List of Tables xii

List of Figures xiv

I Kuiper Belt Objects and Centaurs **1**

Chapter 1: Kuiper Belt Introduction 2

1.1 From Obscurity to Discovery 2

1.2 Current Observational and Theoretical Understanding 4

1.2.1 Kuiper Belt Dynamical Structure 5

1.2.2 KBO Physical Properties 9

1.3 This Thesis: Part 1 12

Chapter 2: A Wide-Field CCD Survey For Bright Centaurs and Kuiper Belt Objects 14

2.1 Abstract 14

2.2 Introduction 15

2.3 Observations 16

2.4 Results and Discussion 28

2.4.1 The Centaurs 29

2.4.2 The Kuiper Belt 36

2.4.3 Collision Clouds 36

2.5 Summary 39
Chapter 3: Rotation and Shape of Kuiper Belt Object (20000) Varuna 41
3.1 Abstract 41
3.2 Introduction 42
3.3 Observations 43
3.4 Results 48
3.5 Interpretation 53
3.5.1 Albedo Models 54
3.5.2 Shape Models 56
3.5.3 Binary 57
3.6 Discussion 59
3.6.1 Density 59
3.6.2 High Angular Momentum in the Kuiper Belt 61
3.7 Summary 63
Chapter 4: Time-Resolved Photometry of Kuiper Belt Objects: Rotations, Shapes and Phase Functions 65
4.1 Abstract 65
4.2 Introduction 66
4.3 Observations 67
4.4 Lightcurve Results 70
4.4.1 (20000) Varuna 85
4.4.2 2000 GN_{171} 88
4.4.3 (33128) 1998 BU_{48} 90
4.4.4 1999 KR_{16} 94
4.4.5 Null Lightcurves 98
4.5 Interpretation 106
4.5.1 Non-uniform Surface Markings 108
4.5.2 Aspherical Shape 110

4.5.3 Lightcurve Model Results 112
4.6 Discussion 113
4.6.1 Other Lightcurve Observations 116
4.6.2 Shape Distribution Models 120
4.6.3 KBO Density Comparisons in the Solar System 125
4.7 Phase Functions of KBOs 128
4.8 Summary 133
Chapter 5: Hawaii Kuiper Belt Variability Project: An Update 135
5.1 Abstract 135
5.2 Introduction 136
5.3 Rotation Results 136
5.3.1 2003 AZ_{84} 138
5.3.2 (24835) 1995 SM_{55} 138
5.3.3 (19308) 1996 TO_{66} 140
5.3.4 (55636) 2002 TX_{300} 143
5.3.5 Flat Rotational Lightcurve Objects 146
5.4 Phase Angle Results 147
Chapter 6: Extreme Kuiper Belt Object 2001 QG_{298} and the Fraction of Contact Binaries 150
6.1 Abstract 150
6.2 Introduction 151
6.3 Observations 152
6.4 Results 154
6.5 Analysis 163
6.5.1 Albedo Variation 163
6.5.2 Aspherical Shape 165
6.5.3 Binary Configurations 167
6.5.4 Fraction of Contact Binaries in the Kuiper Belt 169

6.6 Summary 174
Chapter 7: Kuiper Belt Summary 175

II Outer Planetary Satellites **178**

Chapter 8: Irregular Satellite Introduction 179
8.1 Overview of Planetary Satellites 179
8.2 Irregular Satellite Discovery 184
8.3 Capture of Irregular Satellites 185
8.4 Dynamics of Irregular Satellites 189
8.5 Physical Properties of Irregular Satellites 191
8.6 Giant Planet Formation 193
8.7 This Thesis: Part 2 195
Chapter 9: An Abundant Population of Irregular Satellites Around Jupiter 197
9.1 Introduction 197
9.2 Analysis 198
9.3 Discussion 201
9.3.1 Dynamical Families 201
9.3.2 Comparison to other giant planets 205
Chapter 10:A Search for Outer Irregular Satellites of Mars: Limits to Completeness . 207
10.1 Abstract 207
10.2 Introduction 207
10.3 Observations 210
10.4 Results and Discussion 214
10.5 Conclusions 218
Chapter 11:Ultra Deep Survey for Small Irregular Satellites of Uranus: Limits to Completeness 219
11.1 Abstract 219
11.2 Introduction 220

11.3 Observations 224
11.4 Analysis 225
11.5 Results and Discussion 227
11.5.1 Orbital Element Distribution 229
11.5.2 Size and Population Distribution 235
11.5.3 Comparison of Uranus' and Jupiter's Irregular Satellites 236
11.6 Summary 241
Chapter 12:Satellite Summary and Future 243
12.1 Summary 243
12.2 Future Work 244

List of Tables

2.1 List of large and medium sized searches for Slow Moving Objects.[a] 17

2.2 APT survey data 19

2.3 Observations from the APT 19

2.4 Eye detection efficiency versus magnitude for artificial KBOs and Centaurs. 27

2.5 Automated detection efficiency versus magnitude for artificial KBOs and Centaurs. 28

2.6 Centaur Monte Carlo Simulation Results 34

3.1 Journal of Observations for Varuna 45

3.2 R-Band Photometry of Varuna 46

3.3 Color Measurements of Varuna 52

3.4 Comparison of Rotational Color Variations 55

3.5 Shape Models and Density For Varuna 59

4.1 Geometrical Circumstances of Observations 68

4.2 Parameters of Observed Objects[a] 70

4.3 Observations of KBOs 71

4.4 Properties of Observed KBOs 86

4.5 Colors of Observed Kuiper Belt Objects 87

4.6 2000 GN_{171} Colors 88

4.7 (33128) 1998 BU_{48} Colors 93

4.8 1999 KR_{16} Colors 97
4.9 List of Large Objects with Large Amplitude Lightcurves.[a] 109
4.10 Shape Models and Densities for KBOs with Lightcurves 113
4.11 Other KBOs with Reported Lightcurve Observations 117
4.12 Phase Function Data for KBOs 129

5.1 Properties of Newly Observed KBOs 137
5.2 New Phase Function Data for KBOs 148

6.1 Geometrical Circumstances of the Observations 154
6.2 Observations of 2001 QG_{298} 155
6.3 B-band, V-band and R-band Observations at Keck 158
6.4 Large Objects With Extreme Light Curves[a] 164
6.5 Possible Contact Binaries in the Kuiper Belt 171

8.1 Irregular Satellites of the Giant Planets 180
8.2 Wide-Field CCD Detectors 186

9.1 Jupiter's Irregular satellites 201

10.1 Geometrical Circumstances 209
10.2 Irregular Satellites of the Planets 216

11.1 Irregular Satellites of the Planets 222
11.2 Geometrical Circumstances 229
11.3 Physical and Orbital Properties of Uranus' Irregular Satellites* 230

List of Figures

1.1 Classes of KBOs 7

1.2 Extended Scattered Disk 8

1.3 Two populations of KBOs 11

2.1 Detection of Centaur Chariklo 18

2.2 Sky covered during APT survey 26

2.3 Cumulative luminosity function for Centaurs 31

2.4 Simulation of CLF for Centaurs 33

2.5 Cumulative luminosity function for KBOs 37

3.1 Lightcurve of Varuna 44

3.2 PDM plot for Varuna 50

3.3 High Resolution PDM for Varuna 51

3.4 Rotational lightcurve of Varuna 52

3.5 Colors of Varuna 54

4.1 PDM for 2000 GN171 90

4.2 Phased single-peaked lightcurve 2000 GN171 91

4.3 Phased double-peaked lightcurve 2000 GN171 92

4.4 Close view PDM 2000 GN171 93

4.5 Phased color data of 2000 GN171 95

4.6 Color of 2000 GN171 96

4.7 PDM plot of (33128) 1998 BU_{48} 96
4.8 Phased color lightcurve of (33128) 1998 BU_{48} 97
4.9 PDM plot for 1999 KR_{16} 99
4.10 Close view of PDM for 1999 KR_{16} 100
4.11 Color phased lightcurve of 1999 KR_{16} 100
4.12 Flat lightcurves of KBOs 107
4.13 Periods and amplitudes of KBOs and asteroids 119
4.14 Monte Carlo simulations using constant axis ratios 121
4.15 Monte Carlo simulations using Gaussians 122
4.16 Monte Carlo simulations using power laws 123
4.17 Monte Carlo simulations for KBOs, asteroids and lab fragments 124
4.18 Densities of icy bodies in the solar system 126
4.19 Densities of KBOs and asteroids 127
4.20 Linear phase functions for KBOs 130
4.21 G phase functions for KBOs 131
4.22 KBO vs Pluto phase function 132

5.1 PDM for 2003 AZ_{84} 139
5.2 Phased lightcurve for 2003 AZ_{84} 139
5.3 PDM plot for 1995 SM_{55} 141
5.4 Single-peaked phased period for 1995 SM_{55} 141
5.5 Double-peaked phased period for 1995 SM_{55} 142
5.6 PDM plot for 1996 TO_{66} using our data 143
5.7 Single-peaked period for 1996 TO_{66} 144
5.8 Double-peaked period for 1996 TO_{66} 144
5.9 PDM plot for 1996 TO_{66} using others data 145
5.10 PDM plot for 2002 TX_{300} 145
5.11 Phased R-band data for 2002 TX_{300} 146

5.12 Phase functions for KBOs 149

6.1 PDM plot for 2001QG_{298} 159
6.2 Singled-peaked period for 2001 QG_{298} 160
6.3 Double-peaked period for 2001 QG_{298} 161
6.4 Close view of PDM for2001 QG_{298} 162
6.5 Period vs. Amplitude plot 168
6.6 Histogram of known KBOs ranges 172

8.1 Irregular satellites of the giant planets inclination 182
8.2 Irregular satellites of the giant planets eccentricity 183
8.3 Yearly satellite discoveries 184
8.4 Planets distances versus observable small body sizes 185
8.5 Interrelations among solar system objects 187
8.6 Colors of irregular satellites and other small bodies 192
8.7 Colors of irregular satellite groups 193

9.1 Area searched around Jupiter in 2000 and 2001 200
9.2 Jupiter's irregulars semi-major axis vs. inclination 204

10.1 Area surveyed near Mars 211
10.2 Mars survey detection efficiency 212
10.3 Contour plot of Mars scattered light 213
10.4 Mars survey scattered light detection efficiency 214
10.5 Comparison of known outer planetary satellite systems 217

11.1 Fading factor for more distant planets 223
11.2 Area searched for satellites around Uranus 226
11.3 Detection efficiency of the Uranus survey 227
11.4 Detection efficiency near Uranus 228
11.5 Inclination versus semi-major axis for all irregular satellites 231

11.6 Eccentricity versus semi-major axis for all irregular satellites 232
11.7 Eccentricity versus semi-major axis for Uranus retrograde satellites 233
11.8 Cumulative luminosity function for Uranus and Jupiter 237
11.9 Differential luminosity function for Uranus and Jupiter 239
11.10Cumulative radius function for Uranus satellites 240

Part I

Kuiper Belt Objects and Centaurs

Chapter 1

Kuiper Belt Introduction

1.1 From Obscurity to Discovery

For most of the 20th century the known small bodies in the outer solar system consisted of Pluto, a few known passing comets and the satellites of the giant planets. In the closing decade of the 20th century the situation changed dramatically.

The first known mention of a possible population of small objects existing just beyond Neptune is by Leonard (1930). Prompted by the discovery of Pluto, He asks the question, "Are there not other planets revolving around the Sun beyond the orbit of Neptune (ultra-Neptunian planets) and possibly some beyond the orbit of Pluto itself (ultra-Plutonic planets)?". Leonard goes on to mention that Pluto may be just the first object of many to be discovered beyond Neptune. He vaguely discusses what we today call the third domain of the Solar System, which is remarkably different from the terrestrial planet and gas planet regions. Leonard's discussion is similar to many other authors who wrote about Planet X and like many of those authors he is vague and without much quantitative reasoning.

Edgeworth (1949) wrote a paper entitled "The Evolution of our Planetary System". Though the article covers many topics of solar system formation it has virtually no references which makes it hard to determine if any of the ideas in the paper are original and independent. In a section titled "comets" he writes, "It is not to be supposed that the cloud of scattered material which ultimately condensed to form the solar system was

bounded by the present orbit of the planet Pluto; it is evident that it must have extended to much greater distances". His description is more detailed and more qualitative and intuitive than anything that was written before. His paper was condensed to save paper because of shortages during World War 2 and this may have lead to the absence of references and only a small paragraph devoted to this particular topic.

Finally, Kuiper (1951) gave a more quantitative discussion of why small bodies might lie beyond Neptune. His reasoning again was that the Solar Nebula should not have ended at Neptune. This is probably the best and most detailed independent discussion on the subject. At one point he mentions, "Outside Neptune comet like objects must have formed ...". Kuiper's vision for these small objects was vastly different from what has been observed to date. He believed objects between 30 and 50 AU, which he called "Pluto comets", would have been ejected because of the gravitational influence of Pluto. He then says, "It is probable that particularly beyond 50 AU, where Pluto's effect is small, remnants of the circular comet ring are still present". To date, no low eccentricity Trans-Neptunian object has been found to have a semi-major axis greater than 50 AU.

The idea of small bodies beyond Neptune can not really be attributed to any one individual but a slow realization that the Solar System did not end at Neptune or Pluto. Oort (1950) realized that the long period comets must come from a spherical cloud at a distance greater than 50000 AU. Whipple (1950) first described comets as weak conglomerates of volatile and solid material (the dirty snowball). Everhart (1972) found that long period comets (Periods $>$ 200 years) could become short period comets (Periods $<$ 20 years) through interactions with Jupiter. Joss (1973) argued that this wasn't efficient enough to provide a sufficient source of all the observed short period comets. The most informative work on the origin of short-period comets was from Fernandez (1980). He determined that a Kuiper disk of objects with low inclinations just beyond Neptune would be a good source for short period comets which had mostly low inclinations. These are unlike the long period comets which have an isotropic distribution of inclinations and are most likely to come from the proposed Oort cloud.

Observational work with photographic plates was slow and very inefficient. An extensive photographic survey of the ecliptic by Kowal (1978) found only one outer Solar System object. This object is the first known Centaur, 2060 Chiron, which has an orbit completely within the giant planet region. Kowal's lone discovery was nevertheless important because it showed that some small bodies do have orbits entirely outside of Jupiter's orbit. Soon afterwards a number of stars having IR excesses was observed by IRAS (Aumann et al. (1984)). It was quickly discovered that one of these IR excess stars, β Pic, has a large observable disk of dust that extended out to about 1000 AU in radius (Smith & Terrile (1984)). Weissman (1984) suggested that the IR excess could be from dust produced by collisions in small body populations such as an Oort cloud or Kuiper Belt.

With the development of Charge Coupled Devices (CCDs) in the 1980's surveys could go much deeper and computers allowed for efficient image analysis. In 1992 the first Kuiper Belt object (KBO) other than Pluto was discovered, 1992 QB_1 (Jewitt & Luu (1993)). Soon, moving object detection software and large field-of-view CCD detectors opened up the flood gates for discovering small bodies in the outer solar system.

1.2 Current Observational and Theoretical Understanding

Nearly 1000 Trans-Neptunian Objects (TNOs) have been detected since the discovery of 1992 QB_1 (Jewitt & Luu (1993); Jewitt & Luu (1995); Irwin et al. (1995); Jewitt et al. (1996); Jedicke & Herron (1997); Jewitt et al. (1998); Gladman et al. (1998); Trujillo et al. (2001); Millis et al. (2002)). The Kuiper Belt (or Edgeworth-Kuiper Belt) contains about 80,000 objects with radii greater than 50 km (Trujillo et al. (2001)). This "belt" has been collisionally processed and gravitationally perturbed throughout the age of the Solar System in ways that are not yet fully understood (Holman & Wisdom (1993); Farinella & Davis (1996)).

The Kuiper Belt is the largest known relatively stable ensemble of small bodies in the planetary region, outnumbering the main-belt asteroids and Jovian Trojans by a factor of

$\sim$ 300. The Kuiper Belt's vast distance from the sun suggests the objects are chemically primitive, containing large amounts of volatiles. Thus we may be able to probe some aspects of the early history of the local solar nebula by studying the Kuiper Belt and related objects. The short-period comets and Centaurs are believed to originate from the Kuiper Belt (Fernandez (1980); Duncan et al. (1988)). Centaurs, which have semi-major axes and perihelia between Jupiter and Neptune, are currently in dynamically unstable orbits that will lead either to ejection from the solar system, an impact with a planet or the Sun, or evolution into a short period comet (Dones et al. (1999); Tiscareno & Malhotra (2003)). The long period comets likely come from the more distant and yet undetected Oort cloud.

1.2.1 Kuiper Belt Dynamical Structure

The Kuiper Belt has been found to be dynamically structured (See Figure 1.1). This structuring was a big surprise to most astronomers as it was assumed any Kuiper disk would be dynamically cold (i.e. most objects would have low eccentricities and inclinations). The mean velocity dispersion ($\sim$ 1.2 km s^{-1}) found for KBOs is larger than the escape speed of most KBOs. Thus the current Kuiper Belt is in a state of erosion (Davis & Farinella (1997)). Theoretical and modeling work has largely been devoted to explaining the current dynamical structure seen in the Kuiper Belt. Most invoke the migration of Neptune (Malhotra (1995); Hahn & Malhotra (1999)), the passage of giant planetesimals through the disk (Morbidelli & Valsecchi (1997)), or a passing star (Ida et al. (2000)). Recent modeling suggests that some minor planets which formed between Jupiter and Neptune may have been scattered into the Kuiper Belt region causing the Belt to look much more excited than if they were not present (Gomes (2003)).

There are four known dynamical classes of KBOs (Figures 1.1 and 1.2). Classical KBOs have semi-major axis $40 < a < 50$ AU with moderate eccentricities ($e \sim 0.1$ to 0.2) and inclinations. Resonant KBOs are in mean motion resonances with Neptune and generally have higher eccentricities and inclinations than Classical KBOs. The 3:2 resonance currently

has the most known members, but this may be a selection effect since this resonance is located at the inner regions of the Kuiper belt. The KBOs in the 3:2 resonance are called Plutinos since Pluto occupies this resonance. Scattered disk objects have very large eccentricities with perihelia near the orbit of Neptune ($q \sim 30$ AU). The Scattered disk objects are believed to have been recently scattered out of the main Kuiper Belt by Neptune. Scattered disk objects are probably the progenitors of the Centaurs and short-period comets (Luu et al. (1997); Trujillo et al. (2000)). A fourth class of KBO, the extended scattered disk (Figure 1.2), has only recently been recognized and to date only two members are known (Gladman et al. (2002)). These objects have large eccentricities but unlike the scattered disk objects the extended scattered disk objects have perihelia $q > 45$ AU which can not be directly caused by Neptune interactions alone. These objects may have obtained their orbits from a stellar passage near the Kuiper Belt (Morbidelli & Levison 2004). The bias corrected relative populations of classical : scattered : resonant are 1.0 : 0.8 : 0.1 (Trujillo et al. (2001)).

There is an edge to the classical population around 50 AU (Jewitt et al. (1998); Trujillo et al. (2001); Allen et al. (2002)). Only objects with very large eccentricities are known to have orbits which go beyond 50 AU. The only currently viable explanation known to date is that the disk was truncated by a passing star (Ida et al. (2000); Morbidelli & Levison (2004)).

The Cumulative Luminosity Function (CLF) describes the sky-plane surface density of objects brighter than a given magnitude. For the Centaurs and KBOs the CLF is well known between $19 \lesssim m_R \lesssim 26$ mags. (Jewitt et al. (1996); Jedicke & Herron (1997); Jewitt et al. (1998); Gladman et al. (1998); Sheppard et al. (2000); Larsen et al. (2001); Trujillo et al. (2001); Millis et al. (2002)). The bright end of the KBO CLF is very uncertain because bright KBOs are rare and a limited amount of sky has been searched. The extrapolated CLF currently predicts about one KBO of $m_R \leq 19$ per 500 square degrees of sky. A recent deep survey using the Hubble Space Telescope reached a limiting magnitude of about 29th in the optical (Bernstein et al. 2004, in press). Through extrapolation of the CLF to very

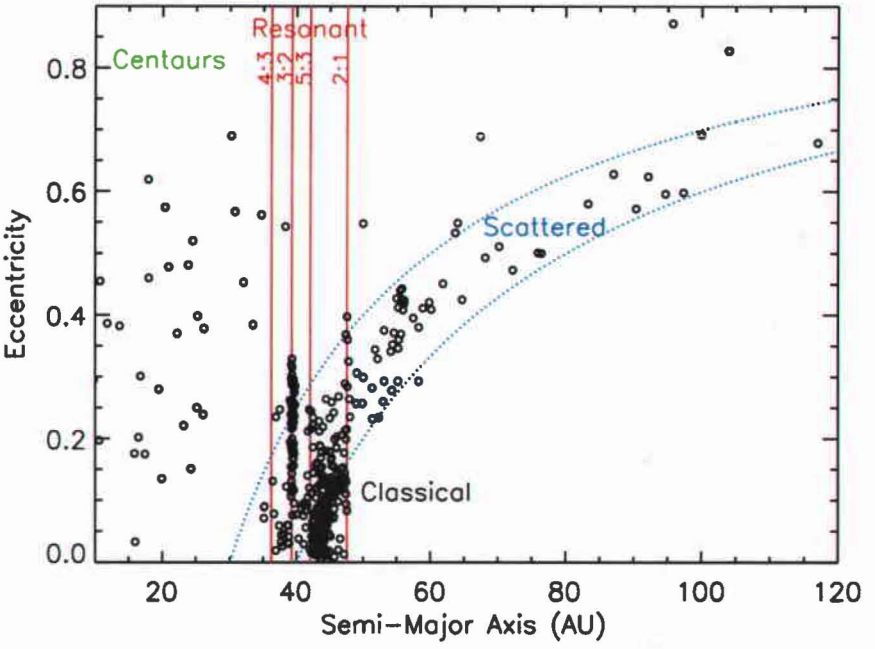

Figure 1.1 Semimajor axis versus eccentricity of known KBOs which show three of the four distinct KBO populations and the Centaurs. Vertical red lines show resonances with Neptune. Scattered disk objects reside between perihelia $30 < q < 40$ AU which are shown in blue. Extended scattered disk objects have perihelia greater than 45 AU (see Figure 1.2). Classical objects are in the lower right portion of the figure.

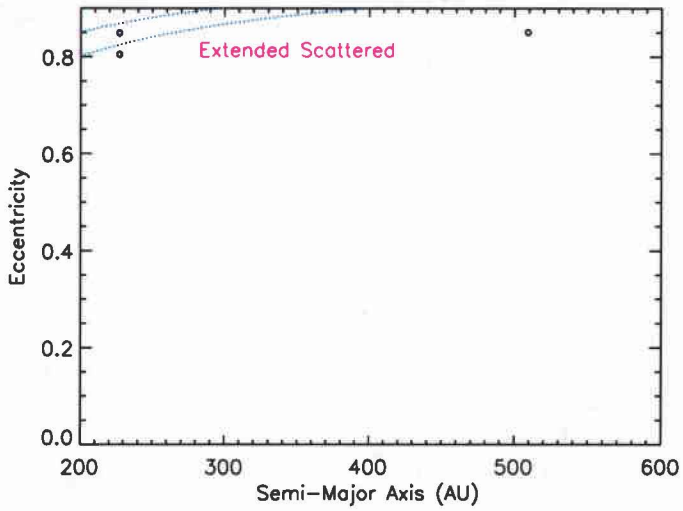

Figure 1.2 Semimajor axis versus eccentricity of extended scattered disk objects which have perihelion greater than 45 AU (which fall below the blue dotted lines).

small KBOs (radii $\sim$ 10 km) the survey was expected to find hundreds of small KBOs. Only three new KBOs were detected in the survey. This strongly indicates that the Kuiper Belt may be deficient of KBOs on the small end.

The inferred mass of the current Kuiper Belt is about 0.1 Earth masses (Trujillo et al. (2001)). This is significantly lower than would be expected from the solar nebula when augmenting the masses of the planets. In addition, the current population size structure of the Kuiper Belt suggests a more massive disk existed in the primordial Kuiper Belt (Stern (1996a)). A detailed accretion model of an earlier denser Kuiper Belt by Kenyon & Luu (1999) showed that several Pluto sized objects could form within the age of the Solar System. The mass may have been lost through Neptune interactions (Holman & Wisdom (1993)) and collisional grinding (Stern (1996a), Kenyon & Luu (1999)). Infrared excesses found around some main sequence stars appears to corroborate dust production produced through collisions between small bodies in possible Kuiper belt analogs (Weissman (1984);

Aumann et al. (1984)). This dust is unstable to radiation pressure from the host star and the Poynting Robertson effect and thus the dust must be constantly replenished through collisions.

It appears that about $4\% \pm 2\%$ of KBOs have companions with separations $\geq 0.15''$ (Noll et al. (2002)). To date the known binaries have mass ratios near unity, though this may be an observational selection effect. These large equal sized components probably did not form by simple direct collisions (Stern (2002)). Formation of such binaries could occur through complex three-body interactions (Weidenschilling (2002)) or when two bodies approach each other and energy is extracted either by dynamical friction from the surrounding sea of smaller KBOs or by a close third body (Goldreich et al. (2002)). These processes both require that the density of KBOs was $\sim 10^2$ to 10^3 times greater than now.

1.2.2 KBO Physical Properties

The surfaces of KBOs may have been altered over their lifetimes by collisions, cometary activity, and irradiation. To date the spectra of KBOs are mostly featureless, some show weak 2μm water ice absorptions (Brown et al. (1999); Jewitt & Luu (2001); Lazzarin et al. (2003)). The range of KBO geometric albedos is still poorly sampled but the larger ones likely have values between 0.04 to 0.10 (Jewitt et al. (2001); Altenhoff et al. (2004)).

Colors of the KBOs have been found to be diverse, ranging from neutral to the reddest objects known in the solar system (V-R$\sim$ 0.3 to V-R$\sim$ 0.8) (Luu & Jewitt (1996); Green et al. (1997); Tegler & Romanishin (1998); Jewitt & Luu (2001)). They show signs of possible correlations between colors, inclination and/or perihelion distance (Tegler & Romanishin (2000); Jewitt & Luu (2001); Trujillo & Brown (2002); Doressoundiram et al. (2002); Tegler et al. (2003); Tegler & Romanishin (2003); Peixinho et al. (2003)). The strongest correlation, that of inclination and color ($\sim 3\sigma$), has prompted the recent modeling work by Gomes (2003). In this scenario the current Kuiper Belt has two separate populations (Figure 1.3). The first are small bodies which formed near their current locations beyond Neptune and which have low to moderate inclinations. The second

population are of bodies which formed in the giant planet region and were scattered into the Kuiper Belt. These objects would be on average larger, more neutral in color and have inclinations ranging from small to large. Objects which formed closer to the Sun could obtain larger sizes because the solar nebula was more dense there. Empirically objects which formed closer to the sun are more neutral in color, which is probably because they have less volatile material on their surfaces.

Currently the most feasible way to determine KBO shapes and surface features is through their photometric light variations. The rotations and shapes of the KBOs may be a function of their size. Small KBOs (diameters $D < 100$ km) are thought to be collisionally produced (Farinella & Davis (1996)). These objects retain no memory of the primordial angular momentum of their parent bodies. Instead, their spins are presumably set by the partitioning of kinetic energy delivered by the projectile responsible for break-up. Larger objects may be structurally damaged bodies held together by gravity (rubble piles). The spins of these objects should be much less influenced by recent impacts. A similar situation prevails in the main asteroid belt, where collisional modification of the rotations and shapes of the smaller objects is observationally well established (Catullo et al. (1984)). The large objects in both the main-belt and the Kuiper Belt may provide a record of the primordial distribution of angular momenta imbued by the growth process. A key attribute of the Kuiper Belt is that the population is very large compared to the main asteroid belt, allowing access to a substantial sample of objects that are too large to have been influenced by recent collisions.

Time-resolved observations of KBOs show that $\sim$ 32% vary by $\geq$ 0.15 magnitudes, 18% by $\geq$ 0.40 magnitudes and 12% by $\geq$ 0.60 magnitudes (Sheppard & Jewitt (2002); Ortiz et al. (2003); Sheppard & Jewitt 2004). One object, (20000) Varuna, displays a large photometric range and fast rotation which is best interpreted as a structurally weak object elongated by its own rotational angular momentum (Jewitt & Sheppard (2002)). Another KBO shows an extremely large amplitude and slow rotation and is best described as a contact binary (Sheppard & Jewitt (2004)). A significant fraction of KBOs appear

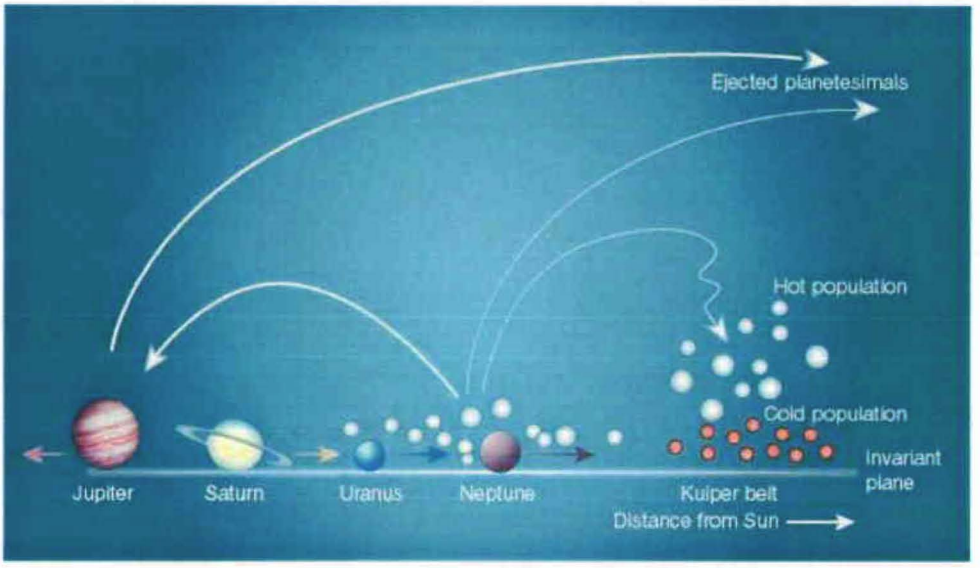

Figure 1.3 There may be two populations in the Kuiper belt. The "Cold" population formed near their present locations beyond Neptune and have low inclinations, are relatively small and red in color. The "Hot" population formed in the giant planet region and were scattered out to the Kuiper Belt. These objects range from small to large, are neutral to red in color and may have a wide range of inclinations. (taken from Morbidelli & Levison (2003))

to be more elongated than main-belt asteroids of similar size (Sheppard & Jewitt (2002)). The KBO phase functions are steep, with a median of 0.16 magnitudes per degree between phase angles of 0 and 2 degrees (Sheppard & Jewitt (2002); Schaefer & Rabinowitz (2002); Sheppard & Jewitt (2004)).

1.3 This Thesis: Part 1

The first part of this thesis consists of chapters 1 to 7 and details a survey for and physical observations of bright Centaurs and Kuiper Belt objects. The practical aim of the survey project was to find bright KBOs and Centaurs, while the physical observations were to determine the rotational characteristics (principally period and shape) of the brightest ($m_R \leq 22$) objects in order to learn about the distributions of rotation periods, shapes, densities, phase functions and binarity in these objects.

Below are listed the following chapters in part 1 of the thesis and a few words describing each. These chapters are composed of published papers which have not been changed but left to appear exactly as they do in their respective journals. Thus the introductions and some sections of chapters may have similar content.

• Chapter 2: "A Wide-Field CCD Survey for Centaurs and Kuiper Belt Objects" by S. Sheppard, D. Jewitt, C. Trujillo, M. Brown, and M. Ashley, 2000, Astronomical Journal, 120, 2687.

This paper presents the first dedicated survey to find Centaurs and was at its time the largest survey to find outer solar system objects to be performed with CCD detectors. The survey helps constrain the population of bright Centaurs and KBOs.

• Chapter 3: "Physical Properties of the Trans-Neptunian Object (20000) Varuna" by D. Jewitt and S. Sheppard, 2002, Astronomical Journal, 123, 2110.

This paper presents the extraordinary short period and large amplitude of 1000 km-scale Kuiper Belt object (20000) Varuna. Rotational elongation, binarity and albedo features are all described in detail as possible causes. The most likely cause is rotational deformation.

• Chapter 4: "Time-Resolved Photometry of Kuiper Belt Objects: Rotations, Shapes and Phase Functions" by S. Sheppard and D. Jewitt, 2002, Astronomical Journal, 124, 1757.

This paper presents the first well-sampled statistical survey for short and long term light variations from the brightest known Kuiper Belt objects. We show that many KBOs show variations and compare these results as an ensemble to the main belt asteroids of similar size.

• Chapter 5: "Hawaii Kuiper Belt Variability Project: An Update" by S. Sheppard and D. Jewitt, Earth, Moon and Planets, in press.

This paper extends the results of Chapter 4 by showing many more KBO lightcurves and also describes two cases where objects appeared to have variable lightcurves.

• Chapter 6: "Extreme Kuiper Belt Object 2001 QG298 and the Fraction of Contact Binaries" by S. Sheppard and D. Jewitt, 2004, Astronomical Journal, 127, 3023

This paper presents the largest known amplitude lightcurve for a Kuiper Belt object observed to date. Its best explanation is that this object is a contact binary and through this analysis we estimate the possible fraction of contact binaries in the Kuiper Belt and compare this population to the main belt asteroids.

• Chapter 7: A summary of the Kuiper belt and Centaur work.

Chapter 2

A Wide-Field CCD Survey For Bright Centaurs and Kuiper Belt Objects

2.1 Abstract

A modified Baker-Nunn camera was used to conduct a wide-field survey of 1428 $\deg^2$ of sky near the ecliptic in search of bright Kuiper Belt objects and Centaurs. This area is an order of magnitude larger than any previously published CCD survey for Centaurs and Kuiper Belt Objects. No new objects brighter than red magnitude $m_R = 18.8$ and moving at a rate $1''$ hr^{-1} to $20''$ hr^{-1} were discovered, although one previously discovered Centaur 1997 CU26 Chariklo was serendipitously detected. The parameters of the survey were characterized using both visual and automated techniques. From this survey the empirical projected surface density of Centaurs was found to be $\Sigma_C(m_R \leq 18.8) = 7.8(^{+16.0}_{-6.6}) \times 10^{-4}$ $\deg^{-2}$ and we found a projected surface density 3σ upper confidence limit for Kuiper Belt objects of $\Sigma_K(m_R \leq 18.8) < 4.1 \times 10^{-3}$ $\deg^{-2}$. We discuss the current state of the cumulative luminosity functions of both Centaurs and Kuiper Belt objects. Through a Monte Carlo simulation we show that the size distribution of Centaurs is consistent with a $q \sim 4$ differential power law, similar to the size distribution of the parent Kuiper Belt Objects. The Centaur population is of order 1×10^7 (radius $\geq$1 km) assuming a geometric albedo of 0.04. About 100 Centaurs are larger than 50 km in radius, of which only 4 are presently known. The current total mass of the Centaurs is 10^{-4} $M_\oplus$. No dust clouds were detected

resulting from Kuiper Belt object collisions, placing a 3σ upper limit < 600 collisionally produced clouds of $m_R < 18.8$ per year.

2.2 Introduction

The outer Solar System has recently been found to be populated by a vast number of minor bodies (e.g., Jewitt, Luu, & Chen 1996, Jedicke & Herron 1997, Jewitt, Luu, & Trujillo 1998). As of June 2000 there are 20 objects, known as Centaurs, which have semi-major axes and perihelia between Jupiter and Neptune and over 300 objects, known as Kuiper Belt objects (KBOs), which have semi-major axes greater than that of Neptune. Centaurs are believed to have originated from the Kuiper Belt and are now in dynamically unstable orbits that will lead either to ejection from the solar system, an impact with a planet or the Sun, or evolution into a short period comet. The brightest known KBO, other than Pluto-Charon, has apparent red magnitude $m_R \sim 20$, whereas several Centaurs are brighter than this. With current technology, physical and chemical properties of only the biggest and brightest minor bodies in the outer solar system can be studied. Centaurs and KBOs could be the most primitive bodies in the solar system and represent a unique opportunity to probe the early history of the local solar nebula.

The Cumulative Luminosity Function (CLF) describes the sky-plane surface density of objects brighter than a given magnitude. Little work has been done on the CLF of Centaurs (Jewitt et al. 1996; Levison & Duncan (1997)), but the CLF of KBOs is well-defined between magnitudes $20 \lesssim m_R \lesssim 26$ (Gladman et al. 1998, Jewitt et al. 1998, Luu & Jewitt 1998, Chiang & Brown 1999). The bright end of the KBO CLF is very uncertain because bright KBOs are rare and a limited amount of sky has been searched. The extrapolated CLF currently predicts about one KBO of $m_R \leq 19$ per 500 square degrees of sky. Observations with possible bearings on large bodies in the outer Solar System include the high eccentricities and inclinations of KBOs which could have come from massive planetesimals in the outer Solar System (Morbidelli & Valsecchi 1997) and

the obliquity of Uranus's spin axis that might imply a collision with a massive body (Singer (1975)). Evolution of the outer Solar System suggests a more massive disk was needed in the primordial Kuiper Belt to explain its current population size structure (Stern (1996a)). A detailed accretion model of the early Kuiper Belt by Kenyon & Luu (1999) showed several Pluto sized objects could form within the age of the Solar System. Direct evidence for large objects in the outer Solar System includes the large irregular satellite Triton, as well as the Pluto-Charon system. To constrain the CLF of both the Centaurs and KBOs at $m_R \leq 20$ requires searches covering large sky areas. To date large surveys have been conducted using photographic plates which are difficult to parametrize. A list of surveys which have covered > 50 deg^2 and which had temporal sampling sufficient to detect Centaurs and/or KBOs is given in Table 2.1. Considering that relatively little of the sky has been searched for these Slow Moving Objects (SMOs), and that recent advances in CCD technology have made large area surveys feasible, this is an excellent time to search for bright SMOs. Accordingly, we undertook a wide-field survey in search of bright objects in the outer Solar System.

2.3 Observations

The 0.5 meter diameter Automated Patrol Telescope (APT) at Siding Spring Observatory in Australia was used during 3 observing runs in early 1999. The APT is a modified Baker-Nunn camera using a 3-element lens to achieve a corrected wide field of view (Carter et al. (1992)). It was originally designed to track satellites in Earth orbit. We used a 770 $\times$ 1152 pixel CCD manufactured by EEV with 22.5 μm pixels and a pixel scale of 9.41$''$/pixel at the f/1 focal plane for imaging. The quantum efficiency of the detector is 0.46 in the R-band. The detector has a 3° $\times$ 2° rectangular field of view with the east-west direction aligned parallel to the long axis. Exposures were taken using a Johnson R-band filter and the telescope was tracked at sidereal rate. The APT site is exceptionally dark. The seeing was usually around 1.5$''$ as measured from other telescopes on the mountain. At the APT the large pixel scale did not allow us to directly measure the seeing and moderate variations

Table 2.1. List of large and medium sized searches for Slow Moving Objects.[a]

Survey	Square Degrees[b]		Limiting Mag.	Detected Objects[c]		Object(s)[d]	Year(s)
	KBOs	Centaurs	(m_R)	KBOs	Centaurs	(m_R)	
Tombaugh(1961)[e]	1530	1530	16.8	0	0	NA	1939–1940
	$\sim$ 19500	$\sim$ 19500	15.5	1	0	14	1929–1945
	$\sim$ 25500	$\sim$ 25500	15		0		
	$\sim$ 28000	$\sim$ 28000	13		0		
Kowal(1989)[e]	6400	6400	19.5	0	1	18	1976–1985
This Work	1428	1428	18.8	0	0[1]	NA	1999
Luu et al.(1988)[e]	297	297	19.5[f]	0	0	NA	1987
Jewitt et al.(1998)	51.5	51.5	22.5	13	0	20.60	1996–1997
Irwin et al.(1995)[e]	50	50	20	0	0	NA	1995
Spacewatch[1]	$\sim$1000	$\sim$10000	20-21[f]	7	8[1]	16.5,17.4, 19.5,20.4[f]	1989–
LONEOS[2]	0	?[g]	$\sim$19	NA	0[2]	NA	1998–
Catalina[3]	0	?[h]	$\sim$19	NA	1[1]	18	1999–

[a](> 50 deg^2)

[b]Area covered in which KBOs ($d\theta/dt < 4''$ hr^{-1}) and Centaurs ($4''$ hr$^{-1} < d\theta/dt < 20''$ hr^{-1}) could be detected.

[c]Shows number of new objects detected as well as serendipitously detected objects in brackets [].

[d]The magnitude of the brightest object(s) detected in the survey.

[e]Surveys were done using photographic plates.

[f]Magnitude was calculated from quoted V-band value using $V - R = 0.5$.

[g]Covers most of sky north of -30 degrees declination

[h]Covers about 300 deg^2 per good night

Note. — Spacewatch, LONEOS, and Catalina are Near Earth Object searches capable of detecting some SMOs.

References. — (1)McMillan (1999); (2)Koehn (1999); (3)Larson (1999).

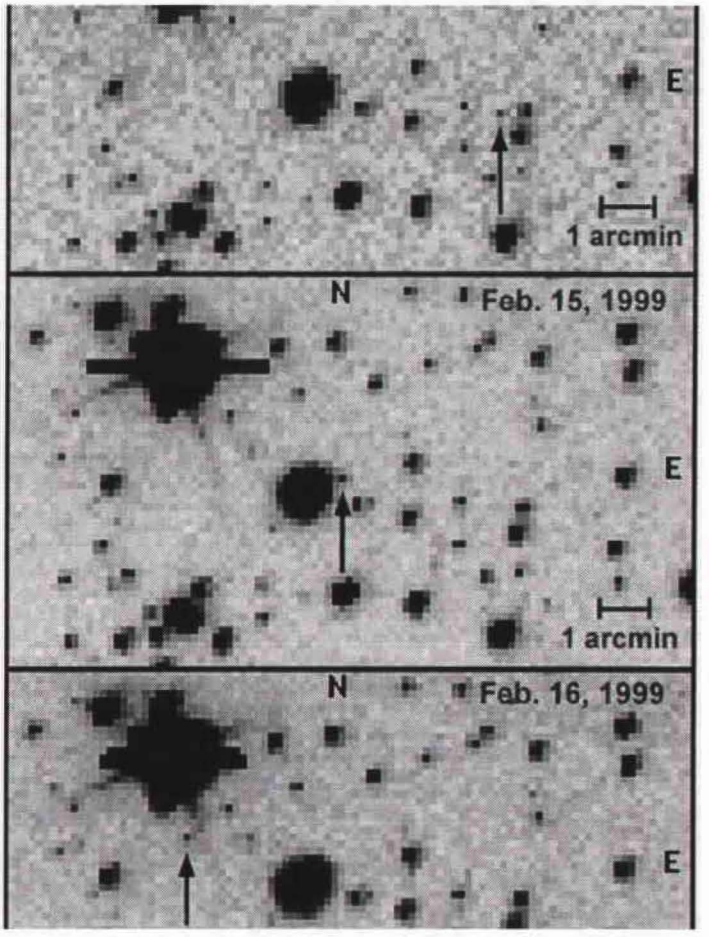

Figure 2.1 Portions of three APT fields collected during the run in February 1999, with a 1 day timebase between images. The width of each image section is 1/4 degree and the height is 1/8 degree. Each image section shows 0.5% of the total area of one field. The arrows show the position of the Centaur 1997 CU26 Chariklo on each night.

in seeing were not noticeable. The data were undersampled which made it difficult to distinguish between galaxies and stars (Figure 2.1).

A total of 238 independent fields covering 1428 deg^2 of sky were imaged during observing runs centered around new moon in January, February, and March 1999 (Table 2.2). A map of the sky areas searched is shown in Figure 2.2 and the specific field centers are given in Table 2.3. The fields were selected to be observed at an airmass ≤ 1.5 and be within 30 degrees of the ecliptic. Selection of the fields was made with no prior knowledge of known SMOs in the area. The search was made between $+10$ and -30 degrees of the ecliptic.

Table 2.2. APT survey data

Date	# Nights	# Images	# Fields	Sky Area (deg^2)
January 1999	10	201	58	348
February 1999	15	468	112	672
March 1999	15	399	68	408
Total	40	1068	238	1428

The observational strategy was to search within ± 1.5 hr of opposition. At opposition the movement of an object is simply related to heliocentric distance by

$$\frac{d\theta}{dt} \approx \frac{148}{R + R^{1/2}} \tag{2.1}$$

where R(AU) is the heliocentric distance and $d\theta/dt$ (arcsec hr^{-1}) is the rate of change of apparent position of the SMO on the CCD. From Equation 2.1, KBOs with $R > 30$ AU will have $d\theta/dt \leq 4''$ hr^{-1} ($\leq$ 10 pixels per day) and Centaurs with $5 < R < 30$ AU have $4''$ $hr^{-1} \leq d\theta/dt \leq 20''$ hr^{-1} (between 10 and 50 pixels per day). Therefore we sought KBOs and Centaurs by comparing images taken on successive nights, allowing the detection of objects moving at rates between $1''$ hr^{-1} and $20''$ hr^{-1}. Trailing of both KBOs and Centaurs was negligible due to the large pixels, slow movement of the objects, and short integration times.

Table 2.3: Observations from the APT

Field	RA(2000)	Dec(2000)	UT Date
f4384	06 : 02 : 01	−16 : 00 : 00	1999/Jan/13,14,15
f4500	06 : 05 : 54	−18 : 00 : 00	1999/Jan/13,14,15
f4615	06 : 10 : 20	−20 : 00 : 00	1999/Jan/13,14,15
f4268	06 : 11 : 01	−14 : 00 : 00	1999/Jan/13,14,15
f4385	06 : 14 : 30	−16 : 00 : 00	1999/Jan/13,14,15
f4501	06 : 18 : 31	−18 : 00 : 00	1999/Jan/13,14,15
f4616	06 : 23 : 06	−20 : 00 : 00	1999/Jan/13,14,15
f0991	07 : 29 : 24	16 : 00 : 00	1999/Jan/13,14,15
f1107	07 : 34 : 13	18 : 00 : 00	1999/Jan/13,14,15

Table 2.3: (continued)

Field	RA(2000)	Dec(2000)	UT Date
f0875	07 : 37 : 35	14 : 00 : 00	1999/Jan/13,14,15
f1222	07 : 39 : 43	20 : 00 : 00	1999/Jan/18,19,22,23
f0992	07 : 41 : 53	16 : 00 : 00	1999/Jan/13,14,15
f0639	07 : 43 : 02	10 : 00 : 00	1999/Jan/13,14,15
f1108	07 : 46 : 50	18 : 00 : 00	1999/Jan/18,19,22,23
f0401	07 : 50 : 34	06 : 00 : 00	1999/Jan/18,22,23
f1223	07 : 52 : 29	20 : 00 : 00	1999/Jan/18,19,22,23
f0521	07 : 52 : 35	08 : 00 : 00	1999/Jan/18,22,23
f0993	07 : 54 : 22	16 : 00 : 00	1999/Jan/18,19,22
f0640	07 : 55 : 13	10 : 00 : 00	1999/Jan/18,22,23
f1109	07 : 59 : 28	18 : 00 : 00	1999/Jan/18,19,22
f0162	08 : 00 : 17	02 : 00 : 00	1999/Jan/13,15,17
f0282	08 : 01 : 10	04 : 00 : 00	1999/Jan/13,15,17
f0877	08 : 02 : 19	14 : 00 : 00	1999/Jan/13,15,17
f0402	08 : 02 : 38	06 : 00 : 00	1999/Jan/13,15,17
f0522	08 : 04 : 43	08 : 00 : 00	1999/Jan/13,15,17
f1224	08 : 05 : 15	20 : 00 : 00	1999/Jan/18,19,22
f0994	08 : 06 : 51	16 : 00 : 00	1999/Jan/18,19,22
f0641	08 : 07 : 24	10 : 00 : 00	1999/Feb/14,15,16
f0760	08 : 10 : 43	12 : 00 : 00	1999/Feb/12,13,14
f0042	08 : 11 : 60	00 : 00 : 00	1999/Jan/15,16,17
f1110	08 : 12 : 05	18 : 00 : 00	1999/Jan/18,19,22
f0163	08 : 12 : 17	02 : 00 : 00	1999/Jan/15,16,17
f0283	08 : 13 : 12	04 : 00 : 00	1999/Jan/15,16,17
f0878	08 : 14 : 41	14 : 00 : 00	1999/Feb/12,13,14
f0403	08 : 14 : 42	06 : 00 : 00	1999/Jan/15,16,17
f0523	08 : 16 : 50	08 : 00 : 00	1999/Jan/15,16,17
f0995	08 : 19 : 20	16 : 00 : 00	1999/Jan/18,19,22
f0043	08 : 24 : 00	00 : 00 : 00	1999/Jan/15,17,18
f0164	08 : 24 : 18	02 : 00 : 00	1999/Jan/15,17,18
f1111	08 : 24 : 42	18 : 00 : 00	1999/Jan/13,15,17
f0284	08 : 25 : 13	04 : 00 : 00	1999/Jan/15,17,18
f0404	08 : 26 : 46	06 : 00 : 00	1999/Jan/13,15,17
f0879	08 : 27 : 03	14 : 00 : 00	1999/Jan/13,15,17
f0524	08 : 28 : 57	08 : 00 : 00	1999/Jan/15,17,18
f0643	08 : 31 : 46	10 : 00 : 00	1999/Jan/13,15,17
f0996	08 : 31 : 49	16 : 00 : 00	1999/Jan/18,19,22
f0762	08 : 35 : 15	12 : 00 : 00	1999/Jan/15,17,18
f0044	08 : 35 : 60	00 : 00 : 00	1999/Jan/15,17,18
f0165	08 : 36 : 18	02 : 00 : 00	1999/Jan/15,17,18
f3565	08 : 36 : 18	−02 : 00 : 00	1999/Jan/15,17,18
f3685	08 : 37 : 15	−04 : 00 : 00	1999/Feb/15,16,17
f0525	08 : 41 : 04	08 : 00 : 00	1999/Feb/12,13,14
f0644	08 : 43 : 57	10 : 00 : 00	1999/Feb/12,13,14
f0763	08 : 47 : 31	12 : 00 : 00	1999/Feb/16,17,21,22
f0045	08 : 48 : 00	00 : 00 : 00	1999/Feb/14,15,16
f0166	08 : 48 : 19	02 : 00 : 00	1999/Feb/11,12,13
f3566	08 : 48 : 19	−02 : 00 : 00	1999/Feb/14,15,16

Table 2.3: (continued)

Field	RA(2000)	Dec(2000)	UT Date
f0286	08 : 49 : 17	04 : 00 : 00	1999/Feb/11,12,13
f3686	08 : 49 : 17	−04 : 00 : 00	1999/Feb/14,15,16
f1113	08 : 49 : 56	18 : 00 : 00	1999/Jan/17,18,22
f0406	08 : 50 : 54	06 : 00 : 00	1999/Feb/11,12,13
f3806	08 : 50 : 54	−06 : 00 : 00	1999/Feb/14,15,16
f0881	08 : 51 : 47	14 : 00 : 00	1999/Jan/17,18,22
f0526	08 : 53 : 11	08 : 00 : 00	1999/Feb/11,12,13
f3926	08 : 53 : 11	−08 : 00 : 00	1999/Feb/17,19,21
f0645	08 : 56 : 08	10 : 00 : 00	1999/Feb/11,12,13
f0998	08 : 56 : 47	16 : 00 : 00	1999/Jan/17,18,22
f0764	08 : 59 : 47	12 : 00 : 00	1999/Jan/17,18,22
f0046	09 : 00 : 00	00 : 00 : 00	1999/Feb/14,15,16
f0167	09 : 00 : 19	02 : 00 : 00	1999/Feb/11,12,13
f3567	09 : 00 : 19	−02 : 00 : 00	1999/Feb/14,15,16
f0287	09 : 01 : 19	04 : 00 : 00	1999/Feb/11,12,13
f3687	09 : 01 : 19	−04 : 00 : 00	1999/Feb/14,15,16
f1114	09 : 02 : 33	18 : 00 : 00	1999/Jan/17,18,22
f0407	09 : 02 : 58	06 : 00 : 00	1999/Feb/11,12,13
f3807	09 : 02 : 58	−06 : 00 : 00	1999/Feb/14,15,16
f0882	09 : 04 : 09	14 : 00 : 00	1999/Jan/17,18,22
f0527	09 : 05 : 18	08 : 00 : 00	1999/Feb/11,12,13
f0646	09 : 08 : 19	10 : 00 : 00	1999/Feb/11,12,13
f0999	09 : 09 : 16	16 : 00 : 00	1999/Jan/17,18,22
f0047	09 : 11 : 60	00 : 00 : 00	1999/Feb/11,12,13
f0765	09 : 12 : 03	12 : 00 : 00	1999/Jan/17,18,22
f0168	09 : 12 : 20	02 : 00 : 00	1999/Feb/11,12,13
f3568	09 : 12 : 20	−02 : 00 : 00	1999/Feb/14,15,16
f0288	09 : 13 : 20	04 : 00 : 00	1999/Feb/11,12,13
f3688	09 : 13 : 20	−04 : 00 : 00	1999/Feb/14,15,16
f0408	09 : 15 : 02	06 : 00 : 00	1999/Feb/11,12,13
f3808	09 : 15 : 02	−06 : 00 : 00	1999/Feb/14,15,16
f1115	09 : 15 : 10	18 : 00 : 00	1999/Jan/17,18,22
f0883	09 : 16 : 31	14 : 00 : 00	1999/Jan/17,18,22
f4283	09 : 16 : 31	−14 : 00 : 00	1999/Jan/17,18,22
f0528	09 : 17 : 25	08 : 00 : 00	1999/Feb/11,12,13
f0647	09 : 20 : 30	10 : 00 : 00	1999/Feb/11,12,13
f1000	09 : 21 : 45	16 : 00 : 00	1999/Feb/11,12,13
f0048	09 : 24 : 00	00 : 00 : 00	1999/Feb/14,15,16
f0766	09 : 24 : 19	12 : 00 : 00	1999/Feb/11,12,13
f0169	09 : 24 : 20	02 : 00 : 00	1999/Feb/14,15,16
f3569	09 : 24 : 20	−02 : 00 : 00	1999/Feb/14,15,16
f0289	09 : 25 : 22	04 : 00 : 00	1999/Feb/14,15,16
f3689	09 : 25 : 22	−04 : 00 : 00	1999/Feb/14,15,16
f0409	09 : 27 : 06	06 : 00 : 00	1999/Feb/14,15,16
f3809	09 : 27 : 06	−06 : 00 : 00	1999/Feb/14,15,16
f1116	09 : 27 : 47	18 : 00 : 00	1999/Feb/11,12,13
f4516	09 : 27 : 47	−18 : 00 : 00	1999/Mar/12,14,15
f0884	09 : 28 : 53	14 : 00 : 00	1999/Feb/11,12,13

Table 2.3: (continued)

Field	RA(2000)	Dec(2000)	UT Date
f0529	09 : 29 : 32	08 : 00 : 00	1999/Feb/16,17,18
f0648	09 : 32 : 42	10 : 00 : 00	1999/Feb/11,13,14
f1001	09 : 34 : 14	16 : 00 : 00	1999/Feb/11,12,13
f0049	09 : 35 : 60	00 : 00 : 00	1999/Feb/17,18,19
f0170	09 : 36 : 21	02 : 00 : 00	1999/Feb/17,18,19
f3570	09 : 36 : 21	−02 : 00 : 00	1999/Feb/17,18,19
f0767	09 : 36 : 36	12 : 00 : 00	1999/Feb/11,13,14
f4167	09 : 36 : 36	−12 : 00 : 00	1999/Feb/20,21,22
f0290	09 : 37 : 24	04 : 00 : 00	1999/Feb/17,18,19
f3690	09 : 37 : 24	−04 : 00 : 00	1999/Feb/17,18,19
f0410	09 : 39 : 10	06 : 00 : 00	1999/Feb/17,18,19
f3810	09 : 39 : 10	−06 : 00 : 00	1999/Feb/17,18,19
f1117	09 : 40 : 24	18 : 00 : 00	1999/Feb/11,13,15
f0885	09 : 41 : 15	14 : 00 : 00	1999/Feb/11,13,14
f0530	09 : 41 : 39	08 : 00 : 00	1999/Feb/14,16,17
f3930	09 : 41 : 39	−08 : 00 : 00	1999/Feb/17,18,19
f0649	09 : 44 : 53	10 : 00 : 00	1999/Feb/15,16,17
f4049	09 : 44 : 53	−10 : 00 : 00	1999/Feb/17,18,19
f1002	09 : 46 : 43	16 : 00 : 00	1999/Feb/11,13,14
f0050	09 : 48 : 00	00 : 00 : 00	1999/Feb/11,13,14
f0171	09 : 48 : 21	02 : 00 : 00	1999/Feb/11,13,14
f3571	09 : 48 : 21	−02 : 00 : 00	1999/Feb/11,13,14
f0768	09 : 48 : 52	12 : 00 : 00	1999/Feb/15,16,17
f4168	09 : 48 : 52	−12 : 00 : 00	1999/Feb/17,18,19
f0291	09 : 49 : 26	04 : 00 : 00	1999/Feb/11,13,14
f3691	09 : 49 : 26	−04 : 00 : 00	1999/Feb/11,13,14
f0411	09 : 51 : 14	06 : 00 : 00	1999/Feb/15,16,17
f3811	09 : 51 : 14	−06 : 00 : 00	1999/Feb/11,13,14
f1118	09 : 53 : 01	18 : 00 : 00	1999/Feb/16,17,18
f0886	09 : 53 : 38	14 : 00 : 00	1999/Feb/16,17,18
f4286	09 : 53 : 38	−14 : 00 : 00	1999/Mar/12,14,15
f0531	09 : 53 : 46	08 : 00 : 00	1999/Feb/15,16,17
f3931	09 : 53 : 46	−08 : 00 : 00	1999/Feb/11,13,14
f0650	09 : 57 : 04	10 : 00 : 00	1999/Feb/15,16,17
f4050	09 : 57 : 04	−10 : 00 : 00	1999/Feb/17,18,19
f1003	09 : 59 : 12	16 : 00 : 00	1999/Feb/16,17,18
f4403	09 : 59 : 12	−16 : 00 : 00	1999/Mar/12,14,15
f0051	10 : 00 : 00	00 : 00 : 00	1999/Feb/16,17,18
f4633	10 : 00 : 11	−20 : 00 : 00	1999/Mar/12,14,15
f0172	10 : 00 : 21	02 : 00 : 00	1999/Feb/16,17,18
f3572	10 : 00 : 21	−02 : 00 : 00	1999/Feb/16,17,18
f0769	10 : 01 : 08	12 : 00 : 00	1999/Feb/19,21,22
f4169	10 : 01 : 08	−12 : 00 : 00	1999/Feb/17,18,19
f0292	10 : 01 : 27	04 : 00 : 00	1999/Feb/16,17,18
f3692	10 : 01 : 27	−04 : 00 : 00	1999/Feb/16,17,18
f0412	10 : 03 : 18	06 : 00 : 00	1999/Feb/17,19,20
f3812	10 : 03 : 18	−06 : 00 : 00	1999/Feb/16,17,18
f1119	10 : 05 : 38	18 : 00 : 00	1999/Feb/19,21,22

Table 2.3: (continued)

Field	RA(2000)	Dec(2000)	UT Date
f4519	10 : 05 : 38	−18 : 00 : 00	1999/Mar/12,14,15
f0532	10 : 05 : 53	08 : 00 : 00	1999/Feb/17,18,19
f3932	10 : 05 : 53	−08 : 00 : 00	1999/Feb/17,18,19
f0887	10 : 06 : 00	14 : 00 : 00	1999/Feb/19,21,22
f0651	10 : 09 : 15	10 : 00 : 00	1999/Feb/17,18,19
f4051	10 : 09 : 15	−10 : 00 : 00	1999/Feb/17,18,19
f1004	10 : 11 : 41	16 : 00 : 00	1999/Feb/19,21,22
f0052	10 : 11 : 60	00 : 00 : 00	1999/Mar/11,12,14
f0173	10 : 12 : 22	02 : 00 : 00	1999/Mar/11,12,14
f3573	10 : 12 : 22	−02 : 00 : 00	1999/Mar/11,12,14
f4634	10 : 12 : 57	−20 : 00 : 00	1999/Mar/12,14,15
f4170	10 : 13 : 24	−12 : 00 : 00	1999/Feb/17,18,19
f0293	10 : 13 : 29	04 : 00 : 00	1999/Mar/11,12,14
f3693	10 : 13 : 29	−04 : 00 : 00	1999/Mar/11,12,14
f0413	10 : 15 : 22	06 : 00 : 00	1999/Mar/11,12,14
f3813	10 : 15 : 22	−06 : 00 : 00	1999/Mar/11,12,14
f0533	10 : 18 : 00	08 : 00 : 00	1999/Mar/11,12,14
f3933	10 : 18 : 00	−08 : 00 : 00	1999/Mar/11,12,14
f1120	10 : 18 : 15	18 : 00 : 00	1999/Feb/19,21,22
f4288	10 : 18 : 22	−14 : 00 : 00	1999/Feb/13,14,15
f0652	10 : 21 : 26	10 : 00 : 00	1999/Mar/11,12,14
f4052	10 : 21 : 26	−10 : 00 : 00	1999/Feb/19,21,22
f0053	10 : 24 : 00	00 : 00 : 00	1999/Mar/11,12,14
f4405	10 : 24 : 10	−16 : 00 : 00	1999/Feb/13,15,16
f0174	10 : 24 : 22	02 : 00 : 00	1999/Mar/11,12,14
f3574	10 : 24 : 22	−02 : 00 : 00	1999/Mar/20,22,23
f0294	10 : 25 : 31	04 : 00 : 00	1999/Mar/11,12,14
f3694	10 : 25 : 31	−04 : 00 : 00	1999/Mar/20,22,23
f4171	10 : 25 : 40	−12 : 00 : 00	1999/Feb/19,21,22
f0414	10 : 27 : 26	06 : 00 : 00	1999/Mar/11,12,14
f3814	10 : 27 : 26	−06 : 00 : 00	1999/Mar/20,23,24
f0534	10 : 30 : 07	08 : 00 : 00	1999/Mar/11,12,14
f3934	10 : 30 : 07	−08 : 00 : 00	1999/Mar/20,23,24
f4289	10 : 30 : 44	−14 : 00 : 00	1999/Feb/13,15,16
f4521	10 : 30 : 52	−18 : 00 : 00	1999/Feb/17,18,19
f0653	10 : 33 : 37	10 : 00 : 00	1999/Mar/11,12,14
f4053	10 : 33 : 37	−10 : 00 : 00	1999/Feb/19,21,22
f0054	10 : 35 : 60	00 : 00 : 00	1999/Mar/20,22,23
f0175	10 : 36 : 23	02 : 00 : 00	1999/Mar/20,22,23
f3575	10 : 36 : 23	−02 : 00 : 00	1999/Mar/10,11,12
f4406	10 : 36 : 39	−16 : 00 : 00	1999/Feb/13,14,15
f0295	10 : 37 : 33	04 : 00 : 00	1999/Mar/20,22,23
f3695	10 : 37 : 33	−04 : 00 : 00	1999/Mar/11,12,14
f4172	10 : 37 : 56	−12 : 00 : 00	1999/Feb/19,21,22
f3815	10 : 39 : 30	−06 : 00 : 00	1999/Mar/20,22,23
f3935	10 : 42 : 15	−08 : 00 : 00	1999/Mar/20,22,23
f4290	10 : 43 : 06	−14 : 00 : 00	1999/Feb/19,21,22
f4522	10 : 43 : 29	−18 : 00 : 00	1999/Feb/17,18,19

Table 2.3: (continued)

Field	RA(2000)	Dec(2000)	UT Date
f4407	10 : 49 : 08	−16 : 00 : 00	1999/Feb/18,19,21
f0296	10 : 49 : 34	04 : 00 : 00	1999/Mar/20,22,23
f4523	10 : 56 : 06	−18 : 00 : 00	1999/Feb/18,19,21
f4055	10 : 57 : 59	−10 : 00 : 00	1999/Mar/11,12,14
f0056	11 : 00 : 00	00 : 00 : 00	1999/Mar/20,22,23
f0297	11 : 01 : 36	04 : 00 : 00	1999/Mar/15,16,19
f0057	11 : 11 : 60	00 : 00 : 00	1999/Mar/20,22,23
f0298	11 : 13 : 38	04 : 00 : 00	1999/Mar/15,20,23
f0058	11 : 24 : 00	00 : 00 : 00	1999/Mar/20,22,23
f0299	11 : 25 : 40	04 : 00 : 00	1999/Mar/20,23,24
f0059	11 : 35 : 60	00 : 00 : 00	1999/Mar/20,22,23
f0300	11 : 37 : 41	04 : 00 : 00	1999/Mar/20,23,24
f0060	11 : 48 : 00	00 : 00 : 00	1999/Mar/20,22,23
f0301	11 : 49 : 43	04 : 00 : 00	1999/Mar/22,23,24
f4060	11 : 58 : 55	−10 : 00 : 00	1999/Mar/12,14,15
f0061	12 : 00 : 00	00 : 00 : 00	1999/Mar/20,22,23
f3702	12 : 01 : 45	−04 : 00 : 00	1999/Mar/22,23,24
f4179	12 : 03 : 49	−12 : 00 : 00	1999/Mar/12,14,15
f3822	12 : 03 : 57	−06 : 00 : 00	1999/Mar/20,22,23
f4643	12 : 07 : 53	−20 : 00 : 00	1999/Mar/12,14,15
f4297	12 : 09 : 40	−14 : 00 : 00	1999/Mar/12,14,15
f4061	12 : 11 : 06	−10 : 00 : 00	1999/Mar/20,22,23
f4529	12 : 11 : 49	−18 : 00 : 00	1999/Mar/12,14,15
f3703	12 : 13 : 47	−04 : 00 : 00	1999/Mar/20,22,23
f4180	12 : 16 : 05	−12 : 00 : 00	1999/Mar/20,22,23
f4414	12 : 16 : 31	−16 : 00 : 00	1999/Mar/12,14,15
f4756	12 : 17 : 43	−22 : 00 : 00	1999/Mar/12,14,15
f4062	12 : 23 : 17	−10 : 00 : 00	1999/Mar/14,15,19
f4757	12 : 30 : 39	−22 : 00 : 00	1999/Mar/12,14,15
f4063	12 : 35 : 28	−10 : 00 : 00	1999/Mar/22,23,24
f4065	12 : 59 : 50	−10 : 00 : 00	1999/Mar/22,23,24
f4066	13 : 12 : 01	−10 : 00 : 00	1999/Mar/20,23,24
f3948	13 : 19 : 47	−08 : 00 : 00	1999/Mar/20,23,24
f4068	13 : 36 : 24	−10 : 00 : 00	1999/Mar/20,22,23
f4069	13 : 48 : 35	−10 : 00 : 00	1999/Mar/20,23,24
f4188	13 : 54 : 13	−12 : 00 : 00	1999/Mar/20,23,24
f4189	14 : 06 : 29	−12 : 00 : 00	1999/Mar/20,23,24

Three consecutive exposures of 200 seconds each were taken on each of 3 separate nights yielding 9 images per field. Weather permitting, the fields were imaged on consecutive nights. The images were bias and dark subtracted, then flat fielded with median twilight skyflats. The 3 images of a field taken during a single night were registered, then combined using the IRAF "crreject" cosmic ray rejection algorithm to remove cosmic rays and increase

signal-to-noise. These 3 images were taken consecutively so there was little or no telescope motion between them. Landolt (1992) standard stars were used for photometric calibration.

Field centers differed by up to 50 arcseconds from night to night due to APT pointing variations. We aligned the fields from different nights by eye. The data were analyzed in two complementary ways, a) by visual "blinking" and b) using an automated search algorithm. For the visual analysis, four criteria were used for SMO identification: (1) the object must appear in all three frames, (2) it must have linear motion, (3) it must have a steady brightness in all 3 frames, and (4) it must have constant velocity appropriate for an SMO ($< 20''$ hr^{-1}). Many asteroids between magnitudes 10 and 19 were quickly identified and rejected by their large motions (>50 pixels in 24 hours). They were not followed up with further observations because of limited telescope time. Centaur 10199 Chariklo (provisional designation 1997 CU26) was at $m_V = 17.8$ when detected serendipitously (Figure 2.1). It was discovered independently by the visual and automated procedures with no knowledge of its location in the field. No other known SMOs in the area searched were bright enough to be detected by our survey. It should also be noted that the January fields were crowded due to the close proximity of the Galactic plane to opposition, while the March fields were hampered by bad weather. During poor weather, the few fields with gaps of 2 or 3 days were observed on 4 nights instead of the usual 3 to ensure that SMO identification efficiency was not significantly reduced compared to fields taken on 3 consecutive nights.

The limiting magnitude of the survey was found by randomly placing 100 artificial SMOs onto a subset of the images. A Moffat profile (Moffat 1969) matched to the point spread function of the APT was used to generate the artificial SMOs. The visual detection efficiencies for KBOs and Centaurs are shown as a function of magnitude in Table 2.4. A KBO detection efficiency equal to half the maximum efficiency was reached at $m_R = 18.8$, which we take as the limiting magnitude of this survey. The Centaur detection efficiency equal to half the maximum efficiency was also reached near $m_R = 18.8$.

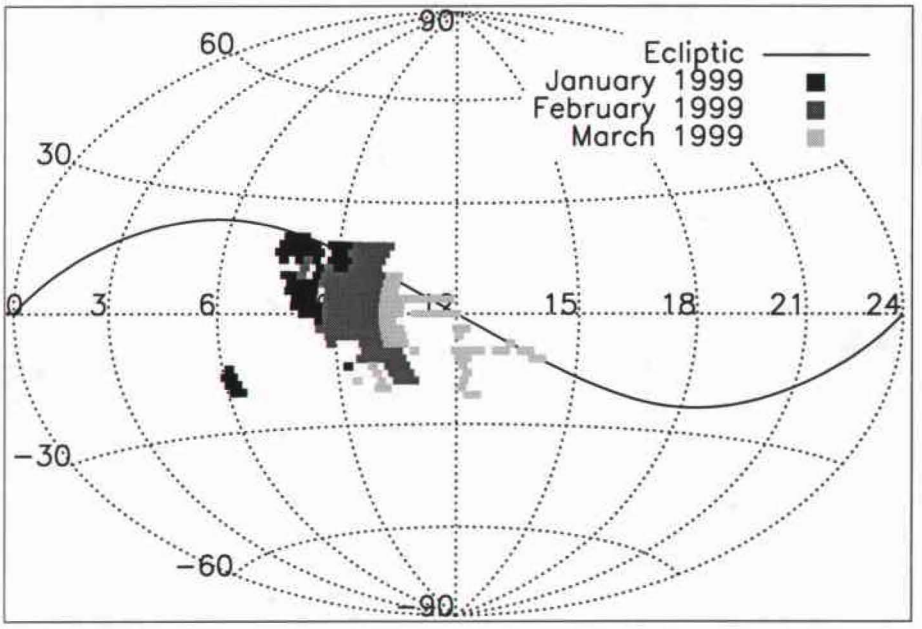

Figure 2.2 Sky covered during this survey. Shaded areas represent the month in which the sky was searched in 1999. Horizontal axis is Right Ascension in hours and vertical axis is Declination in degrees.

Table 2.4. Eye detection efficiency versus magnitude for artificial KBOs and Centaurs.

Magnitude (m_R)	Detection Efficiency(%) KBOs[a]	Detection Efficiency(%) Centaurs[b]
18.00	92	90
18.25	90	86
18.50	77	72
18.75	55	47
19.00	16	7

[a]Artificial KBOs moved between 8 and 10 pixels per day (3 to 4″ hr^{-1}).

[b]Artificial Centaurs moved between 15 and 30 pixels per day (6 to 12″ hr^{-1}).

As a complement to the visual SMO search, a moving object detection program was used to flag potential SMO candidates for scrutinization. The algorithm was optimized for our undersampled data. Objects were detected in each image by searching for maxima in the center of a 3×3 pixel box. An approximate signal-to-noise and flux for the object was then determined using all pixels within the 3×3 pixel box with flux more than 1.5σ above the sky background. While this underestimated the flux of extended objects, it provided a good estimate of the flux of faint undersampled stellar images, which occupied 1 to 4 pixels depending on the location of the image centroid with respect to the pixel grid. Using catalogues of objects in each field with signal-to-noise greater than 4, the software removed stationary objects by searching for objects within ± 1 pixel of the same position in multiple images. Stationary objects with fluxes that varied by more than a factor of 2 are retained in the catalogue as these could be blended objects. The program then flags "objects" with a consistent rate of motion between 1″ hr^{-1} and 12″ hr^{-1} within 20° of the projected direction of the ecliptic. Candidates with fluxes varying by more than a factor of 5 were rejected as these were dominated by spurious objects and variable stars.

Table 2.5. Automated detection efficiency versus magnitude for artificial KBOs and Centaurs.

Magnitude (m_R)	Detection Efficiency(%) SMO[a]
17.00	74
17.25	68
17.50	67
17.75	58
18.00	54
18.25	44
18.50	41
18.75	21
19.00	6

[a]Artificial Slow Moving Objects moved between 3 and 8″ hr^{-1}.

The software successfully detected Centaur Chariklo, which was not unexpected as it was more than a magnitude brighter than the survey limit. As with searching for candidates by eye, the detection efficiency was determined by searching for artificial SMOs. The average detection efficiency as a function of magnitude is summarized in Table 2.5. The KBO detection rate of half the maximum value was reached at $m_R = 18.5$ and is the limiting magnitude for the automated detection technique. The code is not as effective as the eye at deblending merged objects, so the $\sim 50\%$ magnitude limit is ~ 0.3 magnitudes brighter than that determined by eye. However, in high Galactic latitude fields, the efficiency of the code improved significantly with $\sim 70\%$ of $m_R < 18.5$ KBOs being detected.

2.4 Results and Discussion

A total of 238 fields were examined covering 1428 square degrees of sky (about 3.5% of the whole sky). No new SMOs were detected. One previously discovered Centaur (Chariklo) was serendipitously detected. From the one detected Centaur and the efficiency of this

survey we found the empirical projected surface density of Centaurs to be

$$\Sigma_C(m_R \leq 18.8) = 7.8(^{+16.0}_{-6.6}) \times 10^{-4} \text{ deg}^{-2}. \tag{2.2}$$

Assuming Poisson statistics, the 3σ upper confidence limit for the projected surface density of KBOs from our survey is

$$\Sigma_K(m_R \leq 18.8) < 4.1 \times 10^{-3} \text{ deg}^{-2}. \tag{2.3}$$

We plot these and cumulative surface density measurements from other surveys for Centaurs and KBOs in Figures 2.3 and 2.5, respectively. Error bars were calculated at 1σ confidence from detection efficiencies and Poisson error statistics when not explicitly given in the published papers (Gehrels 1986). Quoted upper limits are Poisson 3σ confidence limits. The CLF is modeled by

$$\log[\Sigma(m_R)] = \alpha(m_R - m_o) \tag{2.4}$$

where $\Sigma(m_R)$ is the number of objects per square degree brighter than m_R, m_o is the magnitude at which $\Sigma = 1$ deg^{-2}, and 10^{α} describes the slope of the luminosity function.

2.4.1 The Centaurs

The current state of the CLF of Centaurs is shown in Figure 2.3. Almost half of the known Centaurs have been found by the Spacewatch program (Jedicke & Herron 1997; R. McMillan 1999, private comunication). The parameters of the Spacewatch survey have changed with time as the detector and observing strategy have been modified. Dr. Robert McMillan, head of the Spacewatch program, kindly provided estimates of the Spacewatch survey parameters (Table 2.1). Spacewatch points in Figures 2.3 and 2.4 were calculated using the total area searched with the number of Centaurs found. They are lower limits since the effective area searched is less than the reported total area searched due to some observations in marginal observing conditions and some areas covered multiple times. The Kowal (1989) Centaur

constraint is plotted with a sizeable uncertainty because of the large trailing losses incurred in long (75 minute) photographic integrations on (relatively) fast moving Centaurs. The CLF of the Kuiper Belt (c.f. §2.4.2) is overplotted on the Centaur data in Figure 2.3. A line of the same slope has been vertically shifted to run through the points having one or more Centaur detections. The offset line is consistent with every observational point shown in Figure 2.3, within the uncertainties of measurement. The Centaurs reach $\Sigma = 1$ deg^{-2} at $m_R = 24.6 \pm 0.3$. Thus, Centaurs have an apparent sky-plane-density about 10 times less than that of the KBOs at a given magnitude.

The CLF represents the convolved effects of the size and distance distributions of the objects. A Monte Carlo simulation was used to determine the total number of Centaurs larger than a certain radius. The Centaurs were assumed to follow a differential power-law radius distribution of the form $n(r)dr = \Gamma r^{-q} dr$, where Γ and q are constants, r is the radius of the Centaur, and $n(r)dr$ is the number of Centaurs with radii in the range r to $r + dr$. The radii of the Centaurs were assumed to lie between $r_{\rm min}$ and $r_{\rm max}$. To find the total number of Centaurs, we adopted $r_{\rm min} = 1$ km (since the smaller short period comets are about this size), and $r_{\rm max} = 1000$ km (about the size of the largest known Trans-Neptunian body, Pluto). The derived total number of Centaurs is insensitive to $r_{\rm max}$. The surface density distribution of Centaurs in the plane of the ecliptic varies with heliocentric distance and was assumed to be a power law of the form $n(R)dR = \Sigma_o R^{-\gamma} dR$, where Σ_o and γ are constants, R is the heliocentric distance, and $n(R)dR$ is the number of objects with heliocentric distance in the range R to $R + dR$. The heliocentric distance was taken between 10 and 30 AU. A $\gamma = -1.3$ was chosen as the most likely Centaur distance distribution based on the simulation by Levison and Duncan (1997).

The Monte Carlo simulation was performed by randomly choosing a distance and radius for up to 10^8 Centaurs from the two power law equations above. Each Centaur's apparent magnitude at opposition was then calculated using

$$m_R = m_\odot - 2.5\log(p_R r^2 \phi(\alpha)/2.25 \times 10^{16} R^2 \Delta^2) \qquad (2.5)$$

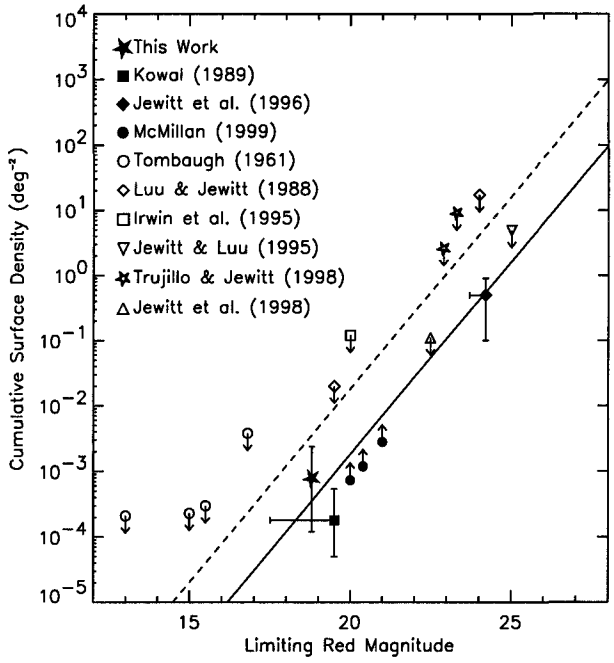

Figure 2.3 The Cumulative Luminosity Function (CLF) of the Centaurs. Symbols with down arrows represent 3σ upper limits from surveys with null results. Symbols with up arrows are lower limits. Other symbols are from published surveys. The dashed line is the fit to the KBO data in Figure 2.5. The solid line is the same fit shifted vertically to fit the Centaur CLF.

in which r is in km, R is in AU, Δ is the geocentric distance in AU taken here to be $\Delta = R - 1$, $m_\odot$ is the apparent red magnitude of the sun (-27.1), m_R is the apparent red magnitude of the Centaur, p_R is the geometric red albedo assumed to be 0.04, and $\phi(\alpha)$ is the phase function in which the phase angle $\alpha = 0$ deg at opposition and thus $\phi(0) = 1$.

The results of the Monte Carlo simulation using $q = 3.5$, 4.0, and 4.5 are shown in Figure 2.4. We obtained the total number of Centaurs with $r > 1$ km by normalizing the simulation to the CLF of the Centaurs at $m_R = 22.0$. We assumed the inclination distribution extends to ± 30 degrees in latitude from the ecliptic: the total sky area occupied by Centaurs is then about 20000 deg^2. We used the relation $N(> r) = \Gamma/(q-1)r^{q-1}$ where N is the cumulative number of Centaurs with radius greater than r to find Γ. Table 2.6 shows the results for the number of Centaurs using different assumed values of the main parameters. For the $q = 4$ index we found there are about 1×10^7 Centaurs with $r > 1$ km. Uncertainties in q of ± 0.5 correspond to uncertainties in the population of factors 3 to 4. Plausible uncertainties in γ have a smaller effect (Table 2.6).

The $q = 3.5$, 4.0 and 4.5 curves are all consistent with the Centaur CLF (Figure 2.4). If we use the closest fit $q = 4$ simulation we obtain $N(r > 50 \text{ km}) \sim 100$ (Table 2.6). The number of Centaurs with $r > 50$ km is comparable to the 300 main-belt asteroids (Tedesco et al. (1989)) in this size regime but much smaller than the 7×10^4 KBOs expected with $r > 50$ km (Jewitt et al. 1998). Our result is about an order of magnitude smaller than the result obtained by Jewitt et al. (1996). These authors detected 2 Centaurs in a narrow field survey and crudely estimated the Centaur population based on only 1 of the Centaurs and in the absence of a model of the Centaur radial distance distribution. Jedicke & Herron (1997) found, at the 99% confidence level, that there must be fewer than 250 Centaurs with $r > 50$ km (we scaled the quoted value for $r > 25$ km in Jedicke & Herron (1997) to $r > 50$ km using a q=4 index for the size distribution) and they also concluded there are 3 or fewer Centaurs with $r > 100$ km. Although all three results are consistent, our simulation using the CLF in Figure 2.3 presumably provides a superior estimate of the

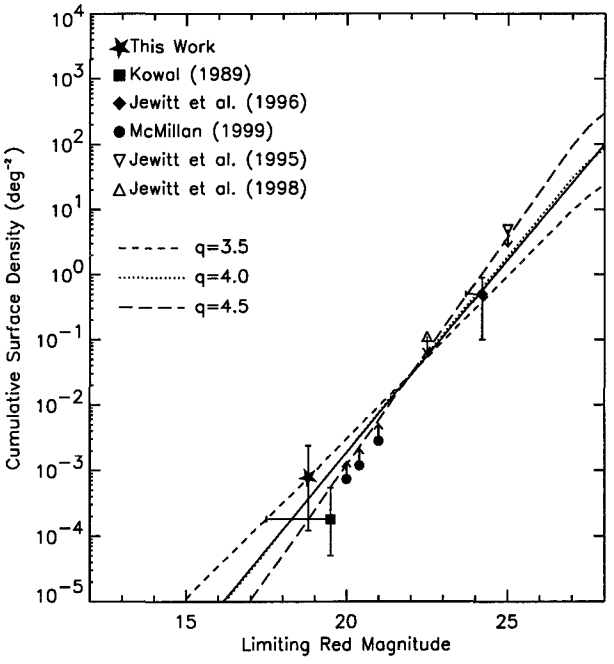

Figure 2.4 Simulation of the Cumulative Luminosity Function (CLF) of the Centaurs. This simulation used parameters q=3.5, 4.0, and 4.5 with $r_{\rm min}$ = 1 km, $r_{\rm max}$ = 1000 km, $\gamma = -1.3$, $R_{\rm min}$ = 10 AU, and $R_{\rm max}$ = 30 AU. The solid line is the fit to the KBO data shifted vertically to fit the lower Centaur CLF. See the text for an explanation of the parameters.

Table 2.6. Centaur Monte Carlo Simulation Results

q^a	γ^b	albedo	Γ	N($r > 1$)^c	N($r > 50$)^c	N($r > 100$)^c
3.0	−1.3	0.04	1.3×10^6	6.7×10^5	270	65
3.5	−1.3	0.04	7.5×10^6	3.0×10^6	170	30
4.0	−1.3	0.04	3.6×10^7	1.2×10^7	100	12
4.5	−1.3	0.04	1.8×10^8	5.0×10^7	60	5
4.0	−0.3	0.04	2.3×10^7	7.6×10^6	60	8
4.0	−0.8	0.04	3.0×10^7	1.0×10^7	80	10
4.0	−1.8	0.04	4.8×10^7	1.6×10^7	130	15
4.0	−2.3	0.04	6.3×10^7	2.1×10^7	170	20
4.0	−1.3	0.10	9.6×10^6	3.2×10^6	25	3
4.0	−1.3	0.40	1.2×10^6	3.9×10^5	3	0

[a]Index of power law size distribution

[b]Index of power law distance distribution

[c]Number of objects with radius greater than r in km

population since more Centaurs are now known and a model of the distance distribution has been incorporated.

Assuming the Centaurs are supplied by the KBOs, in steady-state we should have $N_c \sim N_k t_c/t_k$ where N_c is the number of Centaurs, N_k is the number of KBOs, t_c is the average Centaur lifetime, and t_k is the average KBO lifetime. For KBOs $t_k \approx 10^{10}$ years (Quinn et al. (1990)) and for Centaurs $t_c \approx 10^6$ to 10^7 years (Hahn & Bailey (1990), Asher & Steel (1993), Levison & Duncan 1997). With $N_k \simeq 70000$ ($r > 50$ km) KBOs (Jewitt et al. 1998), we expect $N_c \simeq 7$ to 70 ($r > 50$ km) Centaurs based on the steady state assumption. This is consistent with $N_c \sim 100$ estimated here from the CLF, and consistent with the Kuiper Belt supplying the Centaur population. Since the average Centaur lifetime expressed in years is similar to the number of Centaurs with radii greater than 1 km ($N(r > 1\text{km})/t_c \sim 1$), about one Centaur with $r \geq 1$ km must be delivered to the gas giant region per year. Duncan et al. (1995) found the fraction of KBOs which leave the Kuiper Belt from planetary interactions is 5×10^{-11} per year. Assuming that half of the

KBOs which leave the Kuiper Belt end up as Centaurs, then with 7×10^4 KBOs of r >50 km and a Centaur lifetime of 10^6 to 10^7 years we would expect between 2 to 20 Centaurs to be present with radii > 50 km, consistent with our results.

For a $q = 4$ size distribution the total mass is

$$M = \frac{4 \times 10^9 \pi \rho \Gamma}{3} \left[\frac{0.04}{p_R}\right]^{3/2} \ln\left(\frac{r_{\max}}{r_{\min}}\right) \tag{2.6}$$

where ρ (kg m^{-3}) is the bulk density. Using $\rho = 1000$ kg m^{-3} (similar to cometary nuclei), $p_R = 0.04$, $r_{\min} = 1$ km, and $r_{\max} = 200$ km (about the size of the largest known Centaur), we obtain $M \approx 8 \times 10^{20}$ kg ($\sim 10^{-4}$ $M_\oplus$) for the current total mass of the Centaurs. Assuming Centaurs have a lifetime of 5×10^6 years and are in steady state we find that 0.1 $M_\oplus$ has been cycled through the Centaurs during the 4.5×10^9 year age of the solar system. If objects as large as Pluto ($r_{max} = 1200$ km) with $\rho = 2000$ kg m^{-3} are considered then the mass cycled through the Centaurs during the age of the solar system is about 2.5 times greater than the above result. Either way it is comparable to the inferred total mass currently in the Kuiper Belt of ~0.2 $M_\oplus$ (Jewitt et al. 1998).

Centaurs are close enough to the Sun to show cometary activity (e.g., Chiron), which can lead to an overestimate of their size if assuming a constant albedo, as we have done. Observationally, most surveys are only sensitive to bright (large) Centaurs. Thus the smaller Centaur population was obtained by extrapolating from larger Centaurs which may not follow the same distribution. No survey has been specifically targeted at detecting Centaurs. Most surveys which have found Centaurs are optimized instead for finding KBOs or asteroids. This makes it hard to assess the sensitivity to Centaurs of some published surveys. Surveys plotted in Figure 3 are those which were capable of finding Centaurs in at least the range of heliocentric distances 10 AU to 30 AU. Our survey was sensitive to Centaurs from 5 to 30 AU. Only 4 of the 20 currently known Centaurs could have radii > 50 km (assuming geometric albedo 0.04) and our simulation predicts ~ 100 such objects in the whole sky. Most of them would be located near but inside the orbit of Neptune, with

apparent red magnitudes near 23. They would have naturally escaped detection in most wide field surveys conducted to date.

2.4.2 The Kuiper Belt

Surface densities of KBOs from different surveys are in reasonable agreement between $20 \lesssim m_R \lesssim 26$ (Figure 2.5). A weighted least squares fit to the CLF for all the data with at least one detection is shown in Figure 2.5 (we used only the middle of the three Tombaugh points in the fit), yielding $\alpha = 0.59 \pm 0.05$, $m_o = 23.0 \pm 0.2$. The fit is consistent with the fits found by Jewitt et al. (1998) [$\alpha \simeq 0.55 \pm 0.05$, $m_o \simeq 23.25 \pm 0.11$], Gladman et al. (1998) [$\alpha = 0.76^{+0.1}_{-0.11}$, $m_o = 23.40^{+0.20}_{-0.18}$], and Chiang & Brown (1999) [$\alpha = 0.52 \pm 0.02$, $m_o = 23.5 \pm 0.06$]. Our survey's 3σ upper limit is consistent with the constant slope of the CLF but does not rule out a steepening in the CLF for $m_R < 19$.

The above and some other previous works have improperly calculated the surface density from Tombaugh's (1961) survey (see Table 2.1 for the correct results of Tombaugh's survey). They used Tombaugh's follow up survey which was conducted to search for satellites or other objects that might be near Pluto. This survey reached $m_R = 16.8$ and covered 1530 square degrees of sky. However, Pluto was discovered in a survey which reached only $m_R = 15.5$ and covered about 28000 deg^2, initiated earlier and continued later (Table 2.1). The 1530 square degree survey should be interpreted as a null result since Pluto was not detected serendipitously. Therefore, the Tombaugh datum used in some earlier works should be shifted to brighter magnitudes and lower surface densities.

2.4.3 Collision Clouds

The Kuiper Belt was first thought to be collisionless though it now appears collisional effects might be very important (Davis & Farinella 1997). This has the result of removing the primitive and possibly unprocessed material from KBOs and might allow for dust to be observed in the Kuiper Belt. The collision products might be seen directly by the detection of dust clouds around the KBOs (Alcock & Hut 1993, Stern 1996). Assuming there are

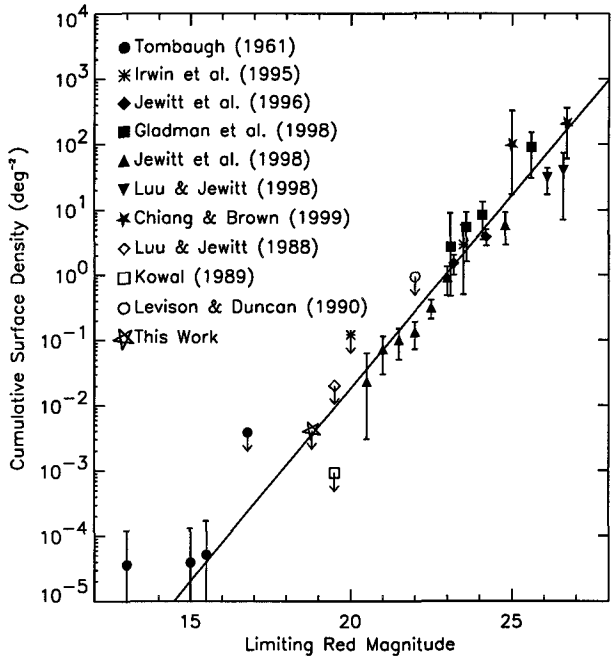

Figure 2.5 The Cumulative Luminosity Function (CLF) of the Kuiper Belt. Symbols with arrows are 3σ upper limits from surveys with null results. Other symbols are from various published surveys with 1σ error bars. The solid line is the best fit to the data.

10^9 KBOs with $r > 1$ km and that the Kuiper Belt extends ± 30 degrees from the ecliptic, Stern (1996b) and Alcock & Hut (1993) predicted between 1 and 100 collisions per year producing detectable ($m_R \lesssim 15$) dust clouds.

The characteristic expansion time of a cloud is $t \approx r/v$, where v is the expansion velocity and r is the radius of the expanding cloud. The velocity of the ejected material depends on the energy of the impact and size of the projectile and target. KBOs have Keplerian velocities of a few kilometers per second and escape velocities for 1 km objects are around 1 m s^{-1}. The cloud should reach peak brightness in reflected light when its optical depth is unity. The time to reach peak brightness is $t \approx c/v$, where c is the critical radius at which optical depth unity is reached. The critical radius depends on the size distribution of ejected particles. If constant density is assumed then the critical radius is just the square root of the geometric cross-section of the particles ($c = a[a_i/a]^{1.5}$ where a is the average radius of particles created from the initial projectile radius of a_i). The duration of visibility depends on the limiting magnitude. Using typical values of $v = 1$ to 5 km s^{-1} (the approximate expansion velocity of gas produced by impact vaporization) and a constant size of 0.1 to 10μm for particles in the cloud we find that a dust cloud should reach optical depth unity in only a few days and be brighter than red magnitude 19 for about 20 to 100 days. If 100 clouds are produced in one year and each is visible for 50 days about 14 clouds should be visible at any instant. With 14 clouds in 20,000 square degrees, we expect to find one cloud for every 1430 square degrees of sky. Owing to the large pixels of the APT our survey would not resolve one of these collision clouds if in our field of view, though we would detect the KBO type movement of any clouds brighter than $m_R = 18.8$. No dust clouds brighter than $m_R = 18.8$ were detected in 1428 square degrees of sky searched in this survey. Assuming Poisson spatial distribution this gives a 3σ confidence limit that there are < 82 clouds for 20,000 square degrees at any given time or less than 1 cloud per 244 square degrees of sky with $m_R < 18.8$. This also puts a 3σ limit of < 600 clouds produced per year with $m_R < 18.8$.

More sky must be searched to determine if Pluto is just one of several other large KBOs waiting to be discovered. If the amount of sky searched for slow moving objects were doubled, strong constraints on the bright end of the KBO CLF would be obtained. This survey was hindered by the large pixel size of the CCD. Currently CCDs four times as large and with pixels half the size are routinely available. It is our goal to continue to survey the sky for bright SMOs with a bigger CCD and smaller pixels. This will improve the efficiency of the survey and allow the data to be better sampled.

2.5 Summary

1. A total of 1428 square degrees of sky were searched for KBOs and Centaurs to a limiting magnitude of $m_R = 18.8$. One previously discovered Centaur was detected serendipitously (1997 CU26 Chariklo), and no KBOs were detected.

2. This survey, the largest published CCD survey to date sensitive to Centaurs and Kuiper Belt Objects, was analyzed both by an automated technique and by eye. The survey parameters were well established.

3. The cumulative surface density is $\Sigma_C = 7.8(^{+16.0}_{-6.6}) \times 10^{-4}$ deg^{-2} for Centaurs at $m_R = 18.8$ with error bars at the 1σ level. The Centaur cumulative luminosity function (CLF) has a slope ($\alpha \sim 0.6$) similar to the Kuiper Belt CLF but shifted about 1.5 magnitudes fainter. The number of Centaurs per unit sky area is about 1/10th the number of KBOs, at any given magnitude.

4. A Monte Carlo simulation was performed to obtain the expected number distribution of Centaurs. Differential power-law size distribution indices between q=3.5 and 4.5 are consistent with the Centaur CLF. Using q=4, we find there are about 1×10^7 Centaurs with radii larger than 1 km and ~ 100 larger than 50 km in radius, of which only 4 (Chiron, Pholus, Chariklo(1997 CU26), and 1995DW2) are presently known. The combined mass of all Centaurs is $10^{-4}\ M_\oplus$. Assuming a steady state this implies that 0.1 $M_\oplus$ has been cycled from the Kuiper Belt through the Centaurs during the age of the solar system.

5. The surface density of Kuiper Belt objects at $m_R = 18.8$ is $\Sigma_K < 4.1 \times 10^{-3}$ deg^{-2} at the 3σ confidence level. This result is consistent with the previously determined CLF for Kuiper Belt objects but does not rule out a steepening in the slope for $m_R < 19$.

6. No collisionally produced dust clouds were observed in the Kuiper Belt. We place a 3σ upper limit of < 600 visible collisional clouds ($m_R < 18.8$) produced per year.

Acknowledgments

We thank Jill Rathborne for observational assistance and Robert McMillan, Jeff Larsen, Bruce Koehn, and Steve Larson for very helpful information about their Near Earth Object surveys. This work was supported by a grant to D.J. from NASA.

Chapter 3

Rotation and Shape of Kuiper Belt Object (20000) Varuna

3.1 Abstract

We present new time-resolved photometric observations of the bright trans-Neptunian object (20000) Varuna and use them to study the rotation period, shape, and color. In observations from 2001 February and April, we find a best-fit two-peaked lightcurve with period 6.3436 ± 0.0002 hr. The peak-to-peak photometric range in the R-band is 0.45 ± 0.03 mag. We find no rotational variation in colors over the $0.45 \leq \lambda \leq 0.85 \mu$m wavelength range, suggesting that the surface is uniformly coated in a single material. From the short double-peaked period and large amplitude we suggest that Varuna is an elongated, prolate body perhaps close in shape to one of the Jacobi ellipsoids. If so, the ratio of the axes projected into the plane of the sky is 1.5:1. (20000) Varuna may be a rotationally distorted rubble pile, with a density near 1000 kg m^{-3} and a weak internal constitution due to fracturing by past impacts. The high specific angular momentum implied by our observations, together with the recent detection of three binary Kuiper Belt Objects, points to an early epoch in which collisions between large Kuiper Belt Objects were much more common than now.

3.2 Introduction

The trans-Neptunian objects (TNOs) have semi-major axes larger than that of Neptune (Jewitt & Luu (2000)) and are thought to be the products of arrested growth in the tenuous outer parts of the accretion disk of the sun (Kenyon and Luu 1999). Their large mean heliocentric distances and resulting low surface temperatures suggest that they may retain a substantial volatile fraction. Indeed, the trans-Neptunian region is widely held to be the source of the ice-rich nuclei of short period (specifically Jupiter-family) comets. In this sense, the TNOs are repositories of some of the solar system's least evolved, most primitive material. There is widespread interest in the physical (and chemical) properties of these bodies. Unfortunately, most known TNOs are too faint to permit easy investigation even when using the largest available telescopes. For this reason, bright TNO (20000) Varuna (hereafter, simply called Varuna) has already attracted considerable observational attention.

Varuna was discovered on 2000 November 28 and given the provisional designation 2000 WR106 (McMillan et al. (2000)). Prediscovery observations from 1955 were soon uncovered (Knofel and Stoss 2000), leading to the accurate determination of the orbit and the classification as a "classical TNO" (Jewitt and Luu 2000), with semimajor axis 43.274 AU, inclination 17.1° and eccentricity 0.056. Simultaneous thermal and optical observations give red geometric albedo $p_R = 0.07^{+0.030}/_{-0.017}$ and equivalent circular diameter $900^{+129}/_{-145}$ km (Jewitt, Aussel and Evans 2001). Varuna is currently one of the biggest known Kuiper Belt objects and is comparable in size to the largest main-belt asteroid, 1 Ceres. Farnham (2001) reported a rotational lightcurve from observations taken 2001 Jan $24 - 27$ with a single-peaked period 3.17 hr and "amplitude" 0.5 mag. Farnham also found other plausible periods including 2.78 and 3.67 hrs. Motivated by this spectacular result, we immediately undertook observations to secure an independent determination of the lightcurve, and to search for rotational color variations. Such variations are predicted by the impact resurfacing model (Luu & Jewitt (1996)). In this paper we will discuss

Varuna's lightcurve, possible causes of the variations, and what the variations may tell us about Varuna's physical characteristics and the Kuiper Belt collisional environment.

3.3 Observations

Optical observations were taken UT 2001 February 17 - 21 and April 22, 24 and 25 at the University of Hawaii 2.2-m telescope atop Mauna Kea, Hawaii. We used a Tektronix 2048 × 2048 pixel charge-coupled device (CCD), having 0.219 arcsec per pixel image scale and a 7 arcminute field of view. Images were secured through standard broadband BVRI filters based on the Johnson Kron-Cousins system. The CCD bias level was determined from an overclocked region of the chip. Flat field calibration was obtained using a mixture of images of the twilight sky with data frames. The image quality (including contributions from the telescope, wind shake and atmosphere) varied from 0.6 to 0.9 arcseconds Full Width at Half Maximum (FWHM), while all nights but UT 2001 February 19 were photometric. Absolute calibration of the data was obtained through repeated observations of standard stars from the list by Landolt (1992). The position of Varuna was dithered over the detector to prevent pathological problems in the photometry associated with bad pixels.

For the purposes of lightcurve determination, Varuna was compared to a network of field reference stars in each image. The field stars were selected to be near Varuna in the sky and to have Sun-like or slightly redder colors. Where possible, we employed the same field reference stars each night to minimize systematic photometric errors. This procedure effectively removes the influence of atmospheric extinction (which, at the high altitude of Mauna Kea, is already small, amounting to only about 0.08 mag. per airmass in the R-band). The latter part of the night of UT 2001 February 19 was slightly non-photometric (deviations were ~few 0.01 mag.) but, otherwise, we benefited from clear skies. Effects of seeing variations between images were minimized by using multi-aperture photometry. Small apertures (typical radii ~1 arcsec) were used to relate Varuna to the field star network in each field. Large apertures (radius 3.3 arcsec) were used to relate the field stars to the

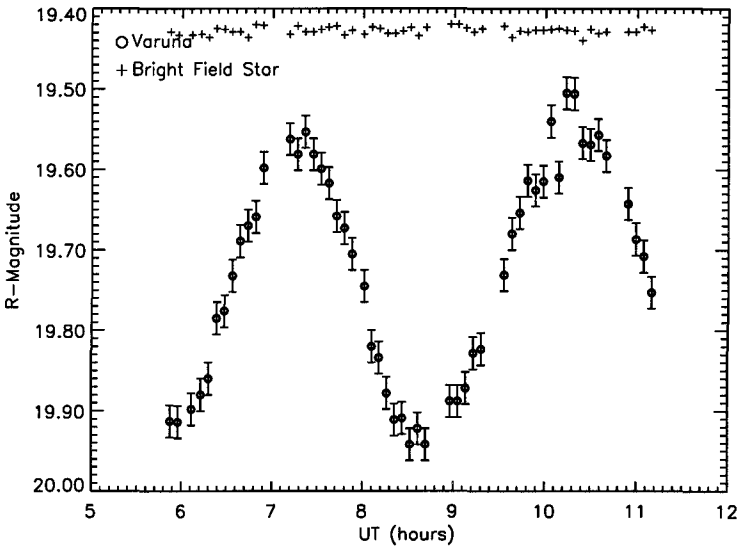

Figure 3.1 Sample rotational lightcurve data for Varuna from UT 2001 February 17. Error bars of 0.02 mag. have been plotted for reference.

Landolt standards. The median sky level was determined within a contiguous annulus having outer radius 5 arcsec. At the time of the observations, Varuna moved westward at about 2 arcseconds per hour. The image trailing due to the motion of Varuna was only $\sim$0.1 arcseconds during a typical 200 second integration. This is small compared to our 0.7 - 0.9 arcsecond FWHM image quality and, therefore, trailing losses are an unimportant source of error in our photometry.

A journal of observations including the geometric circumstances is given in Table 3.1. The R-band photometry is listed in Table 3.2. Periodicity in the photometry was obvious even in preliminary reductions of the first night's data conducted at the telescope, as may be seen in Figure 3.1.

Table 3.1. Journal of Observations for Varuna

UT Date[a] (2001)	JD[b] (2450000+)	Filters[c]	Seeing[d] [arcsec]	R[e] [AU]	Δ[f] [AU]	α[g] [deg]	t_L[h] [min]
Feb 17	1957.5	R	1.1	43.0539	42.4039	0.99	352.6621
Feb 18	1958.5	V,R	0.7	43.0540	42.4171	1.01	352.7725
Feb 19	1959.5	R,B,I	0.6	43.0542	42.4306	1.02	352.8845
Feb 20	1960.5	R	0.7	43.0543	42.4443	1.04	352.9981
Apr 22	2021.5	V,R	0.7	43.0632	43.4447	1.23	361.3187
Apr 24	2023.5	R	0.7	43.0635	43.4764	1.21	361.5823
Apr 25	2024.5	R	0.7	43.0636	43.4921	1.20	361.7126

[a]Universal Time date of the observation

[b]Corresponding Julian Date at 0hr UT

[c]Filters based on the Johnson-Kron-Cousins system

[d]Image FWHM

[e]Heliocentric Distance

[f]Geocentric Distance

[g]Phase angle

[h]Light travel time

Table 3.2: R-band Photometry of Varuna

Image[a]	UT Date [2001][b]	JD_c[c]	m_R[d]	$m_R(1,1,0)$[e]
2019	Feb 17.2447	1957.49983	19.913	3.450
2020	Feb 17.2484	1957.50464	19.914	3.451
2021	Feb 17.2547	1957.51099	19.898	3.435
2022	Feb 17.2592	1957.51550	19.880	3.417
2023	Feb 17.2627	1957.51904	19.860	3.397
2024	Feb 17.2662	1957.52246	19.785	3.322
2025	Feb 17.2698	1957.52600	19.776	3.313
2026	Feb 17.2733	1957.52954	19.732	3.269
2027	Feb 17.2769	1957.53320	19.689	3.226
2028	Feb 17.2805	1957.53674	19.670	3.207
2029	Feb 17.2840	1957.54028	19.659	3.196
2030	Feb 17.2876	1957.54382	19.598	3.135
2032	Feb 17.2998	1957.55603	19.562	3.099
2033	Feb 17.3033	1957.55957	19.581	3.118
2034	Feb 17.3068	1957.56311	19.553	3.090
2035	Feb 17.3105	1957.56677	19.581	3.118
2036	Feb 17.3140	1957.57019	19.599	3.136
2037	Feb 17.3175	1957.57373	19.617	3.154
2038	Feb 17.3211	1957.57739	19.658	3.195
2039	Feb 17.3247	1957.58093	19.673	3.210
2040	Feb 17.3282	1957.58447	19.705	3.242
2041	Feb 17.3339	1957.59009	19.745	3.282
2042	Feb 17.3374	1957.59363	19.820	3.357
2043	Feb 17.3410	1957.59717	19.834	3.371
2044	Feb 17.3445	1957.60083	19.878	3.415
2045	Feb 17.3481	1957.60437	19.911	3.448
2046	Feb 17.3517	1957.60791	19.909	3.446
2047	Feb 17.3552	1957.61145	19.942	3.479
2048	Feb 17.3588	1957.61499	19.922	3.459
2049	Feb 17.3624	1957.61865	19.942	3.479
2051	Feb 17.3736	1957.62976	19.888	3.425
2052	Feb 17.3771	1957.63342	19.888	3.425
2053	Feb 17.3807	1957.63696	19.872	3.409
2054	Feb 17.3842	1957.64050	19.829	3.366
2055	Feb 17.3878	1957.64404	19.824	3.361
2057	Feb 17.3978	1957.65405	19.731	3.268
2058	Feb 17.4014	1957.65759	19.679	3.217
2059	Feb 17.4050	1957.66125	19.654	3.191
2060	Feb 17.4085	1957.66479	19.614	3.151
2061	Feb 17.4121	1957.66833	19.626	3.163
2062	Feb 17.4157	1957.67200	19.615	3.152
2063	Feb 17.4193	1957.67554	19.540	3.077
2064	Feb 17.4228	1957.67908	19.610	3.147
2065	Feb 17.4264	1957.68262	19.505	3.042
2066	Feb 17.4300	1957.68628	19.506	3.043
2067	Feb 17.4337	1957.68994	19.567	3.104
2068	Feb 17.4373	1957.69360	19.569	3.106
2069	Feb 17.4409	1957.69714	19.557	3.094

Table 3.2: (continued)

Image[a]	UT Date [2001][b]	JD_c[c]	m_R[d]	$m_R(1,1,0)$[e]
2070	Feb 17.4445	1957.70081	19.583	3.120
2072	Feb 17.4543	1957.71057	19.643	3.180
2073	Feb 17.4579	1957.71411	19.687	3.224
2074	Feb 17.4614	1957.71765	19.708	3.245
2075	Feb 17.4650	1957.72131	19.753	3.290
3025	Feb 18.2337	1958.48987	19.536	3.071
3026	Feb 18.2396	1958.49585	19.603	3.138
3027	Feb 18.2432	1958.49939	19.613	3.148
3028	Feb 18.2468	1958.50305	19.634	3.169
3029	Feb 18.2503	1958.50647	19.661	3.196
3031	Feb 18.2575	1958.51367	19.758	3.293
3033	Feb 18.2646	1958.52075	19.836	3.371
3035	Feb 18.2718	1958.52795	19.909	3.444
3037	Feb 18.2789	1958.53503	19.939	3.474
3039	Feb 18.2861	1958.54224	19.969	3.504
3049	Feb 18.3223	1958.57849	19.799	3.334
3051	Feb 18.3295	1958.58569	19.731	3.265
3053	Feb 18.3366	1958.59277	19.673	3.208
3055	Feb 18.3439	1958.60010	19.632	3.167
3057	Feb 18.3510	1958.60718	19.581	3.116
3059	Feb 18.3582	1958.61438	19.573	3.108
3074	Feb 18.4277	1958.68384	19.931	3.466
3075	Feb 18.4314	1958.68762	19.955	3.490
3076	Feb 18.4349	1958.69104	19.864	3.399
3077	Feb 18.4385	1958.69470	19.852	3.387
3078	Feb 18.4421	1958.69824	19.833	3.368
3079	Feb 18.4457	1958.70178	19.801	3.336
3080	Feb 18.4492	1958.70532	19.766	3.301
4025	Feb 19.2381	1959.49414	19.835	3.367
4026	Feb 19.2417	1959.49780	19.798	3.330
4027	Feb 19.2452	1959.50134	19.771	3.303
4030	Feb 19.2586	1959.51465	19.628	3.160
4033	Feb 19.2753	1959.53137	19.537	3.069
4036	Feb 19.2883	1959.54443	19.544	3.076
4039	Feb 19.3016	1959.55774	19.625	3.157
4044	Feb 19.3273	1959.58350	19.891	3.423
4047	Feb 19.3405	1959.59656	19.928	3.460
4050	Feb 19.3536	1959.60974	19.951	3.483
4062	Feb 19.4036	1959.65967	19.592	3.124
4065	Feb 19.4167	1959.67285	19.565	3.097
5024	Feb 20.2402	1960.49622	19.754	3.283
5025	Feb 20.2437	1960.49976	19.792	3.321
5026	Feb 20.2473	1960.50330	19.841	3.370
5030	Feb 20.2722	1960.52820	19.961	3.490
5031	Feb 20.2758	1960.53186	19.965	3.494
5032	Feb 20.2794	1960.53540	19.933	3.462
5033	Feb 20.2830	1960.53906	19.915	3.444
5034	Feb 20.2866	1960.54260	19.893	3.422

Table 3.2: (continued)

Image[a]	UT Date [2001][b]	JD_c[c]	m_R[d]	$m_R(1,1,0)$[e]
5035	Feb 20.2902	1960.54614	19.849	3.378
5036	Feb 20.2937	1960.54980	19.855	3.384
5041	Feb 20.3273	1960.58337	19.574	3.103
5042	Feb 20.3312	1960.58716	19.565	3.094
5044	Feb 20.3430	1960.59900	19.548	3.077
5045	Feb 20.3468	1960.60278	19.569	3.098
5046	Feb 20.3506	1960.60669	19.583	3.112
5047	Feb 20.3545	1960.61047	19.566	3.095
3022	Apr 22.2417	2021.49219	19.776	3.224
3023	Apr 22.2458	2021.49634	19.746	3.194
3036	Apr 22.2861	2021.53699	19.655	3.103
3038	Apr 22.2958	2021.54663	19.745	3.193
5015	Apr 24.2523	2023.50269	19.615	3.064
5016	Apr 24.2565	2023.50696	19.616	3.065
5021	Apr 24.2853	2023.53564	19.807	3.256
5022	Apr 24.2896	2023.53992	19.857	3.306
6018	Apr 25.2382	2024.48853	20.005	3.455
6019	Apr 25.2425	2024.49280	20.037	3.487
6026	Apr 25.2863	2024.53662	19.718	3.168
6027	Apr 25.2906	2024.54089	19.695	3.145

[a] Image number.
[b] Decimal Universal Date at the start of the integration.
[c] Julian Date corrected to the midpoint of each integration and for light travel time, less 245,0000.
[d] Apparent red magnitude, uncertainties are ±0.02.
[e] Absolute magnitude found using $m_R(1,1,0) = m_R - 5\log(R\Delta) - \beta_{opp}\alpha$ where $\beta_{opp} = 0.156$ magnitudes per degree.

3.4 Results

Periodicity in the R-band photometry was sought using a) the PDM (phase dispersion minimization) method (Stellingwerf (1978)) and b) the related but different SLM (string length minimization) method (Dworetsky (1983)). The PDM and SLM results were in all cases consistent; for brevity we here present only the results from PDM. Figure 3.2 shows the PDM theta parameter as a function of rotational frequency for the entire R-band photometry data set (for an explanation of the theta parameter see Stellingwerf (1978), the closer to zero the better the period fit). Broad, deep minima occur near the lightcurve frequencies $P^{-1} = 7.57$ day^{-1} and $P^{-1} = 3.78$ day^{-1} . The first corresponds to a single-

peaked lightcurve with a period near $P = 3.17$ hr, similar to the 3.17 hr period reported by Farnham (2001). The second minimum corresponds to the double-peaked lightcurve of 6.34 hr. The minima are flanked by aliases due to the 24 hour sampling periodicity that is imposed on the data by the day-night cycle (see the theta minima in Figure 3.2 displaced from the primary by $\pm n$ day^{-1}, where $n = 1, 2, 3 ...$). The phased lightcurves produced using the 24-hr alias periods of the single-peaked lightcurve ($P^{-1} = 6.5$ day^{-1}, 8.6 day^{-1}) are unconvincing. When viewed at high resolution, the primary minimum of the theta plot for the single-peaked lightcurve is seen to be split by a finely spaced series of minima due to the ~65 day data gap between the February 2001 and April 2001 observations (Figure 3.3). The lightcurves produced by phasing the data at each of the lowest 3 minima in Figure 3.3 (3.1653, 3.1718, and 3.1782 hours) appear comparably good to the eye. In this sense, the rotation period cannot be exactly determined from the present data, although we are confident that the true period is given by one of the 3 minima in Figure 3. We adopt $P = 3.1718 \pm 0.0001$ hrs as the best fit to the single-peaked lightcurve period.

Is the lightcurve single or double-peaked? Close inspection of the raw and phased data suggests that the lightcurve of Varuna has two maxima per rotation period. This is evident even in the single night of data shown in Figure 3.1, where the brightness maxima near UT 7.2 hr and 10.2 hr have slightly different heights. It is more evident in the phased lightcurves, where the first and second lightcurve minima have slightly different shapes. Therefore, we adopt the double-peaked lightcurve ($P_{rot} = 6.3436 \pm 0.0002$ hrs) as the probable rotation period of Varuna (subject to the caveat that very nearby alias periods 6.3305 and 6.3565 hours are also plausible fits to the data as discussed for the single peaked aliases above). The lightcurve phased to this rotation period is shown in Figure 3.4.

We used the preliminary photometry to target color measurements near the extrema of the R-band brightness, in order to search for rotational color variations. Color measurements were interleaved with R-band photometry so as to correct for photometric trends caused by the rotation. The color measurements are summarized in Table 3.3 and plotted versus rotation phase in Figure 3.5. There it may be seen that our data provide no evidence

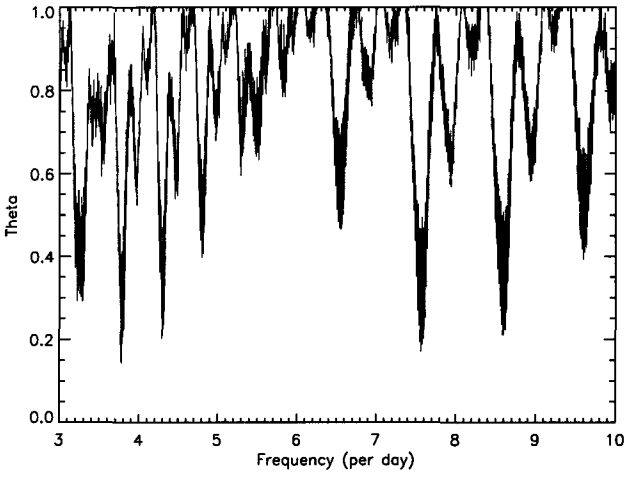

Figure 3.2 Phase dispersion minimization (PDM) plot computed from the entire R-band data set of Varuna (February 2001 and April 2001 observations). The best fit is the frequency near 3.78 cycles per day (double-peaked period of 6.34 hours). The other large peaks flanking the 3.78 frequency are the 24 hour sampling aliases. The single-peaked period is at 7.57 cycles per day (period of 3.17 hours) with associated flanking 24 hour alias periods.

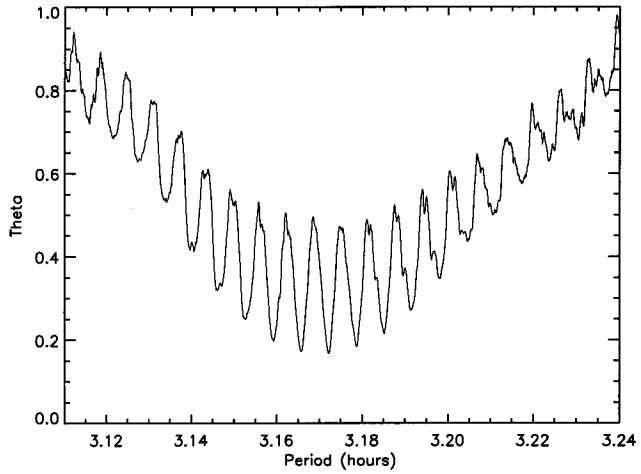

Figure 3.3 Same as Figure 2 but plotted with the Period as the x-axis and at higher resolution on the single-peaked best fit to show the aliases caused by the ~60 day gap between the February 2001 and April 2001 observations. The 3 lower peaks are all reasonable fits to the data, with the middle peak at 3.1718 hours being the best fit for the single-peaked lightcurve.

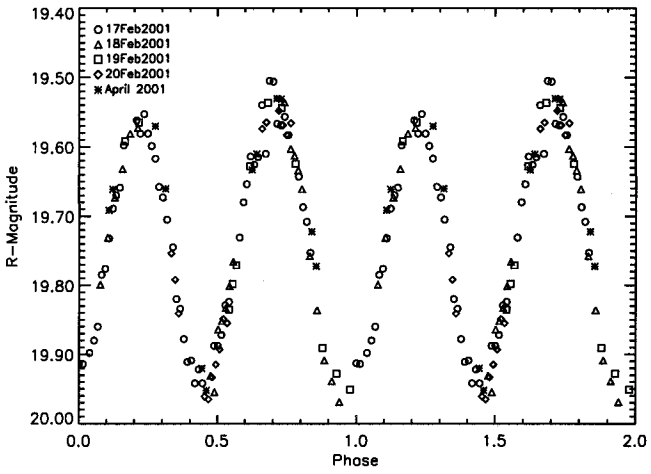

Figure 3.4 The R-band photometry of Varuna phased according to the double-peaked rotation period $P_{rot} = 6.3436$ hours. The April data has been brightened by 0.09 magnitudes to correct for the dimming effects of a higher phase angle (see Sheppard and Jewitt 2001) and further distance of Varuna compared to the February observations.

for rotational modulation of the color of the scattered radiation. Specifically, the B-V, V-R and R-I color indices are constant with rotational phase at the level of accuracy of the measurements, as seen in Table 3.3. The mean colors found for Varuna, $B-V = 0.93 \pm 0.02$, $V-R = 0.64 \pm 0.01$, $R-I = 0.55 \pm 0.01$ and $B-I = 2.12 \pm 0.02$ (Table 3.3) are compatible with the mean colors of 12 other classical TNOs measured independently (Jewitt and Luu 2001: $B-V = 1.00 \pm 0.04$, $V-R = 0.61 \pm 0.03$, $R-I = 0.60 \pm 0.04$ and $B-I = 2.22 \pm 0.10$). Although large, Varuna is not colorimetrically distinguished from the other KBOs.

Table 3.3: Color Measurements of Varuna

UT Date	Image	JD_c[a]	Phase[b]	R[c]	B-R	V-R	R-I
2001 Feb 18	3030	1958.5101	0.818	19.71	–	0.63	–
2001 Feb 18	3032	1958.5172	0.845	19.78	–	0.64	–
2001 Feb 18	3034	1958.5244	0.872	19.85	–	0.66	–
2001 Feb 18	3036	1958.5316	0.899	19.90	–	0.69	–
2001 Feb 18	3038	1958.5387	0.926	19.94	–	0.68	–
2001 Feb 18	3050	1958.5786	0.090	19.77	–	0.63	–
2001 Feb 18	3052	1958.5894	0.117	19.70	–	0.62	–

Table 3.3: (continued)

UT Date	Image	JD_c[a]	Phase[b]	R[c]	B-R	V-R	R-I
2001 Feb 18	3054	1958.5966	0.144	19.64	–	0.64	–
2001 Feb 18	3056	1958.6038	0.171	19.59	–	0.62	–
2001 Feb 18	3058	1958.6108	0.199	19.56	–	0.64	–
2001 Feb 19	4028	1959.5052	0.139	19.66	–	–	0.63
2001 Feb 19	4029	1959.5099	0.157	19.62	1.48	–	–
2001 Feb 19	4031	1959.5183	0.257	19.58	–	–	0.64
2001 Feb 19	4032	1959.5266	0.294	19.66	1.49	–	–
2001 Feb 19	4034	1959.5349	0.596	19.69	–	–	0.61
2001 Feb 19	4035	1959.5396	0.659	19.57	1.50	–	–
2001 Feb 19	4037	1959.5480	0.708	19.54	–	–	0.61
2001 Feb 19	4038	1959.5530	0.758	19.58	1.48	–	–
2001 Feb 19	4040	1959.5612	0.809	19.69	–	–	0.65
2001 Feb 19	4041	1959.5663	0.905	19.92	1.51	–	–
2001 Feb 19	4045	1959.5870	0.955	19.96	–	–	0.59
2001 Feb 19	4046	1959.5917	0.005	19.94	1.48	–	–
2001 Feb 19	4048	1959.6001	0.194	19.57	–	–	0.61
2001 Feb 19	4049	1959.6047	0.253	19.58	1.48	–	–
2001 Feb 19	4051	1959.6132	0.583	19.72	–	–	0.63
2001 Feb 19	4052	1959.6179	0.632	19.61	1.49	–	–
2001 Feb 19	4063	1959.6632	0.695	19.54	–	–	0.60
2001 Feb 19	4064	1959.6680	0.744	19.56	1.49	–	–
2001 Feb 19	4066	1959.6777	0.795	19.65	–	–	0.61
2001 Feb 19	4067	1959.6812	0.892	19.89	1.52	–	–
2001 Apr 22	3024	2021.5009	0.941	19.95	–	0.64	–
2001 Apr 22	3025	2021.5057	0.991	19.95	–	0.62	–
2001 Apr 22	3035	2021.5303	0.180	19.58	–	0.64	–
2001 Apr 22	3037	2021.5420	0.240	19.57	–	0.64	–
MEAN					1.49 ± 0.01	0.64 ± 0.01	0.62 ± 0.01

[a] Julian day at mid-exposure and corrected for light travel time, less 245,0000.

[b] Rotational phase of Varuna lightcurve with period 6.34 hours. The phase corresponds to Figure 4 where 0.45 and 0.95 are minimum light ($\sim$ 19.9) and 0.20 and 0.70 are maximum light ($\sim$ 19.5) of the double-peaked lightcurve.

[c] R magnitude interpolated to the time of the corresponding BVI data.

3.5 Interpretation

The rotational lightcurve of a Solar System body results from the combined effects of aspherical body shape and azimuthal albedo variations. Double-peaked lightcurves are the expected signature of a prolate body in rotation about its minor axis. However, this interpretation is not unique: an appropriate arrangement of albedo markings can reproduce

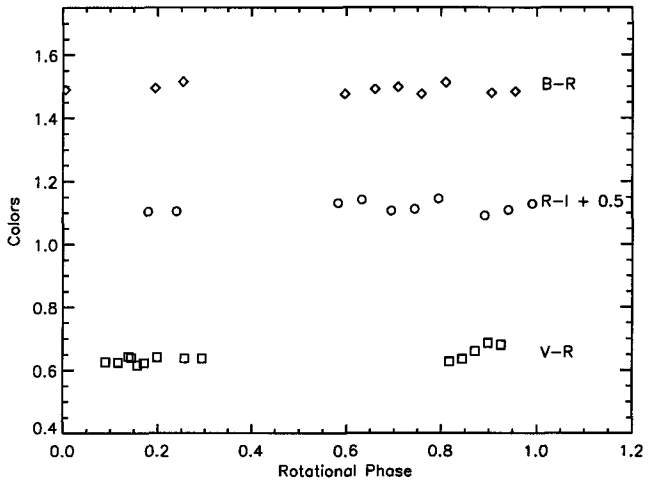

Figure 3.5 The B-V, R-I, and V-R colors of Varuna showing no significant variation over its rotation. The R-I colors have been shifted up by 0.5 magnitudes for clarity in distinguishing them from the V-R plotted colors.

any lightcurve (Russell (1906)). The large size of Varuna suggests that any elongation of the body is probably caused by a large specific angular momentum and the resulting rotational deformation. Here, we consider the two limiting cases in which a) the lightcurve is produced entirely by albedo variations across the surface of Varuna and b) the lightcurve is produced by rotational modulation of the geometric cross section of Varuna due to aspherical shape. The real situation of Varuna will naturally lie somewhere between these two extremes.

3.5.1 Albedo Models

A complex distribution of albedo markings could produce the observed lightcurve. If so, the $\Delta m_R = 0.45$ magnitude photometric range would imply an albedo contrast $10^{0.4\Delta m} \approx 3:2$ or greater (depending on the projection of the rotation vector into the line of sight). Some spherical outer Solar System bodies show large albedo contrasts, notably Iapetus and Pluto. On Iapetus, the albedo contrast is associated with a color variation, the dark material being

Table 3.4. Comparison of Rotational Color Variations

Object	Δm [mag.]	Δm(B-V) [mag.]	Reference
Varuna	0.45 ± 0.03	< 0.02	This Work
Iapetus	~ 2	$0.07 - 0.10$	Millis (1977)
Pluto	0.35	0.01	Buie, Tholen and Wasserman (1997)

redder than the bright material (Table 3.4). Rotational color variations on Varuna as large as those on Iapetus would be apparent in our data if they were present. Pluto's hemispherical albedo contrast is matched by a corresponding color variation that is barely measurable even in this bright object (Table 3.4). Large color differences exist between local surface units on Pluto ($0.77 \leq B - V \leq 0.98$; Young et al. (2001)) but hemispherically averaged color variations occur only at the 0.01 mag. level and are so small that they would not be detected in the present work (Table 3.4). From the example set by Pluto, we conclude that the absence of color variations on Varuna larger than a few $\times 0.01$ magnitudes places no useful constraint on the albedo modulation hypothesis.

If Varuna is spherical and rotating at period P, we can obtain a lower limit to the density by requiring that the body not be in a state of internal tension. Simple force balance then gives

$$\rho = \frac{3\pi}{GP^2} \tag{3.1}$$

where $G = 6.67 \times 10^{-11}$ [N kg^{-2} m^2] is the Gravitational Constant and $P[s]$ is the rotation period. With $P = 3.17$ hr, Equation (3.1) gives a lower limit to the density as $\rho = 1090$ kg m^{-3}. This geometry is unphysical, however, because a body as large as Varuna will almost certainly not possess the strength needed to maintain spherical shape when rotating with a 3 hr period (note that rotations of the comparison objects Iapetus

and Pluto are tidally locked, with periods 79 and 6.4 *days*, respectively, so that rotational deformation is small). Accordingly, we next discuss models in which the shape, not the albedo, is primarily responsible for the observed lightcurve variations (3.5).

3.5.2 Shape Models

A more likely model is one in which Varuna is rotationally deformed by the centripetal forces associated with its rapid rotation. As in the main-belt of asteroids, large impacts that do not completely destroy a body may disrupt it into a self-gravitationally bound "rubble pile" (Farinella et al. (1981)). Rubble-pile bodies will re-assemble after impact into a shape determined by their angular momentum, H, and density, ρ. Following the convention of Chandrasekhar (1987), we write the angular momentum in units of $(GM^3a')^{1/2}$, where G is the Gravitational constant, M [kg] is the body mass and a' [m] is the radius of the equal-volume sphere. At $H = 0$, the equilibrium shape is the sphere. As H increases, the shape deforms first into an oblate (so- called MacLaurin) spheroid in rotation about its minor axis (Chandrasekhar 1987). The MacLaurin spheroids become progressively more flattened up to the critical value $H = 0.304$, above which the body becomes triaxial (a Jacobi spheroid). At $H \geq 0.390$, the Jacobi spheroids are rotationally unstable and the object splits into a binary. This rotational deformation sequence is highly idealized when applied to solid bodies, of course, because even a rubble pile will not respond to rotational stresses in the same way as a perfectly strengthless fluid. A fractured body will have a "grainy" structure, perhaps with large, coherent internal blocks that will retain expression in the final body shape. Nevertheless, the MacLaurin-Jacobi spheroids represent a limiting case with which the asteroids and TNOs may usefully be compared. Evidence for the existence of rubble-piles among the main-belt asteroids is limited and indirect but nevertheless suggestive. Small asteroids ($D \leq 100$ km) have a distribution of body shapes that is consistent with those of fragments from hypervelocity impact experiments in the laboratory (Catullo et al. (1984)). On the other hand, larger asteroids are deficient in highly elongated bodies relative to the fragment shape distribution, perhaps because their shapes have relaxed towards rotational

equilibrium (Farinella et al. 1981). KBOs larger than about 100 km are massive enough to survive collisional disruption over the age of the solar system but may nevertheless have been internally fractured into rubble piles (Farinella & Davis (1996)).

An oblate spheroid in principal axis rotation about its axis of maximum moment of inertia offers no rotational modulation of the cross-section. We conclude that the MacLaurin spheroids cannot explain the lightcurve of Varuna, and that $H > 0.304$ for this object. However, the triaxial Jacobi spheroids with $0.304 \leq H \leq 0.390$ present plausible solutions for the shape of Varuna. For the Jacobi spheroids, knowledge of the rotation period and the shape (from Δm) provide a unique measure of the density. With $P = 6.34$ hr and axis ratio $10^{0.4\Delta m} \approx 3:2$, we obtain $\rho = 1050$ kg m^{-3} from the tables of Chandrasekhar (1987). Since the axis ratio is a lower limit (because of projection), the density is also a lower limit. This value is close to the density estimated from the spherical albedo model, above, but has the advantage that it derives from a physically more plausible model. A Jacobi ellipsoid's three axes ($a > b > c$) depend strongly on each other. By using the axis ratio for a and b above we find the ratio for all three as 3:2:1.4 (Chandrasekhar 1987). Here 1.4 refers to the rotation axis (c) which can not be observed directly through the lightcurve if the object is in principal axis rotation.

3.5.3 Binary

We also consider the possibility that Varuna is a binary, in which case the lightcurve would result from occultation of one component by the other. The short period and lightcurve shape of Varuna require that the binary components must be close or even in contact, leading to mutual gravitational deformation of the components. We will consider these effects momentarily. However, it is physically illuminating to first discuss the limiting case in which the binary components retain a spherical shape. Suppose that the primary and secondary components have radii a_p and a_s, respectively. The barycenter of the contact binary will be separated from the center of the secondary by a distance

$$l = (a_p + a_s)\left(\frac{m_p}{m_p + m_s}\right) \tag{3.2}$$

where m_p and m_s are the masses of the primary and secondary, respectively. Force balance then gives a relation between the angular frequency, density and mass ratio, namely $l\omega^2 = Gm_p/(a_p + a_s)^2$. Assuming that both components have density ρ [kg m^{-3}], we obtain

$$\rho = \frac{3\pi}{GP^2}\left[\frac{(1 + (a_s/a_p))^3}{1 + (a_s/a_p)^3}\right] \tag{3.3}$$

The ratio a_s/a_p can be estimated from the photometric range of the lightcurve. Specifically, the range in magnitudes is given by

$$\Delta m = 2.5\log\left[\frac{a_s^2 + a_p^2}{a_p^2}\right] \tag{3.4}$$

which can be rearranged to yield

$$\frac{a_s}{a_p} = (10^{0.4\Delta m} - 1)^{1/2} \tag{3.5}$$

The Varuna lightcurve range ($\Delta m = 0.45$ mag.) suggests an axis ratio $a_s/a_p = 0.72$ by Equation 3.5, corresponding to mass ratio $m_s/m_p = (a_s/a_p)^3 = 0.37$. Equations 3.3 and 3.5 can be combined to give

$$\rho = \frac{3\pi}{GP^2}\left[\frac{(1 + (10^{0.4\Delta m} - 1)^{1/2})^3}{1 + (10^{0.4\Delta m} - 1)^{3/2}}\right] \tag{3.6}$$

which defines the density in terms of the two observable quantities P and Δm. Substitution of $P = 6.3$ hrs, $\Delta m = 0.45$ mag. into Equation 3.6 gives $\rho = 920$ kg m^{-3}. This is a lower limit to the density since the observations provide only a lower limit to Δm, because of the effects of projection. However, given the crudeness of this model, it is interesting that we obtain essentially the same density as from the Jacobi spheroid approximation. We conclude that binary models with the observed period and physically

Table 3.5. Shape Models and Density For Varuna

Model	Shape	Axis Ratios	Density [kg m^{-3}]
Albedo Spots	Sphere	1:1:1	$\geq$ 1090
Jacobi	Ellipsoid	$\geq$1.5:1.0:0.7	$\geq$ 1050
Binary	Contact Spheres	$\geq$1.4:1	$\geq$ 920
Binary	Roche Ellipsoids	1.06:1, 1.67:1	3600

plausible densities can account for the Varuna lightcurve. There remains, however, no specific evidence that Varuna is a binary object.

Lastly, Leone et al. (1984) present calculations that partially account for the mutual deformation of the components in a close binary. The solutions are non-unique, since different combinations of m_s/m_p and density lead to the same P, Δm pair. Here, we simply refer to their Table 1, and note a plausible solution near $\rho \approx 3600$ kg m^{-3} and $m_s/m_p \approx 0.2$. A higher bulk density is required than in our simple, spherical contact binary model since the components are more widely separated (the Roche radius is $\approx$ twice the component radius) and therefore orbit more slowly for a given mass. For several reasons we believe the Roche model and the Leone et al. calculations are not well-suited to the case of Varuna. In particular, the wide separation reduces the probability that the system would be aligned so as to produce mutual eclipses. Furthermore, the nearly sinusoidal lightcurve shape is not easily produced by a wide pair in which we would expect the eclipses and occultations to occupy a smaller fraction of rotational phase space. Varuna's lightcurve does not show the notched appearance characteristic of eclipsing binary stars.

3.6 Discussion

3.6.1 Density

The nuclei of short-period comets are now widely thought to originate as fragments of TNOs (Farinella and Davis 1996). Published estimates of comet nucleus densities cluster

near $500 - 1000$ kg m^{-3} (Sagdeev et al. (1988), Rickman (1989), Asphaug & Benz (1996)) but these are all indirectly obtained and, therefore, highly uncertain. Such densities would be consistent with derivation of the comets from the TNOs, given our estimate of the density of Varuna.

Several of the outer planet satellites are similar to Varuna in both size and density. For example, Saturnian satellite SIII Tethys has density $\rho = 1210 \pm 160$ kg m^{-3} and is 524 ± 5 km in radius (Smith et al. (1982)). The Uranian satellite UII Umbriel has density 1440 ± 280 kg m^{-3} and radius 595 ± 10 km (Smith et al. (1986)). Both have tidally locked rotation periods measured in days, not hours, and are nearly spherical in shape. If rotating with Varuna's angular momentum, they would both adopt prolate body shapes and display large rotational lightcurves. Physical models show that densification due to central compression becomes important for ice bodies with radii ≥ 500 km (Lupo & Lewis (1979)) but even the much larger and, presumably, self-compressed object Iapetus (radius 730 ± 10 km) has a low density of only 1160 ± 90 kg m^{-3} (Smith et al. 1982). Pluto and Charon have $\rho \approx 2000$ kg m^{-3} (Tholen & Buie (1997)), requiring a greater rock fraction than in Varuna or the satellites mentioned above. The 50 km diameter and (presumably) rocky main-belt asteroid 253 Mathilde is of surprisingly low density (1300 ± 200 kg m^{-3}; Yeomans et al. (1997)), perhaps reflecting internal porosity.

Varuna is one of the largest known trans-Neptunians, with a diameter $D = 900(+125/-145)$ km (1σ error bars; Jewitt, Aussel and Evans 2001). Even the 3σ lower limit to the diameter, 465 km, leaves this as an object of imposing dimensions. For comparison, there are a few large asteroids which have both large photometric ranges and short periods. Notable examples include 15 Eunomia (diameter 256 km, period 6.08 hr, photometric range 0.56 mag.), 87 Sylvia (270 km, 5.18 hr, 0.62 mag.) and 107 Camilla (222 km, 4.84 hr, 0.52 mag.). Like Varuna, these may be bodies of low strength which are rotationally deformed due to a large amount of angular momentum delivered by collisions (Farinella et al. 1981). We conclude that neither the elongated shape nor the derived low density of Varuna is exceptional when viewed in the context of other, better known solar system bodies.

3.6.2 High Angular Momentum in the Kuiper Belt

The preceeding discussion indicates that Varuna must possess a high specific angular momentum, $0.304 \leq H \leq 0.390$, close to the value needed to cause rotational breakup. This immediately suggests a parallel with the 3 known Kuiper Belt binaries, Pluto-Charon (Tholen and Buie 1997), 1998 WW31 (Veillet et al. (2002)) and 2001 QT297 (Elliot & Osip (2001)). Of these systems, Pluto-Charon is by far the best known. There, the angular momentum is primarily contained within the orbital motion of the components (i.e. the spin angular momentum is small). If the mass and angular momentum of Pluto and Charon were to be combined into a single body, that object would have $H \approx 0.45$ (McKinnon (1989)) and would be unstable to rotational breakup. This high angular momentum suggests that Pluto and Charon were formed by a glancing impact between precursor objects. The other two known binaries are not yet well characterised, but they are clearly candidates for formation in a similar way. We believe that Varuna is an intermediate case in which a collision between massive precursors produced spin rapid enough to cause global deformation but not sufficient to cause rotational breakup.

The current collision rate amongst Kuiper Belt Objects is too low to substantially modify the spin of objects as large as Pluto and Varuna. Instead, their H must have been acquired through collisions in the $\sim$ 100 Myr (Kenyon and Luu 1999) formation period. We use this to constrain the collisional environment in the young Kuiper Belt. Since the applicable parameters are not well known, an order of magnitude (particle in a box) type calculation is appropriate. Our objective is to estimate the density of objects in the Kuiper Belt needed to produce collisional breakup of a measurable fraction of the Varuna-sized objects within the 100 Myr formation period. Collisional breakup does not guarantee the formation of a binary, and may not lead to a high specific angular momentum in the target object, but it is a necessary step towards these ends.

We first represent the KBO size distribution by a power law, in which the number of objects per unit volume with radii in the range a to $a + da$ is $n(a)da = \Gamma a^{-q} da$, where Γ

and q are constants. The timescale for the collisional disruption of a non-rotating, spherical target KBO of radius a_T is given by

$$\tau^{-1} = \int_{a_C}^{\infty} 4\pi \left(a_T + a\right)^2 \Gamma a^{-q} \Delta V da. \tag{3.7}$$

Here, a_C is the critical radius of the smallest projectile capable of producing disruption and ΔV is the impact velocity. The constant Γ is obtained from the data by normalizing to the Kuiper Belt population, such that

$$\int_{a_{50}}^{\infty} \Gamma a^{-q} da = \frac{N_{50}}{W} \tag{3.8}$$

where N_{50} is the number of KBOs larger than a_{50} = 50 km in radius, and W is the effective volume swept by the classical KBOs. We take q = 4, ΔV = 1.3 km s^{-1}, N_{50} = 4 $\times 10^4$ (Trujillo, Jewitt and Luu 2001) and represent the classical belt as an annulus with inner and outer radii of 40 AU and 50 AU, respectively, and thickness 10 AU, giving $W \approx 9.5 \times 10^{38}\ m^3$. Hence, Γ = 1.6 $\times 10^{-20}$ by Eq. (3.8).

For spherical target and projectile KBOs of equal density, the critical projectile radius for disruption is given by

$$\frac{a_C}{a_T} = \left(\frac{2\epsilon}{\Delta V^2}\right)^{1/3}. \tag{3.9}$$

where $\epsilon \approx 10^5\ Jkg^{-1}$ is the specific energy for disruption (Love & Ahrens (1996)).

Combining these relations and substituting, we obtain

$$\tau \approx 10 Gyr \left[\frac{a_T}{1km}\right] \left[\frac{4 \times 10^4}{N_{50}}\right] \tag{3.10}$$

as our estimate of the collisional lifetime of a KBO of radius a_T in the present day, low-density Kuiper Belt. Varuna-scale objects ($a_T \sim$ 450 km) have lifetimes to collisional disruption $\tau \sim 4.5 \times 10^{12}$ yr (Eq. 3.10), much longer than the 4.6 $\times 10^9$ yr age of the

solar system (Farinella and Davis 1996). Under these circumstances, collisionally produced binaries and objects of high specific angular momentum should not be common.

The frequencies of occurence of rotationally distorted and binary KBOs both remain to be determined with accuracy. However, from the available data it appears likely that large amplitude objects like Varuna are common, as are binary KBOs. We conservatively estimate that a fraction $f \geq 1\%$ of the KBOs are binaries and/or rotationally distorted objects of high intrinsic angular momentum. If the formation phase took $\tau_f \sim 10^8$ yr (Kenyon and Luu 1999), then the disruption timescale is of order $f^{-1}\tau_f \leq 10^{10}$ yrs. With this timescale and $a_T = 450$ km (for Varuna), Eq. (3.10) gives $N_{50} \sim 2 \times 10^7$, about 450 times the current number of large KBOs. The current mass of the KBOs is about 0.1 $M_\oplus$ (Jewitt, Luu and Trujillo 1998; Trujillo, Jewitt and Luu 2000). We infer an initial mass $M_i \geq 45\ M_\oplus$ in the Classical region of the Kuiper Belt. Numerical accretion calculations give the time for Kuiper Belt objects to grow to 1000 km scale as $\tau \sim 280$ Myr (10 $M_\oplus$ / M_i) (Kenyon and Luu 1999). Substituting for M_i we obtain $\tau \sim 60$ Myr. The collisional events leading to Varuna's rapid rotation and the break-up of KBOs occured at the end of this period, once the velocity dispersion was pumped up towards its current, high value.

On-going measurements of the lightcurves, spin states and binarity of a statistical sample of TNOs will show the extent to which the shapes of these bodies are determined by their angular momenta (see Sheppard and Jewitt 2002). Detection of a large proportion of high H objects would strengthen our conclusion that the past environment in the Kuiper Belt was one in which collisions between massive bodies were common.

3.7 Summary

1) High precision, time series photometry of trans-Neptunian object (20000) Varuna reveals a sustained, periodic modulation of the apparent brightness. In data from 2001 February and April, the best-fit rotation period is double-peaked with a 6.3436 ± 0.0002 hour period. The photometric range is $\Delta m = 0.45 \pm 0.03$ mag. The B-V, V-R and R-I colors are

completely typical of TNOs and show no variation with rotational phase, down to the level of a few per cent.

2) We interpret Varuna as a centripetally distorted, prolate ellipsoid, with an axis ratio $\geq$ 3:2 and density $\rho \approx 1000$ kg m^{-3}. The specific angular momentum, $0.304 \leq H \leq 0.390$, is high (objects with $H > 0.390$ are rotationally unstable and break up).

3) The high specific angular momentum of Varuna cannot have been supplied by collisions in the present-day, low-density Kuiper Belt. High H leading to rotational deformation and binary formation suggests an early, high density phase in the Kuiper Belt. We infer an initial mass $M_i \geq 45\ M_\oplus$ from the apparently high incidence of binaries and rapidly rotating Kuiper Belt Objects.

Acknowledgments

We thank John Dvorak and Paul deGrood for operating the UH telescope. This work was supported by a grant to DCJ from the National Science Foundation.

Chapter 4

Time-Resolved Photometry of Kuiper Belt Objects: Rotations, Shapes and Phase Functions

4.1 Abstract

We present a systematic investigation of the rotational lightcurves of trans-Neptunian objects based on extensive optical data from Mauna Kea. Four of 13 objects (corresponding to 31%) in our sample ((33128) 1998 BU_{48}, 2000 GN_{171}, (20000) Varuna and 1999 KR_{16}) were found to exhibit lightcurves with peak-to-peak range ≥ 0.15 magnitude. In a larger sample obtained by combining our data with reliably determined lightcurves from the literature, 7 of 22 objects (32%) display significant (≥ 0.15 magnitude range) lightcurves. About 23% of the sampled objects have lightcurve ranges ≥ 0.4 magnitudes. Curiously, the objects are very large ($\gtrsim 250$ km diameter, assuming an albedo of 0.04) and, in the absence of rotation, should be near spherical due to self compression. We propose that the large amplitude, short period objects are rotationally distorted, low density rubble piles. Statistically, the trans-Neptunian objects are less spherical than their main-belt asteroid counterparts, indicating a higher specific angular momentum perhaps resulting from the formation epoch. In addition to the rotational lightcurves, we measured phase darkening for 7 Kuiper Belt objects in the 0 to 2 degree phase angle range. Unlike Pluto, the measured values show steep slopes and moderate opposition surge indicating backscatter from low albedo porous surface materials.

4.2 Introduction

More than 500 Trans-Neptunian Objects (TNOs) have been discovered in the decade since the discovery of 1992 QB_1 (Jewitt & Luu 1993). These objects comprise the Kuiper Belt (also known as the Edgeworth-Kuiper Belt) which is thought to contain about 70,000 objects with radii greater than 50 km (Jewitt, Luu and Chen 1996). The Kuiper Belt is thought to be a relic from the original protoplanetary disk, albeit one that has been dynamically disturbed and collisionally processed in ways that are not yet fully understood.

The Kuiper Belt is the most likely source of the Jupiter-family comets (Fernandez 1980, Duncan, Quinn and Tremaine 1988). It is by far the largest long-lived reservoir of small bodies in the planetary region, outnumbering the main-belt asteroids and Jovian Trojans by a factor of $\sim$ 300. The Kuiper Belt Objects (KBOs) are further thought to be chemically primitive, containing trapped volatiles and having experienced relatively little thermal evolution since formation. Thus we may be able to probe some aspects of the early history of the local solar nebula by studying the Kuiper Belt and related objects.

The determination of the physical characteristics of the KBOs has proceeded very slowly. This is because even the brightest known KBOs (other than Pluto and Charon) reach only apparent red magnitude $m_R \sim 19.5$ and thus are challenging with current spectroscopic technology. The surfaces of KBOs may have been altered over their lifetimes by collisions, cometary activity, and irradiation. The largest KBOs might even be partially differentiated from radiogenic heating. This could lead to the spinning up of objects to conserve angular momentum. Colors of the KBOs have been found to be diverse, ranging from neutral to very red (V-R$\sim$ 0.3 to V-R$\sim$ 0.8) (Luu & Jewitt 1996; Green et al. 1997; Tegler & Romanishin 2000; Jewitt & Luu 2001). While spectra of KBOs are mostly featureless, some show weak 2μm water ice absorptions (Brown, Cruikshank, & Pendleton 1999; Jewitt & Luu 2001). Most KBOs are too distant ($\gtrsim$ 30 AU) and small to resolve with current technology. They are also very cold objects ($\sim$ 50K) which emit most of their thermal radiation in the inaccessible far infrared wavelengths, requiring observations from above the

Earth's atmosphere. Thus the most feasible way to determine KBOs shapes and surface features is through their photometric light variations.

The rotations and shapes of the KBOs may be a function of their size. Small KBOs (diameters $D < 100$ km) are thought to be collisionally produced (Farinella and Davis 1996). These objects retain no memory of the primordial angular momentum of their parent bodies. Instead, their spins are presumably set by the partitioning of kinetic energy delivered by the projectile responsible for break-up. Larger objects may be structurally damaged bodies held together by gravity (rubble piles). The spins of these objects should be much less influenced by recent impacts. A similar situation prevails in the main asteroid belt, where collisional modification of the rotations and shapes of the smaller objects is observationally well established (Catullo et al. 1984). The large objects in both the main-belt and the Kuiper Belt may provide a record of the primordial distribution of angular momenta imbued by the growth process. A key attribute of the Kuiper Belt is that the population is very large compared to the main asteroid belt, allowing access to a substantial sample of objects that are too large to have been influenced by recent collisions.

We here use voluminous time resolved photometric observations to determine the rotational lightcurves, colors, and phase functions of KBOs. As our sample, we select the intrinsically brightest (presumably largest) KBOs. Specifically, we observed KBOs having absolute magnitude $H_R \leq 7.5$, corresponding to $D \geq 200$ km if a red geometric albedo of $p_R = 0.04$ is assumed. We use most of the known KBOs with $H_R \leq 6.0$ which corresponds to $D \geq 375$ km in our analysis. The objects observed were all bright in order to guarantee high signal-to-noise ratios in short exposures to adequately sample the KBO lightcurves.

4.3 Observations

The University of Hawaii 2.2 m diameter telescope atop Mauna Kea in Hawaii was used with a 2048 × 2048 pixel Tektronix CCD (24 μm pixels) and a $0.''219$ pixel^{-1} scale at the f/10 Cassegrain focus. An antireflection coating provides very high average quantum

efficiency (0.90) in the R-band. The field-of-view was $7'.5 \times 7'.5$. Exposures were taken using BVRI filters based on the Johnson-Kron-Cousins system, while the telescope was autoguided on bright nearby stars. The seeing ranged from $0''.6$ to $1''.5$ during the many nights of observation throughout 1999, 2000, and 2001. Objects moved relative to the fixed stars at a maximum of $4''$ hr^{-1} corresponding to trail lengths $\leq 0''.45$ in the longest (400 sec) exposures. Even for the fastest moving objects in the longest exposures the trailing motion is small compared to the seeing and so can be neglected as a source of error in the photometry.

Table 4.1: Geometrical Circumstances of the Observations

Name		UT Date	R (AU)	Δ (AU)	α (deg)
(38628)	2000 EB_{173}	2001 Feb 21	29.77	29.12	1.45
(38628)	2000 EB_{173}	2001 Apr 21	29.75	28.77	0.47
(38628)	2000 EB_{173}	2001 Apr 22	29.74	28.77	0.49
(38628)	2000 EB_{173}	2001 Jun 30	29.71	29.52	1.93
(26375)	1999 DE_9	2000 Apr 28	33.79	33.36	1.55
(26375)	1999 DE_9	2000 Apr 30	33.79	33.39	1.58
(26375)	1999 DE_9	2000 May 1	33.79	33.40	1.59
(26375)	1999 DE_9	2001 Feb 19	33.96	32.98	0.18
(26375)	1999 DE_9	2001 Feb 21	33.96	32.97	0.12
(26375)	1999 DE_9	2001 Apr 24	34.00	33.47	1.45
(26375)	1999 DE_9	2001 Apr 25	34.00	33.49	1.47
(26181)	1996 GQ_{21}	2001 Feb 21	39.25	38.75	1.26
(26181)	1996 GQ_{21}	2001 Apr 20	39.28	38.27	0.12
(26181)	1996 GQ_{21}	2001 Apr 21	39.28	38.27	0.11
(26181)	1996 GQ_{21}	2001 Apr 22	39.28	38.27	0.11
(26181)	1996 GQ_{21}	2001 Apr 23	39.28	38.28	0.11
(26181)	1996 GQ_{21}	2001 Apr 25	39.28	38.28	0.14
	2000 GN_{171}	2001 Apr 20	28.80	27.82	0.44
	2000 GN_{171}	2001 Apr 21	28.80	27.82	0.48
	2000 GN_{171}	2001 Apr 22	28.80	27.83	0.51
	2000 GN_{171}	2001 Apr 23	28.80	27.83	0.54
	2000 GN_{171}	2001 Apr 24	28.80	27.84	0.58
	2000 GN_{171}	2001 Apr 25	28.80	27.84	0.61
	2000 GN_{171}	2001 May 11	28.79	27.95	1.11
	2000 GN_{171}	2001 May 12	28.79	27.96	1.14
	2000 GN_{171}	2001 May 13	28.79	27.97	1.17
(19521) Chaos	1998 WH_{24}	1999 Nov 09	42.39	41.42	0.28
(19521) Chaos	1998 WH_{24}	1999 Nov 10	42.39	41.42	0.26
(33340)	1998 VG_{44}	1999 Nov 11	30.46	29.49	0.32
(33340)	1998 VG_{44}	1999 Nov 12	30.46	29.48	0.29
	2001 FZ_{173}	2001 Apr 24	33.23	32.42	1.04

Table 4.1: (continued)

Name		UT Date	R (AU)	Δ (AU)	α (deg)
	2001 FZ_{173}	2001 Apr 25	33.23	32.43	1.06
(33128)	1998 BU_{48}	2001 Feb 21	27.60	26.64	0.45
(33128)	1998 BU_{48}	2001 Apr 25	27.68	27.42	2.02
(33128)	1998 BU_{48}	2001 Nov 14	27.93	27.96	2.03
(33128)	1998 BU_{48}	2001 Nov 16	27.94	27.92	2.03
(33128)	1998 BU_{48}	2001 Nov 17	27.94	27.91	2.03
(33128)	1998 BU_{48}	2001 Nov 18	27.94	27.89	2.03
(33128)	1998 BU_{48}	2001 Nov 19	27.94	27.88	2.03
	1999 KR_{16}	2000 Apr 28	38.04	37.05	0.31
	1999 KR_{16}	2000 Apr 30	38.03	37.05	0.36
	1999 KR_{16}	2000 May 01	38.03	37.06	0.38
	1999 KR_{16}	2001 Feb 18	37.84	37.33	1.30
	1999 KR_{16}	2001 Feb 19	37.84	37.32	1.28
	1999 KR_{16}	2001 Apr 24	37.80	36.80	0.16
	1999 KR_{16}	2001 Apr 25	37.80	36.80	0.18
	1999 KR_{16}	2001 May 11	37.80	36.86	0.59
	1999 KR_{16}	2001 May 12	37.79	36.86	0.62
	1999 KR_{16}	2001 May 13	37.79	36.87	0.64
	1997 CS_{29}	2001 Feb 21	43.59	42.77	0.73
	2001 CZ_{31}	2001 Feb 20	41.41	40.47	0.44
	2001 CZ_{31}	2001 Feb 21	41.41	40.48	0.46
	2001 CZ_{31}	2001 Apr 20	41.41	41.19	1.36
	1998 HK_{151}	2001 May 01	30.38	29.40	0.46
	1998 HK_{151}	2001 May 02	30.38	29.40	0.43

The images were bias subtracted and then flat-fielded using the median of a set of dithered images of the twilight sky. Landolt (1992) standard stars were used for the absolute photometric calibration. Photometry of faint objects, such as the KBOs, must be done very carefully to achieve accurate results. To optimize the signal-to-noise ratio we performed aperture correction photometry by using a small aperture on the KBOs (0.″65 to 0.″88 in radius) and both the same small aperture and a large aperture (2.″40 to 3.″29 in radius) on (four or more) nearby bright field stars. We corrected the magnitude within the small aperture used for the KBOs by determining the correction from the small to the large aperture using the field stars (c.f. Tegler and Romanishin 2000; Jewitt & Luu 2001). Since the KBOs moved slowly we were able to use the same field stars from night to night within each observing run. Thus relative photometric calibration from night to night was very constant. The few observations that were taken in mildly non-photometric conditions

Table 4.2. Parameters of Observed Objects[a]

Name		Class[b]	H (mag)	i (°)	e	a (AU)
(38628)	2000 EB_{173}	R	4.7	15.5	0.273	39.3
(20000) Varuna	2000 WR_{106}	C	3.7	17.1	0.055	43.2
(26375)	1999 DE_9	S	4.7	7.6	0.423	55.9
(26181)	1996 GQ_{21}	S	5.2	13.4	0.588	92.8
	2000 GN_{171}	R	5.8	10.8	0.279	39.3
(19521) Chaos	1998 WH_{24}	C	4.9	12.0	0.110	46.1
(33340)	1998 VG_{44}	R	6.5	3.0	0.260	39.6
	2001 FZ_{173}	S	6.2	12.2	0.622	88.0
(33128)	1998 BU_{48}	S	7.2	14.2	0.387	33.5
	1999 KR_{16}	C	5.8	24.9	0.298	48.5
	1997 CS_{29}	C	5.2	2.2	0.015	44.2
	2001 CZ_{31}	C	5.5	10.2	0.097	45.3
	1998 HK_{151}	R	7.6	6.0	0.224	39.1

[a]Parameters from the Minor Planet Center. H is the absolute magnitude which is its brightness if the object were at 1 AU from the Sun and Earth and the phase angle is zero, i is the inclination, e is the eccentricity, and a is the semimajor axis.

[b]S is a Scattered type object, C is a Classical type object, and R is a Resonance type object.

were calibrated to observations of the same field stars on the photometric nights. The observational circumstances, geometry, and orbital characteristics of the 13 observed KBOs are shown in Tables 4.1 and 4.2 respectively.

4.4 Lightcurve Results

The photometric results for the 13 KBOs are listed in Table 4.3, where the columns include the start time of each integration, the corresponding Julian date, and the magnitude. No correction for light travel time has been made. Results of the lightcurve analysis for all the KBOs observed are summarized in Table 4.4 while the mean colors can be found in

Table 4.5. We first discuss the lightcurves of (20000) Varuna, 2000 GN_{171}, (33128) 1998 BU_{48}, and 1999 KR_{16} and give some details about the null results below.

We employed the phase dispersion minimization (PDM) method (Stellingwerf 1978) to search for periodicity in the data. In PDM, the metric is the so-called Θ parameter, which is essentially the variance of the unphased data divided by the variance of the data when phased by a given period. The best fit period should have a very small dispersion compared to the unphased data and thus $\Theta << 1$ indicates that a good fit has been found.

Table 4.3: Observations of Kuiper Belt Objects

Object		Image[a]	UT Date[b]	Julian Date[c]	Exp[d] (sec)	Mag.[e] (m_R)
(38628)	2000 EB_{173}					
		6066	2001 Feb 21.4853	2451961.9853	200	19.318
		6067	2001 Feb 21.4889	2451961.9889	200	19.323
		6072	2001 Feb 21.5195	2451962.0195	200	19.360
		6073	2001 Feb 21.5231	2451962.0231	200	19.363
		6081	2001 Feb 21.5658	2451962.0658	200	19.364
		6082	2001 Feb 21.5695	2451962.0695	200	19.362
		6087	2001 Feb 21.5939	2451962.0939	200	19.352
		6088	2001 Feb 21.5975	2451962.0975	200	19.364
		6094	2001 Feb 21.6273	2451962.1273	200	19.347
		6095	2001 Feb 21.6310	2451962.1310	200	19.355
		6096	2001 Feb 21.6347	2451962.1347	200	19.343
		6097	2001 Feb 21.6384	2451962.1384	200	19.377
		6101	2001 Feb 21.6573	2451962.1573	200	19.352
		6102	2001 Feb 21.6610	2451962.1610	200	19.356
		2039	2001 Apr 21.3006	2452020.8006	200	19.178
		2040	2001 Apr 21.3043	2452020.8043	200	19.184
		2044	2001 Apr 21.3270	2452020.8270	200	19.215
		2045	2001 Apr 21.3308	2452020.8308	200	19.183
		2048	2001 Apr 21.3474	2452020.8474	200	19.207
		2056	2001 Apr 21.3914	2452020.8914	200	19.189
		2057	2001 Apr 21.3951	2452020.8951	200	19.201
		2064	2001 Apr 21.4159	2452020.9158	200	19.193
		2074	2001 Apr 21.4702	2452020.9702	200	19.166
		2075	2001 Apr 21.4739	2452020.9739	200	19.199
		2078	2001 Apr 21.4891	2452020.9891	200	19.196
		2079	2001 Apr 21.4928	2452020.9928	200	19.184
		2083	2001 Apr 21.5117	2452021.0117	200	19.165
		2084	2001 Apr 21.5154	2452021.0154	200	19.185
		2087	2001 Apr 21.5298	2452021.0297	200	19.174
		2088	2001 Apr 21.5334	2452021.0334	200	19.164
		2092	2001 Apr 21.5536	2452021.0536	300	19.234
		2093	2001 Apr 21.5585	2452021.0585	300	19.180

Table 4.3: (continued)

Object		Image[a]	UT Date[b]	Julian Date[c]	Exp[d] (sec)	Mag.[e] (m_R)
		2094	2001 Apr 21.5634	2452021.0634	300	19.147
		2095	2001 Apr 21.5682	2452021.0682	300	19.188
		3076	2001 Apr 22.4437	2452021.9437	200	19.195
		3078	2001 Apr 22.4510	2452021.9507	200	19.198
		3024	2001 Jun 30.2807	2452090.7807	300	19.394
		3025	2001 Jun 30.2857	2452090.7857	300	19.384
		3039	2001 Jun 30.3349	2452090.8349	300	19.345
(26375)	1999 DE_9					
		2026	2000 Apr 28.2686	2451662.7686	300	20.073
		2027	2000 Apr 28.2739	2451662.7739	300	20.081
		2028	2000 Apr 28.2788	2451662.7788	300	20.025
		2029	2000 Apr 28.2837	2451662.7836	300	20.053
		2030	2000 Apr 28.2885	2451662.7885	300	20.040
		2034	2000 Apr 28.3111	2451662.8111	300	20.032
		2035	2000 Apr 28.3163	2451662.8163	300	20.026
		2036	2000 Apr 28.3212	2451662.8212	300	20.051
		2038	2000 Apr 28.3359	2451662.8358	300	20.098
		2039	2000 Apr 28.3408	2451662.8408	300	20.028
		2040	2000 Apr 28.3457	2451662.8457	300	20.038
		2041	2000 Apr 28.3506	2451662.8505	300	20.039
		2043	2000 Apr 28.3611	2451662.8611	300	20.014
		2044	2000 Apr 28.3659	2451662.8659	300	20.008
		2045	2000 Apr 28.3707	2451662.8706	300	20.025
		2046	2000 Apr 28.3754	2451662.8754	300	20.025
		2047	2000 Apr 28.3802	2451662.8802	300	20.040
		2048	2000 Apr 28.3850	2451662.8849	300	19.985
		2052	2000 Apr 28.4085	2451662.9085	300	20.028
		2053	2000 Apr 28.4133	2451662.9133	300	20.014
		2054	2000 Apr 28.4183	2451662.9182	300	20.012
		2055	2000 Apr 28.4232	2451662.9231	300	20.038
		4021	2000 Apr 30.2664	2451664.7664	300	20.096
		4022	2000 Apr 30.2714	2451664.7714	300	20.067
		4023	2000 Apr 30.2762	2451664.7762	300	20.055
		4024	2000 Apr 30.2811	2451664.7811	300	20.075
		4026	2000 Apr 30.2967	2451664.7967	300	20.095
		4027	2000 Apr 30.3015	2451664.8015	300	20.080
		4028	2000 Apr 30.3062	2451664.8062	300	20.072
		4029	2000 Apr 30.3110	2451664.8110	300	20.068
		4030	2000 Apr 30.3158	2451664.8158	300	20.082
		4033	2000 Apr 30.3307	2451664.8308	300	20.099
		4034	2000 Apr 30.3356	2451664.8356	300	20.074
		4035	2000 Apr 30.3405	2451664.8405	300	20.089
		4036	2000 Apr 30.3455	2451664.8455	300	20.051
		4040	2000 Apr 30.3713	2451664.8713	300	20.061
		4041	2000 Apr 30.3762	2451664.8762	300	20.042
		4044	2000 Apr 30.3908	2451664.8908	300	20.015
		5028	2000 May 1.28693	2451665.7869	300	20.079

Table 4.3: (continued)

Object		Image[a]	UT Date[b]	Julian Date[c]	Exp[d] (sec)	Mag.[e] (m_R)
		5035	2000 May 1.33803	2451665.8380	300	20.082
		5041	2000 May 1.37821	2451665.8782	300	20.060
		4068	2001 Feb 19.4342	2451959.9342	200	19.850
		4072	2001 Feb 19.4486	2451959.9486	200	19.836
		6039	2001 Feb 21.3302	2451961.8302	200	19.738
		6040	2001 Feb 21.3339	2451961.8339	200	19.749
		6045	2001 Feb 21.3640	2451961.8640	200	19.753
		6046	2001 Feb 21.3677	2451961.8677	200	19.801
		6052	2001 Feb 21.4045	2451961.9045	200	19.759
		6053	2001 Feb 21.4082	2451961.9082	200	19.772
		6060	2001 Feb 21.4505	2451961.9505	200	19.780
		6061	2001 Feb 21.4541	2451961.9541	200	19.817
		5017	2001 Apr 24.2621	2452023.7621	250	20.133
		5018	2001 Apr 24.2663	2452023.7663	250	20.159
		5023	2001 Apr 24.2949	2452023.7949	250	20.120
		5024	2001 Apr 24.2991	2452023.7991	250	20.146
		5027	2001 Apr 24.3173	2452023.8173	250	20.139
		5028	2001 Apr 24.3215	2452023.8215	250	20.129
		5031	2001 Apr 24.3393	2452023.8393	250	20.122
		5032	2001 Apr 24.3435	2452023.8435	250	20.133
		5035	2001 Apr 24.3617	2452023.8617	250	20.126
		5036	2001 Apr 24.3659	2452023.8659	250	20.099
		5039	2001 Apr 24.3835	2452023.8835	250	20.106
		5040	2001 Apr 24.3877	2452023.8877	250	20.077
		5043	2001 Apr 24.4056	2452023.9056	250	20.067
		5044	2001 Apr 24.4098	2452023.9098	250	20.081
		5048	2001 Apr 24.4333	2452023.9333	250	20.008
		5049	2001 Apr 24.4375	2452023.9375	250	20.040
		6034	2001 Apr 25.3339	2452024.8339	250	20.137
		6035	2001 Apr 25.3383	2452024.8383	200	20.117
(26181)	1996 GQ_{21}					
		6076	2001 Feb 21.5371	2451962.0371	300	20.545
		6077	2001 Feb 21.5419	2451962.0419	300	20.603
		6085	2001 Feb 21.5838	2451962.0838	300	20.556
		6086	2001 Feb 21.5887	2451962.0887	300	20.587
		6090	2001 Feb 21.6074	2451962.1074	300	20.563
		6091	2001 Feb 21.6122	2451962.1122	300	20.581
		6092	2001 Feb 21.6170	2451962.1170	300	20.562
		6093	2001 Feb 21.6219	2451962.1219	300	20.555
		6098	2001 Feb 21.6425	2451962.1425	300	20.535
		6099	2001 Feb 21.6473	2451962.1473	300	20.555
		6100	2001 Feb 21.6522	2451962.1522	300	20.556
		1053	2001 Apr 20.3924	2452019.8924	300	20.374
		1054	2001 Apr 20.3974	2452019.8974	300	20.380
		1058	2001 Apr 20.4167	2452019.9167	300	20.377
		1059	2001 Apr 20.4214	2452019.9214	300	20.387
		1062	2001 Apr 20.4360	2452019.9360	300	20.376

Table 4.3: (continued)

Object	Image[a]	UT Date[b]	Julian Date[c]	Exp[d] (sec)	Mag.[e] (m_R)
	1063	2001 Apr 20.4408	2452019.9408	300	20.367
	1067	2001 Apr 20.4586	2452019.9586	300	20.359
	1068	2001 Apr 20.4633	2452019.9633	300	20.404
	1071	2001 Apr 20.4782	2452019.9782	300	20.369
	1072	2001 Apr 20.4830	2452019.9830	300	20.379
	1075	2001 Apr 20.4983	2452019.9983	300	20.358
	1076	2001 Apr 20.5031	2452020.0031	300	20.343
	1079	2001 Apr 20.5185	2452020.0185	300	20.349
	1080	2001 Apr 20.5233	2452020.0233	300	20.378
	1084	2001 Apr 20.5435	2452020.0435	300	20.410
	1086	2001 Apr 20.5540	2452020.0540	300	20.367
	1087	2001 Apr 20.5588	2452020.0588	300	20.367
	1088	2001 Apr 20.5636	2452020.0636	300	20.410
	1089	2001 Apr 20.5684	2452020.0684	300	20.383
	1090	2001 Apr 20.5732	2452020.0732	300	20.361
	1091	2001 Apr 20.5782	2452020.0782	300	20.356
	1092	2001 Apr 20.5830	2452020.0830	300	20.304
	2042	2001 Apr 21.3169	2452020.8169	300	20.336
	2043	2001 Apr 21.3217	2452020.8217	300	20.374
	2058	2001 Apr 21.3996	2452020.8996	300	20.365
	2059	2001 Apr 21.4045	2452020.9045	300	20.370
	2065	2001 Apr 21.4200	2452020.9200	300	20.382
	3066	2001 Apr 22.4071	2452021.9070	300	20.369
	3068	2001 Apr 22.4168	2452021.9168	300	20.367
	3084	2001 Apr 22.4767	2452021.9767	300	20.347
	3085	2001 Apr 22.4815	2452021.9814	300	20.328
	3086	2001 Apr 22.4862	2452021.9862	300	20.343
	3088	2001 Apr 22.4966	2452021.9966	300	20.367
	3089	2001 Apr 22.5014	2452022.0014	300	20.331
	3090	2001 Apr 22.5062	2452022.0062	300	20.366
	3092	2001 Apr 22.5271	2452022.0271	300	20.389
	3093	2001 Apr 22.5319	2452022.0319	300	20.372
	3095	2001 Apr 22.5469	2452022.0469	350	20.339
	3096	2001 Apr 22.5522	2452022.0522	350	20.305
	3098	2001 Apr 22.5633	2452022.0633	350	20.345
	3099	2001 Apr 22.5686	2452022.0686	350	20.357
	3100	2001 Apr 22.5740	2452022.0740	350	20.388
	4071	2001 Apr 23.4500	2452022.9500	300	20.347
	4072	2001 Apr 23.4548	2452022.9548	300	20.325
	4077	2001 Apr 23.4667	2452022.9667	300	20.341
	4078	2001 Apr 23.4716	2452022.9716	300	20.386
	4080	2001 Apr 23.4814	2452022.9814	300	20.356
	4082	2001 Apr 23.4912	2452022.9912	300	20.312
	4083	2001 Apr 23.4960	2452022.9960	300	20.339
	4084	2001 Apr 23.5008	2452023.0008	300	20.329
	4085	2001 Apr 23.5056	2452023.0056	300	20.369
	4086	2001 Apr 23.5103	2452023.0103	300	20.388

Table 4.3: (continued)

Object	Image[a]	UT Date[b]	Julian Date[c]	Exp[d] (sec)	Mag.[e] (m_R)
	4087	2001 Apr 23.5151	2452023.0151	300	20.300
	4088	2001 Apr 23.5198	2452023.0198	300	20.357
	4090	2001 Apr 23.5296	2452023.0296	300	20.379
	4091	2001 Apr 23.5345	2452023.0345	300	20.300
	4092	2001 Apr 23.5392	2452023.0392	300	20.356
	4093	2001 Apr 23.5440	2452023.0440	300	20.346
	4094	2001 Apr 23.5488	2452023.0488	300	20.336
	4095	2001 Apr 23.5535	2452023.0535	300	20.359
	4096	2001 Apr 23.5583	2452023.0583	300	20.340
	4098	2001 Apr 23.5684	2452023.0684	300	20.321
	4099	2001 Apr 23.5732	2452023.0732	300	20.322
	6060	2001 Apr 25.4942	2452024.9942	300	20.350
	6061	2001 Apr 25.4990	2452024.9990	300	20.382
	6064	2001 Apr 25.5154	2452025.0154	300	20.349
	6065	2001 Apr 25.5201	2452025.0201	300	20.323
	6066	2001 Apr 25.5251	2452025.0250	300	20.338
	6067	2001 Apr 25.5299	2452025.0299	300	20.372
	6072	2001 Apr 25.5618	2452025.0617	300	20.310
	6073	2001 Apr 25.5665	2452025.0665	300	20.323
	6074	2001 Apr 25.5713	2452025.0713	300	20.282
2000 GN_{171}					
	1042	2001 Apr 20.3331	2452019.8331	300	20.553
	1043	2001 Apr 20.3379	2452019.8379	300	20.524
	1047	2001 Apr 20.3634	2452019.8634	300	20.397
	1048	2001 Apr 20.3682	2452019.8682	300	20.383
	1049	2001 Apr 20.3730	2452019.8740	300	20.349
	1050	2001 Apr 20.3778	2452019.8778	300	20.346
	1051	2001 Apr 20.3826	2452019.8825	300	20.352
	1052	2001 Apr 20.3876	2452019.8875	250	20.354
	1056	2001 Apr 20.4073	2452019.9073	250	20.420
	1057	2001 Apr 20.4116	2452019.9116	250	20.468
	1060	2001 Apr 20.4272	2452019.9272	250	20.550
	1061	2001 Apr 20.4314	2452019.9314	250	20.616
	1064	2001 Apr 20.4460	2452019.9460	250	20.755
	1065	2001 Apr 20.4502	2452019.9502	250	20.754
	1069	2001 Apr 20.4693	2452019.9693	250	20.881
	1070	2001 Apr 20.4735	2452019.9735	250	20.880
	1073	2001 Apr 20.4883	2452019.9883	300	20.774
	1074	2001 Apr 20.4931	2452019.9931	300	20.686
	1077	2001 Apr 20.5085	2452020.0085	300	20.549
	1078	2001 Apr 20.5133	2452020.0133	300	20.482
	1081	2001 Apr 20.5285	2452020.0285	300	20.333
	1082	2001 Apr 20.5333	2452020.0333	300	20.315
	1083	2001 Apr 20.5381	2452020.0381	300	20.302
	2036	2001 Apr 21.2854	2452020.7854	300	20.348
	2037	2001 Apr 21.2903	2452020.7903	300	20.380
	2046	2001 Apr 21.3360	2452020.8360	300	20.770

Table 4.3: (continued)

Object	Image[a]	UT Date[b]	Julian Date[c]	Exp[d] (sec)	Mag.[e] (m_R)
	2047	2001 Apr 21.3409	2452020.8409	300	20.806
	2050	2001 Apr 21.3571	2452020.8571	300	20.731
	2054	2001 Apr 21.3805	2452020.8805	300	20.507
	2068	2001 Apr 21.4354	2452020.9354	300	20.360
	2072	2001 Apr 21.4583	2452020.9583	300	20.476
	2081	2001 Apr 21.5017	2452021.0017	300	20.782
	3053	2001 Apr 22.3364	2452021.8364	350	20.381
	3055	2001 Apr 22.3470	2452021.8470	300	20.511
	3058	2001 Apr 22.3615	2452021.8615	300	20.676
	3062	2001 Apr 22.3865	2452021.8865	300	20.798
	3065	2001 Apr 22.4010	2452021.9010	300	20.757
	3075	2001 Apr 22.4380	2452021.9380	300	20.412
	4039	2001 Apr 23.2983	2452022.7983	300	20.386
	4041	2001 Apr 23.3080	2452022.8080	300	20.317
	4045	2001 Apr 23.3315	2452022.8315	350	20.266
	4049	2001 Apr 23.3562	2452022.8562	350	20.271
	4065	2001 Apr 23.4156	2452022.9156	300	20.793
	4069	2001 Apr 23.4387	2452022.9387	300	20.785
	5060	2001 Apr 24.5193	2452024.0193	300	20.450
	5061	2001 Apr 24.5242	2452024.0241	300	20.391
	5064	2001 Apr 24.5421	2452024.0421	300	20.350
	6053	2001 Apr 25.4524	2452024.9524	300	20.435
	6054	2001 Apr 25.4572	2452024.9572	300	20.442
	6062	2001 Apr 25.5048	2452025.0048	300	20.840
	6063	2001 Apr 25.5096	2452025.0096	300	20.806
	1029	2001 May 11.3078	2452040.8078	350	20.893
	1032	2001 May 11.3262	2452040.8262	350	20.678
	1033	2001 May 11.3318	2452040.8318	300	20.632
	1037	2001 May 11.3550	2452040.8550	300	20.464
	1038	2001 May 11.3598	2452040.8598	300	20.433
	1042	2001 May 11.3831	2452040.8831	300	20.384
	1043	2001 May 11.3880	2452040.8880	300	20.379
	1048	2001 May 11.4174	2452040.9174	300	20.458
	1052	2001 May 11.4409	2452040.9409	300	20.723
	1053	2001 May 11.4457	2452040.9457	300	20.747
	1058	2001 May 11.4735	2452040.9735	300	20.834
	2070	2001 May 12.4380	2452041.9380	300	20.426
	2071	2001 May 12.4428	2452041.9428	300	20.379
	3027	2001 May 13.2696	2452042.7695	300	20.481
	3028	2001 May 13.2744	2452042.7744	300	20.460
	3052	2001 May 13.3786	2452042.8786	300	20.981
	3054	2001 May 13.3882	2452042.8882	300	20.878
	3067	2001 May 13.4643	2452042.9643	300	20.362
	3069	2001 May 13.4740	2452042.9740	300	20.348
(19521) Chaos 1998 WH_{24}					
	1036	1999 Nov 9.5220	2451492.0220	300	20.631
	1037	1999 Nov 9.5266	2451492.0267	300	20.637

Table 4.3: (continued)

Object		Image[a]	UT Date[b]	Julian Date[c]	Exp[d] (sec)	Mag.[e] (m_R)
		1038	1999 Nov 9.5313	2451492.0314	300	20.651
		1040	1999 Nov 9.5515	2451492.0516	300	20.641
		1041	1999 Nov 9.5562	2451492.0562	300	20.632
		1042	1999 Nov 9.5608	2451492.0609	300	20.684
		1043	1999 Nov 9.5655	2451492.0656	300	20.669
		1046	1999 Nov 9.5910	2451492.0910	300	20.724
		1047	1999 Nov 9.5956	2451492.0957	300	20.724
		1048	1999 Nov 9.6003	2451492.1003	300	20.700
		1049	1999 Nov 9.6049	2451492.1050	300	20.705
		2041	1999 Nov 10.443	2451492.9430	300	20.625
		2042	1999 Nov 10.447	2451492.9477	300	20.665
		2045	1999 Nov 10.477	2451492.9773	300	20.667
		2046	1999 Nov 10.482	2451492.9820	300	20.677
		2050	1999 Nov 10.493	2451492.9939	300	20.665
		2051	1999 Nov 10.498	2451492.9986	300	20.685
		2052	1999 Nov 10.503	2451493.0033	300	20.645
		2056	1999 Nov 10.533	2451493.0337	300	20.630
		2057	1999 Nov 10.538	2451493.0383	300	20.662
		2058	1999 Nov 10.543	2451493.0430	300	20.644
		2060	1999 Nov 10.561	2451493.0618	300	20.610
		2061	1999 Nov 10.566	2451493.0665	300	20.613
		2062	1999 Nov 10.571	2451493.0711	300	20.617
		2065	1999 Nov 10.585	2451493.0853	300	20.616
		2066	1999 Nov 10.590	2451493.0900	300	20.626
		2068	1999 Nov 10.599	2451493.0993	300	20.639
(33340)	1998 VG_{44}					
		3044	1999 Nov 11.4635	2451493.9635	400	20.936
		3046	1999 Nov 11.4775	2451493.9775	400	20.933
		3050	1999 Nov 11.4941	2451493.9941	400	20.922
		3052	1999 Nov 11.5089	2451494.0089	400	20.946
		3054	1999 Nov 11.5229	2451494.0229	400	20.930
		3056	1999 Nov 11.5368	2451494.0368	400	20.921
		3057	1999 Nov 11.5438	2451494.0438	400	20.921
		3060	1999 Nov 11.5648	2451494.0648	400	20.933
		3061	1999 Nov 11.5717	2451494.0717	400	20.950
		3064	1999 Nov 11.5883	2451494.0883	400	20.974
		3066	1999 Nov 11.6023	2451494.1023	400	20.947
		3067	1999 Nov 11.6093	2451494.1093	400	20.923
		4058	1999 Nov 12.4784	2451494.9784	400	20.952
		4059	1999 Nov 12.4854	2451494.9854	400	20.980
		4060	1999 Nov 12.4924	2451494.9924	400	21.034
		4062	1999 Nov 12.5124	2451495.0124	400	20.979
		4063	1999 Nov 12.5194	2451495.0194	400	21.015
		4066	1999 Nov 12.5403	2451495.0403	400	20.967
		4067	1999 Nov 12.5474	2451495.0474	400	20.977
		4069	1999 Nov 12.5614	2451495.0614	400	21.002
		4073	1999 Nov 12.5830	2451495.0830	400	20.959

Table 4.3: (continued)

Object		Image[a]	UT Date[b]	Julian Date[c]	Exp[d] (sec)	Mag.[e] (m_R)
		4074	1999 Nov 12.5877	2451495.0877	400	20.954
	2001 FZ_{173}					
		5019	2001 Apr 24.2717	2452023.7717	400	21.083
		5020	2001 Apr 24.2778	2452023.7777	400	21.031
		5025	2001 Apr 24.3042	2452023.8042	400	21.053
		5026	2001 Apr 24.3102	2452023.8102	400	21.073
		5029	2001 Apr 24.3265	2452023.8265	400	21.087
		5030	2001 Apr 24.3324	2452023.8324	400	21.111
		5037	2001 Apr 24.3709	2452023.8709	400	21.129
		5038	2001 Apr 24.3768	2452023.8768	400	21.103
		5041	2001 Apr 24.3930	2452023.8930	400	21.087
		5042	2001 Apr 24.3989	2452023.8989	400	21.110
		5046	2001 Apr 24.4207	2452023.9207	400	21.103
		5047	2001 Apr 24.4267	2452023.9266	400	21.070
		5050	2001 Apr 24.4534	2452023.9533	400	21.066
		5054	2001 Apr 24.4810	2452023.9810	400	20.994
		5055	2001 Apr 24.4870	2452023.9869	400	21.025
		6022	2001 Apr 25.2610	2452024.7610	400	21.066
		6023	2001 Apr 25.2669	2452024.7669	400	21.059
		6030	2001 Apr 25.3088	2452024.8088	400	21.041
		6031	2001 Apr 25.3147	2452024.8147	400	21.067
		6040	2001 Apr 25.3697	2452024.8697	400	21.026
		6041	2001 Apr 25.3756	2452024.8755	400	21.069
		6046	2001 Apr 25.4079	2452024.9079	400	21.087
		6047	2001 Apr 25.4157	2452024.9157	400	21.073
		6058	2001 Apr 25.4814	2452024.9814	400	21.025
		6059	2001 Apr 25.4873	2452024.9873	400	21.076
(33128)	1998 BU_{48}					
		6064	2001 Feb 21.4720	2451961.9720	400	20.648
		6065	2001 Feb 21.4780	2451961.9780	400	20.652
		6070	2001 Feb 21.5064	2451962.0064	400	20.653
		6071	2001 Feb 21.5123	2451962.0123	400	20.626
		6079	2001 Feb 21.5525	2451962.0525	400	20.763
		6080	2001 Feb 21.5585	2451962.0585	400	20.809
		6020	2001 Apr 25.2478	2452024.7477	400	21.296
		6021	2001 Apr 25.2537	2452024.7537	400	21.242
		6024	2001 Apr 25.2738	2452024.7738	400	21.086
		6025	2001 Apr 25.2797	2452024.7797	400	21.060
		6028	2001 Apr 25.2955	2452024.7955	400	20.985
		6029	2001 Apr 25.3014	2452024.8014	400	20.962
		6032	2001 Apr 25.3216	2452024.8216	400	20.884
		6033	2001 Apr 25.3275	2452024.8275	400	20.866
		6036	2001 Apr 25.3432	2452024.8432	400	20.886
		6037	2001 Apr 25.3491	2452024.8491	400	20.859
		6042	2001 Apr 25.3823	2452024.8823	400	20.926
		6043	2001 Apr 25.3882	2452024.8882	400	20.961
		1080	2001 Nov 14.6182	2452228.1182	400	21.437

Table 4.3: (continued)

Object	Image[a]	UT Date[b]	Julian Date[c]	Exp[d] (sec)	Mag.[e] (m_R)
	1081	2001 Nov 14.6242	2452228.1241	400	21.477
	1082	2001 Nov 14.6301	2452228.1301	400	21.470
	1083	2001 Nov 14.6360	2452228.1360	400	21.638
	1084	2001 Nov 14.6419	2452228.1419	400	21.643
	2063	2001 Nov 15.5516	2452229.0516	400	20.888
	2064	2001 Nov 15.5582	2452229.0582	400	20.864
	2066	2001 Nov 15.5739	2452229.0739	400	20.888
	2067	2001 Nov 15.5799	2452229.0799	400	20.923
	2069	2001 Nov 15.5944	2452229.0944	400	20.986
	2070	2001 Nov 15.6004	2452229.1004	400	20.957
	2071	2001 Nov 15.6064	2452229.1064	400	21.019
	2072	2001 Nov 15.6124	2452229.1124	400	21.089
	2074	2001 Nov 15.6272	2452229.1272	400	21.156
	2075	2001 Nov 15.6333	2452229.1333	400	21.190
	2076	2001 Nov 15.6392	2452229.1392	400	21.185
	2077	2001 Nov 15.6452	2452229.1452	400	21.178
	2078	2001 Nov 15.6511	2452229.1511	400	21.183
	3115	2001 Nov 16.5378	2452230.0378	400	21.113
	3116	2001 Nov 16.5444	2452230.0444	400	21.113
	3117	2001 Nov 16.5509	2452230.0509	400	21.058
	3119	2001 Nov 16.5628	2452230.0628	400	20.988
	3120	2001 Nov 16.5695	2452230.0694	400	20.981
	3121	2001 Nov 16.5761	2452230.0761	400	20.958
	3124	2001 Nov 16.5962	2452230.0962	400	20.950
	3125	2001 Nov 16.6027	2452230.1027	400	20.945
	3128	2001 Nov 16.6225	2452230.1225	400	20.916
	3129	2001 Nov 16.6291	2452230.1291	400	20.959
	3130	2001 Nov 16.6356	2452230.1356	400	20.997
	3131	2001 Nov 16.6422	2452230.1422	400	20.960
	3132	2001 Nov 16.6488	2452230.1488	400	20.979
	4087	2001 Nov 17.5219	2452231.0219	400	21.519
	4088	2001 Nov 17.5285	2452231.0285	400	21.508
	4089	2001 Nov 17.5351	2452231.0351	400	21.534
	4092	2001 Nov 17.5541	2452231.0541	400	21.439
	4093	2001 Nov 17.5601	2452231.0601	400	21.353
	4096	2001 Nov 17.5788	2452231.0788	400	21.192
	4097	2001 Nov 17.5847	2452231.0847	400	21.121
	4100	2001 Nov 17.6028	2452231.1027	400	21.070
	4101	2001 Nov 17.6087	2452231.1087	400	21.057
	4105	2001 Nov 17.6339	2452231.1339	400	20.945
	4106	2001 Nov 17.6398	2452231.1398	400	21.003
	4108	2001 Nov 17.6518	2452231.1518	400	20.892
	5082	2001 Nov 18.5263	2452231.9294	400	21.206
	5083	2001 Nov 18.5322	2452231.9353	400	21.225
	5084	2001 Nov 18.5381	2452231.9412	400	21.303
	5085	2001 Nov 18.5440	2452231.9471	400	21.341
	5086	2001 Nov 18.5499	2452231.9530	400	21.492

Table 4.3: (continued)

Object	Image[a]	UT Date[b]	Julian Date[c]	Exp[d] (sec)	Mag.[e] (m_R)
	5089	2001 Nov 18.5695	2452231.9726	400	21.609
	5092	2001 Nov 18.5878	2452231.9909	400	21.625
	5093	2001 Nov 18.5937	2452231.9968	400	21.571
	5096	2001 Nov 18.6115	2452232.0146	400	21.407
	5097	2001 Nov 18.6174	2452232.0205	400	21.398
	5100	2001 Nov 18.6351	2452232.0382	400	21.230
	5101	2001 Nov 18.6439	2452232.0470	400	21.161
	5102	2001 Nov 18.6498	2452232.0529	400	21.098
	6076	2001 Nov 19.5284	2452232.9298	400	20.910
	6077	2001 Nov 19.5344	2452232.9358	400	20.898
	6080	2001 Nov 19.5524	2452232.9538	400	20.991
	6081	2001 Nov 19.5583	2452232.9597	400	21.068
	6082	2001 Nov 19.5661	2452232.9675	400	21.110
	6083	2001 Nov 19.5723	2452232.9738	400	21.250
	6084	2001 Nov 19.5782	2452232.9797	400	21.257
	6089	2001 Nov 19.6051	2452233.0066	400	21.525
	6090	2001 Nov 19.6111	2452233.0125	400	21.552
	6095	2001 Nov 19.6391	2452233.0405	400	21.514
	6096	2001 Nov 19.6450	2452233.0464	400	21.451
1999 KR_{16}					
	2061	2000 Apr 28.4409	2451662.9409	400	21.253
	2062	2000 Apr 28.4468	2451662.9468	400	21.262
	2063	2000 Apr 28.4528	2451662.9527	400	21.320
	2064	2000 Apr 28.4587	2451662.9587	400	21.317
	2065	2000 Apr 28.4647	2451662.9646	400	21.281
	2070	2000 Apr 28.4959	2451662.9959	400	21.295
	2071	2000 Apr 28.5019	2451663.0019	400	21.181
	2072	2000 Apr 28.5078	2451663.0078	400	21.211
	2073	2000 Apr 28.5138	2451663.0137	400	21.135
	2076	2000 Apr 28.5317	2451663.0317	400	21.133
	2077	2000 Apr 28.5376	2451663.0376	400	21.325
	2078	2000 Apr 28.5436	2451663.0435	400	21.200
	4037	2000 Apr 30.3519	2451664.8519	400	21.085
	4038	2000 Apr 30.3579	2451664.8579	400	21.114
	4039	2000 Apr 30.3639	2451664.8639	400	21.111
	4045	2000 Apr 30.3968	2451664.8968	400	21.257
	4046	2000 Apr 30.4028	2451664.9028	400	21.279
	4047	2000 Apr 30.4087	2451664.9087	400	21.292
	4052	2000 Apr 30.4252	2451664.9252	400	21.247
	4053	2000 Apr 30.4312	2451664.9312	400	21.226
	4054	2000 Apr 30.4372	2451664.9372	400	21.203
	4055	2000 Apr 30.4431	2451664.9431	400	21.207
	4056	2000 Apr 30.4490	2451664.9490	400	21.204
	4059	2000 Apr 30.4671	2451664.9671	400	21.148
	4060	2000 Apr 30.4731	2451664.9731	400	21.149
	4061	2000 Apr 30.4790	2451664.9790	400	21.181
	4062	2000 Apr 30.4850	2451664.9850	400	21.129

Table 4.3: (continued)

Object	Image[a]	UT Date[b]	Julian Date[c]	Exp[d] (sec)	Mag.[e] (m_R)
	4065	2000 Apr 30.5028	2451665.0028	400	21.154
	4066	2000 Apr 30.5088	2451665.0088	400	21.132
	4067	2000 Apr 30.5147	2451665.0147	400	21.085
	4068	2000 Apr 30.5206	2451665.0206	400	21.130
	4069	2000 Apr 30.5266	2451665.0266	400	21.136
	4070	2000 Apr 30.5328	2451665.0328	400	21.058
	5036	2000 May 1.3443	2451665.8443	400	21.227
	5038	2000 May 1.3567	2451665.8567	400	21.182
	5039	2000 May 1.3627	2451665.8627	400	21.228
	5042	2000 May 1.3847	2451665.8847	400	21.264
	5043	2000 May 1.3908	2451665.8908	400	21.219
	5044	2000 May 1.3968	2451665.8968	400	21.204
	5048	2000 May 1.4224	2451665.9224	400	21.157
	5049	2000 May 1.4285	2451665.9285	400	21.160
	5050	2000 May 1.4346	2451665.9346	400	21.118
	5054	2000 May 1.4583	2451665.9583	400	21.162
	5055	2000 May 1.4644	2451665.9644	400	21.121
	5056	2000 May 1.4704	2451665.9704	400	21.178
	5059	2000 May 1.4905	2451665.9905	400	21.147
	5060	2000 May 1.4965	2451665.9965	400	21.075
	5061	2000 May 1.5025	2451666.0025	400	21.153
	5064	2000 May 1.5221	2451666.0221	400	21.068
	5065	2000 May 1.5282	2451666.0282	400	21.070
	5066	2000 May 1.5342	2451666.0342	400	21.174
	3091	2001 Feb 18.4971	2451958.9971	400	21.215
	3092	2001 Feb 18.5030	2451959.0030	400	21.214
	3093	2001 Feb 18.5089	2451959.0089	400	21.202
	3094	2001 Feb 18.5147	2451959.0147	400	21.262
	3099	2001 Feb 18.5667	2451959.0667	400	21.406
	3100	2001 Feb 18.5725	2451959.0725	400	21.356
	3107	2001 Feb 18.6320	2451959.1320	400	21.345
	3108	2001 Feb 18.6379	2451959.1379	400	21.308
	4076	2001 Feb 19.4657	2451959.9657	400	21.189
	4077	2001 Feb 19.4719	2451959.9719	400	21.192
	4083	2001 Feb 19.4889	2451959.9889	400	21.305
	4085	2001 Feb 19.5007	2451960.0007	400	21.317
	4087	2001 Feb 19.5138	2451960.0138	400	21.298
	4089	2001 Feb 19.5257	2451960.0257	400	21.313
	4090	2001 Feb 19.5317	2451960.0317	400	21.313
	4091	2001 Feb 19.5377	2451960.0377	400	21.413
	4092	2001 Feb 19.5437	2451960.0437	400	21.300
	4093	2001 Feb 19.5498	2451960.0498	400	21.436
	4097	2001 Feb 19.5874	2451960.0874	400	21.403
	4098	2001 Feb 19.5933	2451960.0933	400	21.369
	4099	2001 Feb 19.5992	2451960.0992	400	21.331
	4100	2001 Feb 19.6051	2451960.1051	400	21.342
	4101	2001 Feb 19.6110	2451960.1110	400	21.309

Table 4.3: (continued)

Object	Image[a]	UT Date[b]	Julian Date[c]	Exp[d] (sec)	Mag.[e] (m_R)
	4102	2001 Feb 19.6169	2451960.1169	400	21.327
	4103	2001 Feb 19.6228	2451960.1228	400	21.285
	4104	2001 Feb 19.6287	2451960.1287	400	21.266
	4105	2001 Feb 19.6346	2451960.1346	400	21.319
	4106	2001 Feb 19.6467	2451960.1467	400	21.262
	4107	2001 Feb 19.6526	2451960.1526	400	21.268
	4108	2001 Feb 19.6585	2451960.1585	400	21.248
	4109	2001 Feb 19.6644	2451960.1644	400	21.243
	5052	2001 Apr 24.4673	2452023.9673	400	20.975
	5053	2001 Apr 24.4735	2452023.9734	400	21.013
	5056	2001 Apr 24.4948	2452023.9948	400	21.100
	5057	2001 Apr 24.5008	2452024.0008	400	21.085
	5058	2001 Apr 24.5067	2452024.0067	400	21.143
	5059	2001 Apr 24.5126	2452024.0126	400	21.196
	5062	2001 Apr 24.5296	2452024.0296	400	21.214
	5063	2001 Apr 24.5357	2452024.0356	400	21.220
	5065	2001 Apr 24.5476	2452024.0476	400	21.184
	5066	2001 Apr 24.5536	2452024.0536	400	21.201
	5067	2001 Apr 24.5595	2452024.0595	400	21.183
	5068	2001 Apr 24.5654	2452024.0654	400	21.164
	6038	2001 Apr 25.3570	2452024.8570	400	21.113
	6039	2001 Apr 25.3629	2452024.8629	400	21.107
	6044	2001 Apr 25.3954	2452024.8954	400	21.012
	6045	2001 Apr 25.4013	2452024.9013	400	21.012
	6048	2001 Apr 25.4223	2452024.9223	400	20.992
	6049	2001 Apr 25.4283	2452024.9282	400	20.987
	6050	2001 Apr 25.4343	2452024.9343	400	21.004
	6051	2001 Apr 25.4402	2452024.9402	400	20.999
	6052	2001 Apr 25.4462	2452024.9462	400	21.053
	6055	2001 Apr 25.4626	2452024.9626	400	21.033
	6056	2001 Apr 25.4685	2452024.9685	400	21.071
	6057	2001 Apr 25.4745	2452024.9745	400	21.050
	6068	2001 Apr 25.5358	2452025.0358	400	21.134
	6069	2001 Apr 25.5418	2452025.0418	400	21.193
	6070	2001 Apr 25.5478	2452025.0478	400	21.185
	6071	2001 Apr 25.5538	2452025.0538	400	21.195
	1021	2001 May 11.2553	2452040.7552	400	21.122
	1022	2001 May 11.2613	2452040.7613	400	21.139
	1023	2001 May 11.2673	2452040.7673	400	21.166
	1026	2001 May 11.2879	2452040.7879	400	21.145
	1027	2001 May 11.2939	2452040.7939	400	21.161
	1030	2001 May 11.3140	2452040.8140	400	21.250
	1031	2001 May 11.3200	2452040.8200	400	21.262
	1034	2001 May 11.3368	2452040.8368	400	21.253
	1035	2001 May 11.3428	2452040.8428	400	21.286
	1036	2001 May 11.3488	2452040.8488	400	21.258
	2030	2001 May 12.2574	2452041.7574	400	21.153

Table 4.3: (continued)

Object	Image[a]	UT Date[b]	Julian Date[c]	Exp[d] (sec)	Mag.[e] (m_R)
	2032	2001 May 12.2694	2452041.7694	400	21.200
	2036	2001 May 12.2959	2452041.7959	400	21.267
	2039	2001 May 12.3149	2452041.8149	400	21.271
	2040	2001 May 12.3209	2452041.8209	400	21.267
	2050	2001 May 12.3418	2452041.8418	400	21.258
	2052	2001 May 12.3539	2452041.8539	400	21.269
	2056	2001 May 12.3803	2452041.8803	400	21.240
	2058	2001 May 12.3922	2452041.8922	400	21.217
	2059	2001 May 12.3982	2452041.8982	400	21.215
	2067	2001 May 12.4194	2452041.9194	400	21.155
	2068	2001 May 12.4254	2452041.9254	400	21.137
	2072	2001 May 12.4478	2452041.9478	400	21.130
	2074	2001 May 12.4598	2452041.9598	400	21.107
	2078	2001 May 12.4862	2452041.9862	400	21.102
	2079	2001 May 12.4922	2452041.9922	400	21.146
	3025	2001 May 13.2574	2452042.7574	400	21.209
	3026	2001 May 13.2634	2452042.7634	400	21.224
	3032	2001 May 13.2963	2452042.7963	400	21.222
	3034	2001 May 13.3085	2452042.8085	400	21.242
	3036	2001 May 13.3205	2452042.8205	400	21.262
	3039	2001 May 13.3384	2452042.8384	400	21.263
	3049	2001 May 13.3623	2452042.8623	400	21.159
	3050	2001 May 13.3683	2452042.8683	400	21.219
	3056	2001 May 13.3980	2452042.8980	400	21.094
	3058	2001 May 13.4102	2452042.9102	400	21.125
	3060	2001 May 13.4222	2452042.9222	400	21.108
	3063	2001 May 13.4403	2452042.9403	400	21.122
	3065	2001 May 13.4523	2452042.9523	400	21.071
	3066	2001 May 13.4583	2452042.9583	400	21.127
1997 CS_{29}					
	6023	2001 Feb 21.2469	2451961.7469	400	21.361
	6024	2001 Feb 21.2529	2451961.7529	400	21.364
	6031	2001 Feb 21.2818	2451961.7818	400	21.354
	6032	2001 Feb 21.2877	2451961.7877	400	21.368
	6033	2001 Feb 21.2936	2451961.7936	400	21.370
	6037	2001 Feb 21.3172	2451961.8172	400	21.375
	6038	2001 Feb 21.3231	2451961.8231	400	21.386
	6043	2001 Feb 21.3505	2451961.8505	400	21.372
	6044	2001 Feb 21.3565	2451961.8564	400	21.365
	6049	2001 Feb 21.3846	2451961.8846	400	21.367
	6050	2001 Feb 21.3906	2451961.8906	400	21.367
	6051	2001 Feb 21.3966	2451961.8966	400	21.368
	6054	2001 Feb 21.4129	2451961.9129	400	21.354
	6055	2001 Feb 21.4190	2451961.9190	400	21.323
	6058	2001 Feb 21.4372	2451961.9372	400	21.333
	6059	2001 Feb 21.4432	2451961.9432	400	21.361
	6062	2001 Feb 21.4590	2451961.9590	400	21.311

Table 4.3: (continued)

Object	Image[a]	UT Date[b]	Julian Date[c]	Exp[d] (sec)	Mag.[e] (m_R)
	6063	2001 Feb 21.4650	2451961.9650	400	21.335
	6068	2001 Feb 21.4938	2451961.9938	400	21.346
	6069	2001 Feb 21.4998	2451961.9998	400	21.329
2001 CZ_{31}					
	5037	2001 Feb 20.2983	2451960.7982	300	21.639
	5038	2001 Feb 20.3117	2451960.8117	300	21.651
	5039	2001 Feb 20.3164	2451960.8164	300	21.671
	5040	2001 Feb 20.3211	2451960.8211	300	21.676
	5049	2001 Feb 20.3643	2451960.8643	300	21.780
	5050	2001 Feb 20.3691	2451960.8691	300	21.780
	5051	2001 Feb 20.3738	2451960.8738	300	21.732
	5052	2001 Feb 20.3785	2451960.8785	300	21.854
	5053	2001 Feb 20.3833	2451960.8833	300	21.747
	5054	2001 Feb 20.3880	2451960.8880	300	21.681
	5055	2001 Feb 20.3927	2451960.8927	300	21.705
	5056	2001 Feb 20.3975	2451960.8975	300	21.577
	5057	2001 Feb 20.4022	2451960.9022	300	21.669
	5058	2001 Feb 20.4070	2451960.9070	300	21.662
	5059	2001 Feb 20.4117	2451960.9117	300	21.632
	5060	2001 Feb 20.4165	2451960.9165	300	21.652
	5061	2001 Feb 20.4212	2451960.9212	300	21.635
	5062	2001 Feb 20.4260	2451960.9260	300	21.660
	5063	2001 Feb 20.4307	2451960.9307	300	21.725
	5064	2001 Feb 20.4354	2451960.9354	300	21.791
	5065	2001 Feb 20.4402	2451960.9402	300	21.794
	5066	2001 Feb 20.4449	2451960.9449	300	21.799
	5067	2001 Feb 20.4498	2451960.9498	300	21.752
	5068	2001 Feb 20.4545	2451960.9545	300	21.775
	5069	2001 Feb 20.4593	2451960.9593	300	21.789
	5075	2001 Feb 20.4991	2451960.9991	300	21.611
	5076	2001 Feb 20.5039	2451961.0039	300	21.739
	5077	2001 Feb 20.5086	2451961.0086	300	21.582
	5078	2001 Feb 20.5133	2451961.0133	300	21.628
	5079	2001 Feb 20.5181	2451961.0181	300	21.716
	6034	2001 Feb 21.3003	2451961.8003	350	21.729
	6035	2001 Feb 21.3058	2451961.8058	350	21.796
	6036	2001 Feb 21.3113	2451961.8113	350	21.679
	6041	2001 Feb 21.3387	2451961.8387	350	21.686
	6042	2001 Feb 21.3442	2451961.8442	350	21.663
	6047	2001 Feb 21.3722	2451961.8722	350	21.864
	6048	2001 Feb 21.3776	2451961.8776	350	21.796
	6056	2001 Feb 21.4258	2451961.9258	350	21.668
	6057	2001 Feb 21.4312	2451961.9312	350	21.610
	1029	2001 Apr 20.2553	2452019.7553	400	21.869
	1030	2001 Apr 20.2613	2452019.7613	400	21.939
	1034	2001 Apr 20.2850	2452019.7850	400	21.940
	1036	2001 Apr 20.2968	2452019.7968	400	21.816

Table 4.3: (continued)

Object	Image[a]	UT Date[b]	Julian Date[c]	Exp[d] (sec)	Mag.[e] (m_R)
	1037	2001 Apr 20.3028	2452019.8028	400	21.839
	1038	2001 Apr 20.3089	2452019.8089	400	21.779
	1039	2001 Apr 20.3150	2452019.8150	400	21.811
	1040	2001 Apr 20.3213	2452019.8213	400	21.775
	1044	2001 Apr 20.3458	2452019.8458	400	21.829
	1045	2001 Apr 20.3518	2452019.8518	400	21.907
1998 HK_{151}					
	4080	2000 Apr 30.5807	2451665.0807	400	21.813
	4081	2000 Apr 30.5866	2451665.0866	400	21.687
	4082	2000 Apr 30.5926	2451665.0926	400	21.827
	4083	2000 Apr 30.5985	2451665.0985	400	21.608
	5045	2000 May 1.4036	2451665.9036	400	21.771
	5046	2000 May 1.4098	2451665.9098	400	21.711
	5047	2000 May 1.4158	2451665.9158	400	21.770
	5052	2000 May 1.4457	2451665.9456	400	21.760
	5053	2000 May 1.4517	2451665.9517	400	21.716
	5057	2000 May 1.4780	2451665.9780	400	21.788
	5058	2000 May 1.4840	2451665.9840	400	21.778
	5062	2000 May 1.5093	2451666.0093	400	21.782
	5063	2000 May 1.5154	2451666.0153	400	21.747
	5067	2000 May 1.5411	2451666.0411	400	21.588
	5068	2000 May 1.5471	2451666.0471	400	21.806
	5069	2000 May 1.5530	2451666.0530	400	21.766
	5070	2000 May 1.5589	2451666.0589	400	21.722
	5071	2000 May 1.5648	2451666.0649	400	21.678
	5072	2000 May 1.5708	2451666.0708	400	21.804
	5073	2000 May 1.5767	2451666.0767	400	21.663
	5074	2000 May 1.5827	2451666.0827	400	21.688
	5075	2000 May 1.5889	2451666.0889	400	21.656
	5076	2000 May 1.5949	2451666.0949	400	21.658

[a] Image number.

[b] Decimal Universal Date at the start of the integration.

[c] Julian Date at the start of the integration.

[d] Exposure time for the image.

[e] Apparent red magnitude, uncertainties are ±0.02 to 0.03 for the brighter objects (< 21.0 mags.) and ±0.04 to 0.05 for fainter objects.

4.4.1 (20000) Varuna

Varuna shows a large, periodic photometric variation (Farnham 2001). We measured a range $\Delta m_R = 0.42 \pm 0.02$ mag. and best-fit, two-peaked lightcurve period $P = 6.3436 \pm 0.0002$ hrs (about twice the period reported by Farnham), with no evidence for a rotational

Table 4.4. Properties of Observed KBOs

Name		m_R[a] (mag)	Nights[b] (#)	Δm_R[c] (mag)	Single[d] (hrs)	Double[e] (hrs)
(38628)	2000 EB_{173}	19.18 ± 0.03	3	< 0.06	-	-
(20000) Varuna	2000 WR_{106}[f]	19.70 ± 0.25	8	0.42 ± 0.03	-	6.34 ± 0.01
(26375)	1999 DE_9	20.02 ± 0.03	3	< 0.10	> 12?	-
(26181)	1996 GQ_{21}	20.35 ± 0.04	6	< 0.10	-	-
	2000 GN_{171}	20.60 ± 0.30	9	0.61 ± 0.03	-	8.329 ± 0.005
(19521) Chaos	1998 WH_{24}	20.65 ± 0.10	2	< 0.10	?	?
(33340)	1998 VG_{44}	20.95 ± 0.10	3	< 0.10	-	-
	2001 FZ_{173}	21.05 ± 0.05	2	< 0.06	-	-
(33128)	1998 BU_{48}	21.25 ± 0.35	7	0.68 ± 0.04	4.9 ± 0.1	9.8 ± 0.1
					6.3 ± 0.1	12.6 ± 0.1
	1999 KR_{16}	21.15 ± 0.15	10	0.18 ± 0.04	5.929 ± 0.001	11.858 ± 0.002
					5.840 ± 0.001	11.680 ± 0.002
	1997 CS_{29}	21.36 ± 0.04	1	< 0.08	-	-
	2001 CZ_{31}	21.70 ± 0.10	5	< 0.20	?	?
	1998 HK_{151}	21.75 ± 0.05	2	< 0.15	-	-

[a]Mean red magnitude on the date having the majority of observations.

[b]Number of nights used to determine the lightcurve.

[c]The peak to peak range of the lightcurve.

[d]The lightcurve period if there is one maximum per period.

[e]The lightcurve period if there is two maximum per period.

[f]See Jewitt and Sheppard (2002) for details.

Table 4.5. Colors of Observed Kuiper Belt Objects

Name		B-V (mag)	V-R (mag)	R-I (mag)
(38628)	2000 EB_{173}[a]	0.93 ± 0.04	0.65 ± 0.03	0.59 ± 0.03
(20000) Varuna	2000 WR_{106}[b]	0.85 ± 0.01	0.64 ± 0.01	0.62 ± 0.01
(26375)	1999 DE_9[a]	0.94 ± 0.03	0.57 ± 0.03	0.56 ± 0.03
(26181)	1996 GQ_{21}	-	0.69 ± 0.03	-
	2000 GN_{171}	0.92 ± 0.04	0.63 ± 0.03	0.56 ± 0.03
(19521) Chaos	1998 WH_{24}[c]	0.94 ± 0.03	0.62 ± 0.03	-
(33340)	1998 VG_{44}[d]	0.93 ± 0.05	0.61 ± 0.04	0.77 ± 0.04
	2001 FZ_{173}	-	-	-
(33128)	1998 BU_{48}	0.77 ± 0.05	0.68 ± 0.04	0.50 ± 0.04
	1999 KR_{16}	0.99 ± 0.05	0.75 ± 0.04	0.70 ± 0.04
	1997 CS_{29}[a]	1.16 ± 0.06	0.61 ± 0.05	0.66 ± 0.05
	2001 CZ_{31}	0.60 ± 0.15	0.5 ± 0.1	0.3 ± 0.1
	1998 HK_{151}[d]	-	0.45 ± 0.04	0.42 ± 0.04

[a]From Jewitt & Luu 2001.

[b]See Jewitt & Sheppard 2002.

[c]From Tegler & Romanishin 2000.

[d]From Boehnhardt et al. 2001.

modulation in the $B-V$, $V-R$ or $R-I$ color indices. These results, and their interpretation in terms of a rotating, elongated rubble pile of low bulk density, are described in detail in Jewitt and Sheppard (2002).

4.4.2 2000 GN_{171}

PDM analysis shows that 2000 GN_{171} has strong PDM minima near periods $P = 4.17$ hours and $P = 8.33$ hours, with weaker 24 hour alias periods flanking each of these (Figure 4.1). We phased the data to all the peaks with $\Theta < 0.4$ and found only the 4.17 and 8.33 hour periods to be consistent with all the data. The $P = 4.17$ hour period gives a lightcurve with a single maximum per period while the $P = 8.33$ hour lightcurve has two maxima per period as expected for rotational modulation caused by an aspherical shape. Through visual inspection of the phased lightcurves we find that the phase plot for $P = 4.17$ hour (Figure 4.2) is more scattered than that for the longer period of $P = 8.33$ hour (Figure 4.3). This is because the double-peaked phase plot shows a significant asymmetry of $\Delta \sim 0.08$ magnitudes between the two upper and lower peaks. A closer view of the PDM plot in Figure 4.4 around the double-peaked period allows us to obtain a rotation period of $P_{rot} = 8.329 \pm 0.005$ hours with a peak-to-peak variation of $\Delta m = 0.61 \pm 0.03$ magnitudes. We believe that the photometric variations in 2000 GN_{171} are due to its elongated shape rather than to albedo variations on its surface.

Broadband BVRI colors of 2000 GN_{171} show no variation throughout its rotation within the photometric uncertainties of a few % (Figures 4.5 and 4.6 and Table 4.6). This again suggests that the lightcurve is mostly caused by an elongated object with a nearly uniform surface. The colors $B - V = 0.92 \pm 0.04$, $V - R = 0.63 \pm 0.03$, and $R - I = 0.56 \pm 0.03$ (Table 4.5 and Table 4.6) show that 2000 GN_{171} is red but unremarkably so as a KBO (Jewitt and Luu 2001).

Table 4.6: Color Measurements of 2000 GN_{171}

Image	UT Date	JD_c[a]	Ph[b]	R[c]	B-R	V-R	R-I
2049	2001 Apr 21.3523	2452020.8523	0.93	20.74	-	0.68	-

Table 4.6: (continued)

Image	UT Date	JD_c[a]	Ph[b]	R[c]	B-R	V-R	R-I
2055	2001 Apr 21.3853	2452020.8853	0.03	20.51	-	0.63	-
2067	2001 Apr 21.4306	2452020.9306	0.16	20.34	-	0.58	-
2071	2001 Apr 21.4535	2452020.9535	0.22	20.43	-	0.69	-
2080	2001 Apr 21.4969	2452020.9969	0.35	20.82	-	0.63	-
2051	2001 Apr 21.3619	2452020.8619	0.96	20.67	-	-	0.52
2053	2001 Apr 21.3753	2452020.8752	0.00	20.57	-	-	0.57
2069	2001 Apr 21.4401	2452020.9401	0.19	20.36	-	-	0.51
2073	2001 Apr 21.4632	2452020.9632	0.25	20.52	-	-	0.55
2082	2001 Apr 21.5066	2452021.0066	0.38	20.85	-	-	0.62
2052	2001 Apr 21.3668	2452020.8668	0.97	20.64	1.56	-	-
2070	2001 Apr 21.4452	2452020.9452	0.20	20.38	1.63	-	-
3052	2001 Apr 22.3304	2452021.8303	0.75	20.38	-	0.59	-
3054	2001 Apr 22.3417	2452021.8417	0.78	20.50	-	0.56	-
3057	2001 Apr 22.3566	2452021.8566	0.83	20.67	-	0.60	-
3061	2001 Apr 22.3817	2452021.8817	0.90	20.79	-	0.70	-
3064	2001 Apr 22.3962	2452021.8962	0.94	20.72	-	0.68	-
3074	2001 Apr 22.4333	2452021.9333	0.05	20.47	-	0.61	-
3056	2001 Apr 22.3518	2452021.8518	0.81	20.62	-	-	0.64
3059	2001 Apr 22.3663	2452021.8663	0.85	20.75	-	-	0.60
3063	2001 Apr 22.3914	2452021.8914	0.93	20.75	-	-	0.50
3060	2001 Apr 22.3711	2452021.8711	0.87	20.77	1.49	-	-
4040	2001 Apr 23.3032	2452022.8031	0.55	20.39	-	0.58	-
4044	2001 Apr 23.3261	2452022.8261	0.62	20.29	-	0.60	-
4048	2001 Apr 23.3508	2452022.8508	0.69	20.28	-	0.61	-
4064	2001 Apr 23.4109	2452022.9109	0.86	20.77	-	0.50	-
4068	2001 Apr 23.4338	2452022.9338	0.93	20.74	-	0.64	-
4042	2001 Apr 23.3128	2452022.8128	0.58	20.34	-	-	0.64
4046	2001 Apr 23.3370	2452022.8370	0.65	20.27	-	-	0.56
4050	2001 Apr 23.3617	2452022.8616	0.72	20.31	-	-	0.52
4066	2001 Apr 23.4204	2452022.9204	0.89	20.79	-	-	0.49
4070	2001 Apr 23.4435	2452022.9435	0.96	20.68	-	-	0.54
4043	2001 Apr 23.3177	2452022.8177	0.60	20.32	1.43	-	-
4047	2001 Apr 23.3424	2452022.8424	0.67	20.27	1.49	-	-
4067	2001 Apr 23.4253	2452022.9253	0.91	20.78	1.65	-	-
3029[d]	2001 May 13.2793	2452042.7793	0.11	20.36	-	0.61	-
3030[d]	2001 May 13.2847	2452042.7847	0.13	20.35	-	0.63	-
3053[d]	2001 May 13.3834	2452042.8834	0.41	20.82	-	0.68	-
3055[d]	2001 May 13.3931	2452042.8931	0.44	20.75	-	0.62	-
3068[d]	2001 May 13.4691	2452042.9691	0.66	20.27	-	0.63	-
3070[d]	2001 May 13.4788	2452042.9788	0.69	20.28	-	0.60	-
MEAN					$1.55 \pm .03$	$0.63 \pm .03$	$0.56 \pm .03$

[a] Julian day at start of exposure.

[b] Phase of 2000 GN_{171} corresponding to color measurement. Phases of 0.2 and 0.7 correspond to maximum brightness (~ 20.3) and 0.4 and 0.9 correspond to minimum brightness (~ 20.9).

[c] R magnitude interpolated to the time of the corresponding BVI data.

[d] R and V magnitudes are corrected for phase and distance difference from April data.

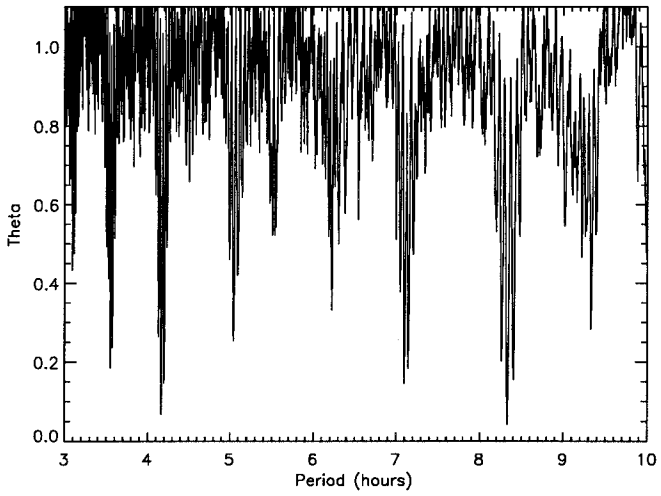

Figure 4.1 The phase dispersion minimization (PDM) plot for 2000 GN_{171}. A smaller theta corresponds to a better fit. Best fits from this plot are the 4.12 hour single-peaked fit and the 8.32 hour double-peaked fit. Both are flanked by 24 hour alias periods.

4.4.3 (33128) 1998 BU_{48}

The KBO 1998 BU_{48} showed substantial variability (> 0.4 magnitude with period > 4.0 hour) in R-band observations from 2 nights in 2001 February and April. However, a convincing lightcurve could not be found from just these 2 nights separated by 2 months. Additional observations were obtained in the period 2001 November $14-19$. One minimum and one maximum in brightness within a single night was observed and put the full single-peaked lightcurve between about 4 and 6 hours. Through PDM analysis, 1998 BU_{48} was found to have a peak-to-peak variation of $\Delta m = 0.68 \pm 0.04$ magnitudes with possible single-peaked periods near 4.1, 4.9, and 6.3 hours which are 24 hour aliases of each other (Figure 4.7). By examining the phased data using these three possible periods we find that the single-peaked periods of 4.9 ± 0.1 and 6.3 ± 0.1 hours are both plausible (Figure 4.8). The colors, $B - V = 0.77 \pm 0.05$, $V - R = 0.68 \pm 0.04$, and $R - I = 0.50 \pm 0.04$ (Table 4.5)

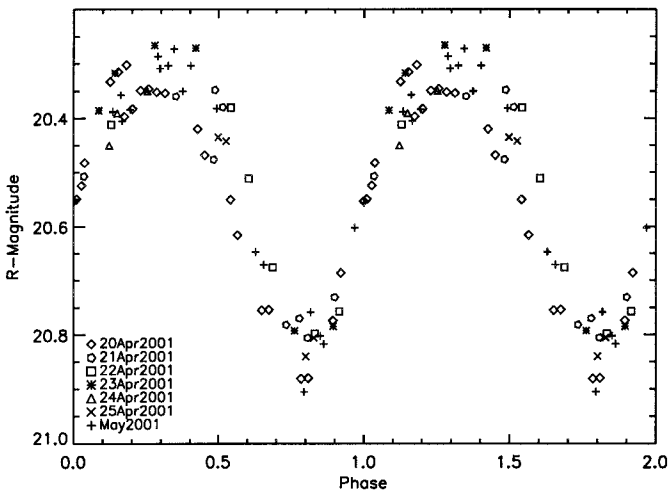

Figure 4.2 Phased R-band data from the UT April 20−25 and May 11−13, 2001 observations of 2000 GN_{171}. The period has been phased to 4.17 hours which is the best fit single-peaked period. The May data have been corrected for geometry and phase angle differences relative to the April data (see Table 4.1). The points are much more scattered here than for the better fit double-peaked period (Figure 4.3).

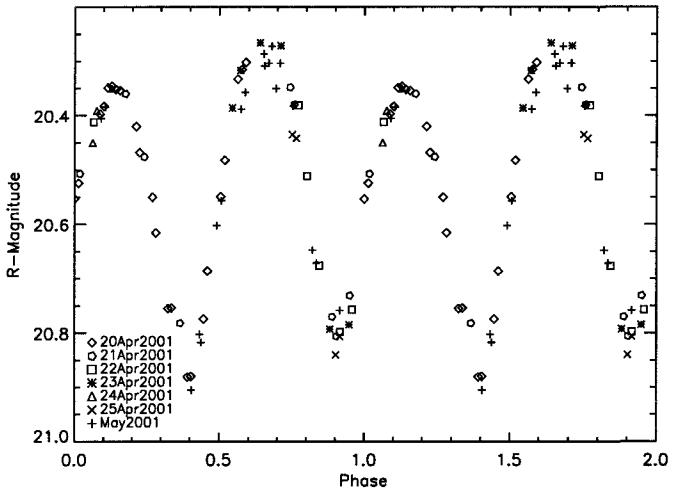

Figure 4.3 Phased R-band data from the UT April 20−25 and May 11−13, 2001 observations for 2000 GN_{171}. The period has been phased to 8.329 hours which is the best fit double-peaked period. The May data have been corrected for geometry and phase angle differences relative to the April data (see Table 4.1).

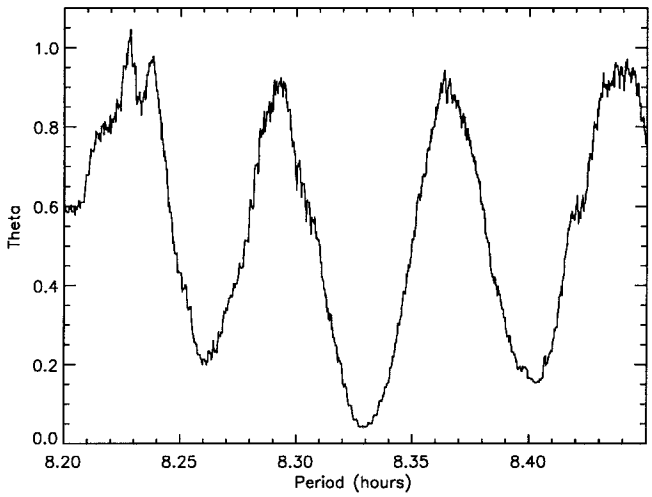

Figure 4.4 Closer view of the phase dispersion minimization (PDM) plot for 2000 GN_{171} around the doubled-peaked period near 8.33 hours. The best fit at 8.329 hours is flanked by aliases from the $\sim$ 15 day separation of the 2 data sets obtained for this object.

show no sign of variation throughout the lightcurve, within the measurement uncertainties (Table 4.7 and Figure 4.8).

Table 4.7: Color Measurements of (33128) 1998 BU_{48}

Image	UT Date	JD_c[a]	Ph[b]	R[c]	B-R	V-R	R-I
4098	2001 Nov 17.5907	2452231.0907	0.34	21.13	-	0.61	-
4107	2001 Nov 17.6458	2452231.1458	0.55	20.93	-	0.65	-
4099	2001 Nov 17.5968	2452231.0967	0.36	21.09	-	-	0.54
5088	2001 Nov 18.5635	2452231.9666	0.19	21.49	1.49	-	-
5091	2001 Nov 18.5819	2452231.9850	0.30	21.22	1.40	-	-
5095	2001 Nov 18.6056	2452232.0087	0.05	21.52	-	0.77	-
5087	2001 Nov 18.5558	2452231.9589	0.12	21.56	-	0.69	-
5090	2001 Nov 18.5760	2452231.9791	0.21	21.44	-	0.64	-
5098	2001 Nov 18.6233	2452232.0264	0.02	21.48	-	-	0.51
5094	2001 Nov 18.5997	2452232.0028	0.10	21.56	-	-	0.38
5099	2001 Nov 18.6292	2452232.0323	0.28	21.28	-	-	0.57
MEAN					$1.45 \pm .05$	$0.68 \pm .04$	$0.50 \pm .04$

[a] Julian day at start of exposure.

[b] Phase of (33128) 1998 BU_{48} corresponding to color measurement of the single-peaked 6.29 hour lightcurve. The phase of 0.6 corresponds to maximum brightness ($\sim$ 20.9) and 0.1 corresponds

Table 4.7: (continued)

Image	UT Date	JD_c[a]	Ph[b]	R[c]	B-R	V-R	R-I

to minimum brightness (~ 21.6).
[c] R magnitude interpolated to the time of the corresponding BVI data.

4.4.4 1999 KR_{16}

This object was observed on four different observing runs during the course of 2000 and 2001. The data from 2001 are more numerous and of better quality than the data from 2000. We observed one brightness minimum and one maximum within a single night of data and from this estimated that the full single-peaked lightcurve should be near 6 hours. In a PDM plot constructed using only the inferior data from 2000 we found single-peaked minima at 4.66 and 5.82 hours. Phased lightcurves at these periods are acceptable for the year 2000 data, but the 4.66 hour period is inconsistent with the data from 2001. In the PDM plot using the R-band data from February, April, and May 2001 the best fit single-peaked period is shown to be around 5.9 hours with associated flanking peaks from 24 hours and 15 and 60 day sampling aliases (Figure 4.9). Closer examination of the PDM fit near 5.9 hours shows the 15 and 60 day aliasing much better and gives two best fit periods, one at 5.840 and the other at 5.929 hours (Figure 4.10). We phased the 2001 data to both single peaks and found neither to be significantly better than the other. The true single-peaked period for 1999 KR_{16} is at one of these two values. The data phased to the 5.840 hour single-peaked period are shown in Figure 4.11. Neither of the possible double-peaked periods of 11.680 and 11.858 hours show differences between the peaks. The peak-to-peak amplitude of 1999 KR_{16} is 0.18 ± 0.04 in the 2001 data consistent with that found in the 2000 data. Colors of 1999 KR_{16}, $B - V = 0.99 \pm 0.05$, $V - R = 0.75 \pm 0.04$, and $R - I = 0.70 \pm 0.04$, are on the red end of the KBO distribution (Table 4.5). The colors show no signs of variation through the rotation of the object to the accuracy of our measurements (Table 4.8 and Figure 4.11).

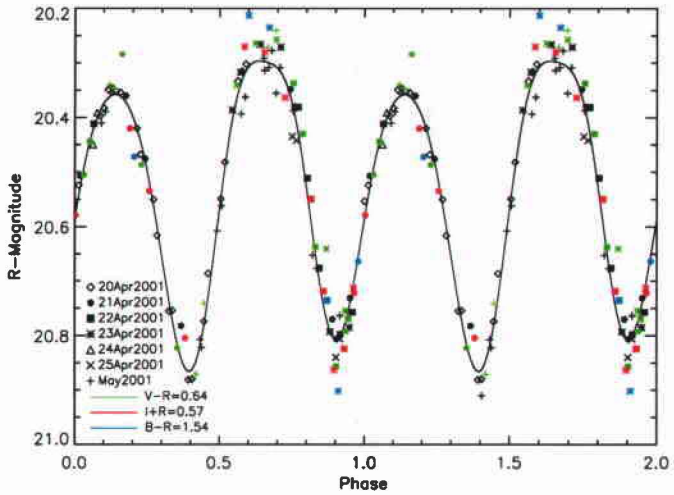

Figure 4.5 The phased BVRI data from the UT April 20 – 25 and May 11 – 13, 2001 observations of 2000 GN_{171}. The period has been phased to 8.329 hours which is the best fit double-peaked period. The May data have been corrected for geometry and phase angle differences relative to the April data (Table 4.1). The BVI data have been shifted by the amount indicated on the graph in order to correspond to the R data. No color variation is seen within our uncertainties. A Fourier fit shows the two pronounced maximum and minimum.

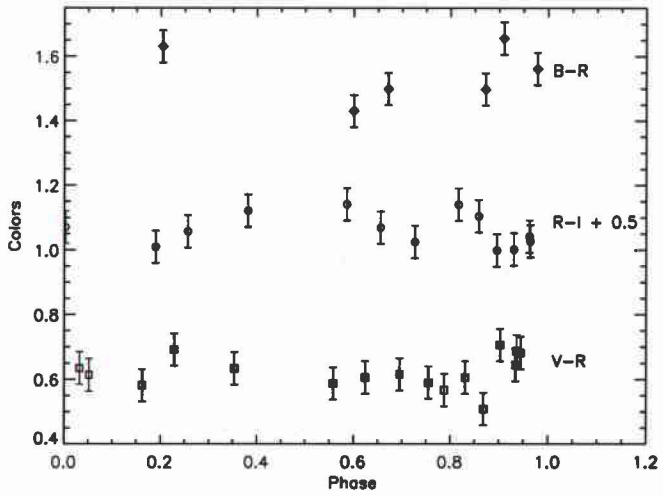

Figure 4.6 The colors of 2000 GN_{171} plotted against rotational phase.

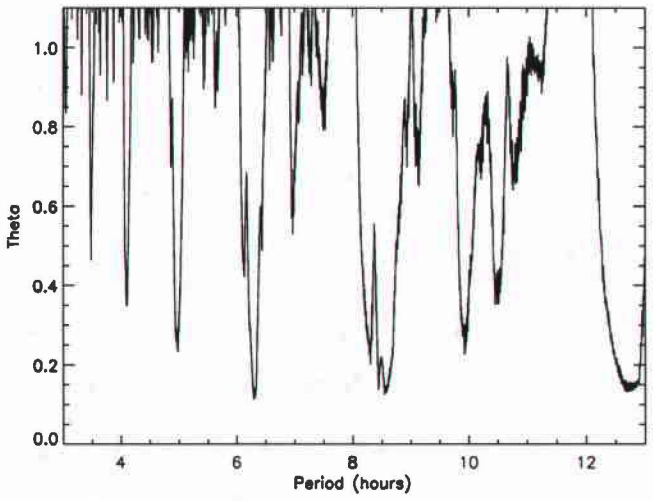

Figure 4.7 Phase dispersion minimization (PDM) plot for (33128) 1998 BU_{48} from the November 2001 data. Best fits from this plot are the 4.9 and 6.3 hour single-peaked fits and the 9.8 and 12.6 hour double-peaked fits.

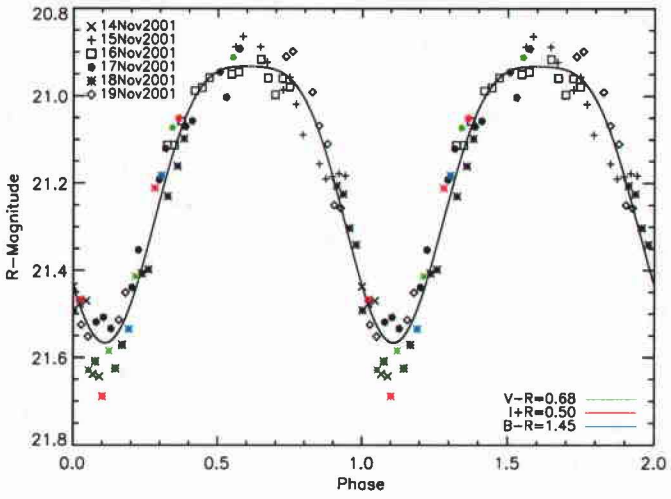

Figure 4.8 BVRI phased data from the UT November 14 – 19 observations of (33128) 1998 BU_{48}. The period has been phased to 6.29 hours which is one of the best fit single-peaked periods for (33128) 1998 BU_{48}, the other being around 4.9 hours.

Table 4.8: Color Measurements of 1999 KR_{16}

Image	UT Date	JD_c[a]	Ph[b]	R[c]	B-R	V-R	R-I
2031	2001 May 12.2634	2452041.7634	0.13	21.10	-	0.70	-
2035	2001 May 12.2899	2452041.7899	0.24	21.17	-	0.75	-
2051	2001 May 12.3479	2452041.8479	0.48	21.18	-	0.74	-
2055	2001 May 12.3743	2452041.8743	0.59	21.16	-	0.77	-
2069	2001 May 12.4314	2452041.9314	0.82	21.04	-	0.79	-
2073	2001 May 12.4538	2452041.9538	0.91	21.01	-	0.77	-
2033	2001 May 12.2754	2452041.7754	0.18	21.14	-	-	0.71
2037	2001 May 12.3020	2452041.8019	0.29	21.18	-	-	0.73
2053	2001 May 12.3599	2452041.8599	0.53	21.17	-	-	0.69
2057	2001 May 12.3862	2452041.8862	0.64	21.14	-	-	0.66
2034	2001 May 12.2815	2452041.7814	0.20	21.15	1.74	-	-
2054	2001 May 12.3659	2452041.8659	0.55	21.16	1.73	-	-
3035	2001 May 13.3145	2452042.8144	0.45	21.18	-	0.69	-
3038	2001 May 13.3325	2452042.8325	0.52	21.17	-	0.80	-
3057	2001 May 13.4042	2452042.9042	0.82	21.05	-	0.78	-
3059	2001 May 13.4162	2452042.9161	0.87	21.02	-	0.72	-
3062	2001 May 13.4342	2452042.9342	0.94	21.01	-	0.73	-
3037	2001 May 13.3265	2452042.8265	0.50	21.17	-	-	0.70
3040	2001 May 13.3444	2452042.8444	0.57	21.16	-	-	0.72
3061	2001 May 13.4282	2452042.9282	0.92	21.01	-	-	0.69
3064	2001 May 13.4463	2452042.9463	0.99	21.02	-	-	0.65

Table 4.8: (continued)

Image	UT Date	JD_c[a]	Ph[b]	R[c]	B-R	V-R	R-I
MEAN					$1.74 \pm .04$	$0.75 \pm .03$	$0.70 \pm .03$

[a] Julian day at start of exposure.

[b] Phase of 1999 KR_{16} corresponding to color measurement of the single-peaked 5.84 hour lightcurve. The phase of 0.9 corresponds to maximum brightness ($\sim$ 21.0) and 0.4 corresponds to minimum brightness ($\sim$ 21.2).

[c] R magnitude interpolated to the time of the corresponding BVI data. R magnitudes are corrected for phase and distance difference from April data so they can be compared to the plots directly.

4.4.5 Null Lightcurves

Nine of the TNOs (2001 FZ_{173}, 2001 CZ_{31}, (38628) 2000 EB_{173}, (26375) 1999 DE_9, 1998 HK_{151}, (33340) 1998 VG_{44}, (19521) Chaos 1998 WH_{24}, 1997 CS_{29}, and (26181) 1996 GQ_{21}) show no measurable photometric variations. Practically, this means that their lightcurves have range $\leq$ 0.15 magnitudes and/or period $\geq$ 24 hours (Figures 4.12 and Table 4.4). A few objects show hints of variability that might, with better data, emerge as rotationally modulated lightcurves. Inspection of the 2001 CZ_{31} data hints at a single-peaked lightcurve of period $\sim$ 3 hours and amplitude $\sim$ 0.15 magnitudes, but since the photometry has large error bars we can not be sure of this result. The TNO 1999 DE_9 may have a long period lightcurve of about 0.1 mag. range since the brightness on 2001 April 24 slowly increases towards the end of the night and the February data appear to have base magnitudes different by about 0.1 mag. The data from 2000 on 1999 DE_9 show the object to have a flat lightcurve. (33340) 1998 VG44 may also have a long period lightcurve since its base magnitudes on 1999 November 11 and 12 are different by about 0.05 mag. The bright TNO (19521) 1998 WH_{24} may have a possible lightcurve of about 4 hours single-peaked period and peak-to-peak range of 0.07 mag. Confirmation of these subtle lightcurves will require more accurate data, probably from larger telescopes than the one employed here.

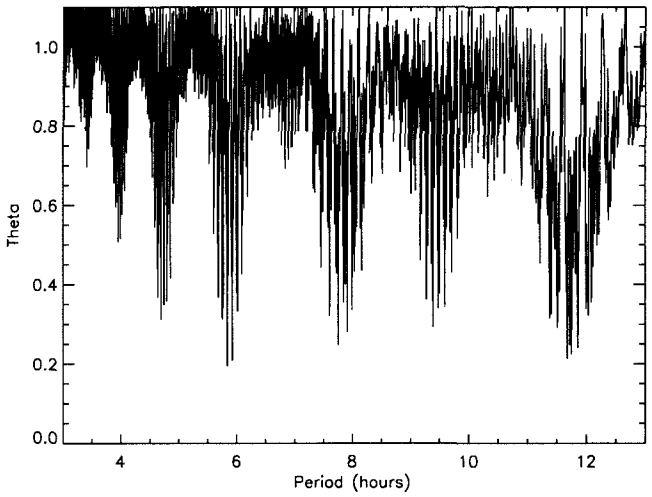

Figure 4.9 Phase dispersion minimization (PDM) plot for 1999 KR_{16} using all the R-band data from February, April and May 2001. Best fits from this plot are near the 5.9 hour single-peak period and the 11.8 hour double-peaked period. Both are flanked by aliases of the 24 hr and $\sim$ 15 and $\sim$ 60 day sampling periodicities.

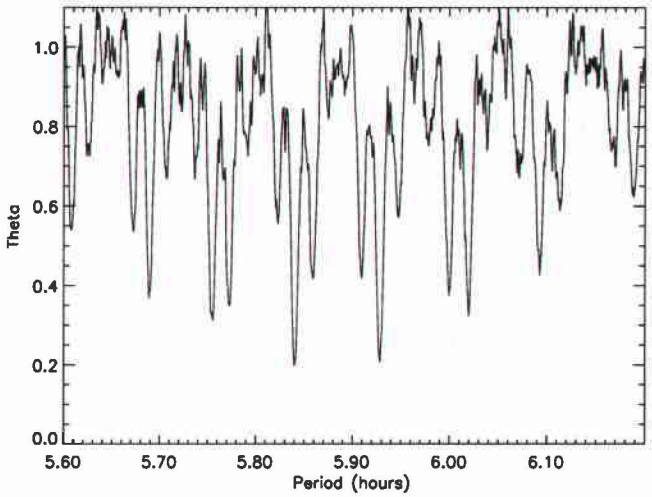

Figure 4.10 A closer view of the phase dispersion minimization (PDM) plot for 1999 KR_{16} around the best fit single-peaked periods near 5.9 hours.

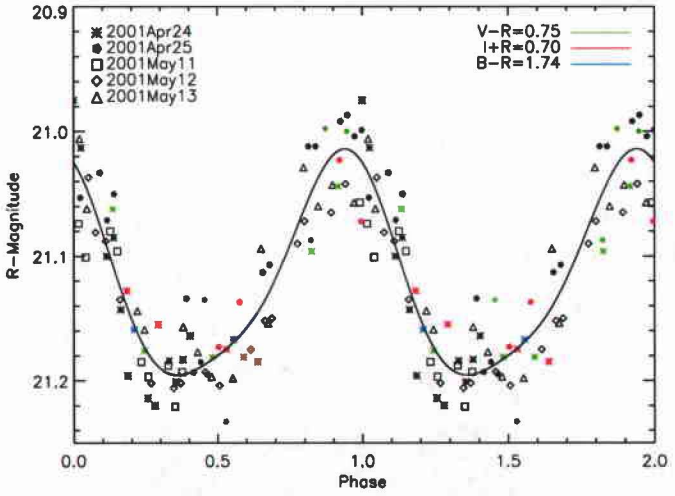

Figure 4.11 The phased BVRI data from the UT April 24 – 25 and May 11 – 13, 2001 observations of 1999 KR_{16}. The period has been phased to 5.840 hours which is one of the best fit single-peaked period for 1999 KR_{16}, the other being at 5.929 hours.

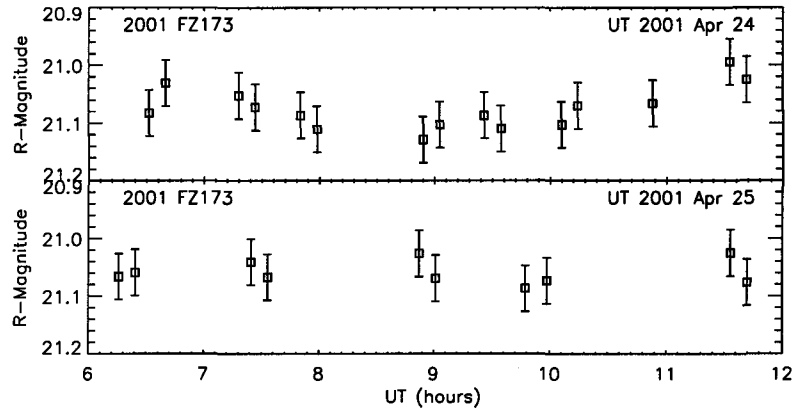
2001 FZ173
UT 2001 Apr 24
2001 FZ173
UT 2001 Apr 25
R-Magnitude
UT (hours)

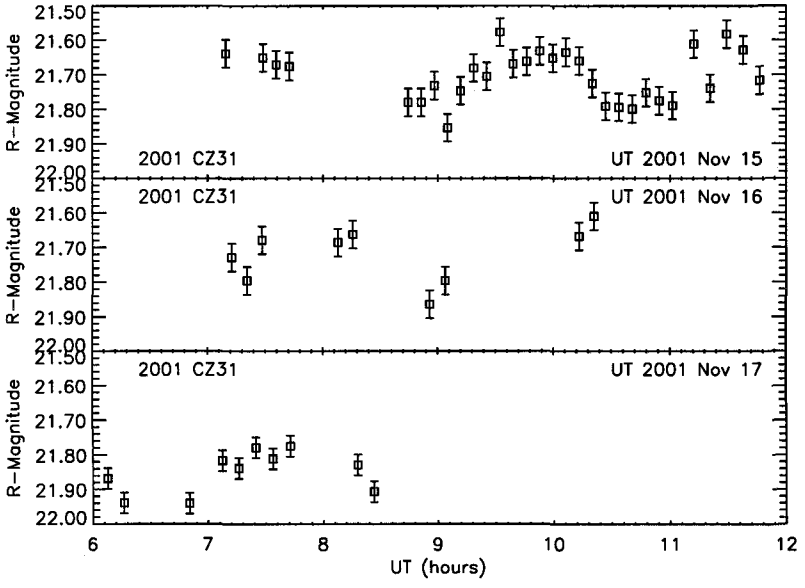
2001 CZ31
UT 2001 Nov 15
2001 CZ31
UT 2001 Nov 16
2001 CZ31
UT 2001 Nov 17
R-Magnitude
UT (hours)

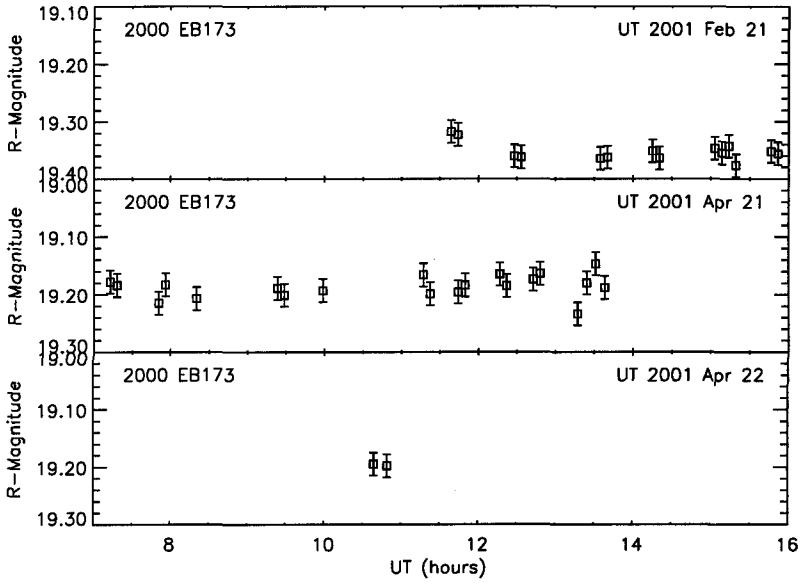
2000 EB173
UT 2001 Feb 21
2000 EB173
UT 2001 Apr 21
2000 EB173
UT 2001 Apr 22
R-Magnitude
19.10
19.20
19.30
19.40
19.00
19.10
19.20
19.30
19.00
19.10
19.20
19.30
8
10
12
14
16
UT (hours)

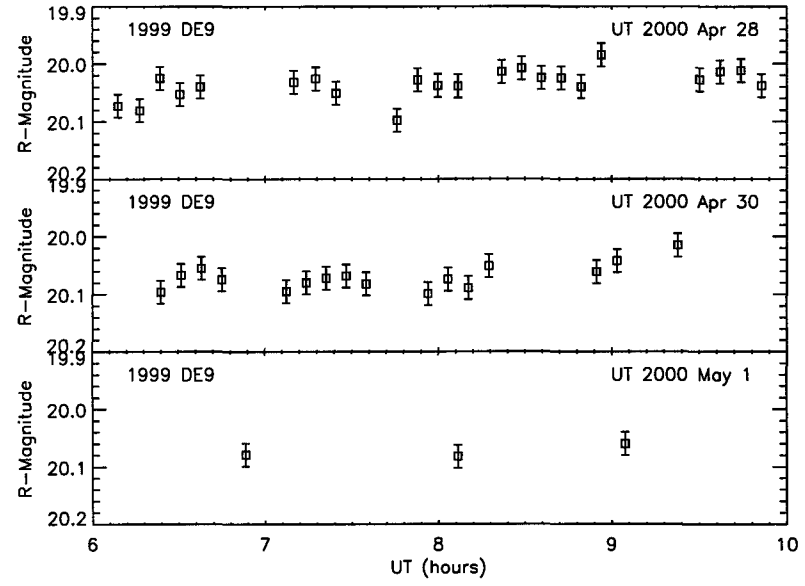
1999 DE9
UT 2000 Apr 28
1999 DE9
UT 2000 Apr 30
1999 DE9
UT 2000 May 1
R-Magnitude
19.9
20.0
20.1
20.2
6
7
8
9
10
UT (hours)

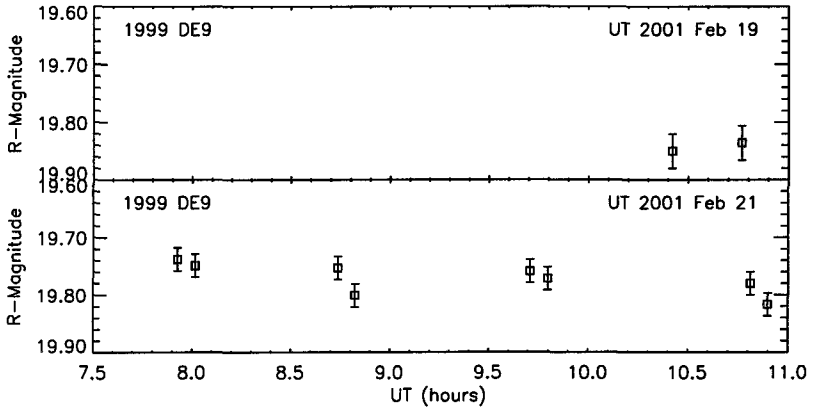
1999 DE9
UT 2001 Feb 19
1999 DE9
UT 2001 Feb 21
R-Magnitude
19.60
19.70
19.80
19.90
7.5
8.0
8.5
9.0
9.5
10.0
10.5
11.0
UT (hours)

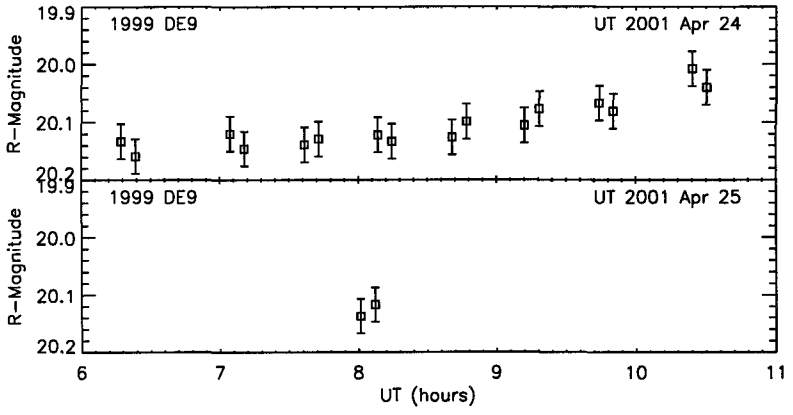
1999 DE9
UT 2001 Apr 24
1999 DE9
UT 2001 Apr 25
R-Magnitude
19.9
20.0
20.1
20.2
6
7
8
9
10
11
UT (hours)

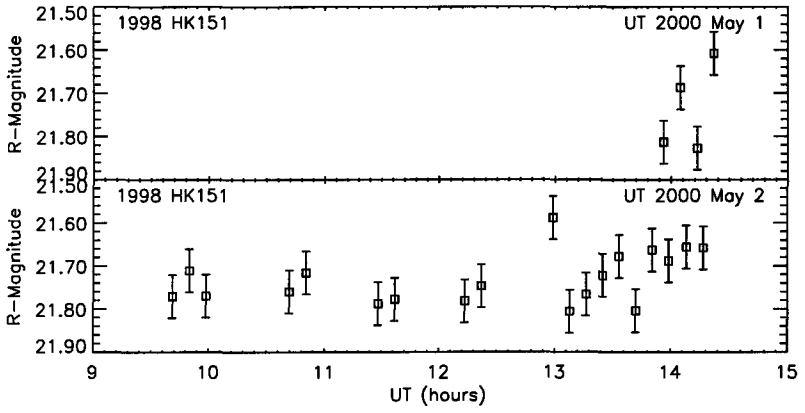
1998 HK151
UT 2000 May 1
1998 HK151
UT 2000 May 2
R-Magnitude
21.50
21.60
21.70
21.80
21.90
9
10
11
12
13
14
15
UT (hours)

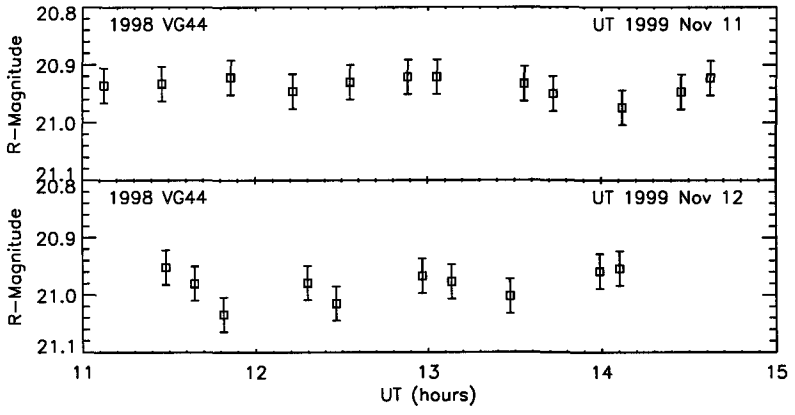
1998 VG44
UT 1999 Nov 11
1998 VG44
UT 1999 Nov 12
R-Magnitude
20.8
20.9
21.0
21.1
11
12
13
14
15
UT (hours)

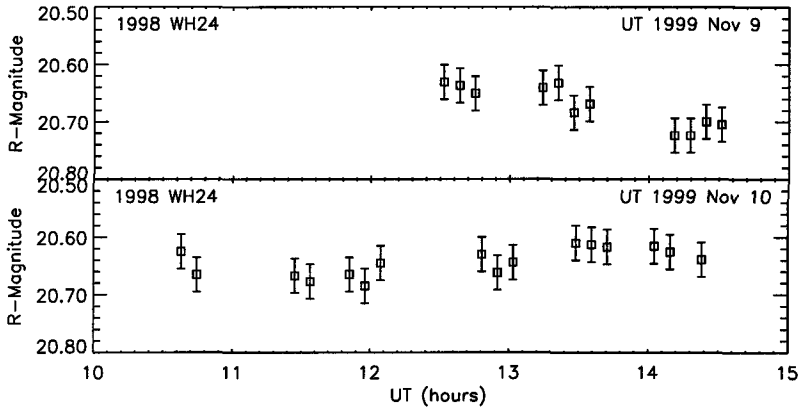
1998 WH24
UT 1999 Nov 9
1998 WH24
UT 1999 Nov 10
R-Magnitude
20.50
20.60
20.70
20.80
10
11
12
13
14
15
UT (hours)

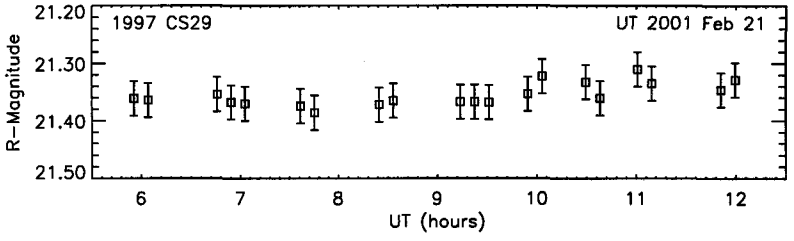
1997 CS29
UT 2001 Feb 21
R-Magnitude
21.20
21.30
21.40
21.50
6
7
8
9
10
11
12
UT (hours)

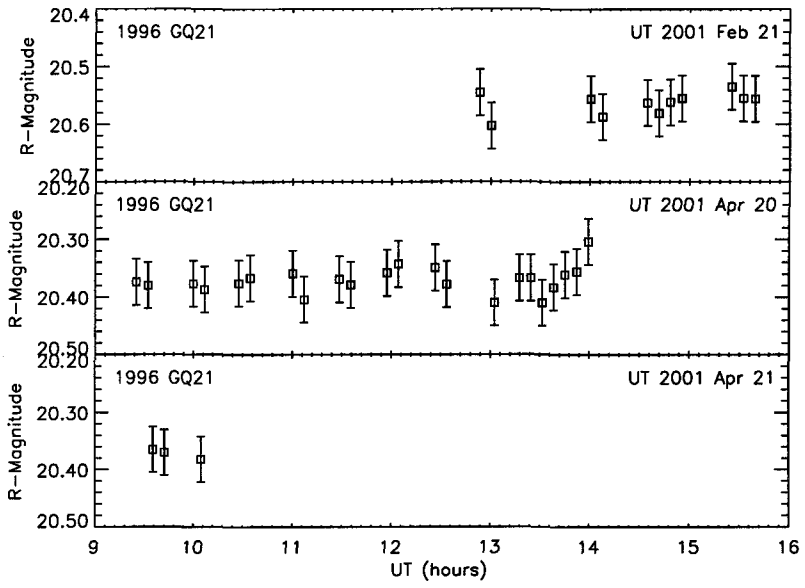

4.5 Interpretation

The KBOs should be in principal axis rotation since the expected damping time of any other wobbles is much less than the age of the Solar System (Burns & Safronov (1973); Harris (1994)). Orbital periods of KBOs are long (> 200 years) and thus the pole orientation to our line of sight should not change significantly between epochs. The apparent magnitude of a KBO depends on its physical characteristics and geometrical circumstances and can be represented as

$$m_R = m_\odot - 2.5\log\left[p_R r^2 \phi(\alpha)/(2.25 \times 10^{16} R^2 \Delta^2)\right] \tag{4.1}$$

in which r [km] is the radius of the KBO, R [AU] is the heliocentric distance, Δ [AU] is the geocentric distance, $m_\odot$ is the apparent red magnitude of the sun (-27.1), m_R is the apparent red magnitude, p_R is the red geometric albedo, and $\phi(\alpha)$ is the phase function in which the phase angle $\alpha = 0$ deg at opposition and $\phi(0) = 1$. The apparent brightness of an inert body viewed in reflected light may vary because of 1) changes in

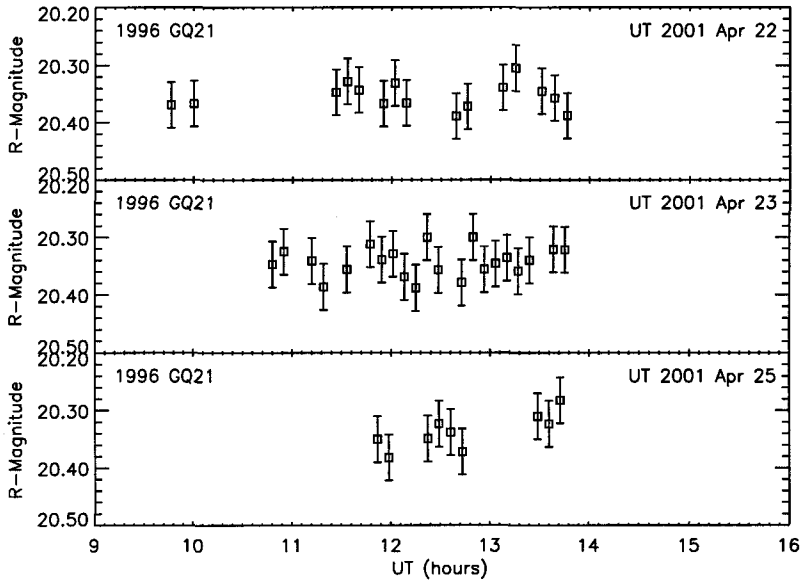

Figure 4.12 The null lightcurves of KBOs found to have no significant variation: a) 2001 FZ_{173} b) 2001 CZ_{31} c) (38628) 2000 EB_{173} d) (26375) 1999 DE_9 e) 1998 HK_{151} f) (33340) 1998 VG_{44} g) (19521) Chaos 1998 WH_{24} h) 1997 CS_{29} i) (26181) 1996 GQ_{21}.

the observing geometry, including the effects of phase darkening as in Eq. (4.1) and 2) rotational modulation of the scattered light. These different effects are discussed below.

4.5.1 Non-uniform Surface Markings

Surface albedo markings or topographical shadowing can potentially influence the lightcurves. Judging by other planetary bodies, the resulting light variations are typically smaller than those caused by elongated shape, with fluctuations due to albedo being mostly less than about 10 to 20 percent (Degewij et al. (1979)). A color variation at the maximum and minimum of a lightcurve may be seen if albedo is the primary cause for the lightcurve since materials with markedly different albedos often also have markedly different colors. For example, many pure ices and frosts have a very high albedo and are neutral to bluish in color. A lightcurve caused by an ice or frost patch should show a bluish color when at maximum brightness. Some of the most extreme albedo contrasts are found on Pluto and the Saturnian satellite Iapetus (Table 4.9). The latter is in synchronous rotation around Saturn with its leading hemisphere covered in a very low albedo material thought to be deposited from elsewhere in the Saturn system. Iapetus shows clear rotational color variations ($\Delta(B-V) \sim$ 0.1 mag.) that are correlated with the rotational albedo variations. On the other hand, Pluto has large albedo differences across its surface but the hemispherically averaged color variations are only of order 0.01 mag. We feel that neither Iapetus nor Pluto constitutes a particularly good model for the KBOs. The large albedo contrast on Iapetus is a special consequence of its synchronous rotation and the impact of material trapped in orbit about Saturn. This process is without analog in the Kuiper Belt. Pluto is also not representative of the other KBOs. It is so large that it can sustain an atmosphere which may contribute to amplifying its lightcurve amplitude by allowing surface frosts to condense on brighter (cooler) spots. Thus brighter spots grow brighter while darker (hotter) spots grow darker through the sublimation of ices. This positive feedback mechanism requires an atmosphere and is unlikely to be relevant on the smaller KBOs studied here.

Table 4.9. List of Large Objects with Large Amplitude Lightcurves.[a]

Name	Type	$a \times b \times c$ (km)	ρ (kg m^3)	Δ mag (mag)	Period (hrs)	comment
Pluto	planet	2300	2061	0.33	6.4d	albedo
Iapetus	satellite	1430	1025	2	79.3d	albedo
Hyperion	satellite	$350 \times 240 \times 200$	~ 1250	0.5	chaos	fragment?
624 Hektor	Trojan	300×150	~ 2500	1.2	6.9	contact binary?
Amalthea	satellite	$270 \times 166 \times 150$	~ 3000	-	-	frag?/albedo
15 Eunomia	asteroid	$\sim 270 \times 160 \times 115$	1160	0.56	6.1	Jacobi?
87 Sylvia	asteroid	$\sim 270 \times 150 \times 115$	1640	0.62	5.2	Jacobi?
16 Psyche	asteroid	$\sim 260 \times 175 \times 120$	2340	0.42	4.2	Jacobi?
107 Camilla	asteroid	$\sim 240 \times 150 \times 105$	1850	0.52	4.8	Jacobi?
Janus	satellite	$220 \times 190 \times 160$	656	-	-	fragment?
45 Eugenia	asteroid	$\sim 210 \times 145 \times 100$	1270	0.41	5.7	Jacobi?

[a]Objects that have diameters > 200 km and lightcurves with peak-to-peak amplitudes > 0.40 magnitudes. Pluto is the only exception since its lightcurve is slightly less than 0.40 magnitudes.

Note. — The Jacobi type main belt asteroids had their axis ratios and densities calculated from their amplitudes and periods as described for the KBOs in the text. Data for the other objects were culled from the best measurements in the literature.

4.5.2 Aspherical Shape

The critical rotation period (T_{crit}) at which centripetal acceleration equals gravitational acceleration towards the center of a rotating spherical object is

$$T_{crit} = \left(\frac{3\pi}{G\rho}\right)^{1/2} \tag{4.2}$$

where G is the gravitational constant and ρ is the density of the object. With $\rho = 10^3$ kg m^{-3} the critical period is about 3.3 hours. Even at longer periods, real bodies will suffer centripetal deformation into aspherical shapes. For a given density and specific angular momentum (H), the nature of the deformation depends on the strength of the object. In the limiting case of a strengthless (fluid) body, the equilibrium shapes have been well studied (Chandrasekhar 1987). For $H \leq 0.304$ (in units of $(GM^3a')^{1/2}$, where M[kg] is the mass of the object and a'[m] is the radius of an equal volume sphere) the equilibrium shapes are the oblate "MacLaurin" spheroids. Oblate spheroids in rotation about their minor axis exhibit no rotational modulation of the cross-section and therefore are not candidate shapes for explaining the lightcurves of the KBOs. However, for $0.304 \leq H \leq 0.390$ the equilibrium figures are triaxial "Jacobi" ellipsoids which generate lightcurves of substantial amplitude when viewed equatorially. Strengthless objects with $H > 0.390$ are rotationally unstable to fission.

The KBOs, being composed of solid matter, clearly cannot be strengthless. However, it is likely that the interior structures of these bodies have been repeatedly fractured by impact, and that their mechanical response to applied rotational stress is approximately fluid-like. Such "rubble pile" structure has long been suspected in the main asteroid belt (Farinella et al. 1981) and has been specifically proposed to explain the short period and large amplitude of (20000) Varuna (Jewitt and Sheppard 2002). The rotational deformation of a rubble pile is uniquely related to its bulk density and specific angular momentum. Therefore, given that the shape and specific angular momentum can be estimated from the amplitude and period of the lightcurve, it is possible to use photometric data to estimate the density.

Elongated Objects exhibit rotational photometric variations caused by changes in the projected cross-section. The rotation period of an elongated object should be twice the single-peaked lightcurve variation due to its projection of both long axes (2 maxima) and short axes (2 minima) during one full rotation. From the ratio of maximum to minimum brightness we can determine the projection of the body shape into the plane of the sky. The rotational brightness range of a triaxial object with semiaxes $a \geq b \geq c$ in rotation about the c axis is given by (Binzel et al. 1989)

$$\Delta m = 2.5\log\left(\frac{a}{b}\right) - 1.25\log\left(\frac{a^2cos^2\theta + c^2sin^2\theta}{b^2cos^2\theta + c^2sin^2\theta}\right) \tag{4.3}$$

where Δm is expressed in magnitudes, and θ is the angle at which the rotation (c) axis is inclined to the line of sight (an object with $\theta = 90$ deg. is viewed equatorially).

It is to be expected that, through collisions, fragments would have random pole vector orientations. For example, the collisionally highly evolved asteroid belt shows a complete randomization of pole vector orientations, θ. Only the largest asteroids may show a preference for rotation vectors aligned perpendicular to the ecliptic ($\theta = 90°$), though this is debatable (Binzel et al. (1989); Drummond et al. (1991); de Angelis (1995)). In the absence of any pole orientation data for the KBOs, we will assume they have a random distribution of spin vectors. Given a random distribution, the probability of viewing an object within the angle range θ to $\theta + d\theta$ is proportional to $\sin(\theta)d\theta$. In such a distribution, the average viewing angle is $\theta = 60$ degrees. Therefore, on average, the sky-plane ratio of the axes of an elongated body is smaller than the actual ratio by a factor $\sin(60) \approx 0.87$.

In addition to rotational deformation, it is possible that some asteroids and KBOs consist of contact binaries (Jewitt & Sheppard 2002). For a contact binary consisting of equal spheres, the axis ratio of 2:1 corresponds to a peak-to-peak lightcurve range $\Delta m = 0.75$ mag., as seen from the rotational equator. For such an object at the average viewing angle $\theta = 60$ degrees we expect $\Delta m = 0.45$ mag.

Collisionally produced fragments on average have axis ratios $2 : 2^{1/2} : 1$ (Fujiwara et al. (1978); Capaccioni et al. (1984)). When viewed equatorially, such fragments will have Δm = 0.38 mag. At the mean viewing angle $\theta = 60$ degrees we obtain $\Delta m = 0.20$ mag.

4.5.3 Lightcurve Model Results

The KBOs in our sample are very large ($D > 250$ km assuming a low albedo) and should, in the absence of rotational deformation, be spherical in shape from gravitational self compression. The large amplitudes and fast rotations of (20000) Varuna, 2000 GN_{171}, and (33128) 1998 BU_{48} suggest that the lightcurves are caused by elongation and not surface albedo features. In support of this is the finding that (33128) 1998 BU_{48} and (20000) Varuna have no color variations throughout their lightcurves and 2000 GN_{171} has only a slight if any variation in color. Independently 2000 GN_{171} shows two distinct lightcurve maxima and minima which is a strong reason to believe the object is elongated. The other lightcurve we found was for 1999 KR_{16}. Since its amplitude is much smaller and period longer, the lightcurve of 1999 KR_{16} may be more dominated by nonuniform albedo features on its surface, though we found no measurable color variation over the rotation.

Table 4.10 lists the parameters of albedo, Jacobi ellipsoid and binary models that fit the axis ratios estimated from the lightcurve data (Table 4.4). For each object and model, we list the minimum bulk density, ρ, required to maintain a stable configuration, as described in Jewitt and Sheppard (2002). We briefly describe the procedure below for 2000 GN_{171}. Results for the rest of the significant light variation objects in our sample ((20000) Varuna, (33128) 1998 BU_{48}, and 1999 KR_{16}) can be seen in Table 4.10 using the data from Table 4.4.

We use Equation 4.3 to estimate the axis ratio a/b. If we assume that the rotation axis is perpendicular to our line of sight ($\theta = 90$) we obtain

$$\frac{a}{b} = 10^{0.4\Delta m_R} \tag{4.4}$$

Table 4.10. Shape Models and Densities for KBOs with Lightcurves

Name	H	D[a]	Albedo		Jacobi		Binary	
	(mag)	(km)	$a:b$	ρ	$a:b:c$	ρ	$a_1:a_2$	ρ
Varuna[b]	3.7	900	1 : 1	≥ 1090	$\geq 1.5:1:0.7$	≥ 1050	$\geq 1.4:1$	≥ 996
2000 GN_{171}	5.8	400	1 : 1	≥ 157	$\geq 1.75:1:0.74$	≥ 635	$\geq 1.15:1$	≥ 585
1998 BU_{48}	7.2	240	1 : 1	≥ 109	$\geq 1.87:1:0.75$	≥ 456	$\geq 1.07:1$	≥ 435
1999 KR_{16}	5.8	400	1 : 1	≥ 77	$\geq 1.18:1:0.63$	≥ 280	$\geq 2.35:1$	≥ 210

[a]Diameter computed assuming that the albedo is 0.04.

[b]See Jewitt and Sheppard 2002.

Using $\Delta m_R = 0.61$ magnitudes we obtain from Equation 4.4 $a/b = 1.75 : 1$ for 2000 GN_{171}. This is a lower limit to the intrinsic axis ratio because of the effects of projection into the plane of the sky. If 2000 GN_{171} is a Jacobi triaxial ellipsoid with $P = 8.329$ hours then its $a : b : c$ axis ratio would be $1.75 : 1 : 0.735$ and the lower limit on the density would be $\rho = 635$ kg m^{-3} (Chandrasekhar 1987; see Jewitt & Sheppard 2002 for a KBO context discussion of Jacobi ellipsoids). Finally if 2000 GN_{171} were a contact binary the ratio of the two radii, $a_1 : a_2$, would be $1.15 : 1$ with a lower limit to the density of $\rho = 585$ kg m^{-3} (see Jewitt & Sheppard 2002 for a discussion of contact binaries in the KBO context). Finally, though it is unlikely, if 2000 GN_{171} is spherical and the lightcurve is due to a $1.75 : 1$ contrast in albedo then the lower limit to the density of the KBO would be $\rho = 157$ kg m^{-3} from Equation 4.2 and using $P = 8.329$ hours.

4.6 Discussion

In Table 4.9 we show objects in the Solar System which have one axis of at least 200 km and which show large amplitude lightcurves. Interestingly there is a group of asteroids that are large (D = 200 to 300 km) and which have substantial lightcurve amplitudes. They also possess fast rotations. These objects are probably rotationally deformed "rubble piles" which may be similar to a Jocabi ellipsoid type object (Farinella et al. 1981). Such rubble

pile structures may form in the main asteroid belt because all objects have been effected by the high-velocity ($\sim$ 5 km/s) collisions that occur there (Farinella et al. (1982)). The effect of collisions is highly dependent on the object size. Objects with $D > 300$ km are large enough not to be completely turned into rubble piles or have their momentum greatly altered. Objects with diameters 200 to 300 km are large enough to be gravitationally bound but impacts over the age of the Solar System will transform them into rubble piles and may significantly change their angular momentum. Most asteroids with $D < 200$ km are thought to be fragments from catastrophic collisions and are not massive enough to be gravitationally spherical.

How does the collisional outcome scale with velocity and density differences in the asteroid belt versus the Kuiper Belt? We assume the target body has catastrophic break up when the projectile kinetic energy equals the gravitational binding energy of the target

$$\frac{1}{2}M_p\Delta v^2 = \frac{3GM_t^2}{5r_t} \tag{4.5}$$

where Δv is the mean collisional speed, M is mass, r is radius, and subscripts p and t refer to projectile and target, respectively. For collisions with a target of given radius, the ratio of the sizes of the projectiles needed to cause disruption in the main-belt and in the Kuiper Belt is

$$\frac{r_{p,KB}}{r_{p,MB}} = \left[\left(\frac{\rho_{t,MB}}{\rho_{t,KB}}\right)\left(\frac{\Delta v_{KB}}{\Delta v_{MB}}\right)^2\right]^{-1/3} \tag{4.6}$$

where we have assumed all Kuiper Belt objects have density ρ_{KB}, all main belt asteroids have density ρ_{MB}. Here $r_{p,MB}$ and $r_{p,KB}$ are the radii of the projectile in the main belt and Kuiper Belt which are needed to fracture the target in their respective belts, $\rho_{t,MB}$ and $\rho_{t,KB}$ are the densities of the target body in the main belt and Kuiper Belt respectively, and Δv_{MB} and Δv_{KB} are the respective collision velocities. If we put in nominal values of $\rho_{t,MB} = 3000$ kg m^3, $v_{MB} = 5$ km s^{-1} and $\rho_{t,KB} = 1000$ kg m^3, $v_{KB} = 1.5$ km s^{-1} for the

main belt asteroids and Kuiper Belt respectively we find

$$r_{p,KB} \approx 1.5 r_{p,MB}. \tag{4.7}$$

Thus for targets of equal size, a projectile has to be about 50% larger in the Kuiper Belt than in the main belt to be able to cause catastrophic break up of the target body. This difference is not large and since the current collisional timescales for the asteroids and Kuiper Belt objects are similar (Davis & Farinella 1997; Durda & Stern (2000)), other factors such as material strength and the number density of objects during early formation of each belt will be important in determining collisional differences.

The current Kuiper Belt has been found to be erosive for KBOs with $D < 100$ km while many of the larger objects are probably rubble piles (Davis & Farinella 1997). Laboratory and computer simulations show that self-gravitating targets are more easily fractured than dispersed (Asphaug et al. 1998). Once formed, rubble pile structures can insulate the rest of the body from the energy of impact, further inhibiting disruption. Collision experiments by Ryan et al. (1999) also show that porous ices dissipate energy efficiently. The outcome of impact into a rubble pile depends heavily on the angle of impact. We note that glancing low velocity collisions substantially alter the spin of the target body and can create elongated objects and contact binaries (Leinhardt et al. (2000)). These simulations all hint that rubble pile structures are able to remain gravitationally bound after an impact, but that their angular momentum may be altered in the process which could produce elongated shapes.

To date eight binary Kuiper Belt objects have been reported. It seems that there may be a large fraction of binary KBOs. It also appears that about 32% of KBOs are highly elongated. Both the binaries and the highly elongated shapes indicate large specific angular momentum, most likely delivered by glancing collisions. The current rate of collisions is too small however for any substantial modifications of the spins or shapes of KBOs (Jewitt and Sheppard 2002). Instead, we prefer the hypothesis that the binaries and elongated

shapes are products of an early, denser phase in the Kuiper Belt, perhaps associated with its formation.

4.6.1 Other Lightcurve Observations

We now consider lightcurve observations of KBOs published by others in order to make a larger sample. Unfortunately, few KBOs to date have been shown through independent observations to have repeatable lightcurves. Hainaut et al. (2000) reported that (19308) 1996 TO_{66} has a lightcurve which varies in amplitude over the course of one year and interpreted this as a result of possible on-going cometary activity. Object 1996 TO_{66} may show a color difference throughout its rotation (Sekiguchi et al. (2002)). In contrast, 1996 TO_{66} was reported to have a flat lightcurve by Romanishin & Tegler (1999) during the same year in which Hainaut et al. (2000) detected variation. Our own observations show that 1996 TO_{66} does have a significant lightcurve, basically confirming the variation originally observed by Hainaut et al. (2000) and contradicting the null detection by Romanishin & Tegler (Sheppard 2002). Conversely, an object reported to have a lightcurve by Romanishin & Tegler (1999), (15820) 1994 TB, was found by us to display no significant variation (Sheppard 2004). Because of these conflicts of unrepeatability, and since many of the Romanishin & Tegler targets were very sparsely sampled with raw data that remains unpublished, we use their work with caution in the following analysis.

Our combined sample of 22 KBOs comprises only well observed objects with numerous observations that could constrain any significant photometric variation from this (Table 4.4) and other (Table 4.11) works. Among the objects newly observed in this survey (Table 4.4), the fraction with significant lightcurve variation is $f(\Delta m_R \geq 0.15) = \frac{4}{13}$ (31%) and $f(\Delta m_R \geq 0.40) = \frac{3}{13}$ (23%). Including the objects reliably observed by others (Table 4.11) yields $f(\Delta m_R \geq 0.15) = \frac{7}{22}$ (32%) and $f(\Delta m_R \geq 0.40) = \frac{5}{22}$ (23%). Although we have evidence that some of their lightcurves are unrepeatable, we note that Romanishin & Tegler (1999) found a comparable $f(\Delta m_R \geq 0.10) = \frac{3}{11}$ (27%). We consider that these results all point to a similar fraction $f(\Delta m_R \geq 0.15) \sim 32\%$ and $f(\Delta m_R \geq 0.40) \sim 23\%$.

Table 4.11. Other KBOs with Reported Lightcurve Observations

Name	Class[a]	H (mag)	Δ mag (mag)	P (hr)	i (°)	e	a (AU)	Ref[b]
(28978) Ixion 2001 KX_{76}	R	3.2	–	–	19.7	0.246	39.3	SS,OR
(19308) 1996 TO_{66}	C	4.5	0.25	7.9	27.4	0.115	43.4	SS,OH
(24835) 1995 SM_{55}	C	4.8	–	–	27.0	0.110	42.1	SS
(15874) 1996 TL_{66}	S	5.4	–	–	23.9	0.587	84.9	RT,LJ
(26308) 1998 SM_{165}	C	5.8	0.45	7.1	13.5	0.371	47.8	SS,R
(15875) 1996 TP_{66}	R	6.8	–	–	5.7	0.336	39.7	RT,CB
(15789) 1993 SC	R	6.9	–	–	5.2	0.185	39.6	RT,D
(15820) 1994 TB	R	7.1	–	–	12.1	0.321	39.7	SS
(32929) 1995 QY_9	R	7.5	0.60	7.3	4.8	0.266	39.8	SS,RT

[a]S is a Scattered type object, C is a Classical type object, and R is a Resonance type object.

[b]References where SS is Sheppard 2002; OH is Hainaut et al. 2000; RT is Romanishin & Tegler 1999; OR is Ortiz et al. 2001; R is Romanishin et al. 2001.; CB is Collander-Brown et al. 1999; LJ is Luu and Jewitt 1998; D is Davies et al. 1997

The samples of objects with significant lightcurves and flat lightcurves were tested for correlations with orbital parameters and colors. No significant correlations were found. From the sample of 22 objects, 2 of the 9 (22%) resonant objects, 4 of the 8 (50%) classical objects, and 1 of the 5 (20%) scattered objects had measurable lightcurves ($\Delta m_R \geq 0.15$). Many of the objects shown in Table 4.11 are detailed elsewhere by us (Sheppard and Jewitt 2003) because they were objects particularly targeted by us to confirm their reported lightcurves and determine amplitudes and periods if a lightcurve was seen. The 13 objects reported in this paper (Table 4.4) were selected because of their size and brightness and not because of previous reports of their variability.

In comparison to the percentages of KBOs with large amplitude lightcurves (> 0.40 or about 1.5 difference in brightness), the four main belt asteroids with $D > 400$ km have $f(\Delta m_R \geq 0.40) = \frac{0}{4}$ (0%), the largest being only about 0.15 magnitudes (Lagerkvist et al. (1989); Tedesco (1989)). For main-belt asteroids with $D > 200$ km $f(\Delta m_R \geq 0.40) = \frac{5}{27}$ (19%) when their poles orientations are $\theta = 90$ degrees to our line of site. With the average

pole orientation of $\theta = 60$ degrees only (11%) ($f(\Delta m_R \geq 0.40) = \frac{3}{27}$) have large amplitude lightcurves. These large amplitude lightcurve objects are thought to be the Jacobi ellipsoid type objects. Asteroids with $D < 200$ km have $f(\Delta m_R \geq 0.40) = \frac{111}{482}$ (23%) while the Centaurs (Chiron, Asbolus, Pholus, Chariklo, Hylonome, (31824) 1999 UG5, and (32532) 2001 PT13) have $f(\Delta m_R \geq 0.40) = \frac{0}{7}$ (0%). These objects are small and thus thought to be collisional fragments.

Figure 4.13 shows how the largest ($D > 200$ km) main belt asteroids compare with the Kuiper Belt objects. Many of the Kuiper Belt objects fall in the upper and upper left parts of this figure, where the Jacobi ellipsoids are encountered in the asteroid belt. There is a bias in the KBO sample since light variations of less than about 0.1 magnitudes are very hard to detect, as are long single-peak periods > 24 hours.

The Student's t-test was used to measure the significance of the differences between the means of the asteroid and KBO periods and amplitudes. In order to reduce the effects of observational bias we used only periods less than 10 hours and amplitudes greater than 0.2 magnitudes from Figure 4.13. We found that the period distributions of the asteroids are significantly shorter than for the KBOs. The mean periods are 5.56 ± 0.89 and 7.80 ± 1.20 hours for the asteroids and KBOs respectively, giving a t-statistic of -3.84 (12 degrees of freedom) which is significant at the 99.7% confidence level. This difference is formally significant at the 3σ level by the Student's t-test, but it would be highly desirable to obtain more data from another large unbiassed survey in order to be sure of the effect. The KBOs have a larger mean amplitude, but the significance between the difference of means, 0.36 ± 0.11 vs. 0.50 ± 0.16 magnitudes for the asteroids and KBOs respectively, is only 95% (2σ) with a t-statistic of -1.83. This may be because the KBOs are less dense and more elongated, on average, than asteroids. Below we discuss in more detail the shape distribution of the Kuiper Belt.

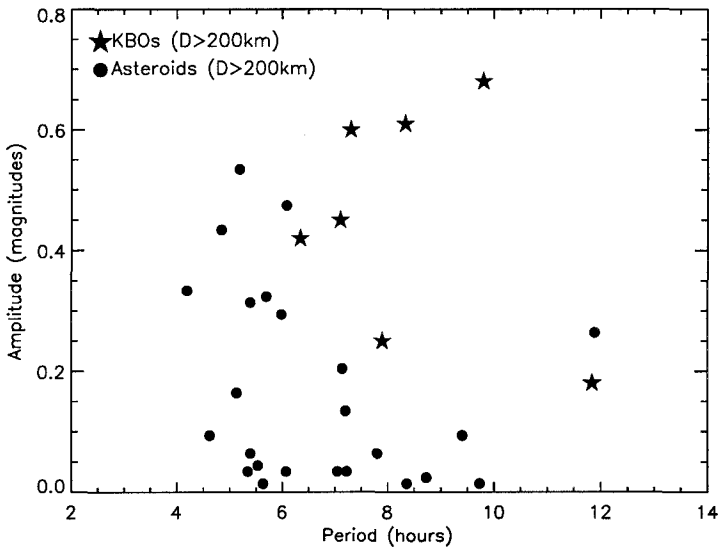

Figure 4.13 Rotational variability and periods of all the asteroids with diameters > 200 km and of Kuiper Belt objects in our sample. Objects in the upper and upper left portions of the graph are possibly rotationally deformed rubble piles. The asteroid amplitudes which were taken from pole orientations of 90 degrees have been corrected to a mean pole orientation at 60 degrees to better compare them with the KBOs of unknown orientation. KBOs with amplitudes $\leq$ 0.1 magnitudes and periods $\geq$ 12 hours are subject to observational bias against detection.

4.6.2 Shape Distribution Models

What constraints can be placed on the intrinsic distribution of KBO shapes from the apparent (sky-plane projected) distribution? We used a Monte-Carlo model to project several assumed intrinsic distributions into the plane of the sky and then compared them with the observations. This was done by using a pole orientation distribution proportional to $\sin\theta$. The apparent axis ratio for each object was then calculated from this pole orientation distribution and the intrinsic axis ratio selected from one of several assumed distributions.

Firstly, as an extreme case, we ask whether the data are consistent with selection from intrinsic distributions in which all the objects have a single axis ratio $x = b/a$, with $x = 0.80, 0.66, 0.57$ or 0.50 (Figure 4.14). The Figure shows that the form of the resulting amplitude distribution differs dramatically from what is observed. We conclude that the distribution KBO lightcurve amplitudes cannot be modeled as the result of projection on any single axis ratio. A range of shapes must be present. While not surprising, this result does serve to demonstrate that the KBO lightcurve sample is of sufficient size to be diagnostic.

Secondly, we explored the effect of the width of the distribution using

$$\Psi(x)dx = exp\left[\frac{-(x-x_0)^2}{2\sigma^2}\right]dx \tag{4.8}$$

where $\Psi(x)dx$ is the number of KBOs with axis ratios in the range x to $x + dx$, σ is the standard deviation or width parameter and x_0 is the mean axis ratio. Examples for $x_0 = 0.66$ and $\sigma = 0$, 0.35, 0.75, and 1.0 are plotted in Figure 4.15. We assumed that all objects had axis ratios $0.5 \leq x \leq 1.0$. The Figure shows that the data require an intrinsically broad distribution of body shapes, specifically with a dispersion comparable to the mean axis ratio.

Thirdly, we assumed that the axis ratios of the KBOs followed a differential power-law distribution of the form

$$\Psi(x)dx = x^{-q}dx \tag{4.9}$$

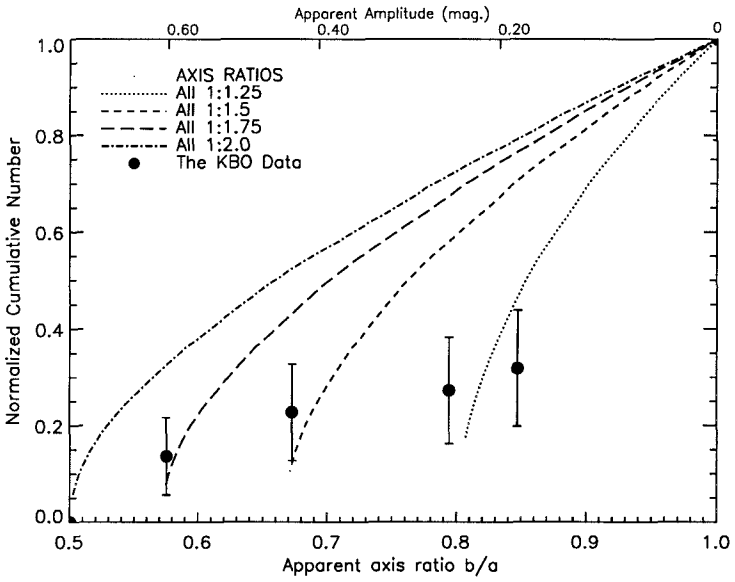

Figure 4.14 Monte Carlo simulations using a constant axis ratio for all KBOs. Error bars for the KBO points are based on a Poisson distribution.

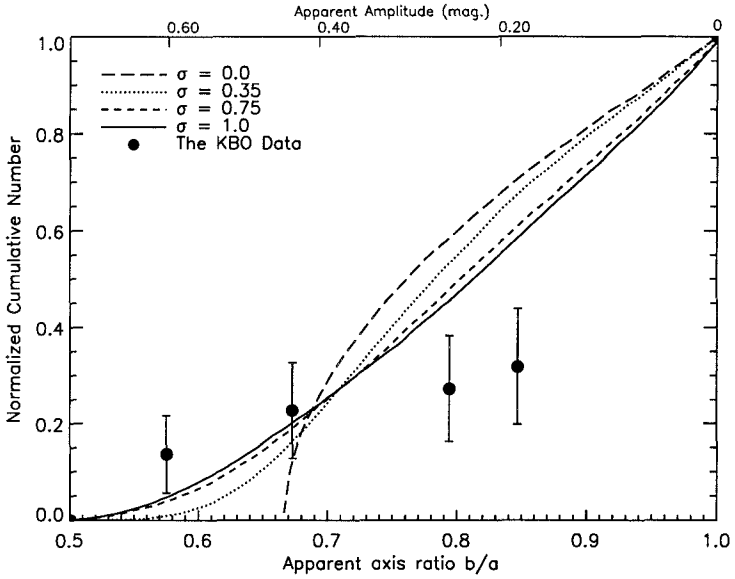

Figure 4.15 Monte Carlo simulations using Gaussians centered on the axis ratio of 1:1.5 with different standard deviations (Equation 4.8). Error bars for the KBO points are based on a Poisson distribution.

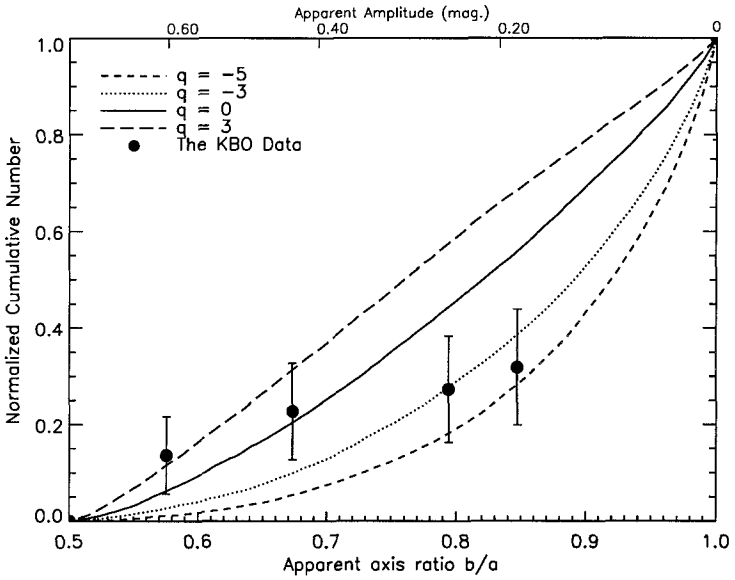

Figure 4.16 Monte Carlo simulations using power laws of different slopes (Equation 4.9). Error bars for the KBO points are based on a Poisson distribution.

where q is a constant, and $\Psi(x)dx$ is again the number of KBOs with axis ratios in the range x to $x + dx$. We assumed $0.5 \leq x \leq 1.0$. A positive q favors objects with small axis ratios while negative q favors objects that are near spherical. The results can be seen in Figure 4.16. The $q = -5$ distribution is very similar to an exponential distribution with its peak at an axis ratio of $x = 1$. Again we see that the models fit the data better with a broader distribution of axis ratios.

Fourthly, we ask whether the data are consistent with selection from an intrinsic distribution of shapes caused by collisional fragmentation. The fragment shape distribution is taken from Catullo et al. (1984). Figure 4.17 shows that the KBO Δm distribution is inconsistent with the collisional fragment distribution in the sense that more highly elongated KBOs are found than would be expected from the impact fragments. This finding is consistent with collisional models (Farinella and Davis 1996, Kenyon and Luu 1999) in

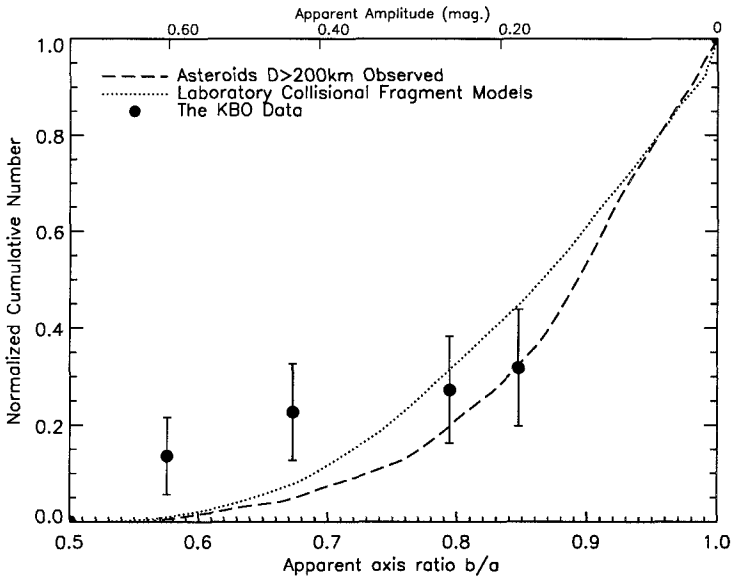

Figure 4.17 Monte Carlo simulations using all large asteroids ($D > 200$ km) and a collisional distribution from Catullo et al. (1984). Error bars for the KBO points are based on a Poisson distribution.

the sense that only KBOs smaller than a critical diameter $\sim$ 100 km are likely to be impact fragments, while the observed KBOs are all larger than this.

Finally, we ask whether the data are consistent with selection from an intrinsic distribution of shapes like that measured in the large (D > 200 km) main-belt asteroid population. We take this distribution from the published lightcurve data base of Lagerkvist, Harris, & Zappala (1989) which has been updated by A. Harris on the world wide web at http://cfa-www.harvard.edu/iau/lists/LightcurveDat.html. The results are shown in Figure 4.17, where we see that the KBOs contain a larger fraction of highly elongated objects than are found amongst the main-belt asteroids. A plausible explanation for such a large fraction of the highly elongated Kuiper Belt objects is that the objects are very large yet structurally weak and of low density. This would allow many of the Kuiper Belt objects

to be gravitationally bound rubble piles easily distorted by centripetal forces due to their rotation.

4.6.3 KBO Density Comparisons in the Solar System

The Kuiper Belt objects are thought to consist of water ice with some rocky material mixed in, similar to the comets. How do the densities of the outer satellites compare to what we have found for our sample of Kuiper Belt objects? In Figure 4.18 we plot all the outer icy bodies in the Solar System that have well known densities and are less than 3000 km in diameter. There is a clear trend, with larger objects being denser. The KBOs seem to follow this trend. We also note there appears to be an object size vs. lightcurve amplitude and size vs. period trend for the KBOs in our data. Objects that have densities less than that of water ice (1000 kg m^{-3}) must have significant internal porosity or be composed of ices less dense than water (see Jewitt and Sheppard 2002).

To date only about 10 main belt asteroids have reliably measured bulk densities. Most of these are from perturbation calculations between asteroids though two have been measured by passing spacecraft and a few others found from the orbital motions of known companions. Most asteroid densities are consistent with that of rock, $2000 \leq \rho \leq 3000$ kg m^{-3}. Some of the asteroids densities have been found to be lower than expected and attributed to internal porosity possibly from rubble pile structure (Yeomans et al. 1997).

In Table 4.9 we present new densities for five main belt asteroids calculated under the assumption that they are equilibrium rotational (Jacobi ellipsoid) figures. We used their lightcurves as seen at maximum amplitude, to eliminate the effects of projection. The densities are higher than those of the Kuiper Belt objects obtained using the same method (Figure 4.19) but lower than expected for solid rock objects. This provides another hint that these objects may be internally porous. The densities of 15 Eunomia (790 ± 210 kg m^{-3}) and 16 Psyche (1800 ± 600 kg m^{-3}) were reported separately from measurements of gravitational perturbations (Hilton (1997); Viateau (2000)). The higher density for 16 Psyche is particularly interesting because this object is an M-type asteroid and thus

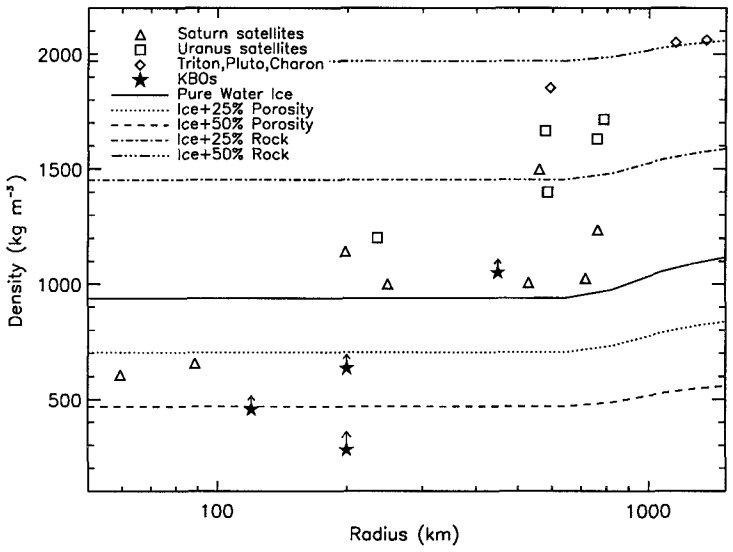

Figure 4.18 Sizes and densities of icy bodies. A trend is observed in which the larger the object the higher the density. The solid line is over plotted to show the expected bulk density of a pure water ice sphere with size (Lupo and Lewis 1979). Other lines indicate how the density would behave with added porosity and rock. Data points for satellite densities are from the JPL Solar System Dynamics web page.

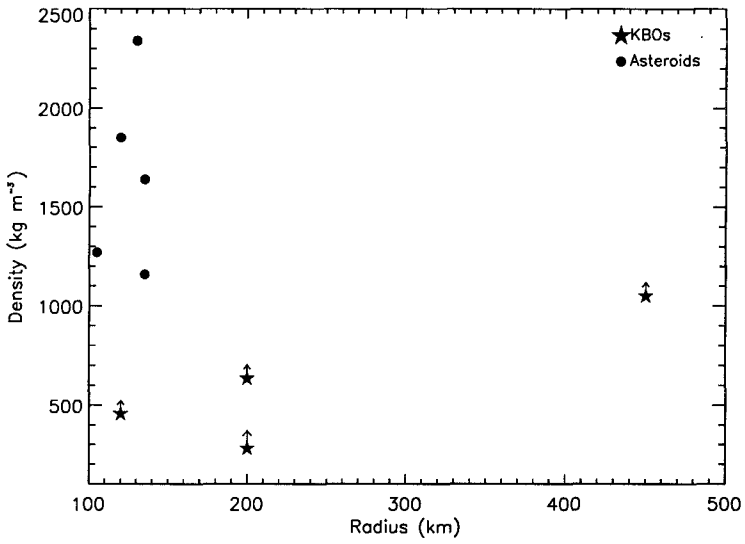

Figure 4.19 Size and densities of possible rotationally deformed KBOs and main belt asteroids. The asteroids have lower densities than expected for solid rock, but are still denser than the KBOs.

expected to have a high density. The main belt asteroid 45 Eugenia was found to have a companion which was used by Merline et al. (1999) to find a density of 1200^{+600}_{-200} kg m^{-3}. Asteroid densities found by others are probably underestimated since they assumed that the objects were spheres. A sphere has the highest volume to projected area ratio and thus any deviation from a sphere will cause the object to appear to have a lower density. We calculated the density for these objects using the assumption they are Jacobi ellipsoids and thus the parameters used are the well known period and amplitude from the lightcurves. Interestingly the five best examples of main belt rotationally deformed asteroids (Table 4.9) are found in all the main classes, 2 C-type, 1 each of S, P, and M-types.

4.7 Phase Functions of KBOs

At large phase angles, the phase function in Equation 4.1 may be approximated as

$$\phi(\alpha) = 10^{-\beta\alpha} \tag{4.10}$$

where α is the phase angle in degrees, and β is the "linear" phase coefficient. Empirically, the magnitude of β is inversely correlated with the surface albedo (Gehrels et al. (1970); Bowell et al. (1989); Belskaya & Shevchenko (2000)), suggesting that we might be able to indirectly assess the albedos of KBOs from their phase functions. Unfortunately, this is not possible. The maximum phase angle attained by an object at distance R [AU] is roughly α_{max} [degrees] $= \frac{180}{\pi R}$. At $R = 30$ AU, for instance, $\alpha_{max} = 1.9$ degrees. This is exactly the phase angle range in which the opposition surge is potentially important (Scaltriti and Zappala 1980; Belskaya and Shevchenko 2000). The opposition surge is a complex, multiple scattering phenomenon which occurs in the grains of a porous regolith. The magnitude of the opposition surge, which causes an increase in scattered intensity over and above that predicted by Equation 4.10 at small α, is determined by coherent-backscattering and is a complex function of regolith physical and optical properties. It is not simply related to the albedo and Equation 4.10 must be modified to take account of this surge. Nevertheless, the phase functions provide a new basis for comparison of the KBOs, and should be measured if we are to accurately assess the sizes of KBOs from their optical data.

Seven of the KBOs were observed over a range of phase angles sufficient for us to measure the phase darkening. We plot the quantity $m_R(1,1,\alpha) = m_R - 5\log(R\Delta)$ against α for these 7 KBOs in Figures 4.20 and Figure 4.21. When observations from consecutive nights were available we averaged the phase angle and apparent magnitude over those nights to create a single point with small uncertainty. If an object showed a lightcurve, its time-averaged mean apparent magnitude was used. The linear least squares fits to the KBO data are listed in Table 4.12 and shown in Figure 4.20. Within the uncertainties, we find that photometry of the 7 KBOs is compatible with $\beta(\alpha < 2^\circ) = 0.15 \pm 0.01$ mag deg^{-1}. In contrast the phase

Table 4.12. Phase Function Data for KBOs

Name	H	G	$\beta(\alpha < 2°)$[a]
2000 EB_{173}	4.44 ± 0.02	-0.15 ± 0.05	0.14 ± 0.02
Varuna	3.21 ± 0.05	-0.58 ± 0.10	0.19 ± 0.06
1999 DE_9	4.53 ± 0.03	-0.44 ± 0.07	0.18 ± 0.06
1996 GQ_{21}	4.47 ± 0.02	-0.04 ± 0.05	0.14 ± 0.03
2000 GN_{171}	5.98 ± 0.02	-0.12 ± 0.05	0.14 ± 0.03
1999 KR_{16}	5.37 ± 0.02	-0.08 ± 0.05	0.14 ± 0.02
2001 CZ_{31}	5.53 ± 0.03	-0.05 ± 0.07	0.13 ± 0.04
MEAN	-	-0.21 ± 0.04	0.15 ± 0.01
Pluto[b]	-1.00 ± 0.01	0.88 ± 0.02	0.0372 ± 0.0016

[a] $\beta(\alpha < 2°)$ is the phase coefficient at phase angles $< 2°$.

[b] Data for Pluto from Tholen and Tedesco (1994) while the G value was calculated by us.

function for Pluto was found to be linear throughout the 0 to 2 degrees phase angle range with $\beta(\alpha < 2°) = 0.0372 \pm 0.0016$ mag deg^{-1}, indicating a very shallow if any opposition surge and consistent with a high albedo surface (Tholen & Tedesco (1994)).

Since the small phase angle observations are affected by the "opposition surge", caused by multiple scattering within the porous regolith, we also fit the data using the Bowell et al. (1989) $H - G$ scattering parametrization. This technique gives a curved relation at small phase angles that becomes asymptotically like the linear β relation at large phase angles and thus attempts to account for the opposition surge. In the Bowell et al. formalism H is the absolute magnitude of the object, analogous to $m_R(1, 1, 0)$. The parameter G provides a measure of the slope of the phase function at large angles, analogous to β. It is scaled so that $G = 0$ corresponds to the darkest surfaces found on the asteroids while $G = 1$ corresponds to the brightest (Bowell et al. 1989). The results of the $H - G$ fits are presented in Table 4.12 and Figures 4.21 and 4.22. The KBOs show steep slopes with

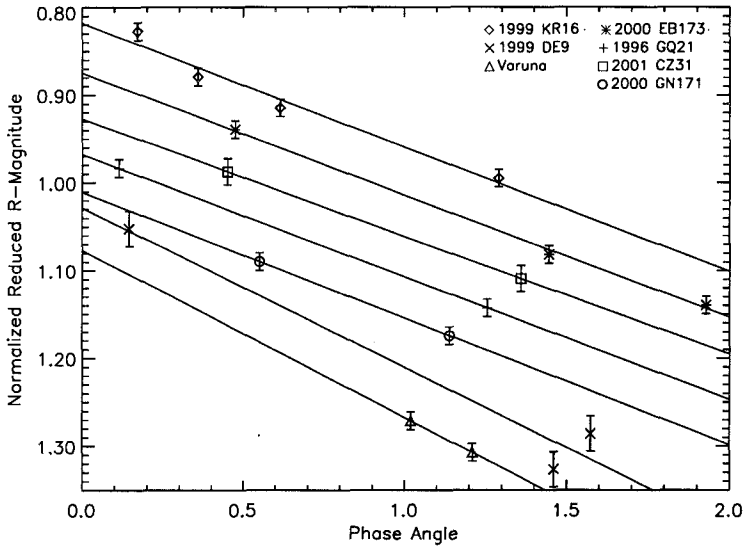

Figure 4.20 Phase functions for Kuiper Belt objects observed at several phase angles. The best linear fit gives a phase coefficient of $\beta(\alpha < 2°) = 0.15$ magnitudes per degree. Objects with more than two data points show evidence of the nonlinear opposition surge.

a possible moderate opposition surge. The best-fit values of the G parameter are very low with an average of -0.21. This small G value more closely resembles that of dark, C-type asteroids ($G \sim 0.15$) than the brighter, S-types ($G \sim 0.25$) in the main-belt. This is consistent with, though does not prove, the assumption that the majority of KBOs are of very low albedo. The similarity of the slopes of the phase functions of all KBOs in our sample suggests comparative uniformity of the surface compositions, physical states, and albedos. As a comparison, Pluto was found to have a best fit $G = 0.88 \pm 0.02$ using data from Tholen & Tedesco (1994). The dramatic difference between the backscattering phase functions of Pluto and the smaller KBOs studied here is shown in Figure 4.22. This difference is again consistent with the smaller KBOs having low albedo (0.04?) surfaces qualitatively different from the high albedo (0.6), ice-covered surface of Pluto.

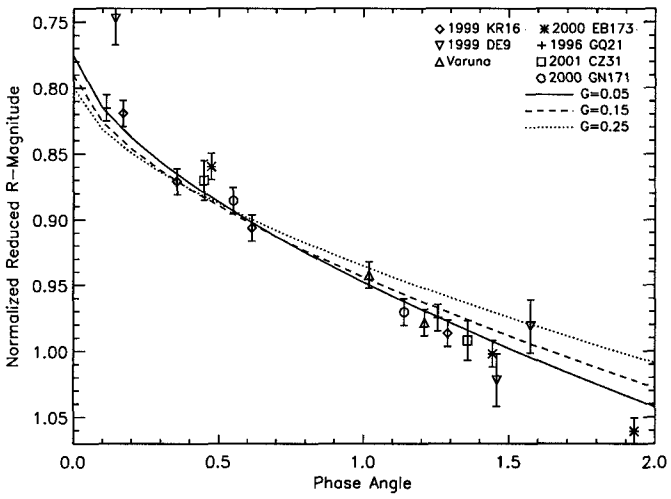

Figure 4.21 Phase functions of all 7 KBOs observed at multiple phase angles. The reduced magnitudes have been normalized to show all objects relative slopes. Over plotted are fits of the slope parameter $G = 0.05$, 0.15 (C-type), and 0.25 (S-type). The best fit slope parameters of all KBOs are below $G = 0.05$ which is consistent with scattering from low albedo surfaces.

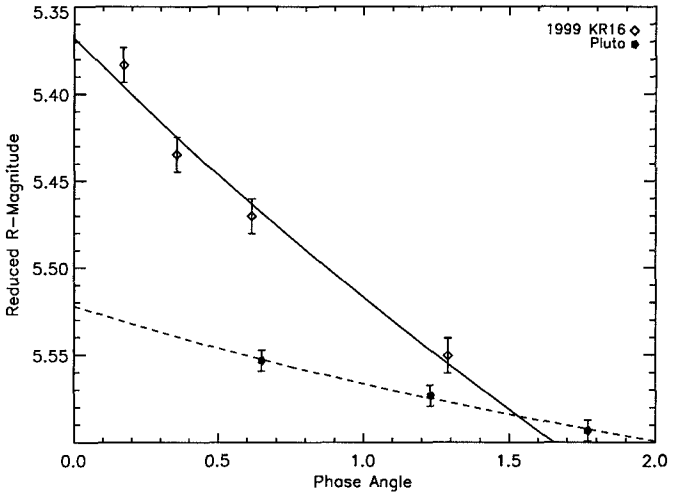

Figure 4.22 Comparison of phase functions for the typical KBO 1999 KR_{16} and Pluto. The Solid line is the best fit Bowell et al. HG phase function for 1999 KR16 with $G = -0.08$. Data points for Pluto are from Tholen & Tedesco (1994) and are offset in the vertical direction from -1.0. Pluto has a best fit $G = 0.88$ shown with the dashed line.

4.8 Summary

We have conducted a systematic program to assess the rotations and sky-plane shapes of Kuiper Belt Objects from their optical lightcurves.

1. Four of 13 (31%) bright Kuiper Belt objects in our sample ((33128) 1998 BU_{48}, 2000 GN_{171}, (20000) Varuna, and 1999 KR_{16}) show lightcurves with range $\Delta m \geq 0.15$ mag. In an enlarged sample combining objects from the present work with objects from the literature, 7 of 22 (32%) objects have $\Delta m \geq 0.15$ mag.

2. The fraction of KBOs with $\Delta m \geq 0.4$ mag (23%) exceeds the corresponding fraction in the main-belt asteroids (11%) by a factor of two. The KBO Δm distribution is inconsistent with the distribution of impact fragment shapes reported by Catullo et al. (1984).

3. The large Kuiper Belt Objects (33128) 1998 BU_{48}, 2000 GN_{171} and (20000) Varuna show large periodic variability with photometric ranges 0.68 ± 0.04, 0.61 ± 0.03 and 0.45 ± 0.03 magnitudes, respectively, and short double-peaked periods of 9.8 ± 0.1, 8.329 ± 0.005 and 6.3565 ± 0.0002 hours, respectively. Their BVRI colors are invariant with respect to rotational phase at the few percent level of accuracy.

4. If these objects are equilibrium rubble piles distorted by centripetal forces due to their own rotation, the implied densities must be comparable to or less than that of water. Such low densities may be naturally explained if the KBOs are internally porous.

5. In the phase angle range $0 \leq \alpha \leq 2$ deg the average slope of the phase function of 7 KBOs is $\beta(\alpha < 2^\circ) = 0.15 \pm 0.01$ mag deg^{-1} (equivalently, $G = -0.2$). The corresponding slope for ice-covered Pluto is $\beta(\alpha < 2^\circ) \approx 0.04$ mag/deg (equivalently, $G = 0.88$). The large difference is caused by pronounced opposition brightening of the KBOs, strongly suggesting that they possess porous, low albedo surfaces unlike that of ice-covered Pluto.

Acknowledgments

We thank John Dvorak, Paul deGrood, Ian Renaud-Kim, and Susan Parker for their operation of the UH telescope, Alan Harris for a quick and thoughtful review. This work was supported by a grant to D.J. from NASA.

Chapter 5

Hawaii Kuiper Belt Variability Project: An Update

5.1 Abstract

We have been systematically monitoring a large sample of bright Kuiper Belt objects for possible light variations due to rotational and phase angle effects. Here we report on three objects, 2003 AZ_{84}, (24835) 1995 SM_{55} and (55636) 2002 TX_{300} observed to have measurable rotational lightcurves with peak-to-peak amplitudes of 0.14 ± 0.03, 0.19 ± 0.05 and 0.08 ± 0.02 magnitudes and single-peaked periods of 6.71 ± 0.05, 4.04 ± 0.03 and 8.12 ± 0.08 hours respectively. We observed a further ten objects which showed no rotational photometric variation within measurement uncertainties. In addition, we find that the lightcurve of 1995 SM_{55} may have a variable amplitude. We discuss this peculiar object as well as our observations of the reportedly variable Kuiper Belt object (19308) 1996 TO_{66}. Finally, we continue to find the phase functions of the Kuiper Belt objects to be very steep and linear, to first order, with a median slope of 0.16 ± 0.01 magnitudes per degree in the phase angle range 0 to 2 degrees.

5.2 Introduction

The rotations and shapes of the KBOs are probably a function of their size. KBOs may be structurally weak bodies held together by gravity in a rubble pile type structure (Jewitt and Sheppard 2002). The spins of the larger objects are probably primordial with little modification by post-formation impacts. The smaller objects are probably collisional fragments with sizes, shapes and spins determined at the moment of catastrophic break-up (Farinella & Davis 1996). The vast majority of Kuiper Belt Objects (KBOs) currently can not be resolved at their large heliocentric distances ($\gtrsim$ 30 AU). Presently, the only feasible way to determine KBO shapes and surface features is by observing their light variations.

We are obtaining voluminous time resolved optical photometric observations to determine the rotational lightcurves and phase functions of KBOs. The University of Hawaii 2.2 meter telescope with its Tektronix 2048 $\times$ 2048 CCD was used for the observations (see section 2 of Sheppard and Jewitt (2002) for further observational and data reduction details). As our sample, we select the intrinsically brightest (presumably largest) KBOs. The 33 large KBOs ($\geq$ 200 km in diameter, assuming a low albedo) we have observed already exceed the number of asteroids of this size.

This short note is a continuation of Jewitt and Sheppard (2002) and Sheppard and Jewitt (2002) and a more detailed write-up will soon follow. The present work is intended as a timely pointer to a manuscript that is in preparation and our already published articles and is not a substitute for them.

5.3 Rotation Results

Rotational lightcurve analyses for the newly observed KBOs are shown in Table 5.1 and discussed below. We employed the phase dispersion minimization (PDM) method (Stellingwerf 1978) to search for periodicity in the data. The best-fit period should have a very small normalized dispersion, Θ, compared with the unphased data, and thus $\Theta \ll 1$ indicates that a good fit has been found.

Table 5.1. Properties of Newly Observed KBOs

Name		m_R[a] (mag)	Nights[b] (#)	Δm_R[c] (mag)	Single[d] (hrs)	Double[e] (hrs)
(55636)	2002 TX_{300}	19.29 ± 0.04	3	0.08 ± 0.02	8.12 ± 0.08	16.24 ± 0.08
					12.10 ± 0.08	24.20 ± 0.08
(55637)	2002 UX_{25}	19.65 ± 0.02	2	< 0.06	-	-
(55638)	2002 VE_{95}	19.68 ± 0.02	1	< 0.06	-	-
(47171)	1999 TC_{36}	19.80 ± 0.02	2	< 0.05	-	-
(42355)	2002 CR_{46}	19.82 ± 0.02	4	< 0.05	-	-
(28978) Ixion	2001 KX_{76}[f]	19.84 ± 0.02	3	< 0.05	-	-
	2003 AZ_{84}	20.14 ± 0.07	3	0.14 ± 0.03	6.72 ± 0.05	13.44 ± 0.05
(24835)	1995 SM_{55}[f]	20.20 ± 0.10	9	0.19 ± 0.05	4.04 ± 0.03	8.08 ± 0.03
	2000 YW_{134}	20.67 ± 0.05	2	< 0.1	?	?
(42301)	2001 UR_{163}	20.86 ± 0.03	3	< 0.08	-	-
(19308)	1996 TO_{66}[f]	21.12 ± 0.13	5	0.26 ± 0.03	3.96 ± 0.04	7.92 ± 0.04
	2001 FP_{185}	21.15 ± 0.03	4	< 0.06	-	-
	2001 QF_{298}	21.41 ± 0.06	4	< 0.12	?	?
	2001 KD_{77}	21.48 ± 0.03	3	< 0.07	-	-

[a]Mean R-band magnitude on the date having the majority of observations.

[b]Number of nights used to determine the lightcurve.

[c]The peak to peak range of the lightcurve.

[d]The lightcurve period if there is one maximum per period.

[e]The lightcurve period if there is two maxima per period.

[f]Initial details were given in our secondary sample in Sheppard and Jewitt (2002). Additional observations have been obtained and thus we give further details on the objects here.

When combining the newly observed objects with our previous data (Sheppard and Jewitt 2002) we find that 9 of 33 (27%) objects in our sample show peak-to-peak amplitudes ≥ 0.15 magnitudes while 15% have amplitudes ≥ 0.4 magnitudes and 9% have amplitudes ≥ 0.6 magnitudes. The large main-belt asteroids have a larger fraction of objects with amplitudes ≥ 0.15 magnitudes, a comparable fraction with amplitudes ≥ 0.4 magnitudes but a smaller fraction with amplitudes ≥ 0.6 magnitudes.

Please see Jewitt and Sheppard (2002) as well as Sheppard and Jewitt (2002) for further discussion on the interpretation of KBO lightcurves. The complete data from these new results will soon be published along with further observations in Sheppard and Jewitt (2003).

5.3.1 2003 AZ_{84}

PDM analysis shows that 2003 AZ_{84} has a single-peaked lightcurve period of $P = 6.72 \pm 0.05$ hours (Figure 5.1). One minimum and one maximum in brightness within a single night were observed and put the full single-peaked lightcurve just over 6 hours, in agreement with the PDM analysis. We phased the data and found the 6.72 hour period to be very good (Figure 5.2). The peak-to-peak variation is $\Delta m = 0.14 \pm 0.03$ magnitudes. We possess no evidence to show whether the lightcurve is singly periodic (as expected from surface albedo variations) or doubly periodic (consistent with aspherical shape).

5.3.2 (24835) 1995 SM_{55}

We observed (24835) 1995 SM_{55} for five nights in October 2001. The KBO was found to have very scattered photometry for its brightness (error bars on the photometry are only 0.03 magnitudes), and a good periodic lightcurve could not be identified. We thus reported this object as having a flat lightcurve in our secondary sample in Sheppard and Jewitt (2002). Further observations were obtained in November 2001 to determine if the scattered photometry was caused by noise. With the additional photometry we were able to find a rotational lightcurve with single-peaked period near $P = 4$ hours (Figure 5.3). Phasing the data together again showed that the single-peaked lightcurve was extremely noisy given

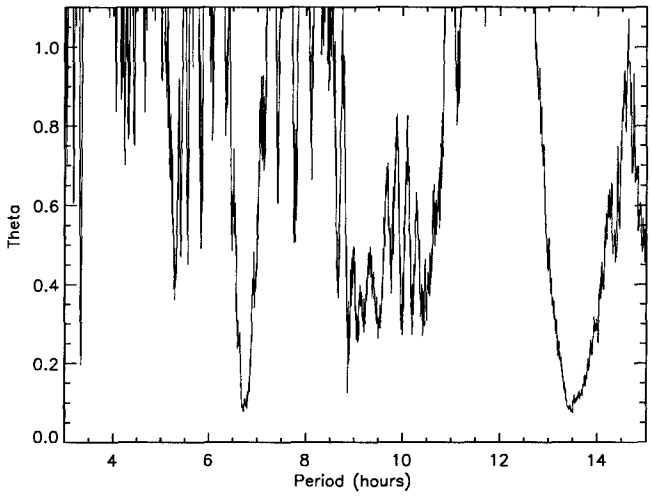

Figure 5.1 The phase dispersion minimization (PDM) plot for 2003 AZ_{84}. Best fits from this plot are the 6.72 hour single-peaked fit and the 13.44 hour double-peaked fit.

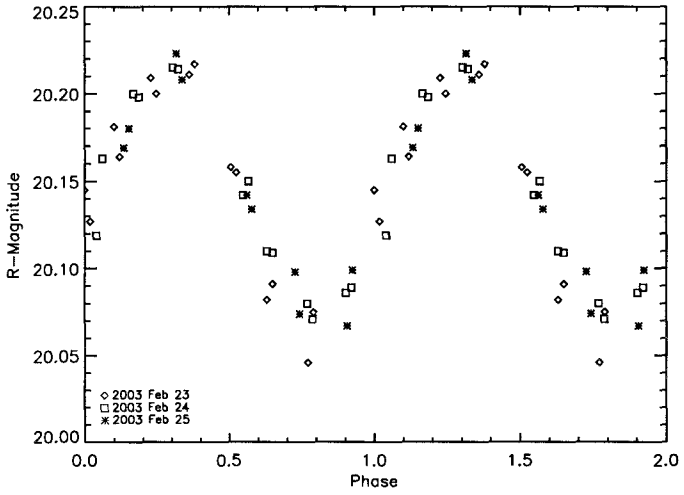

Figure 5.2 Phased R-band data from the UT February 2003 observations for 2003 AZ_{84}. The period has been phased to the single-peaked period of 6.72 hours. Uncertainties for individual points are ± 0.03.

our uncertainties (Figure 5.4). Phasing the data to a possible double-peaked lightcurve of 8 hours is also very noisy (Figure 5.5). An average peak-to-peak lightcurve amplitude is 0.19 ± 0.05. It appears that the amplitude of the rotational lightcurve may be variable from night to night.

Trujillo and Brown (private communication, 2003) observed 1995 SM_{55} with the Hubble Space Telescope and found no evidence that it is a binary object. However, their constraint applies only to satellites with separation ≥ 0.1 arcseconds and having a magnitude difference ≤ 2.5. Therefore it remains possible that the "noisy" lightcurve of 1995 SM_{55} is due to the presence of multiple periods in the photometric data. Only protracted, highly accurate photometric series can show whether or not this is the case. It is interesting that 1995 SM_{55} is one of the bluest KBOs known (V-R= 0.38; see Hainaut & Delsanti (2002)). It may be that blue objects have recently had their volatile rich insides exposed, possibly by a recent collision. Thus the amplitude variation seen for 1995 SM_{55} may be affected by cometary activity from this freshly exposed material. The large scatter in photometry could also be due to the object being in a complex rotational state, although it is difficult to see how such a state could be maintained other than by forced precession due to a satellite or a very unlikely recent collision since the damping time for wobbles is short (Burns & Safronov 1973). Further observations of 1995 SM_{55} are needed to understand its peculiar lightcurve nature.

5.3.3 (19308) 1996 TO_{66}

A similar situation has been invoked for the very blue object (19308) 1996 TO_{66} in which the lightcurve was reported to show signs of variability (Hainaut et al. 2000; Sekiguchi et al. 2002). We observed 1996 TO_{66} in November 2001 and PDM analysis of our data shows there are possible rotational single-peaked lightcurves at about 3.96 ± 0.04 and 4.80 ± 0.05 hours and double-peaked periods around 5.90 ± 0.05, 7.92 ± 0.04 and 9.6 ± 0.1 hours (Figure 5.6). When phasing the data to these values, all seem plausible, but the single-peaked period near 3.96 hours and the corresponding double-peaked period near 7.92 hours are significantly

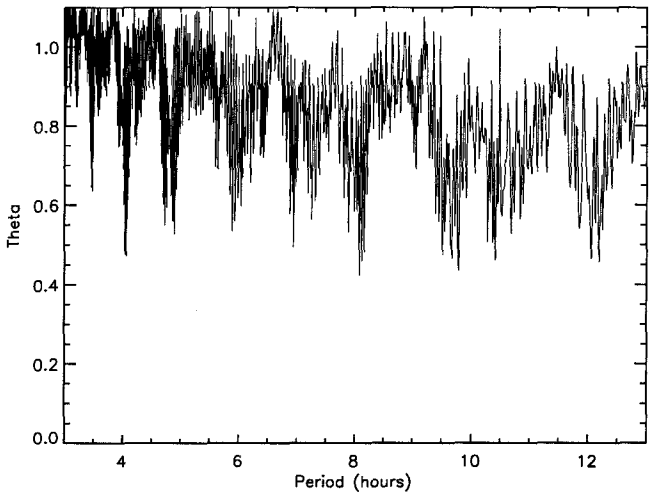

Figure 5.3 The PDM plot for 1995 SM_{55}. Best fits from this plot are the 4.04 hour single-peaked fit and the 8.08 hour double-peaked fit. Both are flanked by aliases.

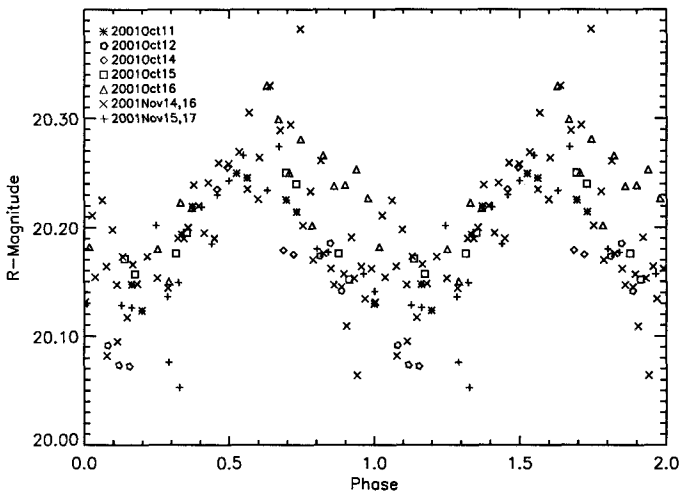

Figure 5.4 Single-peaked 4.04 hour phased R-band data from the UT October and November 2001 observations for 1995 SM_{55}. Uncertainties for individual points are ± 0.03.

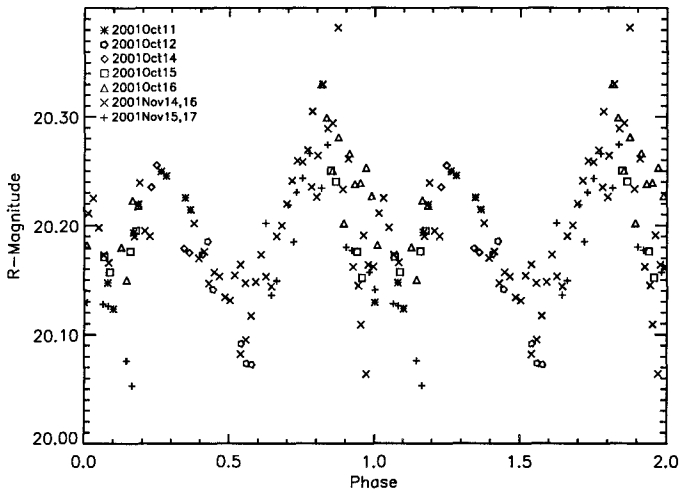

Figure 5.5 Double-peaked 8.08 hour phased R-band data from the UT October and November 2001 observations for 1995 SM_{55}. Uncertainties for individual points are ± 0.03.

better (Figures 5.7 and 5.8). We find the peak-to-peak amplitude of 1996 TO_{66} to be 0.26 ± 0.03 magnitudes in our 2001 observations.

Hainaut et al. (2000) reported a 6.25 hour period for 1996 TO_{66} in data taken in 1997 (0.12 magnitudes in amplitude) and 1998 (0.33 magnitudes) and later affirmed this period in photometry from 1999 (0.21 magnitudes; Sekiguchi et al. 2002). They suggest that changes in the lightcurve period from double-peaked to single-peaked as well as in the amplitude between 1997 and 1998 can be attributed to activity, possibly outgassing, in 1996 TO_{66}. Phasing our 2001 data to 6.25 hours gives an implausible lightcurve. We found that the very sparsely sampled Sekiguchi et al. (2002) data from 1999 observations of 1996 TO_{66} are consistent with many periods, including the periods found in our 2001 data. O. Hainaut kindly provided us with the photometric measurements for the 1997 and 1998 observations of 1996 TO_{66} described in Hainaut et al. (2000); the data currently can also be found on the Small Bodies Node of the Planetary Data System at http://www.psi.edu/pds/tnolc.html. In examining these data we could not find a significant lightcurve in the 1997 data (≤ 0.1

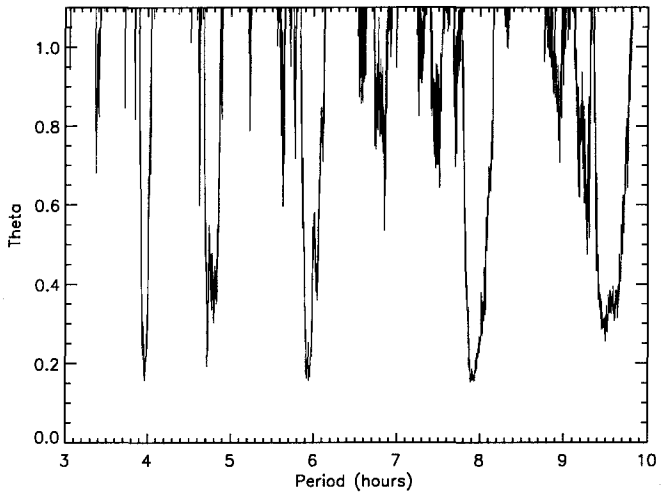

Figure 5.6 The PDM plot for 1996 TO_{66}. Best fits from this plot are the 3.96 hour single-peaked fit and the 7.92 hour double-peaked fit.

magnitudes in amplitude). In our PDM analysis of the Hainaut el al. data from 1998 we found similar periods for 1996 TO_{66} as our 2001 observations (Figure 5.9). We do not find strong evidence for the 6.25 hour period in the Hainaut et al. data from 1998.

We do not see any evidence that the period of 1996 TO_{66} has changed between the 1997, 1998, 1999 and 2001 observations. Romanishin and Tegler (1999) found the lightcurve for 1996 TO_{66} in 1997 to be ≤ 0.1 magnitudes, seemingly corroborating the small amplitude reported by Hainaut et al. Thus, while there is no evidence for a change in rotation period, the lightcurve amplitude of 1996 TO_{66} may have changed since 1997.

5.3.4 (55636) 2002 TX_{300}

PDM analysis shows that (55636) 2002 TX_{300} has a single-peaked lightcurve period of either $P = 8.12 \pm 0.08$ or $P = 12.10 \pm 0.08$ hours (Figure 5.10). Both single-peaked periods appear acceptable in the phased data (Figure 5.11) with a peak-to-peak variation of $\Delta m = 0.08 \pm 0.02$ magnitudes.

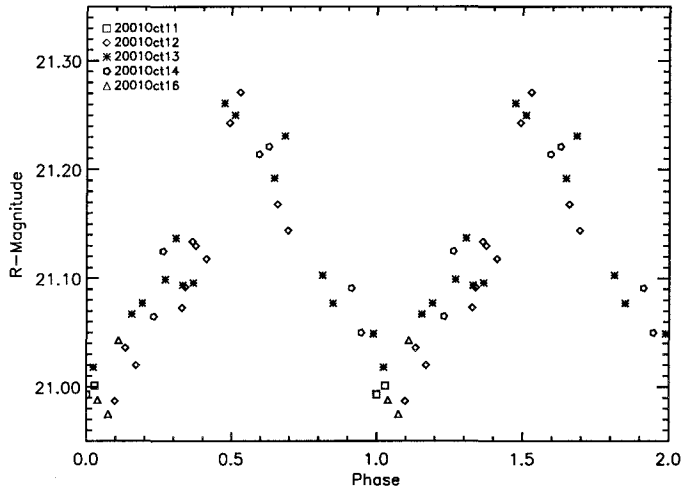

Figure 5.7 Single-peaked 3.96 hour phased R-band data from the UT October 2001 observations for 1996 TO_{66}. Uncertainties for individual points are ± 0.03.

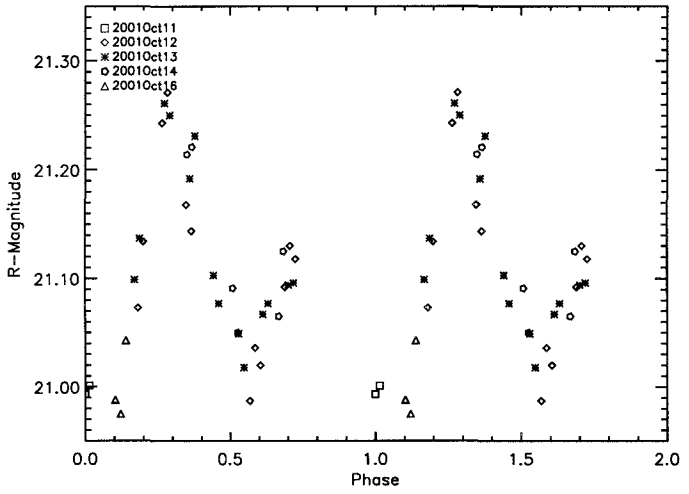

Figure 5.8 Double-peaked 7.92 hour phased R-band data from the UT October 2001 observations for 1996 TO_{66}. Uncertainties for individual points are ± 0.03.

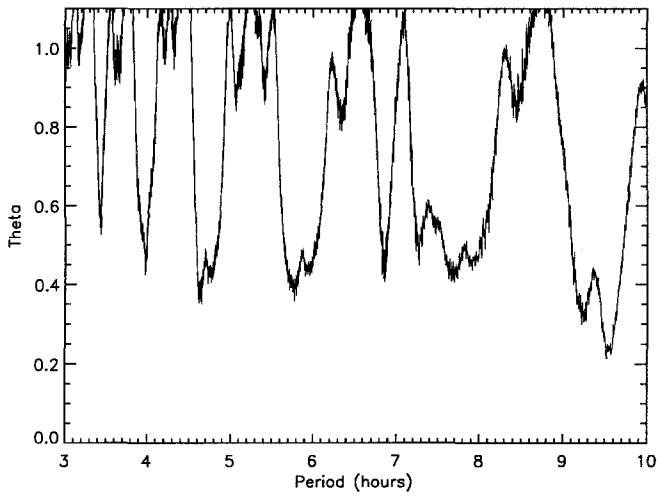

Figure 5.9 The PDM plot for 1996 TO_{66} using the observations in 1998 taken by Hainaut et al. (2000). This PDM plot looks very similar to our 2000 observations PDM plot with good 3.96 hour single-peaked and 7.92 hour double-peaked fits.

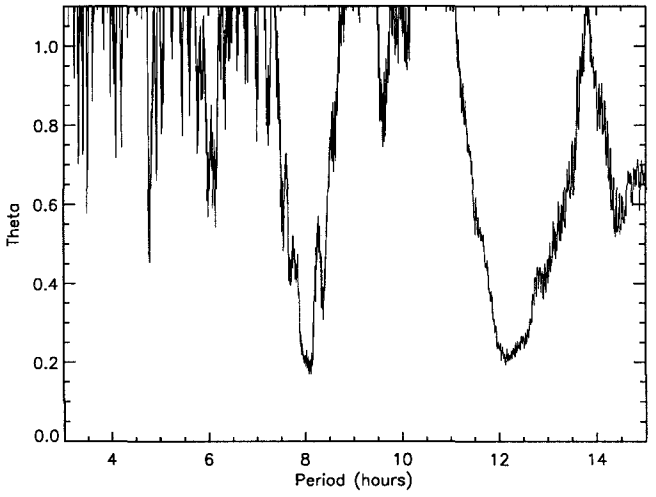

Figure 5.10 The phase dispersion minimization (PDM) plot for 2002 TX_{300}. Best fits from this plot are the 8.12 and 12.10 hour single-peaked fits.

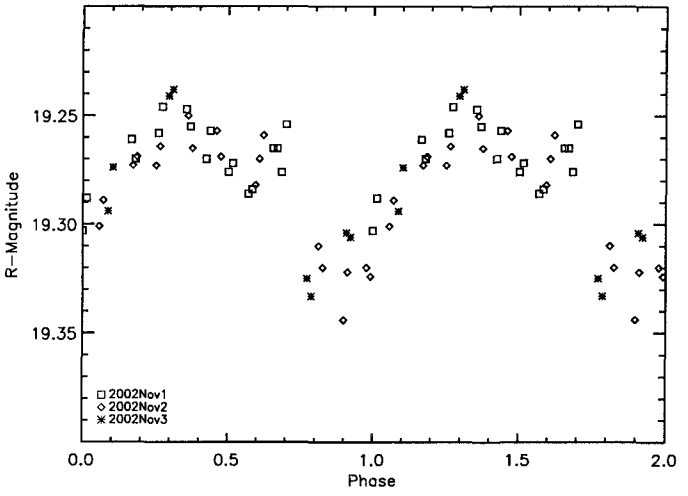

Figure 5.11 Phased R-band data from the UT November 2002 observations for 2002 TX_{300}. The period has been phased to the single-peaked period of 8.12 hours. Uncertainties for individual points are ± 0.02.

5.3.5 Flat Rotational Lightcurve Objects

Ten KBOs ((55637) 2002 UX_{25}, (55638) 2002 VE_{95}, (47171) 1999 TC_{36}, (42355) 2002 CR_{46}, (28978) Ixion 2001 KX_{76}, 2000 YW_{134}, (42301) 2001 UR_{163}, 2001 QF_{298}, 2001 FP_{185}, and 2001 KD_{77}) showed no measurable photometric variations (Table 5.1), by which we mean that their lightcurves have range ≤ 0.1 magnitudes and/or period > 24 hours. A few objects show hints of variability that might, with more data, emerge as rotationally modulated lightcurves. The KBO 2001 YW_{134} has a variation of about 0.1 magnitudes near a 5 hour single-peaked period on one night, but the object appears mostly flat on the second night over 5 hours. Finally, the faint KBO 2001 QF_{298} appears to have variations of about 0.1 magnitudes. Confirmation of these subtle lightcurves will require more data, with a larger telescope most likely required.

5.4 Phase Angle Results

We add additional measurements for four KBO phase functions reported in Sheppard and Jewitt (2002) as well as six new KBOs (Table 5.2). We continue to find that the slopes are very steep and the additional points show that the phase functions are linear to first order between phase angles of 0 and 2 degrees (Figure 5.12). For the phase functions we use the notation $\phi(\alpha) = 10^{-0.4\beta\alpha}$, where α is the phase angle in degrees and β is the "linear" phase coefficient. The median phase coefficient using all 13 KBOs observed at significantly different phase angles from Sheppard and Jewitt (2002) and this work is $\beta = 0.16 \pm 0.01$ magnitudes per degree. Though not necessarily useful at the low phase angles for which KBOs can be observed, we also include the H and G formalism as described in Bowell et al. (1989) in Table 5.2 in order to fully compare our results with other works. As previously, we note that the large, high albedo object Pluto has a much lower phase function than the smaller KBOs (0.0294 ± 0.0011 mag/deg; Buie et al. (1997)). The intermediate albedo/sized Charon has an intermediate phase function (0.0866 ± 0.0078 mag/deg; Buie, Tholen and Wasserman 1997). Although there exists no unique correlation between albedo and phase function at low phase angles, our data are consistent with low albedos for the 100-1000 km scale KBOs.

This work was supported by a grant to D.J. from the NASA Origins Program.

Table 5.2. New Phase Function Data for KBOs

Name		H	G	$\beta(\alpha < 2°)$[a]	N[b]
(42301)	2001 UR163	3.75 ± 0.05	-1.00 ± 0.30	0.25 ± 0.05	2
	2000 YW134	4.29 ± 0.20	$+0.57 \pm 0.50$	0.07 ± 0.12	2
(38628) Huya	2000 EB173	4.45 ± 0.01	$+0.10 \pm 0.03$	0.11 ± 0.01	4
(26181)	1996 GQ21	4.47 ± 0.01	$+0.12 \pm 0.03$	0.12 ± 0.02	4
(26375)	1999 DE9	4.55 ± 0.02	-0.34 ± 0.05	0.17 ± 0.05	4
(26375)	1997 CS29	4.78 ± 0.10	-1.42 ± 0.30	0.31 ± 0.10	3
	2001 QF298	4.95 ± 0.10	-0.19 ± 0.10	0.16 ± 0.03	2
	2001 CZ31	5.54 ± 0.02	-0.03 ± 0.05	0.13 ± 0.03	3
	2001 FZ173	5.63 ± 0.03	-0.77 ± 0.08	0.23 ± 0.03	4
	2001 FP185	5.79 ± 0.05	-1.13 ± 0.20	0.28 ± 0.05	2

[a] $\beta(\alpha < 2°)$ is the phase coefficient at phase angles $< 2°$.

[b] N is the number of different observing runs used and thus the number of points plotted. Most objects were observed on many consecutive nights during each of several observing runs. These data were all averaged together to obtain points with very small uncertainties.

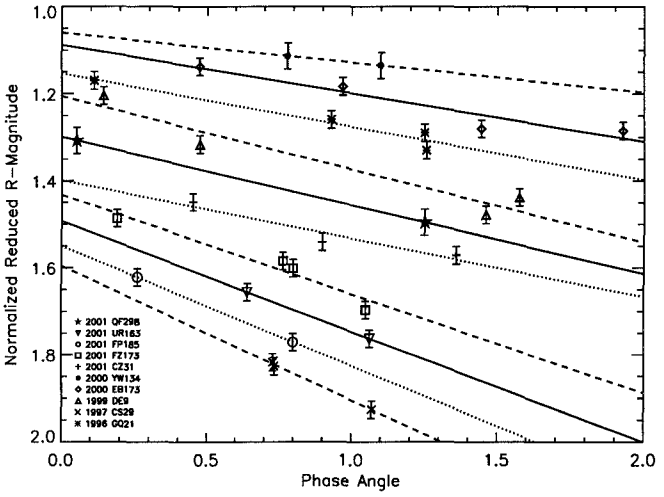

Figure 5.12 Phase functions for the new observations of KBOs observed at several phase angles. The KBO phase functions appear linear to first order. Reduced magnitudes have been normalized and offset in order to display the phase functions efficiently.

Chapter 6

Extreme Kuiper Belt Object 2001 QG_{298} and the Fraction of Contact Binaries

6.1 Abstract

Extensive time-resolved observations of Kuiper Belt object 2001 QG_{298} show a lightcurve with a peak-to-peak variation of 1.14 ± 0.04 magnitudes and single-peaked period of 6.8872 ± 0.0002 hr. The mean absolute magnitude is 6.85 magnitudes which corresponds to a mean effective radius of 122 (77) km if an albedo of 0.04 (0.10) is assumed. This is the first known Kuiper Belt object and only the third minor planet with a radius > 25 km to display a lightcurve with a range in excess of 1 magnitude. We find the colors to be typical for a Kuiper Belt object ($B - V = 1.00 \pm 0.04$, $V - R = 0.60 \pm 0.02$) with no variation in color between minimum and maximum light. The large light variation, relatively long double-peaked period and absence of rotational color change argue against explanations due to albedo markings or elongation due to high angular momentum. Instead, we suggest that 2001 QG_{298} may be a very close or contact binary similar in structure to what has been independently proposed for the Trojan asteroid 624 Hektor. If so, its rotational period would be twice the lightcurve period or 13.7744 ± 0.0004 hr. By correcting for the effects of projection, we estimate that the fraction of similar objects in the Kuiper Belt is at least $\sim$10% to 20% with the true fraction probably much higher. A high abundance of close

and contact binaries is expected in some scenarios for the evolution of binary Kuiper Belt objects.

6.2 Introduction

The Kuiper Belt is a long-lived region of the Solar System just beyond Neptune where the planetisimals have not coalesced into a planet. It contains about 80,000 objects with radii greater than 50 km (Trujillo, Jewitt & Luu 2001) which have been collisionally processed and gravitationally perturbed throughout the age of the Solar System. The short-period comets and Centaurs are believed to originate from the Kuiper Belt (Fernandez 1980; Duncan, Quinn & Tremaine 1988).

Physically, the Kuiper Belt objects (KBOs) show a large diversity of colors from slightly blue to ultra red ($V - R \sim 0.3$ to $V - R \sim 0.8$, Luu and Jewitt 1996) and may show correlations between colors, inclination and/or perihelion distance (Jewitt & Luu 2001; Trujillo & Brown 2002; Doressoundiram et al. 2002; Tegler & Romanishin 2003). Spectra of KBOs are mostly featureless with a few showing hints of water ice (Brown, Cruikshank & Pendleton 1999; Jewitt & Luu 2001; Lazzarin et al. 2003). The range of KBO geometric albedos is still poorly sampled but the larger ones likely have values between 0.04 to 0.10 (Jewitt, Aussel & Evans 2001; Altenhoff, Bertoldi & Menten 2004). Time-resolved observations of KBOs show that $\sim$ 32% vary by $\geq$ 0.15 magnitudes, 18% by $\geq$ 0.40 magnitudes and 12% by $\geq$ 0.60 magnitudes (Sheppard & Jewitt 2002; Ortiz et al. 2003; Lacerda & Luu 2003; Sheppard & Jewitt 2004). One object, (20000) Varuna, displays a large photometric range and fast rotation which is best interpreted as a structurally weak object elongated by its own rotational angular momentum (Jewitt & Sheppard 2002). A significant fraction of KBOs appear to be more elongated than main-belt asteroids of similar size (Sheppard & Jewitt 2002). The KBO phase functions are steep, with a median of 0.16 magnitudes per degree between phase angles of 0 and 2 degrees (Sheppard & Jewitt 2002; Schaefer & Rabinowitz 2002; Sheppard & Jewitt 2004).

About 4%±2% of the KBOs are binaries with separations $\geq 0.15''$ (Noll et al. 2002) while binaries with separations $\geq 0.1''$ may constitute about 15% of the population (Trujillo 2003, private communication). All the binary KBOs found to date appear to have mass ratios near unity, though this may be an observational selection effect. The mechanism responsible for creating KBO binaries is not clear. Formation through collisions is unlikely (Stern 2002). Weidenschilling (2002) has proposed formation of such binaries through complex three-body interactions which would only occur efficiently in a much higher population of large KBOs than can currently be accounted for. Goldreich, Lithwick & Sari (2002) have proposed that KBO binaries could have formed when two bodies approach each other and energy is extracted either by dynamical friction from the surrounding sea of smaller KBOs or by a close third body. This process also requires that the density of KBOs was $\sim 10^2$ to 10^3 times greater than now. They predict that closer binaries should be more abundant in the Kuiper Belt while Weidenschilling's mechanism predicts the opposite.

The present paper is the fourth in a series resulting from the Hawaii Kuiper Belt variability project (HKBVP, see Jewitt & Sheppard 2002; Sheppard & Jewitt 2002; Sheppard & Jewitt 2004). The practical aim of the project is to determine the rotational characteristics (principally period and shape) of bright KBOs ($m_R \leq 22$) in order to learn about the distributions of rotation period and shape in these objects. In the course of this survey we found that 2001 QG_{298} had an extremely large light variation and a relatively long period. We have obtained optical observations of 2001 QG_{298} in order to accurately determine the rotational lightcurve and constrain its possible causes. 2001 QG_{298} has a typical Plutino orbit in 3:2 mean-motion resonance with Neptune, semi-major axis at 39.2 AU, eccentricity of 0.19 and inclination of 6.5 degrees.

6.3 Observations

We used the University of Hawaii (UH) 2.2 m diameter telescope atop Mauna Kea in Hawaii to obtain R-band observations of 2001 QG_{298} on three separate observing runs each covering

several nights: UT September 12 and 13 2002; August 22, 26, 27 and 28 2003; September 27, 28 and 30 2003. Two different CCD cameras were employed. For the September 2002 and September 2003 observations we used a 2048×2048 pixel Tektronix CCD (24 μm pixels) camera with a $0.''219$ pixel^{-1} scale at the f/10 Cassegrain focus. An antireflection coating on the CCD gave very high average quantum efficiency (0.90) in the R-band. The field-of-view was $7'.5 \times 7'.5$. For the August 2003 observations we used the Orthogonal Parallel Transfer Imaging Camera (OPTIC). OPTIC has two 4104×2048 pixel Lincoln Lab CCID28 Orthogonal Transfer CCDs developed to compensate for real-time image motion by moving the charge on the chips to compensate for seeing variations (Tonry et al. (1997)). Howell et al. (2003) have demonstrated that these chips are photometrically accurate and provide routine sharpening of the image point spread function. There is a $\sim 15''$ gap between the chips. The total field-of-view was $9'.5 \times 9'.5$ with 15 μm pixels which corresponds to $0.14''$ pixel^{-1} scale at the f/10 Cassegrain focus. The same R-band filter based on the Johnson-Kron-Cousins photometric system was used for all UH 2.2 m observations.

In addition we used the Keck I 10 m telescope to obtain BVR colors of 2001 QG298 at its maximum and minimum light on UT August 30, 2003. The LRIS camera with its Tektronix 2048×2048 pixel CCD and 24 μm pixels (image scale $0.''215$ pixel^{-1}) was used (Oke et al. (1995)) with the facility broadband BVR filter set. Due to a technical problem with the blue camera side we used only the red side for photometry at BV and R. The blue filter response was cut by the use of a dichroic at 0.460 μm.

All exposures were taken in a consistent manner with the telescope autoguided on bright nearby stars. The seeing ranged from $0.''6$ to $1.0''$ during the various observations. 2001 QG_{298} moved relative to the fixed stars at a maximum of $3''.5$ hr^{-1} corresponding to trail lengths $\leq 0.''43$ in the longest (450 sec) exposures. Thus motion of the object was insignificant compared to the seeing.

Images from the UH telescope were bias-subtracted and then flat-fielded using the median of a set of dithered images of the twilight sky. Data from Keck were bias subtracted and flattened using flat fields obtained from an illuminated spot inside the closed dome.

Table 6.1. Geometrical Circumstances of the Observations

UT Date	R (AU)	Δ (AU)	α (deg)
2002 Sep 12	32.0028	30.9994	0.151
2002 Sep 13	32.0026	30.9983	0.119
2003 Aug 22	31.9392	31.0405	0.851
2003 Aug 26	31.9385	31.0112	0.738
2003 Aug 27	31.9384	31.0046	0.709
2003 Aug 28	31.9382	30.9982	0.680
2003 Aug 30	31.9378	30.9863	0.622
2003 Sep 27	31.9330	30.9407	0.253
2003 Sep 28	31.9328	30.9434	0.283
2003 Sep 30	31.9325	30.9497	0.345

Landolt (1992) standard stars were employed for the absolute photometric calibration. To optimize the signal-to-noise ratio we performed aperture correction photometry by using a small aperture on 2001 QG_{298} (0.″65 to 0.″88 in radius) and both the same small aperture and a large aperture (2.″40 to 3.″29 in radius) on (four or more) nearby bright field stars. We corrected the magnitude within the small aperture used for the KBOs by determining the correction from the small to the large aperture using the field stars (c.f. Tegler and Romanishin 2000; Jewitt & Luu 2001; Sheppard & Jewitt 2002). Since 2001 QG_{298} moved slowly we were able to use the same field stars from night to night within each observing run, resulting in very stable relative photometric calibration from night to night. The observational geometry for 2001 QG_{298} on each night of observation is shown in Table 6.1.

6.4 Results

Tables 6.2 and 6.3 show the photometric results for 2001 QG_{298}. We used the phase dispersion minimization (PDM) method (Stellingwerf 1978) to search for periodicity in the data. In PDM, the metric is the so-called Θ parameter, which is essentially the variance of the unphased data divided by the variance of the data when phased by a given period.

The best-fit period should have a very small dispersion compared to the unphased data and thus $\Theta << 1$ indicates that a good fit has been found.

Table 6.2: R-band Observations at the UH 2.2 meter telescope

Image[a]	UT Date[b]	Julian Date[c]	Exp[d] (sec)	Mag.[e] (m_R)
nt3023	2002 Sep 12.32535	2452529.825347	450	21.673
nt3024	2002 Sep 12.33185	2452529.831840	450	21.542
nt3025	2002 Sep 12.33836	2452529.838356	450	21.539
nt3028	2002 Sep 12.35733	2452529.857326	450	21.429
nt3029	2002 Sep 12.36383	2452529.863819	450	21.396
nt3030	2002 Sep 12.37045	2452529.870451	400	21.311
nt3031	2002 Sep 12.37646	2452529.876458	400	21.351
nt3034	2002 Sep 12.39474	2452529.894734	400	21.282
nt3035	2002 Sep 12.40065	2452529.900648	400	21.281
nt3038	2002 Sep 12.42219	2452529.922188	400	21.315
nt3039	2002 Sep 12.42811	2452529.928102	400	21.299
nt3043	2002 Sep 12.45360	2452529.953600	400	21.440
nt3044	2002 Sep 12.45952	2452529.959514	400	21.560
nt4047	2002 Sep 13.32242	2452530.822419	350	21.398
nt4048	2002 Sep 13.32776	2452530.827755	350	21.476
nt4071	2002 Sep 13.40951	2452530.909514	400	22.458
nt4072	2002 Sep 13.41544	2452530.915428	400	22.377
nt4083	2002 Sep 13.44672	2452530.946725	400	22.004
nt4084	2002 Sep 13.45264	2452530.952639	400	21.906
nt4097	2002 Sep 13.50026	2452531.000255	400	21.427
nt4098	2002 Sep 13.50617	2452531.006169	400	21.438
nt4112	2002 Sep 13.56040	2452531.060394	400	21.249
nt4113	2002 Sep 13.56631	2452531.066308	400	21.259
f.114	2003 Aug 22.44983	2452873.949815	400	21.356
f.115	2003 Aug 22.46309	2452873.963079	400	21.341
f.116	2003 Aug 22.46815	2452873.968125	400	21.315
f.117	2003 Aug 22.47331	2452873.973287	380	21.381
f.118	2003 Aug 22.47812	2452873.978090	380	21.343
f.119	2003 Aug 22.48288	2452873.982859	380	21.312
f.124	2003 Aug 22.51473	2452874.014711	380	21.375
f.125	2003 Aug 22.51984	2452874.019815	380	21.452
f.126	2003 Aug 22.52467	2452874.024630	380	21.425
f.127	2003 Aug 22.53082	2452874.030799	380	21.521
f.128	2003 Aug 22.53559	2452874.035567	380	21.549
f.138	2003 Aug 22.57113	2452874.071111	380	21.808
f.139	2003 Aug 22.57589	2452874.075868	380	21.899
f.140	2003 Aug 22.58063	2452874.080613	380	21.946
f.141	2003 Aug 22.58543	2452874.085405	380	21.993
f.142	2003 Aug 22.59016	2452874.090150	380	22.069
f.143	2003 Aug 22.59494	2452874.094919	380	22.093
f.144	2003 Aug 22.59972	2452874.099699	380	22.150
f.147	2003 Aug 22.61900	2452874.118981	380	22.460

Table 6.2: (continued)

Image[a]	UT Date[b]	Julian Date[c]	Exp[d] (sec)	Mag.[e] (m_R)
f.148	2003 Aug 22.62375	2452874.123738	380	22.444
nt1115	2003 Aug 26.52466	2452878.024653	300	21.383
nt1116	2003 Aug 26.52830	2452878.028287	300	21.390
nt1137	2003 Aug 26.56556	2452878.065544	400	21.565
nt1138	2003 Aug 26.57085	2452878.070833	400	21.667
nt1141	2003 Aug 26.58721	2452878.087187	400	21.843
nt1142	2003 Aug 26.59203	2452878.092014	400	21.784
nt1145	2003 Aug 26.60817	2452878.108171	400	22.045
nt1146	2003 Aug 26.61414	2452878.114120	400	22.150
nt2057	2003 Aug 27.34245	2452878.842442	400	21.289
nt2058	2003 Aug 27.34729	2452878.847280	400	21.336
nt2068	2003 Aug 27.37572	2452878.875706	400	21.377
nt2069	2003 Aug 27.38053	2452878.880521	400	21.380
nt2072	2003 Aug 27.40915	2452878.909144	400	21.443
nt2073	2003 Aug 27.41403	2452878.914016	400	21.509
nt2080	2003 Aug 27.43887	2452878.938854	400	21.717
nt2081	2003 Aug 27.44368	2452878.943669	400	21.792
nt2090	2003 Aug 27.46950	2452878.969479	400	22.072
nt2091	2003 Aug 27.47431	2452878.974294	400	22.094
nt2098	2003 Aug 27.49900	2452878.998981	400	22.315
nt2099	2003 Aug 27.50382	2452879.003808	400	22.382
nt2104	2003 Aug 27.52311	2452879.023090	400	22.168
nt2105	2003 Aug 27.52795	2452879.027928	400	22.070
nt2108	2003 Aug 27.54033	2452879.040324	400	21.884
nt2109	2003 Aug 27.54516	2452879.045139	400	21.826
nt2114	2003 Aug 27.56485	2452879.064826	400	21.648
nt2115	2003 Aug 27.56971	2452879.069688	400	21.614
nt2122	2003 Aug 27.59367	2452879.093657	400	21.461
nt2123	2003 Aug 27.59849	2452879.098472	400	21.460
nt2127	2003 Aug 27.61524	2452879.115220	400	21.367
nt2128	2003 Aug 27.62006	2452879.120046	400	21.378
nt3062	2003 Aug 28.29908	2452879.799074	400	21.752
nt3063	2003 Aug 28.30389	2452879.803877	400	21.805
nt3066	2003 Aug 28.32106	2452879.821053	400	22.002
nt3067	2003 Aug 28.32587	2452879.825868	400	22.038
nt3079	2003 Aug 28.35605	2452879.856042	400	22.498
nt3080	2003 Aug 28.36082	2452879.860810	400	22.513
nt3083	2003 Aug 28.37516	2452879.875150	400	22.389
nt3084	2003 Aug 28.37992	2452879.879907	400	22.374
nt3093	2003 Aug 28.40996	2452879.909942	400	21.864
nt3094	2003 Aug 28.41477	2452879.914757	400	21.788
nt3108	2003 Aug 28.44225	2452879.942234	400	21.550
nt3109	2003 Aug 28.44701	2452879.946991	400	21.471
nt3132	2003 Aug 28.48418	2452879.984167	400	21.411
nt3133	2003 Aug 28.49170	2452879.991690	400	21.369
nt3164	2003 Aug 28.53695	2452880.036933	400	21.405
nt3165	2003 Aug 28.54172	2452880.041713	400	21.458

Table 6.2: (continued)

Image[a]	UT Date[b]	Julian Date[c]	Exp[d] (sec)	Mag.[e] (m_R)
nt3187	2003 Aug 28.57313	2452880.073113	400	21.644
nt3188	2003 Aug 28.57790	2452880.077882	400	21.659
nt3215	2003 Aug 28.61676	2452880.116748	400	22.043
nt3216	2003 Aug 28.62153	2452880.121516	400	22.181
nt1.034	2003 Aug 27.27855	2452909.778553	300	21.600
nt1.035	2003 Aug 27.28337	2452909.783368	300	21.553
nt1.067	2003 Aug 27.42997	2452909.929965	300	21.675
nt1.068	2003 Aug 27.43473	2452909.934734	300	21.709
nt1.089	2003 Aug 27.53125	2452910.031238	300	21.948
nt1.090	2003 Aug 27.53605	2452910.036042	300	21.812
nt2.032	2003 Aug 28.27564	2452910.775637	300	21.643
nt2.033	2003 Aug 28.28043	2452910.780428	300	21.631
nt2.053	2003 Aug 28.37271	2452910.872708	300	22.301
nt2.054	2003 Aug 28.37751	2452910.877512	300	22.267
nt2.063	2003 Aug 28.42250	2452910.922500	300	21.719
nt2.064	2003 Aug 28.42730	2452910.927292	300	21.644
nt2.080	2003 Aug 28.49909	2452910.999086	300	21.327
nt2.081	2003 Aug 28.50389	2452911.003889	300	21.321
nt2.090	2003 Aug 28.55245	2452911.052442	300	21.453
nt2.091	2003 Aug 28.55725	2452911.057245	300	21.472
nt2.166	2003 Aug 30.34785	2452912.847847	400	22.267
nt2.167	2003 Aug 30.35398	2452912.853981	400	22.259
nt2.195	2003 Aug 30.48012	2452912.980116	400	21.334
nt2.196	2003 Aug 30.48597	2452912.985961	400	21.379

[a] Image number.

[b] Decimal Universal Date at the start of the integration.

[c] Julian Date at the start of the integration.
No light-time correction has been made in the table.

[d] Exposure time for the image.

[e] Apparent red magnitude, uncertainties are ± 0.03 to ± 0.04.

2001 QG_{298} showed substantial variability ($\sim$ 1.1 magnitudes with a single-peaked period near 6.9 hr) in R-band observations from two nights in September 2002. We obtained further observations of the object in 2003 to determine the lightcurve with greater accuracy. PDM analysis of all the apparent magnitude R-band data from the September 2002 and August and September 2003 observations shows that 2001 QG_{298} has strong Θ minima near the periods $P = 6.88$ hr and $P = 13.77$ hr, with weaker alias periods flanking these (Figure 6.1). We corrected the apparent magnitude data for the minor phase angle effects (we used the nominal 0.16 magnitudes per degree found in Sheppard & Jewitt 2002)

Table 6.3. B-band, V-band and R-band Observations at Keck

Image[a]	UT Date[b]	Julian Date[c]	Exp[d] (sec)	Mag.
lred0078	2003 Aug 30.37786	2452881.877861	150	22.391[e]
lred0084	2003 Aug 30.40107	2452881.901076	150	22.070[e]
lred0120	2003 Aug 30.51921	2452882.019213	150	21.391[e]
lred0121	2003 Aug 30.52202	2452882.022027	150	21.369[e]
lred0082	2003 Aug 30.39546	2452881.895460	150	22.803[f]
lred0083	2003 Aug 30.39828	2452881.898285	150	22.734[f]
lred0118	2003 Aug 30.51329	2452882.013295	150	21.981[f]
lred0119	2003 Aug 30.51642	2452882.016423	150	22.013[f]
lred0079	2003 Aug 30.38170	2452881.881700	300	23.917[g]
lred0080	2003 Aug 30.38623	2452881.886232	300	23.865[g]
lred0081	2003 Aug 30.39075	2452881.890758	300	23.896[g]
lred0114	2003 Aug 30.49488	2452881.994882	300	22.945[g]
lred0115	2003 Aug 30.49949	2452881.999492	300	22.980[g]
lred0116	2003 Aug 30.50404	2452882.004046	300	23.013[g]
lred0117	2003 Aug 30.50860	2452882.008606	300	23.010[g]

[a]Image number.

[b]Decimal Universal Date at the start of the integration.

[c]Julian Date at the start of the integration. No light-time correction has been made in the table.

[d]Exposure time for the image.

[e]Apparent red magnitude, uncertainties are ± 0.02.

[f]The apparent magnitude is for the V-band, uncertainties are ± 0.03

[g]The apparent magnitude is for the B-band, uncertainties are ± 0.04. In the B-band, only light longward of 0.460 μm was observed because of the dichroic.

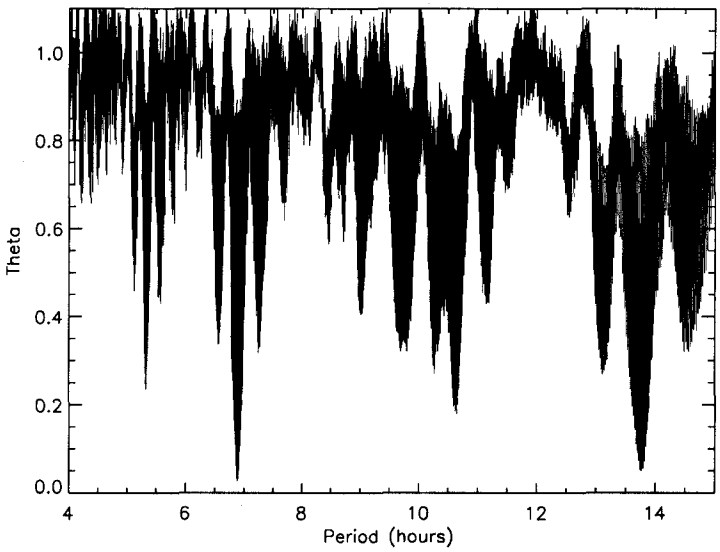

Figure 6.1 The phase dispersion minimization (PDM) plot for 2001 QG_{298}. A smaller theta corresponds to a better fit. Best fits from this plot are the 6.8872 hour single-peaked fit and the 13.7744 hour double-peaked fit. Both are flanked by alias periods.

and light travel-time differences of the observations to correspond to the August 30, 2003 observations. We then phased the data to all the peaks with $\Theta < 0.4$ and found only the 6.8872 and 13.7744 hour periods to be consistent with all the data (Figures 6.2 and 6.3). Through a closer look at the PDM plot (Figure 6.4) and phasing the data we find best fit periods $P = 6.8872 \pm 0.0002$ hr (a lightcurve with a single maximum per period) and $P = 13.7744 \pm 0.0004$ hr (two maxima per period as expected for rotational modulation caused by an aspherical shape). The double-peaked lightcurve appears to be the best fit with the minima different by about 0.1 magnitudes while the maxima appear to be of similar brightness. The photometric range of the lightcurve is $\Delta m = 1.14 \pm 0.04$ magnitudes.

The Keck BVR colors of 2001 QG_{298} show no variation from minimum to maximum light within the photometric uncertainties of a few % (see Figures 6.2 and 6.3). This is again consistent with a lightcurve that is produced by an elongated shape, rather than by

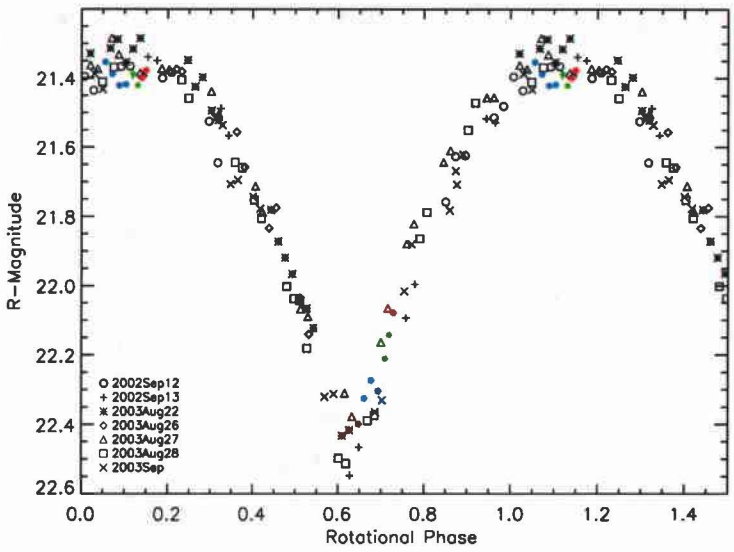

Figure 6.2 Phased data from all the observations in 2002 and 2003 of 2001 QG_{298}. The period has been phased to 6.8872 hr which is the best fit single-peaked period. Filled colored symbols are data taken in the B-band (blue), V-band (green) and R-band (red) at the Keck I telescope on UT August 30. All other symbols are R-band data from the various nights of observations at UH 2.2 m telescope. The B and V points have been shifted according to their color differences from the R-band ($V - R = 0.60$ and $B - V = 1.00$). No color variation is seen between maximum and minimum light. The uncertainty on each photometric observation is ± 0.03 mag.

albedo variations. The colors ($B - V = 1.00 \pm 0.04$, $V - R = 0.60 \pm 0.02$) show that 2001 QG_{298} is red and similar to the mean values ($B - V = 0.98 \pm 0.04$, $V - R = 0.61 \pm 0.02$, 28 objects) for KBOs as a group (Jewitt and Luu 2001).

The absolute magnitude of a Solar System object, $m_R(1,1,0)$, is the hypothetical magnitude the object would have if it where at heliocentric (R) and geocentric (Δ) distances of 1 AU and had a phase angle (α) of 0 degrees. We use the relation $m_R(1,1,0) = m_R - 5\log(R\Delta) - \beta\alpha$ to find the absolute magnitude by correcting for the geometrical and phase angle effects in the 2001 QG_{298} observations. Here m_R is the apparent red magnitude of the object and β is the phase function. Using the nominal value of $\beta = 0.16$ magnitudes

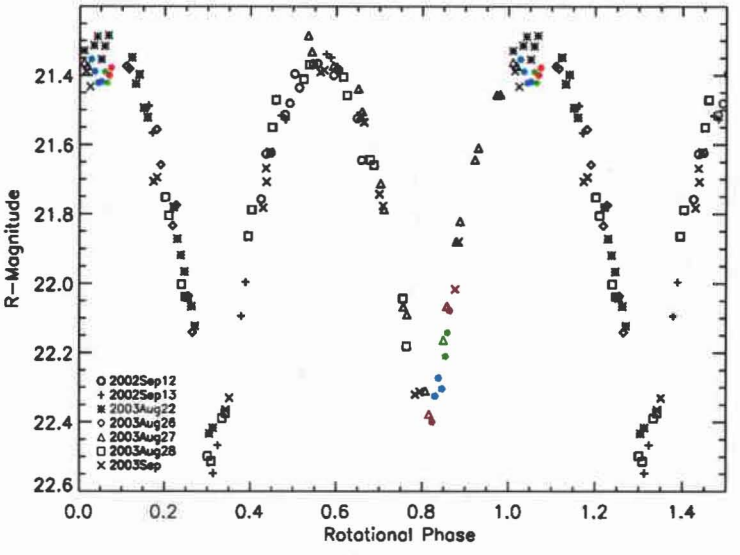

Figure 6.3 Phased data from all the observations in 2002 and 2003 of 2001 QG_{298}. The period has been phased to 13.7744 hr which is the best fit double-peaked period. Filled colored symbols are data taken in the B-band (blue), V-band (green) and R-band (red) at the Keck I telescope on UT August 30. All other symbols are R-band data from the various nights of observations at UH 2.2 m telescope. The B and V points have been shifted according to their color differences from the R-band ($V-R=0.60$ and $B-V=1.00$). There appears to be two distinct minima. The minima appear to be more "notched" compared to the flatter maxima. No color variation is seen between maximum and minimum light. The uncertainty for each photometric observation is ± 0.03 mag.

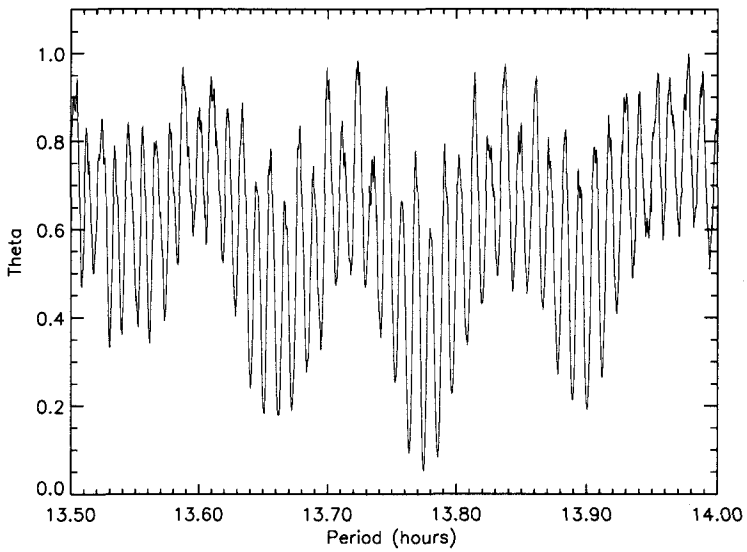

Figure 6.4 A closer view of the phase dispersion minimization (PDM) plot for 2001 QG_{298} around the double-peaked period at 13.7744 hr. The best fit is flanked by aliases from separation of the 3 data sets obtained for this object. Only the center PDM peak fits the data once it is phased together.

per degree for KBOs at low phase angles (Sheppard & Jewitt 2002; Sheppard & Jewitt 2004) and data from Table 6.1 we find that 2001 QG_{298} has $m_R(1,1,0) = 6.28 \pm 0.02$ at maximum light and $m_R(1,1,0) = 7.42 \pm 0.02$ magnitudes at minimum light. If attributed to a rotational variation of the cross-section, this corresponds to a ratio of maximum to minimum areas of 2.85:1.

The effective radius of an object can be calculated using the relation $m_R(1,1,0) = m_\odot - 2.5\log\left[p_R r_e^2/2.25 \times 10^{16}\right]$ where $m_\odot$ is the apparent red magnitude of the sun (−27.1), p_R is the red geometric albedo and r_e (km) is the effective circular radius of the object. If we assume an albedo of 0.04 (0.10) this corresponds to effective circular radii at maximum and minimum light of about 158 (100) km and 94 (59) km, respectively. At the mean absolute magnitude of 6.85 mag, the effective circular radius is 122 (77) km.

6.5 Analysis

Only three other objects in the Solar System larger than 25 km in radius are known to have lightcurve ranges > 1.0 magnitude (Table 6.4). Following Jewitt and Sheppard (2002) we discuss three possible models of rotational variation to try to compare the objects from Table 6.4 with 2001 QG_{298}.

6.5.1 Albedo Variation

On asteroids, albedo variations contribute brightness variations that are usually less than about 10%−20% (Degewij, Tedesco & Zellner 1979). Rotationally correlated color variations may be seen if the albedo variations are large since materials with markedly different albedos may differ compositionally. As seen in Table 6.4, Saturn's satellite Iapetus is the only object in which variations ≥1 mag. are explained through albedo. The large albedo contrast on Iapetus is likely a special consequence of its synchronous rotation and the anisotropic impact of material trapped in orbit about Saturn onto its leading hemisphere (Cook & Franklin (1970)). Iapetus shows clear rotational color variations ($\Delta(B-V) \sim 0.1$ mag.) that are

Table 6.4. Large Objects With Extreme Light Curves[a]

Name	Type	$a \times b$ (km)	Δ mag (mag)	Period (hrs)	Cause[b]	Ref[c]
Iapetus	Saturn Satellite	715×715	2	1903.9	AL	1
624 Hektor	Jupiter Trojan	150×75	1.1	6.921	CB	2
216 Kleopatra	Main-Belt Asteroid	109×47	1.18	5.385	JE/CB	3
2001 QG_{298}	Kuiper Belt Object	267×94	1.14	13.7744	CB	This Work

[a]Objects that have effective radii > 25 km and lightcurves with peak-to-peak amplitudes > 1 magnitudes.

[b]The dominant cause or most probable dominant cause for the amplitude of the lightcurve: AL is albedo, CB is contact binary, JE is Jacobi triaxial rotational ellipsoid

[c]References for specified objects: 1) Millis (1977) 2) Dunlap & Gehrels (1969); Hartmann & Cruikshank (1978); Weidenschilling (1980); Leone et al. (1984); Lagerkvist, Harris & Zappala (1989) 3) Scaltriti & Zappala (1978); Tholen (1980); Leone et al. (1984); Lagerkvist, Harris & Zappala (1989); Ostro et al. (2000); Hestroffer et al. (2002); Washabaugh & Scheeres (2002)

correlated with the rotational albedo variations (Millis (1977)) and which would be detected in 2001 QG_{298} given the quality of our data. The special circumstance of Iapetus is without obvious analogy in the Kuiper Belt and we do not believe that it is a good model for the extreme lightcurve of 2001 QG_{298}.

Pluto shows a much smaller variation (about 0.3 magnitudes) thought to be caused by albedo structure (Buie, Tholen & Wasserman 1997). Pluto is so large that it can sustain an atmosphere which may contribute to amplifying its lightcurve range by allowing surface frosts to condense on brighter (cooler) spots. Thus brighter spots grow brighter while darker (hotter) spots grow darker through the sublimation of ices. This positive feedback mechanism requires an atmosphere and is unlikely to be relevant on a KBO as small as 2001 QG_{298}.

While we cannot absolutely exclude surface markings as the dominant cause of 2001 QG_{298}'s large rotational brightness variation, we are highly skeptical of this explanation. We measure no color variation with rotation, there appear to be two distinct minima and the range is so large as to be beyond reasonable explanation from albedo alone.

6.5.2 Aspherical Shape

Since surface markings are most likely not the cause of the lightcurve, the observed photometric variations are probably caused by changes in the projected cross-section of an elongated body in rotation about its minor axis. The rotation period of an elongated object should be twice the single-peaked lightcurve period because of the projection of both long axes (2 maxima) and short axes (2 minima) during one full rotation. If the body is elongated, we can use the ratio of maximum to minimum brightness to determine the projection of the body shape into the plane of the sky. The rotational brightness range of a triaxial object with semiaxes $a \geq b \geq c$ in rotation about the c axis and viewed equatorially is

$$\Delta m = 2.5 \log \left(\frac{a}{b} \right) \tag{6.1}$$

where Δm is expressed in magnitudes. This gives a lower limit to a/b because of the effects of projection. Using $\Delta m = 1.14$ for 2001 QG_{298}, we find the lower limit is $a/b = 2.85$. This corresponds to $a = 267$ and $b = 94$ km for the geometric albedo 0.04 case and $a = 169$ and $b = 59$ km for an albedo of 0.10.

It is possible that 2001 QG_{298} is elongated and able to resist gravitational compression into a spherical shape by virtue of its intrinsic compressive strength. However, observations of asteroids in the main-belt suggest that only the smallest ($\sim$0.1 km sized) asteroids are in possession of a tensile strength sufficient to resist rotational deformation (Pravec, Harris & Michalowski 2003). Observations of both asteroids and planetary satellites suggest that many objects with radii $\geq$ 50 to 75 km have shapes controlled by self-gravity, not by material strength (Farinella 1987; Farinella & Zappalà (1997)). The widely accepted explanation is that these bodies are internally weak because they have been fractured by numerous past impacts. This explanation is also plausible in the Kuiper Belt, where models attest to a harsh collisional environment at early times (e.g. Davis & Farinella 1997). We feel that the

extraordinarily large amplitude of 2001 QG_{298} is unlikely to be caused by elongation of the object sustained by its own material strength, although we cannot rule out this possibility.

Structurally weak bodies are susceptible to rotational deformation. The 1000-km scale KBO (20000) Varuna (rotation period 6.3442 $\pm$ 0.0002 hr and lightcurve range 0.42 $\pm$ 0.02 mag) is the best current example in the Kuiper Belt (Jewitt and Sheppard 2002). In the main asteroid belt, 216 Kleopatra has a very short period (5.385 hr) and large lightcurve range (1.18 mag., corresponding to axis ratio $\sim$2.95:1 and dimensions $\sim$ 217 $\times$ 94 km, Table 6.4). Kleopatra has been observed to be a highly elongated body through radar and high resolution imaging and the most likely explanation is that 216 Kleopatra is rotationally deformed (Leone et al. 1984; Ostro et al. (2000); Hestroffer et al. (2002); Washabaugh & Scheeres (2002)). Is rotational elongation a viable model for 2001 QG_{298}?

The critical rotation period (T_{crit}) at which centripetal acceleration equals gravitational acceleration towards the center of a rotating spherical object is

$$T_{crit} = \left(\frac{3\pi}{G\rho}\right)^{1/2} \tag{6.2}$$

where G is the gravitational constant and ρ is the density of the object. With ρ = 1000 kg m^{-3} the critical period is about 3.3 hr. Even at longer periods, real bodies will suffer centripetal deformation into triaxial aspherical shapes which depend on their density, ang ular momentum and material strength. The limiting equilibrium shapes of rotating strengthless fluid bodies have been well studied by Chandrasekhar (1987) and a detailed discussion in the context of the KBOs can be found in Jewitt and Sheppard (2002). We briefly mention here that triaxial "Jacobi" ellipsoids with large angular momenta are rotationally elongated and generate lightcurves with substantial ranges when viewed equatorially.

Leone et al. (1984) have analyzed rotational equilibrium configurations of strengthless asteroids in detail (see Figure 6.5). They show that the maximum photometric range of a rotational ellipsoid is 0.9 mag: more elongated objects are unstable to rotational fission.

The 1.14 mag photometric range of 2001 QG_{298} exceeds this limit. In addition, the 13.7744 hr (two-peaked) rotation period is much too long to cause significant elongation for any plausible bulk density (Figure 6.5). For these reasons we do not believe that 2001 QG_{298} is a single rotationally distorted object.

6.5.3 Binary Configurations

A third possible explanation for the extreme lightcurve of 2001 QG_{298} is that this is an eclipsing binary. A wide separation (sum of the orbital semi-major axes much larger than the sum of the component radii) is unlikely because such a system would generate a distinctive "notched" lightcurve that is unlike the lightcurve of 2001 QG_{298}. In addition, a wide separation would require unreasonably high bulk density of the components in order to generate the measured rotational period. If 2001 QG_{298} is a binary then the components must be close or in contact. We next consider the limiting case of a contact binary.

The axis ratio of a contact binary consisting of equal spheres is $a/b = 2$, corresponding to a lightcurve range $\Delta m = 0.75$ magnitudes, as seen from the rotational equator. At the average viewing angle $\theta = 60$ degrees we would expect $\Delta m = 0.45$ mag. The rotational variation of 2001 QG_{298} is too large to be explained as a contact binary consisting of two equal spheres. However, close binary components of low strength should be elongated by mutual tidal forces, giving a larger lightcurve range than possible in the case of equal spheres (Leone et al. 1984). The latter authors find that the maximum range for a tidally distorted nearly contact binary is 1.2 magnitudes, compatible with the 1.14 mag. range of 2001 QG_{298} (Figure 6.5). The contact binary hypothesis is the likely explanation of 624 Hektor's lightcurve (Hartmann & Cruikshank (1978); Weidenschilling (1980); Leone et al. 1984) and could also explain 216 Kleopatra's lightcurve (Leone et al. 1984; Ostro et al. 2000; Hestroffer et al. 2002).

We suggest that the relatively long double-peaked period (13.7744 ± 0.0004 hr) and large photometric range (1.14 ± 0.04 magnitudes) of 2001 QG_{298}'s lightcurve are best understood if the body is a contact binary or nearly contact binary viewed from an approximately

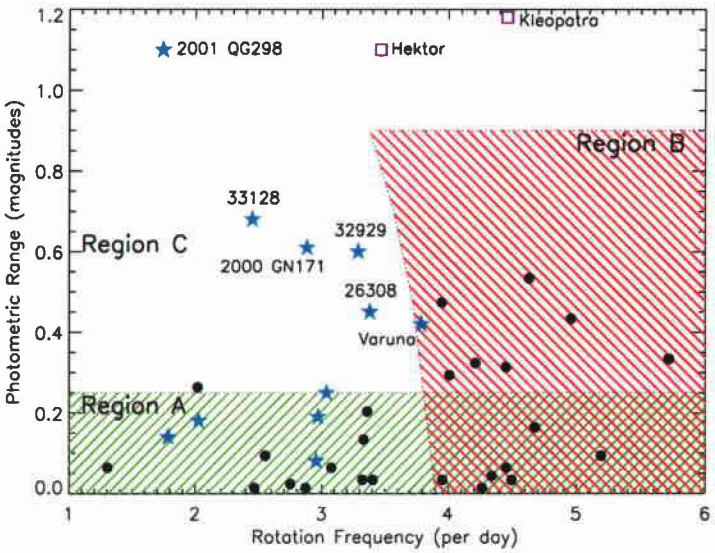

Figure 6.5 This Figure is a modification of Figure 4 from Leone et al. (1984). We here show the rotation periods and photometric ranges of known KBO lightcurves and the larger asteroids. The Regions are defined as A) The range of the lightcurve could be equally caused by albedo, elongation or binarity B) The lightcurve range is most likely caused by rotational elongation C) The lightcurve range is most likely caused by binarity of the object. Stars denote KBOs, Circles denote main-belt asteroids (radii $\geq$ 100 km) and Squares denote the Trojan 624 Hektor and the main-belt asteroid 216 Kleopatra. Objects just to the left of Region B would have densities significantly less than 1000 kg m^{-3} in order to be elongated from rotational angular momentum. Binary objects are not expected to have photometric ranges above 1.2 magnitudes. The 23 KBOs which have photometric ranges below our photometric uncertainties ($\sim$ 0.1 mag) in the Hawaii survey have not been plotted since their periods are unknown. These objects would all fall into Region A. The asteroids have been plotted at their expected mean projected viewing angle of 60 degrees in order to more directly compare to the KBOs of unknown projection angle.

equatorial perspective. The large range suggests that the components are of similar size and are distorted by their mutual tidal interactions. Using the calculations from Leone et al. (1984), who take into account the mutual deformation of close, strengthless binary components, we find the density of these objects must be $\sim$1000 kg m^{-3} in order to remain bound in a binary system separated by the Roche radius (which is just over twice the component radius). If we assume that the albedo of both objects is 0.04, the effective radius of each component is about 95 km as found above. Using this information we find from Kepler's third law that if the components are separated, they would be about 300 km apart. This separation as seen on the sky (0.01″) is small enough to have escaped resolution with current technology.

Further, we point out that the maximum of the lightcurve of 2001 QG_{298} is more nearly "U" shaped (or flattened) than is the "V" shaped minimum (Figure 6.3). This is also true for 624 Hektor (Dunlap & Gehrels (1969)) and may be a distinguishing, though not unique, signature of a contact or nearly contact binary (Zappala (1980); Leone et al. 1984; Cellino et al. (1985)). In comparison, (20000) Varuna, which is probably not a contact binary (see below and Jewitt & Sheppard 2002), does not show significant differences in the curvature of the lightcurve maxima and minima.

In short, while we cannot prove that 2001 QG_{298} is a contact binary, we find by elimination of other possibilities that this is the most convincing explanation of its lightcurve.

6.5.4 Fraction of Contact Binaries in the Kuiper Belt

The distribution of measured lightcurve properties is shown in Figure 6.5 (adapted from Figure 4 of Leone et al. (1984)). There, Region A corresponds to the low rotational range objects (of any period) in which the variability can be plausibly associated with surface albedo markings. Region B corresponds to the rotationally deformed Jacobi ellipsoids while Region C marks the domain of the close binary objects. Plotted in the Figure are the lightcurve periods and ranges for KBOs from the HKBVP (Jewitt & Sheppard

2002; Sheppard & Jewitt 2002; Sheppard & Jewitt 2004). We also show large main belt asteroids (data from http://cfa-www.harvard.edu/iau/lists/LightcurveDat.html updated by A. Harris and B. Warner and based on Lagerkvist, Harris & Zappala 1989). Once again we note that the measured KBO ranges should, in most cases, be regarded as lower limits to the range because of the possible effects of projection into the plane of the sky.

Of the 34 KBOs in our sample, five fall into Region C in Figure 6.5. Of these, 2001 QG_{298} is by far the best candidate for being a contact or nearly contact binary system since it alone has a range between the $\Delta m_R \sim 0.9$ mag. limit for a single rotational equilibrium ellipsoid and the $\Delta m_R \sim 1.2$ mag. limit for a mutually distorted close binary (Table 6.5). It is also rotating too slowly to be substantially distorted by its own spin (Figure 6.5). Both (33128) 1998 BU_{48} and 2000 GN_{171} are good candidates which have large photometric ranges and relatively slow periods. KBOs (26308) 1998 SM_{165} and (32929) 1995 QY_9 could be rotationally deformed ellipsoids, but their relatively slow rotations would require densities much smaller than that of water, a prospect which we consider unlikely.

We next ask what might be the abundance of contact or close binaries in the Kuiper Belt. As a first estimate we assume that we have detected one such object (2001 QG_{298}) in a sample of 34 KBOs observed with adequate time resolution. The answer depends on the magnitude of the correction for projection effects caused by the orientation of the rotation vector with respect to the line of sight. This correction is intrinsically uncertain, since it depends on unknowns such as the scattering function of the surface materials of the KBO as well as on the detailed shape. We adopt two crude approximations that should give the projection correction at least to within a factor of a few.

First, we represent the elongated shape of the KBO by a rectangular block with dimensions a > b = c. The lightcurve range varies with angle from the equator, θ, in this approximation as

$$\Delta m = 2.5 log \left[\frac{1 + tan\theta}{\frac{b}{a} + tan\theta} \right]. \tag{6.3}$$

Table 6.5. Possible Contact Binaries in the Kuiper Belt

Name	H[a] (mag)	Δm_R[b] (mag)	Period[c] (hrs)	Probability[d]	Ref[e]
2001 QG_{298}	6.85	1.14 ± 0.04	13.7744 ± 0.0004	very high	This Work
2000 GN_{171}	5.98	0.61 ± 0.03	8.329 ± 0.005	high	1
(33128) 1998 BU_{48}	7.2	0.68 ± 0.04	9.8 ± 0.1	high	1
(26308) 1998 SM_{165}	5.8	0.45 ± 0.03	7.1 ± 0.1	medium	1,2
(32929) 1995 QY_9	7.5	0.60 ± 0.04	7.3 ± 0.1	medium	1
(20000) Varuna	3.21	0.42 ± 0.03	6.34 ± 0.01	low	3

[a]Absolute magnitude.

[b]The peak to peak range of the lightcurve.

[c]The lightcurve period if there is two maximum per period.

[d]Probability that the object is a contact or nearly contact binary.

[e]References for lightcurve information: 1) Sheppard & Jewitt (2002) 2) Romanishin et al. (2001) 3) Jewitt & Sheppard (2002)

For the limiting case of a highly distorted contact binary with $\Delta m = 1.2$ mag. at $\theta = 0°$, Eq. (3) gives $a/b = 3$. We next assume that the range must fall in the range $0.9 \leq \Delta m \leq 1.2$ mag. in order for us to make an assignment of likely binary structure (Figure 6.6). As noted above, only 2001 QG_{298} satisfies this condition amongst the known objects. We find, from Eq. (3) with $a/b = 3$, that $\Delta m = 0.9$ mag is reached at $\theta = 10°$. The probability that Earth would lie within 10° of the equator of a set of randomly oriented KBOs is $P(\theta \leq 10) = 0.17$. Therefore, the detection of 1 KBO with $0.9 \leq \Delta m \leq 1.2$ mag implies that the fractional abundance of similarly elongated objects is $f \sim 1/(34P) \sim 17\%$.

As a separate check on this estimate, we next represent the object as an ellipsoid, again with axes a > b = c. The photometric range when viewed at an angle θ from the rotational equator is given by

$$\Delta m = 2.5log(a/b) - 1.25log\left[\left[\left(\frac{a}{b}\right)^2 - 1\right] sin^2\,\theta + 1\right] \tag{6.4}$$

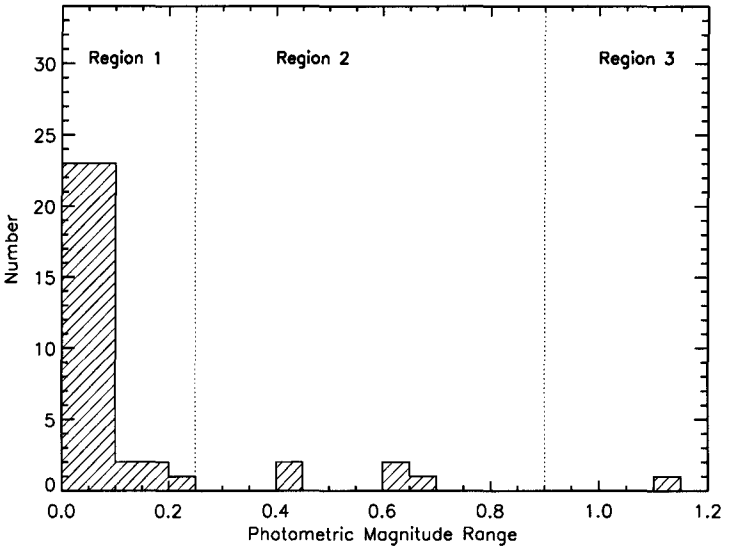

Figure 6.6 A histogram of known KBOs photometric ranges. There is a break in known photometric ranges starting around 0.25 magnitudes. The Regions are defined as 1) The lightcurve range could be dominated by albedo, elongation or binarity 2) The lightcurve is likely dominated from rotational elongation or binarity 3) The lightcurve is likely caused by binarity. Data is from the Hawaii Kuiper Belt object variability project (Sheppard & Jewitt 2002 and Sheppard and Jewitt 2004).

Substituting $a/b = 3$, the range predicted by Eq. (4) falls to 0.9 mag at $\theta \sim 17°$. Given a random distribution of the spin vectors, the probability that Earth would lie within 17° of the equator is $P(\theta \leq 17) = 0.29$. Therefore, the detection of 1 KBO with a range between 0.9 and 1.2 mag in a sample of 34 objects implies, in this approximation, a fractional abundance of similarly elongated objects near $f \sim 1/(34P) \sim 10\%$.

Given the crudity of the model, the agreement between projection factors from Eqs. (3) and (4) is encouraging. Together, the data and the projection factors suggest that in our sample of 34 KBOs, perhaps 3 to 6 objects are as elongated as 2001 QG_{298} but only 2001 QG_{298} is viewed from a sufficiently equatorial perspective that the lightcurve is distinct. This is consistent with Figure 5, which shows that 5 of 34 KBOs (15%) from the HKBVP occupy Region C of the period-range diagram. Our estimate is very crude and is also a lower limit to the true binary fraction because close binaries with components of unequal size will not satisfy the $0.9 \leq \Delta m \leq 1.2$ mag. criterion for detection. The key point is that the data are consistent with a substantial close binary fraction in the Kuiper Belt .

Figure 6.5 also shows that there are no large main-belt asteroids (radii $\geq$ 100 km) in Region C, which is where similar sized component contact binaries are expected to be. To date, no examples of large binary main-belt asteroids with similar sized components have been found, even though the main belt has been extensively searched for binarity (see Margot (2002) and references therein). The main-belt asteroids may have had a collisional history significantly different from that of the KBOs.

The contact binary interpretation of the 2001 QG_{298} lightcurve is clearly non-unique. Indeed, firm proof of the existence of contact binaries will be as difficult to establish in the Kuiper Belt as it has been in closer, brighter populations of small bodies. Nevertheless, the data are compatible with a high abundance of such objects. It is interesting to speculate about how such objects could form in abundance. One model of the formation and long term evolution of wide binaries predicts that such objects could be driven together by dynamical friction or three-body interactions (Goldreich et al. 2002). Objects like 2001 QG_{298} would be naturally produced by such a mechanism.

6.6 Summary

Kuiper Belt Object 2001 QG_{298} has the most extreme lightcurve of any of the 34 objects so far observed in the Hawaii Kuiper Belt Variability Project.

1. The double-peaked lightcurve period is 13.7744 ± 0.0004 hr and peak-to-peak range is 1.14 ± 0.04 mag. Only two other minor planets with radii $\geq$ 25 km (624 Hektor and 216 Kleopatra) and one planetary satellite (Iapetus) are known to show rotational photometric variation greater than 1 mag.

2. The absolute red magnitude is $m_R(1,1,0) = 6.28$ at maximum light and 7.42 mag. at minimum light. With an assumed geometric albedo of 0.04 (0.10) we derive effective circular radii at maximum and minimum light of 158 (100) and 94 (59) km, respectively.

3. No variation in the BVR colors between maximum and minimum light was detected to within photometric uncertainties of a few percent.

4. The large photometric range, differences in the lightcurve minima, and long period of 2001 QG_{298} are consistent with and strongly suggest that this object is a contact or nearly contact binary, viewed equatorially.

5. If 2001 QG_{298} is a contact binary with similarly sized components, then we conclude that such objects constitute at least 10% to 20% of the Kuiper Belt population at large sizes.

Acknowledgments

We thank John Tonry and Andrew Pickles for help with the OPTIC camera and the remote observing system on the University of Hawaii 2.2 meter telescope. We also thank Henry Hsieh for observational assistance and Jane Luu for comments on the manuscript. This work was supported by a grant to D.J. from the NASA Origins Program.

Chapter 7

Kuiper Belt Summary

• A wide-field survey of 1428 deg^2 of sky near the ecliptic was conducted to search for bright Kuiper Belt objects and Centaurs. This area was an order of magnitude larger than any previously published CCD survey for Centaurs and Kuiper Belt Objects. From this survey the empirical projected surface density of Centaurs was found to be $\Sigma_C(m_R \leq 18.8) = 7.8(^{+16.0}_{-6.6}) \times 10^{-4}$ deg^{-2} and a projected surface density 3σ upper confidence limit for Kuiper Belt objects of $\Sigma_K(m_R \leq 18.8) < 4.1 \times 10^{-3}$ deg^{-2} was found. Through a Monte Carlo simulation it was shown that the size distribution of Centaurs is consistent with a $q \sim 4$ differential power law, similar to the size distribution of the parent Kuiper Belt Objects. The Centaur population was found to be of order 1×10^7 (radius $\geq$1 km) assuming a geometric albedo of 0.04. The Centaur population taken along with their average dynamical lifetime is consistent with the Kuiper Belt as the source of the Centaurs. About 100 Centaurs are larger than 50 km in radius, of which only a handful are presently known. The current total mass of the Centaurs is 10^{-4} $M_\oplus$.

• In the Hawaii Kuiper Belt Variability Project (HKBVP) nearly 40 bright Kuiper Belt objects and Centaurs were observed to systematically monitor possible short and long term light variations due to rotational, phase angle, binary and cometary effects. About 29% display significant ($\Delta m \geq 0.15$ magnitude range) short period lightcurves while about 18% of the sampled objects have lightcurve ranges $\Delta m \geq 0.4$ magnitudes and 12% have $\Delta m \geq 0.60$ magnitudes. The objects are thought to be very large ($\gtrsim$ 250 km diameter,

assuming an albedo of 0.04) and, in the absence of rotation, should be near spherical due to self compression. Statistically, the trans-Neptunian objects are less spherical than their main-belt asteroid counterparts, indicating a higher specific angular momentum perhaps resulting from the formation epoch.

Two objects stand out in the HKBVP. The large amplitude, short period object (20000) Varuna is probably a rotationally distorted, low density rubble pile. Kuiper Belt object 2001 QG_{298} is the first known Kuiper Belt object, and only the third minor planet, with a radius > 25 km to display a lightcurve with a range in excess of 1 magnitude. This object is probably a contact binary. By correcting for the effects of projection, it is estimated that the fraction of contact binaries in the Kuiper Belt is at least $\sim$10% to 20% with the true fraction probably much higher. Two objects, 1996 TO_{66} and 1995 SM_{55} may have variable amplitude lightcurves which may result from complex rotation, a satellite or cometary effects.

• Phase darkening coefficients for 13 Kuiper Belt objects in the 0 to 2 degree phase angle range were measured. The measured values show steep linear slopes indicating backscatter from low albedo porous surface materials. The similarity of the slopes of the phase functions of all KBOs in our sample suggests comparative uniformity of the surface compositions, physical states, and albedos. The measured phase slopes are all distinct from that of Pluto, which has a much higher albedo surface due to frosts deposited from its tenuous atmosphere.

Future observations on smaller KBOs would be beneficial to determine if their rotation periods and amplitudes are similar to the larger objects described in this thesis. A transition between gravitational to mechanical structural domination should be observed for objects with radii between 50 and 100 km. The smaller objects ($r < 50$ km) should show a significantly different distribution of rotation periods and amplitudes than the larger objects ($r > 100$ km). KBOs with radii smaller than about 50 km are probably just collisional shards with shapes and rotations presumably set by the partitioning of kinetic energy delivered by the projectile responsible for break-up. Unlike the larger KBOs their rotation states are much more influenced from recent collisional events. These smaller KBOs would be much

fainter than the larger objects and thus would require a number of nights on large class telescopes ($6 - 10$ meters) to obtain the signal-to-noise needed to detect their lightcurves.

Part II

Outer Planetary Satellites

Chapter 8

Irregular Satellite Introduction

8.1 Overview of Planetary Satellites

Satellites are stable in the region callled the Hill sphere in which the planet, rather than the sun, dominates the motion of the object (Henon 1970). The Hill sphere radius of a planet is defined as

$$r_H = a_p \left[\frac{m_p}{3M_\odot} \right]^{1/3} \tag{8.1}$$

where a_p and m_p are the semi-major axis and mass of the planet and $M_\odot$ is the mass of the sun. Table 8.1 shows the sizes of each giant planet's Hill sphere as seen from the Earth at opposition.

Most planetary satellites can be classified into one of two categories: regular or irregular (Kuiper (1956); Peale (1999)).

The regular satellites are within about $0.05 r_H$ and have nearly circular, prograde orbits with low inclinations near the equator of the planet. These satellites are thought to have formed around their respective planets through circumplanetary accretion, similar to how the planets formed in the circumstellar disk around the sun. The regular satellites can be subdivided into two types: classical regulars and collisional shards (Burns (1986a)).

The classical regular satellites are large (several hundred to thousands of kilometers in size) and have evenly spaced orbits. The regular collisional shards are small (less than

Table 8.1. Irregular Satellites of the Giant Planets

Planet	Irr[a] (#)	Groups[b] (#)	r_{min}[c] (km)	a_{crit}[d]	r_H[e] (deg)	A_H[f] (deg^2)
Jupiter	53	6	1.5	0.044	4.7	70
Saturn	14	4-5	4	0.038	3.0	28
Uranus	9	2-3	7	0.019	1.5	7
Neptune	7	3-4	16	0.025	1.5	7

[a]Number of known irregular satellites.

[b]Number of known dynamical groups.

[c]Probable completion radii of observations for irregulars for each planet to date.

[d]Critical semi-major axis in Hill radii. Satellites with semi-major axes larger than this are defined as irregular because their orbits are significantly perturbed by the Sun.

[e]Hill radius of planet.

[f]Hill area of each planet as seen from Earth at opposition.

a few hundred kilometers) and are believed to have once been larger satellites but have been shattered or tidally disrupted over their lifetimes. These shards are usually very near the planet where tidal forces and meteor fluxes are very high. Many collisional shards are associated with known planetary rings.

In contrast, the irregular satellites have semi-major axes $> 0.05 r_H$ with apocenters up to $0.65 r_H$ (Figure 8.1). Irregular satellites have eccentric orbits that are usually highly inclined and distant from the planet. They can have both prograde and retrograde orbits. The irregular satellites can not have formed in their current locations but are likely the product of early capture from heliocentric orbits (Greenberg 1976).

Orbital characteristics displaying strong capture signatures instead of in situ formation around the planet is often used to define an irregular satellite. Throughout this work we will use a more strict definition. We follow others and define irregular satellites as those satellites which are far enough from their parent planet that the precession of their orbital

plane is primarily controlled by the sun instead of the planet's oblateness. In other words, the satellite's inclination is fixed relative to the planet's orbit plane instead of the planet's equator. In practice this means any satellite with a semi-major axis more distant than the critical semi-major axis (Burns (1986b)), $a_{\text{crit}} \sim (2J_2 r_p^2 a_p^3 m_p / M_\odot)^{1/5}$, is an irregular satellite (Table 8.1). Here J_2 is the planet's second gravitational harmonic coefficient and r_p is the planet's equatorial radius. Figures 8.1 and 8.2 show the orbital characteristics of the known irregular satellites. In these figures all known regular satellites would fall very near the origin.

Almost all known planetary satellites fall into one of the three types mentioned above. A few exceptions do exist. The formation of the Earth's Moon is best explained through a collision between a Mars sized body and the young Earth (Canup & Asphaug 2001). Mars' two small satellites Phobos and Deimos resemble regular collisional shards, but some have suggested that they may be captured bodies similar to the irregular satellites of the giant planets (Burns 1992). Both Neptune's Triton and Saturn's Iapetus have at times been considered irregular satellites. These two objects stand out because both Triton and Iapetus are about ten times larger than any other known irregular satellite. Triton has all the characteristics of a regular satellite except that its orbit is retrograde. The best explanation for a retrograde orbit is through capture. Iapetus also has all the characteristics of a regular satellite but its inclination of 7 degrees is significantly larger than any other known regular satellite. Even so, this inclination is not as high as the vast majority of irregular satellites. Iapetus' relatively large inclination is probably because it is the most distant regular satellite of Saturn. At this distance the circumSaturnian nebula was probably of low density which dissipated quickly. These factors would have significantly slowed or stopped the process of orbital evolution.

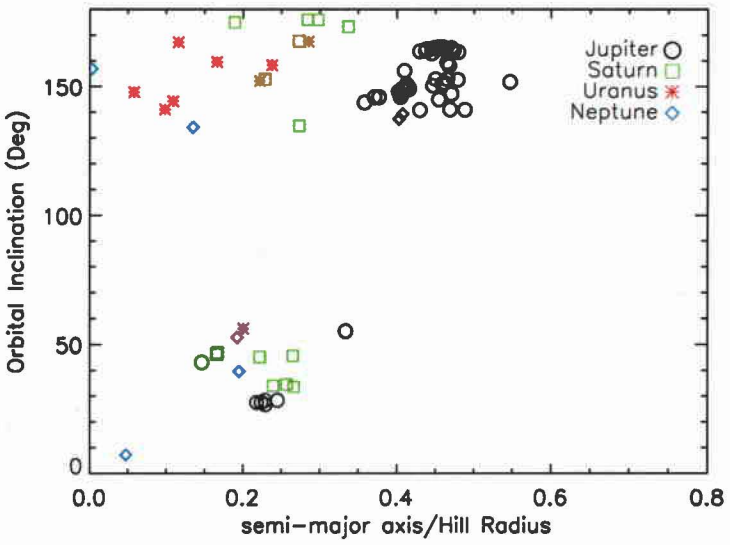

Figure 8.1 Known irregular satellites of the giant planets. The horizontal axis is the ratio of the satellites semi-major axis to the respective planet's Hill radius. The vertical axis is the inclination of the satellite to the equator of its planet. All 53 known regular satellites would fall near the origin of this plot

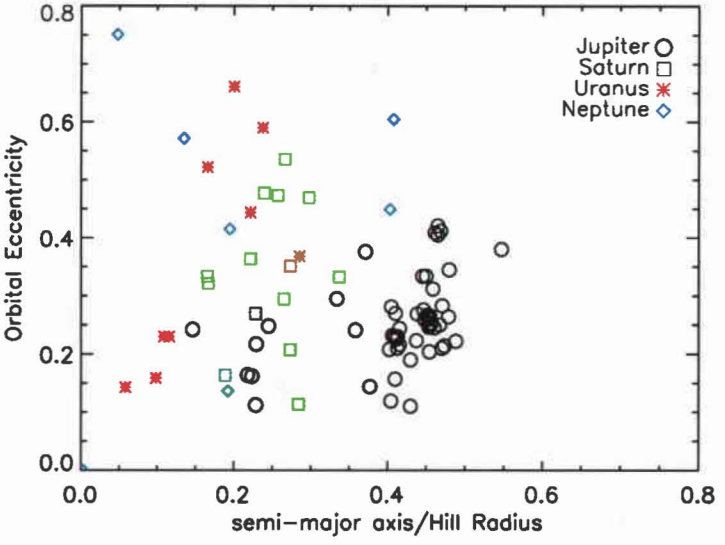

Figure 8.2 Known irregular satellites of the giant planets. The horizontal axis is the ratio of the satellites semi-major axis to the respective planet's Hill radius. The vertical axis is the orbital eccentricity. Again, all 53 known regular satellites would fall near the origin of this plot, where Triton is located.

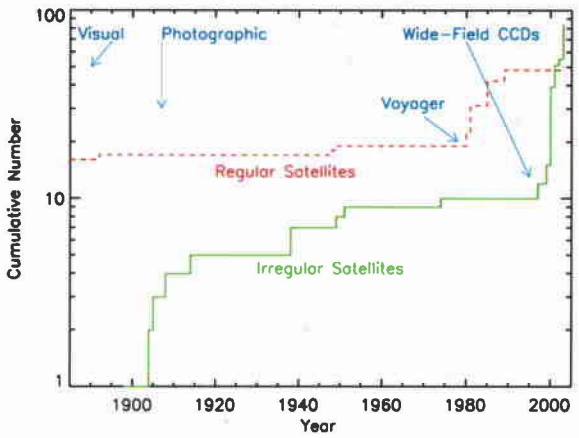

Figure 8.3 The number of irregular and regular satellites discovered since the late 1800's. Key technological advances which resulted in a jump in discoveries are listed.

8.2 Irregular Satellite Discovery

Irregular satellite discovery requires large fields of view because of the large planetary Hill spheres. Sensitivity is needed because the majority of irregular satellites are small (radii < 50 km) and therefore faint. With the use of large field-of-view photographic plates around the end of the 1800's the first distinctive irregular satellites were discovered (Figure 8.3). In 1898 the largest irregular satellite of Saturn, Phoebe (radius ~ 60 km), was discovered and in 1904 the largest irregular of Jupiter, Himalia (radius ~ 92 km), was discovered (see Kuiper 1961 for a review of early photographic surveys).

Until 1997 the last discovered irregular satellite was in 1975 on photographic plates (Kowal 1975). Since 1997 seventy-four irregular satellites have been discovered around the giant planets (Gladman et al. 1998; Gladman et al. 2000; Gladman et al. 2001; Sheppard & Jewitt 2003). Jupiter's retinue of irregular satellites has increased from 8 to 55, Saturn's from 1 to 14, Uranus' from 0 to 9 and Neptune's from 1 to 6 (or seven if including Triton). Table 8.1 shows information about the current irregular satellite systems around the giant planets.

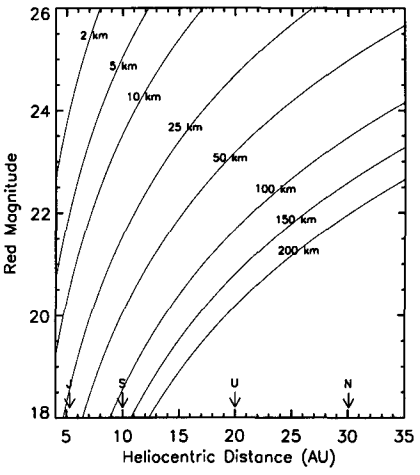

Figure 8.4 The distances of the planets versus the observable small body population diameter for a given red magnitude assuming a low albedo. Jupiter's closer proximity allows us to probe the smallest satellites.

The number of known irregular satellites (83 as of May 2004) have recently surpassed the number of known regular satellites (Figure 8.3). The main reason is new technology. The recent development of sensitive, large scale CCD detectors has allowed these faint outer planetary satellites to be discovered (Table 8.2). Because of the proximity of Jupiter (Figure 8.4), it is currently the best characterized (Sheppard and Jewitt 2003).

8.3 Capture of Irregular Satellites

Only the four giant planets have known irregular satellite populations (Figure 8.1). The likely reason is that the capture process requires something that the terrestrial planets did not have. Capture of a heliocentric orbiting object is likely only if the object approaches the planet near its Lagrangian points and has an orbital velocity within about 1% that of the

Table 8.2. Wide-Field CCD Detectors

Telescope	Camera	FOV[a]	m_R[b]
UH 2.2m	8k	0.20	23
CFHT 3.6m	12k	0.25	24
CFHT 3.6m	MegaCam	1.0	24
Subaru 8.2m	SuprimeCam	0.25	26

[a]Field-of-View of the CCD detector in square degrees.

[b]Approximate red limiting magnitude in a nominal 5 minute integration.

planet. Objects may temporarily orbit a planet (i.e. Shoemaker-Levy 9) but because of the reversibility of Newton's equations of motion some form of energy dissipation is required to permanently capture a body. Without dissipation the object will be lost in less than a few hundred years (Everhart 1973; Heppenheimer 1977). In the present epoch a planet has no known efficient mechanism to permanently capture satellites (Figure 8.5).

Kuiper (1956) first suggested that the irregular satellites were originally regular satellites which escaped from the planet's Hill sphere to heliocentric orbit because of the decreasing mass of the planet. These "lost" satellites would have similar orbits as the parent planet. Eventually the satellite would pass near the planet and be slowed down from the mass escaping from the planet. The satellite would thus be captured in an "irregular" type orbit. It is now believed that the gas giant planets never lost significant amounts of mass and thus irregular satellites are unlikely to be escaped regular satellites.

The dissipation of energy through tidal interactions between the planet and irregular satellites is not significant for such small objects at such large distances (Pollack et al. 1976). The creation of irregular satellites from explosions of the outer portions of the massive ice envelopes of the large regular satellites from saturation by electrolysis seems unlikely and no observational evidence supports such explosions on the regular satellites (Agafonova & Drobyshevski 1984).

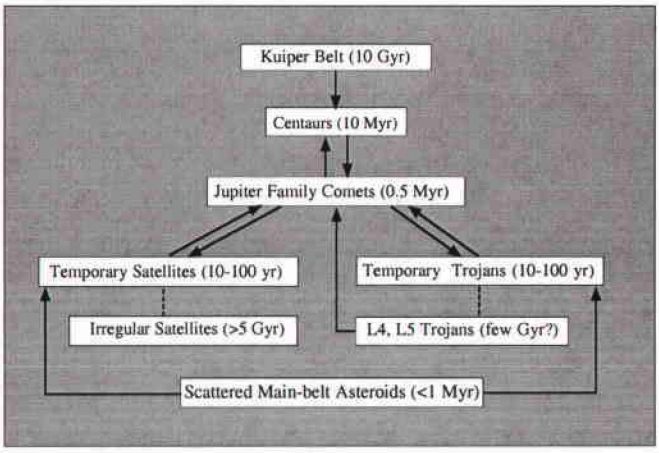

Figure 8.5 Interrelations among the small body populations in the solar system. Solid arrows denote established dynamical pathways. Dashed lines show pathways which currently have no known energy dissipation source and thus can not lead to permanent capture but only temporary capture. During the planet formation epoch such pathways may have existed. Numbers in parentheses indicate the approximate dynamical lifetimes of the different populations. (Figure from Jewitt, Sheppard and Porco (2004))

Three viable mechanisms have been proposed for irregular satellite capture. Satellite capture could have occurred efficiently towards the end of the planet formation epoch due to gas drag from an extended planetary atmosphere (Kuiper 1956; Pollack, Burns & Tauber 1979), the enlargement of the Hill sphere caused by the planet's mass growth (Heppenheimer & Porco 1977) and/or higher collision probabilities with nearby small bodies (Colombo & Franklin 1971). Below we discuss each of these in more detail.

During early planet formation the giant planets likely had primordial circumplanetary nebulae (Pollack et al. 1979; Cuk & Burns 2003). An object passing through this gas and dust near a planet would have experienced gas drag. In order to significantly slow an object for capture it would need to encounter about its own mass within the nebula. Conditions at the distances of the irregular satellites are unknown, but rough estimates suggest that if the object was larger than a few hundred kilometers it would have not have been significantly affected. If the object was very small it would have been highly slowed and would have spiraled into the planet. If the object was just the right size (a few km to a few hundred kilometers) is would have experienced just enough gas drag to be captured (Pollack et al. 1979). Hydrodynamical collapse of the primordial planetary nebula would have to occur within a few thousand years of capture in order for the satellites to not experience significant orbital evolution and eventually spiral into the planet from gas drag. In this scenario the current irregular satellites are only the last few captured bodies which did not have time to spiral into the planet. Retrograde objects would have experienced larger gas drag during their time within the nebula and thus their orbits should be more modified toward smaller eccentricities, inclinations and semi-major axes. Observations currently show that both the progrades and retrogrades have similar modification. Gas drag would also allow for larger objects to be captured closer to the planet since the nebula would be more dense there. In the action of gas drag smaller irregular satellites should have their orbits evolve faster and should have been preferentially removed.

Another way an object can become permanently captured is if Jupiter's mass increased or the Sun's mass decreased while the object was temporarily captured (Heppenheimer

& Porco 1977). Either of these scenarios would cause the Hill sphere of the planet to increase making it impossible for the object to escape with its current energy. Again, the enlargement of the Hill sphere would have to happen over a short timescale. Likely mass changes of the Sun or Jupiter would need to be greater than about 40% over a few thousand years (Pollack et al. 1976). The Hill sphere of the planet would also increase if the planet migrated significantly away from the sun (Brunini 1995). This mechanism is not a likely cause of permanent capture because the large migrations required to make temporary capture permanent within a few thousand years would severely disrupt any satellite systems (Beauge et al. 2002).

Finally, a third identified mechanism of capture could be from the collision or collisionless interaction of two small bodies within the Hill sphere of Jupiter (Colombo & Franklin; Tsui 2000). This could occur as asteroid-asteroid or asteroid-satellite encounters. These encounters could dissipate the required amount of energy from one or both of the objects for permanent capture.

8.4 Dynamics of Irregular Satellites

The known irregular satellites are stable over the age of the Solar System though strongly influenced by solar and planetary perturbations (Henon 1970; Carruba et al. 2002; Nesvorny et al. 2003). The perturbations are most intense when the satellite is near apoapsis. High inclination orbits have been found through numerical simulations to be unstable due to solar perturbations (Carruba et al. 2002; Nesvorny et al. 2003). Satellites with inclinations between $50° < i < 130°$ slowly have their orbits stretched making them obtain very high eccentricities. The high eccentricities are obtained in $10^7 - 10^9$ years and cause the satellite to eventually be lost from the system either through exiting the Hill sphere or colliding with a regular satellite or the planet.

A number of irregular satellites have been found to be in orbital resonances with their planet. These resonances protect the satellites from strong solar perturbations. The

two main types of resonance found to date are Kozai resonances and secular resonances. The Kozai resonance allows objects with high inclinations to be more stable (Kozai 1962; Carruba et al. 2002; Nesvorny et al. 2003). The Kozai resonance is when the pericenter of a satellite occurs near ± 90 degrees in longitude from the sun. If the pericenter is not locked near ± 90 degrees longitude but allowed to rotate from 0 to 360 degrees the satellites will slowly have their eccentricities increased from solar perturbations at the satellites apsis. A secular resonance is when the satellite approaches periapsis when the planet is near perihelion. This allows for the satellite to be nearest the planet when solar perturbations would be strongest.

The irregular satellites known or suspected of being in resonances are Jupiter's irregular satellites Sinope, Pasiphae, Euporie (S/2001 J10), S/2003 J18 and S/2003 J20 and Saturn's irregular satellites S/2000 S3, S/2000 S5 and S/2000 S6 (Saha & Tremaine 1993; Whipple & Shelus 1993; Nesvorny et al. 2003; R. Jacobson person communication). These resonances occupy a very small amount of orbital parameter space. The evolution of satellites into these resonances implies some sort of slow dissipation mechanism which allowed the satellites to acquire the resonances and not jump over them. This could be obtained from weak gas drag, a small increase in the planet's mass or a slow migration of the planet.

From numerical and analytical work it has been found that retrograde orbits are more stable than prograde orbits over large time-scales (Moulton 1914; Hunter 1967; Henon 1970; Hamilton & Krivov 1997). Analytically the retrogrades may be stable up to $\sim 0.7 r_H$ while prograde are only stable up to $0.5 r_H$ (Hamilton & Krivov 1997). This is consistent with known orbits of retrogrades and progrades to date. Known retrograde (prograde) irregular satellites have semi-major axes out to $\sim 0.47 r_H$ ($\sim 0.33 r_H$) and have apocenters up to $\sim 0.65 r_H$ ($\sim 0.47 r_H$).

The irregular satellites have been found to show dynamical groupings similar to families found in the main belt asteroids (Table 8.1) (Gladman et al. 2001; Sheppard & Jewitt 2003; Nesvorny et al. 2003). Each grouping was likely formed from a larger parent satellite which was disrupted into several smaller fragments. Fragmentation of the parent satellites could

be caused by impact with interplanetary projectiles (principally comets) or by collision with other satellites. Collisions with comets are improbable in the current solar system but during the heavy bombardment era nearly 4.5 billion years ago they would have been highly probable (Sheppard & Jewitt 2003). Large populations of now defunct satellites could also have been a collisional source in creating the observed satellite groupings (Nesvorny et al. 2004). No size versus orbital property correlations are seen in the groupings which suggest breakup occurred after any significant amounts of gas were left (Sheppard & Jewitt 2003).

The detection of dust in bound orbits about Jupiter in the outer Jupiter system from the Galileo spacecraft is attributed to high velocity impacts of interplanetary micrometeoroids into the atmosphereless outer satellites (Krivov et al. 2002). The micron sized dust is in prograde and retrograde orbits with a number density (10 km^{-3}) about ten times larger than in the local interplanetary medium.

8.5 Physical Properties of Irregular Satellites

Most of the space in the giant planet region of the solar system is devoid of objects which make irregular satellites one of the only dynamical clues as to what affected most of the mass in the solar system 4.5 billion years ago. Irregular satellites were likely asteroids in heliocentric orbit. They may be some of the only small bodies remaining which are still relatively near their formation locations within the giant planet region. The irregular satellite reservoirs lie between the main belt of asteroids and Kuiper Belt which makes them a key to showing us the complex transition between rocky objects in the main asteroid belt and the expected very volatile rich objects in the Kuiper Belt.

Colors of the irregular satellites are neutral to moderately red (Tholen & Zellner 1984; Luu 1991; Rettig et al. 2001; Maris 2001; Grav et al. 2003). They do not show the ultra red material found in the distant Kuiper Belt (Figure 8.6) (Jewitt et al. 2001). The colors are very similar to the C and D-type carbonaceous outer main belt asteroids (Degewij et al. 1980). Colors of the dynamical groupings are consistent with but do not prove that

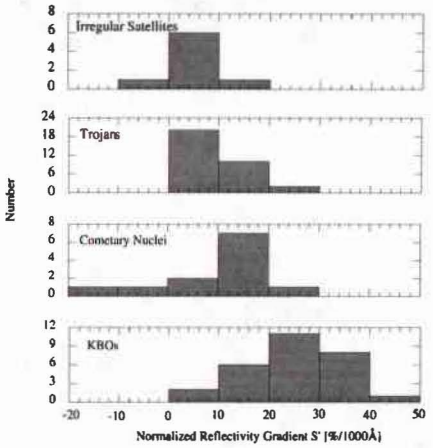

Figure 8.6 The Jupiter irregular satellites are fairly neutral which is similar to the nearby Trojan asteroids and outer main belt asteroids but remarkably different from the distant Kuiper Belt objects. (from Jewitt et al. 2004)

each group originated from a single undifferentiated parent body. Optical colors of the 8 brightest outer satellites of Jupiter show that the prograde group appears redder and more tightly clustered in color space than the retrograde irregulars (Figure 8.7) (Rettig et al. 2002; Grav et al. 2003). Near-infrared colors recently obtained of the brighter satellites agree with this scenario and that the Jupiter irregular's colors are consistent with D and C-type asteroids (Sykes et al. 2000).

Near-Infrared and optical spectra of the brightest Jupiter satellites are mostly featureless (Luu 1991; Brown 2000; Jarvis et al. 2000; Brown 2002; Geballe et al. 2002). Jarvis et al. (2000) finds a possible 0.7 micron absorption feature in Jupiter's Himalia and attributes this to oxidized iron in phyllosilicates which is typically produced by aqueous alteration. The spectra of Jupiter's irregular satellites are consistent with C-type asteroids. The largest

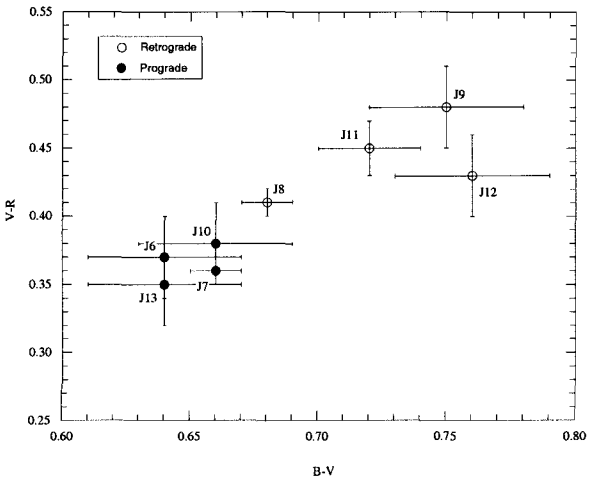

Figure 8.7 The dynamical groups of Jupiter appear to have similar colors strengthing the case that each was formed from a single parent object. (modified from Rettig et al. 2001)

Saturn irregular, Phoebe, has been found to have water ice (Owen et al. 1999) as has the large Neptune irregular satellite Nereid (Brown, Koresko & Blake 1998).

Jupiter's irregular satellites have very low albedos of about 0.04, consistent with dark C and D-type Carbon rich asteroids in the outer main belt (Cruikshank 1977). Phoebe was found to have an albedo of 0.07 from Voyager data (Simonellil et al. 1999). This albedo is similar to albedos found in the Kuiper Belt (Jewitt et al. 2001). Nereid was found to have an albedo of about 0.16 from Voyager data (Thomas et al. 1991).

The first resolved image of a Jupiter irregular satellite was obtained from the Cassini spacecraft. Himalia was shown to be an elongated shaped object with axes of 150 x 120 km and an albedo of about 0.05 (Porco et al. 2003). Cassini obtained a mostly featureless near-infrared spectrum of Jupiter's JVI Himalia (Brown et al. 2004).

8.6 Giant Planet Formation

Irregular satellites are believed to have been captured during the formation of the giant planets. Thus their dynamical and physical properties are valuable clues as to what

happened during the planet formation process. Because of the massive hydrogen and helium envelopes of the gas giants Jupiter and Saturn, they presumably formed quickly in the solar nebula before the gas had time to significantly dissipate. The less massive deficient in hydrogen and helium ice giants Uranus and Neptune appear to have taken a drastically different route of evolution.

There are two main models for giant planet formation. The standard model of core accretion assumes the cores of the giant planets were formed through oligarchic growth for about 10^6 to 10^8 years. Once they obtained a core of about ten Earth masses they quickly accreted their massive gaseous envelopes (Pollack et al. 1996). The disadvantage of this model is that the protoplanetary disk likely dissipated within a few million years while the core accretion model requires long timescales to form the planets. Because of the lower surface density and larger collisional timescales for more distant planets the core accretion model can not adequately form Uranus and Neptune in the age of the solar system.

The second giant planet formation mechanism is through disk instabilities. This model suggests parts of the solar nebula became unstable to gravitational collapse (Boss 2001). In this model the planets would form on timescales of only about 10^4 years. The disadvantages are it doesn't allow for massive cores and does not appear to be applicable to the small masses of Uranus and Neptune.

Both giant planet formation models have trouble forming Uranus and Neptune (Bodenheimer & Pollack 1986; Pollack et al. 1996). Any theory on the different formation scenarios of Uranus and Neptune to that of Jupiter and Saturn should take into account the irregular satellite systems of each. The recent theory that Uranus and Neptune lost their hydrogen and helium envelopes by photoevaporation from nearby OB stars (Boss, Wetherill, & Haghighipour 2002) would have caused all their irregular satellites to be lost because of the significant decrease in the planet's mass (Sheppard and Jewitt (2003); Jewitt et al. (2004)). Another recent theory is that Uranus and Neptune formed in the Jupiter-Saturn region with subsequent scattering to their current locations (Thommes, Duncan, & Levison

2002). Any large migration by the planets would have disrupted any outer satellite orbits (Beauge et al. 2002).

Because of the existence of the irregular satellites we know that objects in the solar nebula had time to grow to at least a few hundred kilometers before planet formation ended. What are the irregular satellite systems like around each of the giant planets? Are they similar or do they show unique differences in their dynamical and physical properties?

8.7 This Thesis: Part 2

The second part of this thesis consists of chapters 8 to 12 and details surveys for irregular satellites of the planets Mars, Jupiter, Saturn, Uranus and Neptune. The practical aims of the surveys are to determine the size distribution, orbital characteristics and population density of each planet's outer satellites. This will allow each planet to be compared and contrasted to determine similarities and differences in the characteristics of their outer satellite systems and give us insight into the planet formation process.

Below are listed the following chapters in part 2 of the thesis and a few words describing each. These chapters are composed of published or papers in preparation and thus they are each independent chapters.

• Chapter 9: "An Abundant Population of Small Irregular Satellites Around Jupiter" by S. Sheppard and D. Jewitt, Nature, 423, 261.

This paper presents the results of surveys around Jupiter in 2000 with the University of Hawaii 2.2 meter and in 2001 with the CFHT for satellites of Jupiter. In total 23 new satellites were discovered. Jupiter was found to have at least five distinct dynamical irregular satellite groups. Jupiter is also found to have a very similar irregular satellite system as the other giant planets independent of their mass or possible formation mechanisms.

• Chapter 10: "A Search for Outer Irregular Satellites of Mars: Limits to Completeness" by S. Sheppard, D. Jewitt and J. Kleyna, to be submitted to Icarus

This paper presents the results of a survey around Mars in 2003 with the CFHT for outer satellites of Mars. No new satellites were discovered, which shows Mars appears to have no outer satellites. Either Mars was unable to capture outer irregular satellites or these bodies are unstable during the age to the solar system.

• Chapter 11: "Ultra Deep Survey for Small Irregular Satellites of Uranus: Limits to Completeness" by S. Sheppard, D. Jewitt and J. Kleyna, to be submitted to AJ.

In this paper we present the results of a survey of Uranus' Hill sphere to a red limiting magnitude of 26.1. We discovered two new outer satellites of Uranus including the first irregular prograde. We compare the Uranus satellite system to that of Jupiter and find both have statistically the same irregular satellite size distributions, population densities and orbital characteristics independent of their mass or formation scenario.

• Chapter 12: "Satellite Summary and Future"

Chapter 9

An Abundant Population of Irregular Satellites Around Jupiter

9.1 Introduction

Irregular satellites have eccentric orbits that can be highly inclined or even retrograde relative to the equatorial planes of their planets. These objects cannot have formed by circumplanetary accretion as did the regular satellites which follow uninclined, nearly circular, prograde orbits (Peale (1999)). Instead, they are likely products of early capture from heliocentric orbit (Kuiper (1956); Colombo & Franklin (1971); Heppenheimer & Porco (1977); Pollack et al. (1979)). While the mechanism of capture remains uncertain, the study of the irregular satellites provides a unique window on processes operating in the young solar system. Recent discoveries around Saturn (12 new satellites) (Gladman et al. (2001)), Uranus (6) (Gladman et al. (2000)), and Neptune (3) (Holman et al. (2003)) show that the gas giant planets all have very similar irregular satellite systems. Jupiter's proximity allows us to probe the fainter, smaller irregular satellites. Here we report the discovery of 23 new irregular satellites of Jupiter, an increase in the known population from 9 to 32. Five distinct dynamical groups are found, each dominated by a relatively large satellite. The satellite groups were most likely produced by collisional shattering of precursor objects after capture by Jupiter.

9.2 Analysis

Starting with JVI Himalia in 1904 most 20th Century discoveries of planetary satellites were made using photographic plates. The recent development of more sensitive, large scale charge-coupled device (CCD) detectors has refreshed the subject by enabling a new wave of satellite discovery. We have begun a systematic survey designed to assess the properties of the Jupiter satellite population. Bound satellites are confined to the region of gravitational influence of Jupiter, known as the Hill Sphere. The Hill sphere radius is

$$r_H = a_J \left[\frac{m_J}{3M_\odot} \right]^{1/3} \tag{9.1}$$

where a_J and m_J are the semi-major axis and mass of Jupiter and $M_\odot$ is the mass of the sun. With $a_J \sim 5$ AU and $m_J/M_\odot \sim 10^{-3}$, Jupiter's Hill radius is $r_H \sim 0.35$ AU ($\approx$ 740 Jupiter Radii) corresponding to a circle of radius 4.7 deg in the plane of the sky, when viewed at opposition (area $\approx$ 70 square degrees). Jupiter's Hill sphere as seen in the plane of the sky is 2.5 times the size of Saturn's and 10 times the size of Uranus's and Neptune's. We surveyed the region around Jupiter from about 0.15 to 4.5 degrees ($0.03 \leq \frac{r}{r_H} \leq 0.95$), eventually finding 23 new satellites (Sheppard et al. (2001); Sheppard et al. (2002)) (Figure 9.1 and Table 9.1). Follow-up astrometry over periods of months was used to confirm association with Jupiter, making use of orbit fitting calculations by Brian Marsden (CFA) and Robert Jacobson (JPL). Satellites in retrograde orbits have semi-major axes that are all less than $0.47r_H$ ($0.27r_H$ for the progrades) as is true for all known irregular satellites (Gladman et al. (2001)). Some Jupiter satellites currently have apojoves up to $0.65r_H$. Twenty-three new Jupiter irregular satellites (S/2003 J1 to 23; $r \sim 1-2$ km) were discovered at the time of writing in early 2003 (Sheppard et al. (2003a)). With the exception of S/2003 J20, the new satellites fall into the retrograde dynamical groupings described in this paper. S/2003 J20 has a prograde orbit unlike any other known satellite ($a \sim 17,100,000$ km ($0.33r_H$), $i \sim 55$ degree, $r \sim 1.5$ km). These new discoveries appear to strengthen the results described in this paper but have uncertain orbital elements and will

not be discussed further here. However, it appears there are many more small retrograde satellites compared to small prograde satellites. If true this may point to different histories for the prograde and retrograde satellites.

At present it is practically impossible for Jupiter to capture satellites permanently since no efficient dissipation mechanism exists (Kuiper (1956)). Satellite capture could have occurred more easily towards the end of Jupiter's formation epoch due to gas drag from an extended Jupiter atmosphere, the enlargement of the Hill sphere caused by the planet's mass growth and/or higher collision probabilities with nearby small bodies (Colombo & Franklin (1971); Heppenheimer & Porco (1977); Pollack et al. (1979)). If so, satellite capture occurred on the same (short but uncertain) timescale as Jupiter's growth, probably in the range 10^4 to 10^7 yr(Pollack et al. (1996); Boss et al. (2002)). The known irregular satellites are stable over the age of the Solar System though strongly influenced by solar and planetary perturbations (Carruba et al. (2002)).

The sizes of the new satellites can be estimated assuming geometric albedos of 4%, as measured for satellites Himalia and Elara (Cruikshank (1977)). We calculate radii (r) from about 1 to 4 kilometers (Table 9.1). Earlier observations appeared to show that the irregular satellites followed a very shallow size distribution (Gehrels (1977)) with $q \sim 2$, where $n(r)dr \propto r^{-q}dr$ is the differential power-law radius distribution with $n(r)dr$ the number of satellites with radii in the range r to $r + dr$. Our observations suggest that the distribution is not well described by a single power law. We confirm $q \sim 2$ for the larger satellites ($r > 10$ km) but find a steeper slope ($q \geq 3.5$) for those with $r < 4$ km. There is a strong flattening in the size distribution between radii of 10 and 4 km ($19 \leq m_R \leq 21.5$). For comparison many asteroid families have $q \geq 4$ (Tanga et al. (1999)), collisional equilibrium gives $q \sim 3.5$ (Dohnanyi (1969)), while nonfamily asteroids show $q \sim 2.0$ to 2.5 (Cellino et al. (1991)). A few large satellites are accompanied by many smaller ones ($r < 4$ km), the latter having a size distribution similar to that of the main-belt asteroid families. By extrapolation, we estimate that, within a factor of two, Jupiter possesses approximately 100

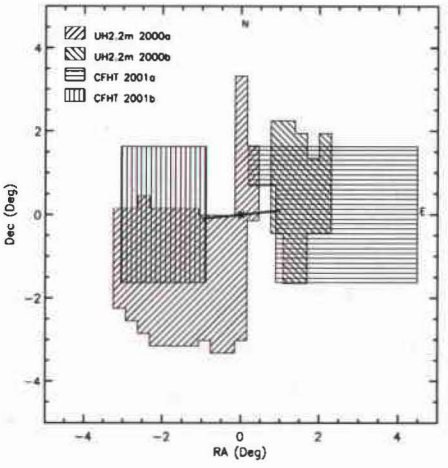

Figure 9.1 The area searched around Jupiter for satellites. Satellites were identified by their characteristic, Jupiter-like proper motions. We used the University of Hawaii 2.2 meter telescope with its 8k CCD camera ($18'.4 \times 18'.4 \approx 0.094$ square degree field-of-view) during late November 2000 and found 10 new satellites (S/2000 J1 - S/2000 J10) (Sheppard et al. (2001)). In mid December 2001 we used the Canada-France-Hawaii 3.6 meter telescope with the facility 12k CCD camera ($43' \times 28' \approx 0.33$ square degrees) and discovered eleven new satellites (S/2001 J1 - S/2001 J11) (Sheppard et al. (2002)). An additional two satellites were discovered in the survey fields during follow-up observations, for a total of 23 new satellites. The dark black line shows the orientation of the ecliptic during the observations. All the search fields of 2000 were examined both by visual blinking and a computer algorithm written by Eugene Magnier. For the 2001 fields we used a computer program written by Jan Kleyna along with visual blinking to find the satellites. A measure of completeness of our survey is provided by our serendipitous detections of previously known satellites. We detected all 6 of the then known 9 irregular satellites of Jupiter that were in our fields in November 2000. In December 2001 we detected 12 of the 15 irregulars predicted to lie within the survey area, with the three undetected because they were near bright stars. Because weather factors varied over the different nights we split the survey up into UH2.2m 2000a: Total area searched was 12.0 square degrees to a limiting R-magnitude of about 21.5 with 1 new satellite discovered. UH2.2m 2000b: 4.4 square degrees, $m_R \approx 22.5$, 9 new satellites. CFHT 2001a: 12.4 square degrees, $m_R \approx 23.2$, 10 new satellites. CFHT 2001b: 6.7 square degrees, $m_R \approx 22.5$, 1 new satellite. Both S/2000 J11 and S/2002 J1 were discovered while recovering other satellites and thus are not included in the above survey statistics.

irregular satellites with $r \geq 1$ km, corresponding to about 24th magnitude. We also find that the completeness limit for satellites at Jupiter is currently $r \sim 3$ km ($m_R \sim 21.5$).

9.3 Discussion

9.3.1 Dynamical Families

The mean orbital inclination and mean semi-major axis distributions show two distinct prograde groups, here named the Himalia and Themisto groups after the largest object in each (Figure 9.2). Clumping in Figure 9.2 suggests that the retrograde satellites comprise at least three groups (we denote these the Pasiphae, Ananke, and Carme groups). The absence of objects with intermediate inclinations $50° < i < 130°$ may be a result of the Kozai effect (Carruba et al. (2002)), which couples variations in inclination and eccentricity and forces highly inclined satellites to dip into the Galilean satellite region where they are removed by collisions.

Table 9.1: Physical and Orbital Properties of the Irregular Satellites*

Name	a[a] (km)	i[b] (deg)	e[c]	Period[d] (days)	mag.[e] (m_R)	D[f] (km)	Year[g]
Themisto Group	Prograde						
XVIII Themisto	7507000	43.08	0.24	130.0	21.0	8	2000
Himalia Group	Prograde						
XIII Leda	11165000	27.46	0.16	240.9	19.2	20	1974
VI Himalia	11461000	27.50	0.16	250.6	14.2	170	1904
X Lysithea	11717000	28.30	0.11	259.2	17.9	36	1938
VII Elara	11741000	26.63	0.22	259.6	16.0	86	1905
S/2000 J11	12555000	28.30	0.25	287.0	22.4	4	2000
Ananke Group	Retrograde						
S/2001 J10	19394000	145.8	0.14	553.1	23.1	2	2001
S/2001 J7	21027000	148.9	0.23	620.0	22.8	3	2001
XXII Harpalyke	21105000	148.6	0.23	623.3	22.2	4	2000
XXVII Praxidike	21147000	149.0	0.23	625.3	21.2	7	2000
S/2001 J9	21168000	146.0	0.28	623.0	23.1	2	2001
S/2001 J3	21252000	150.7	0.21	631.9	22.1	4	2001
XXIV Iocaste	21269000	149.4	0.22	631.5	21.8	5	2000
XII Ananke	21276000	148.9	0.24	610.5	18.3	28	1951
S/2001 J2	21312000	148.5	0.23	632.4	22.3	4	2001
Carme Group	Retrograde						

Table 9.1: (continued)

Name	a[a] (km)	i[b] (deg)	e[c]	Period[d] (days)	mag.[e] (m_R)	D[f] (km)	Year[g]
S/2001 J6	23029000	165.1	0.27	716.3	23.2	2	2001
S/2002 J1	23064000	163.1	0.24	715.6	22.8	3	2002
S/2001 J8	23124000	165.0	0.27	720.9	23.0	2	2001
XXI Chaldene	23179000	165.2	0.25	723.8	22.5	4	2000
XXVI Isonoe	23217000	165.2	0.25	725.5	22.5	4	2000
XXV Erinome	23279000	164.9	0.27	728.3	22.8	3	2000
XX Taygete	23360000	165.2	0.25	732.2	21.9	5	2000
XI Carme	23404000	164.9	0.25	702.3	17.1	46	1938
S/2001 J11	23547000	165.2	0.26	741.0	22.7	3	2001
XXIII Kalyke	23583000	165.2	0.25	743.0	21.8	5	2000
Pasiphae Group	Retrograde						
S/2001 J4	23219000	150.4	0.28	720.8	22.7	3	2001
VIII Pasiphae	23624000	151.4	0.41	708.0	16.6	60	1908
XIX Megaclite	23806000	152.8	0.42	752.8	21.7	6	2000
S/2001 J5	23808000	151.0	0.31	749.1	23.0	2	2001
IX Sinope	23939000	158.1	0.25	724.5	17.6	38	1914
XVII Callirrhoe	24102000	147.1	0.28	758.8	20.3	8	1999
S/2001 J1	24122000	152.4	0.32	765.1	22.0	4	2001

* Orbital data are from Robert Jacobson at JPL, fits are over a 1000 year time span.
[a] Mean semi-major axis with respect to Jupiter.
[b] Mean inclination of orbit with respect to Jupiter's equator.
[c] Mean eccentricity.
[d] Orbital period of satellite around Jupiter.
[e] Apparent red (0.65 μm wavelength) magnitude.
[f] Diameter of satellite assuming a geometric albedo of 0.04.
[g] Year of the discovery.

These dynamical groups suggest origin by the breakup of multiple parent objects. Each retrograde group contains one large object ($r > 14$ km) along with several smaller ones ($r < 4$ km). Sinope, the only other large satellite, may currently be the lone known member of a fourth group or it may be part of the Pasiphae group. In support of a collisional origin, we note that the dispersion velocities (Kessler (1981)) between members of each group are comparable to the escape velocity of the largest body ($\sim$ 30 m/s for each retrograde group). Velocity differences between objects in different groups ($>$ 200 m/s), likely from different parents, are much larger than the escape velocity from any member. Also, observations of the brightest irregulars show that the retrogrades are redder and more spectrally diverse

than the Himalia prograde group (Rettig et al. (2001)), consistent with origin of the former from breakup of four different parent objects.

The sizes of the parent bodies can be estimated by combining the volumes of the satellites within each group. We infer that the Ananke group parent body had a radius of about $r_P \approx 14$ km while the ratio of the mass in the largest fragment to the mass of the parent is $M_L/M_P \approx 0.98$. For the Carme group we find $r_P \approx 23$ km with $M_L/M_P \approx 0.99$ and for the Pasiphae group $r_P \approx 30$ with $M_L/M_P \approx 0.99$ (or 0.79 if including Sinope). For the prograde Himalia group we find $r_P \approx 89$ km with $M_L/M_P \approx 0.87$. Satellite groupings with $M_L/M_P \sim 1$ suggest collisional origin by shattering with a projectile barely above the disruption threshold. Such high mass ratios are atypical of asteroid families (Tanga et al. (1999)) though the Vesta asteroid family, with $M_L/M_P \approx 0.95$, may be similar (Thomas et al. (1997)) in suffering only minimal damage during its lifetime from relatively small impacts.

It is unlikely that the satellite groups were produced by the sole action of aerodynamic forces during capture, because self-gravity would prevent the fragments from dispersing (Pollack et al. (1979)). Additionally, gas drag acting on the fragments would produce a size-dependent sorting of the orbits within each group (Kuiper (1956); Pollack et al. (1979)). No size versus orbital property correlations are seen in the groupings in the ~1 km to ~100 km size range. For these reasons we believe that the disruptions occurred after capture and after the dissipation of the gas left over from Jupiter's formation.

Fragmentation of the parent satellites could be caused by impact with interplanetary projectiles (principally comets) or by collision with other satellites. Breakup requires that the projectile kinetic energy should exceed the gravitational binding energy of the parent. If half of the kinetic energy of the comet goes into breaking apart the target satellite (Melosh (1989)) and if the collision velocity is ~5 km/s, a target satellite with $r = 25$ km must be struck by a $r \approx 1$ km projectile in order to be disrupted. At the present epoch, the flux of Jupiter-crossing comets of this size is 10^3 to 10^4 times too small to shatter the irregular satellite parent bodies (Nakamura & Yoshikawa (1995)). However, lunar crater counts show

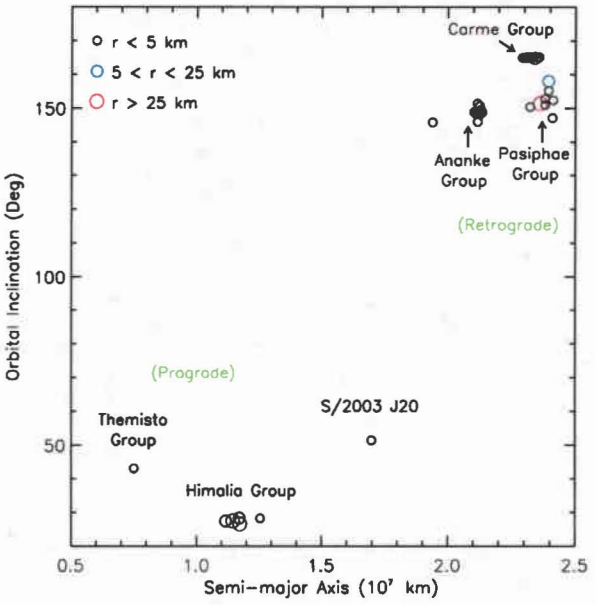

Figure 9.2 The mean semi-major axes vs. the mean inclinations of the irregular satellites of Jupiter. Five distinct clusters are evident with the Ananke, Pasiphae, and Carme retrograde groups at about 300 Jupiter radii with mean inclinations around 149, 151, and 165 degrees respectively, the Himalia (main) prograde group at about 155 Jupiter radii with inclinations near 28 degrees, and the Themisto prograde group with Themisto as the lone member at about 100 Jupiter radii and inclination of 45 degrees. In the graph, satellite symbols are plotted according to size bins. S/2001 J10 is the retrograde satellite to the left of the Ananke group. Its orbit along with Sinope's and Pasiphae's may have been modified through resonances (Saha & Tremaine (1993)). The satellites discovered in 2000 and 2001 have been observed for at least two oppositions except for the small Himalia group prograde object S/2000 J11 which has only about a month of observations.

a very rapid fall in the projectile flux in the first few 100 Myr, approaching the current steady state flux about 3.5×10^9 years ago (Hartmann et al. (2000)). The time-averaged flux of lunar impactors in the last 4.5×10^9 years is roughly 10^5 times the current flux. If applicable at Jupiter, this large initial flux would be sufficient to shatter each of the parent satellites and could explain the observed groups. Particle-in-a-box type calculations show that the timescales for collision amongst the known satellites are very long. For the retrograde satellites the timescale ($\sim 10^{11}$ years) is much larger than the age of the Solar System, while the progrades have a shorter but still long collision timescale ($\sim 10^9$ years). Thus fragmentation by collision amongst the current satellites seems unlikely. However, it is possible that Jupiter once held a much larger population of irregular satellites and that the observed groups are merely the products of disruptive, post-capture collisions amongst them.

9.3.2 Comparison to other giant planets

While Jupiter currently possesses the largest number of known satellites of any of the planets, the other gas giants also have significant irregular satellite populations. All are thought to have been captured by their respective planets (Gladman et al. (2001); Gladman et al. (2000)). In common with Jupiter, the other systems show dynamical grouping, but the satellites of more distant planets are fainter and observationally less well characterized. If Jupiter were displaced to the distances of the other giant planets we would only be able to detect about 11 of the 32 known irregular satellites at Saturn's distance, 6 at Uranus's distance, and 2 at Neptune's distance in a survey of each Hill sphere to 24th magnitude (corresponding to radii of 3.5, 18, and 40 km, respectively). In fact, Saturn has 13 known irregulars within 3 or 4 distinct dynamical groups, Uranus has 5 with 1 or 2 distinct groups, and Neptune has 2 irregulars brighter than 24th magnitude. By this measure, the four giant planets possess about the same number of irregular satellites and satellite groups with no dependence on the planet's mass. This is especially remarkable given that the ice giants

Uranus and Neptune may have had formation histories quite different from the gas giants Jupiter and Saturn (Boss et al. (2002); Thommes et al. (2002)).

Acknowledgments

We thank Yan Fernandez, Jan Kleyna, and Eugene Magnier for help with the observations, Robert Jacobson and Brian Marsden for their orbit fitting expertise. The Canada-France-Hawaii telescope is operated by the National Research Council of Canada, Le Centre National de la Recherche Scientifique de France, and the University of Hawaii. This work was supported by a grant to DJ from NASA.

Chapter 10

A Search for Outer Irregular Satellites of Mars: Limits to Completeness

10.1 Abstract

We searched the Hill sphere of Mars for outer satellites. Our search covered nearly the entire Hill Sphere, but scattered light from Mars excluded the inner few arcminutes around Mars where the satellites Phobos and Deimos reside. No new satellites of Mars were found to an apparent limiting red magnitude of 23.5, which corresponds to radii of about 0.09 km using an albedo of 0.07.

10.2 Introduction

The planets have two main types of satellite (Peale (1999)). Regular satellites have nearly circular, low inclination, prograde orbits. These satellites probably formed within a disk of gas and dust around the planet analogous to the disk from which the planets formed around the Sun. Irregular satellites have large, eccentric orbits that are usually highly inclined and even retrograde relative to the equatorial plane of their planets. These irregular satellites cannot have formed by circumplanetary accretion. Instead, they were probably captured from heliocentric orbit during the epoch of formation of the planets (Kuiper (1956); Pollack, Burns & Tauber (1979)).

Permanent satellites are confined to the region of gravitational influence, known as the Hill Sphere. The Hill sphere radius is

$$r_H = a_p \left[\frac{m_p}{3M_\odot} \right]^{1/3} \tag{10.1}$$

where a_p and m_p are the semi-major axis and mass of the planet and $M_\odot$ is the mass of the sun. From Equation 11.1 and using a mass for Mars of 0.64×10^{24} kg, the mass of the Sun as 1.98×10^{30} kg and data from Table 10.1 we find that Mars' Hill Sphere is about 0.71 degrees in radius which corresponds to about 1.6 square degrees in area as seen from the Earth during our observations.

The availability of sensitive, large scale CCD detectors has refreshed the study of irregular satellites by enabling a new wave of discovery around Jupiter (Sheppard & Jewitt (2003)), Saturn (Gladman et al. (2001)), Uranus (Gladman et al. (2000)) and Neptune (Holman et al. (2003); Sheppard et al. (2003b)). Large fields of view are needed because the Hill spheres are large. Sensitivity is needed because the majority of irregular satellites are small and therefore faint. From these new surveys it appears that the four giant planets possess about the same number of irregular satellites and groupings with no dependence on the planet's mass when comparing them to the same limiting size of satellites (Sheppard & Jewitt (2003)). For an in depth review of irregular satellites see Jewitt, Sheppard & Porco (2004).

Mars is known to have two small inner satellites, Phobos and Deimos (Hall (1878)). The origins of these satellites are still a mystery. Their orbits are not like the irregular satellites of the giant planets since they are close to Mars and have nearly zero eccentricity and inclination. Mars' satellites, from a dynamical perspective, appear to have originated around Mars not far from their current positions since it is hard to produce orbits like those of the known Martian satellites by capture. On the other hand, the physical properties of Phobos and Deimos resemble those of C-type asteroids of which most are found in the outer main belt, not near Mars. Based on their physical characteristics they may be captured

Table 10.1. Geometrical Circumstances

UT Date	R (AU)	Δ (AU)	α (deg)	RA ($''/hr$)	Dec ($''/hr$)
2003 July 5	1.403	0.536	35.68	38.1	7.2
2003 July 7	1.401	0.525	35.00	35.4	6.2

asteroids. In addition, the current orbit of Phobos is short-lived and the satellite will collide with the planet on a timescale $\sim 10^8$ yr (see Burns (1992) and references therein).

The Viking Orbiter 1 spacecraft found no new satellites of Mars larger than about 0.05 km within the orbit of Phobos (Duxbury & Ocampo (1988)). Showalter et al. (2001) used the Hubble Space Telescope (HST) to search for possible Mars dust rings created by Phobos and Deimos that have been predicted by Soter (1971). They did not detect any dust rings or unknown satellites down to about 0.1 km in diameter (assuming an albedo of 0.07) in the very inner portions of Mars space near Phobos and Deimos. The HST observations have not been published, but the small field-of-view (a few arcminutes) allowed them to observe only the very inner portion of the Hill sphere of Mars.

Only the giant planets have been found to possess abundant irregular satellites. Are the distant irregular satellites unique to the giant planets or does the outermost terrestrial planet, Mars, have them as well? Like Jupiter and Neptune, Mars has Trojan asteroids in its leading and trailing Lagrangian points which may or may not be captured in a similar way as irregular satellites (Marzari & Scholl (1998); Fleming & Hamilton (2000)). Kuiper (1961) briefly reviewed some early photographic searches for outer satellites of Mars. These surveys only reached a photographic magnitude of about 17 mag (about 1.4 km in diameter assuming an albedo of 0.05). With modern wide-field digital detectors on medium class telescopes we can now survey the space around Mars to much fainter magnitudes. We thus performed a survey to determine if Mars has any previously unknown outer satellites.

10.3 Observations

We used the Canada-France-Hawaii 3.6 meter diameter telescope atop Mauna Kea in Hawaii with the MegaCam digital CCD camera for imaging (Boulade et al. (2003)). The MegaCam has 36 separate CCDs with each having 2048×4612 (13.5μm) pixels, which at prime focus gives $0.''187$ pixel^{-1} scale. The total number of pixels is about 340 million and each image was about 710 Megabytes in size. The field-of-view is 0.96×0.94 degrees with gaps of about $13''$ between most chips (though a few have gaps of about $80''$). MegaCam uses a wide field corrector in order to produce uniform image quality across the field of view.

Images were obtained by staff observers in queue scheduling mode. An r' filter based on the Sloan Digital Sky Survey (SDSS) filter set was used. The images were bias subtracted and then flat-fielded using twilight flats. During exposures the telescope was autoguided sidereally on bright nearby stars. The seeing was about $0.''7$ during the observations. Integration times were 100 seconds on July 5 and 120 seconds on July 7. The observing geometry and characteristics of Mars at the time of observations are shown in Table 10.1.

Figure 10.1 shows the area searched around Mars for possible satellites. The entire outer Martian Hill sphere was covered on each night of UT July 5 and 7, 2003. Four fields were imaged 3 times each on both nights for a total of 24 images. On a given night, the images of each field were separated by about 13.5 minutes giving 27 minutes between the first and last images. A computer program was used to identify objects which were detected in all three images from one night and had a motion within ± 6 arcseconds per hour of Mars' motion in both Right Ascension and Declination. This motion is consistent with parallactic displacement of an object moving near Mars. There was no confusion with main belt asteroids since they tend to stay away from Mars' orbit and Mars was near perihelion during the observations.

Each night was photometric and Landolt (1992) standards were used to calibrate the data. The apparent red limiting magnitude of the survey was found by placing artificially generated objects with motions similar to Mars into the survey fields. The artificial objects

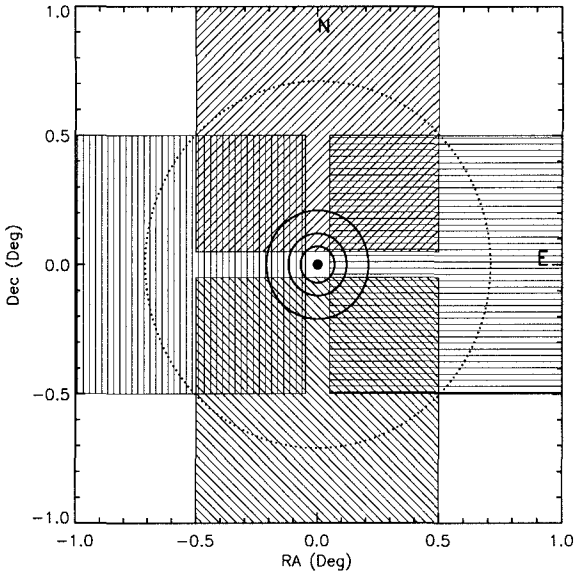

Figure 10.1 The area searched around Mars for satellites using the 3.6 m CFHT telescope. Four fields were imaged 3 times each on 2 separate nights (July 5 and 7, 2003) for a total of 24 images. The black dot at the center represents Mars' position. The dot is larger than the apparent diameter of Mars and incorporates the orbits of Phobos and Deimos. The four different hatched squares represent the four fields imaged around Mars on both nights. Overlapping hatches show where some of the fields overlapped in coverage. The dotted circle shows the Hill sphere of Mars to our line of sight. The scattered light from Mars was not a problem for most of the images but became quickly dominant very near Mars. The inner solid circles show where scattered light became significant compared to the normal sky background. At the outer solid circle near 0.20 degrees the background was 50% higher, at the middle solid circle the background was 100% higher and at the inner solid circle the background was 275% higher than the nominal sky background.

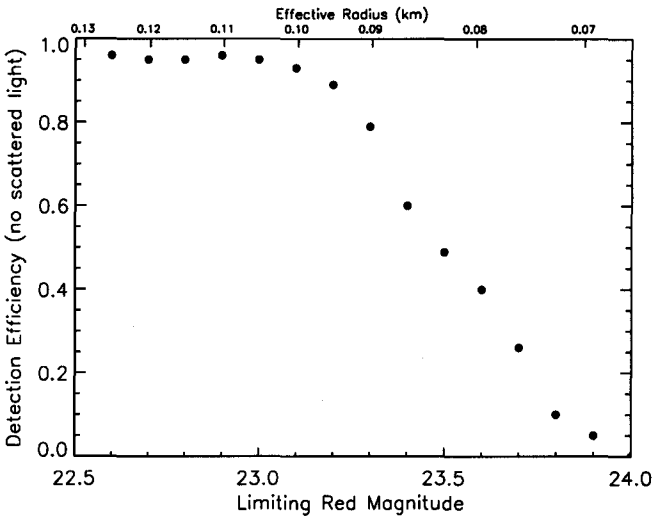

Figure 10.2 Detection efficiency of the moving object search computer program versus the apparent red magnitude. The 50% detection efficiency is at about 23.5 mags. This efficiency is for no significant scattered light in the fields. The efficiency was determined by how many artificially generated moving objects with motions similar to Mars were found by the program at a given magnitude. The calculation of the effective radius assumes an albedo of 0.07.

had a range of magnitudes and were matched to the point spread function of the images in the North-South direction (FWHM $\sim$ 0.7 arcseconds) and were elongated in the East-West direction to simulate the slight trailing any real satellites would have incurred ($\sim$ 1.1 arcseconds) during the exposure. The program found 50% of artificial moving objects in the survey fields with R-band magnitudes of 23.5 mags. Figure 10.2 shows the efficiency of the search program versus limiting red magnitude. The multiple nights of observations which would only help increase our detection rate were not factored into the efficiency.

The above results apply when no significant amount of scattered light was present. Figures 10.1 and 10.3 show the behavior of the scattered light near Mars. Scattered light was noticed up to about 20 arcminutes from Mars. Figure 10.4 shows the 50% R-band limiting magnitude of the program versus the distance from Mars.

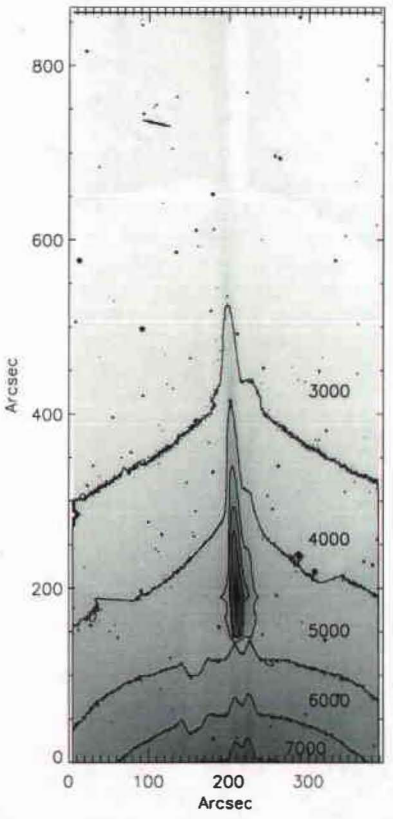

Figure 10.3 A contour plot of a survey image close to Mars to show the scattered light. The contours show 7000 : 6000 : 5000 : 4000 : 3000 surface brightness contours, where the nominal background sky level away from the planet was near 2000 counts. Mars is 3 arcminutes south from the bottom of the plotted region. The vertical spike is caused by diffraction from the telescope's support structure.

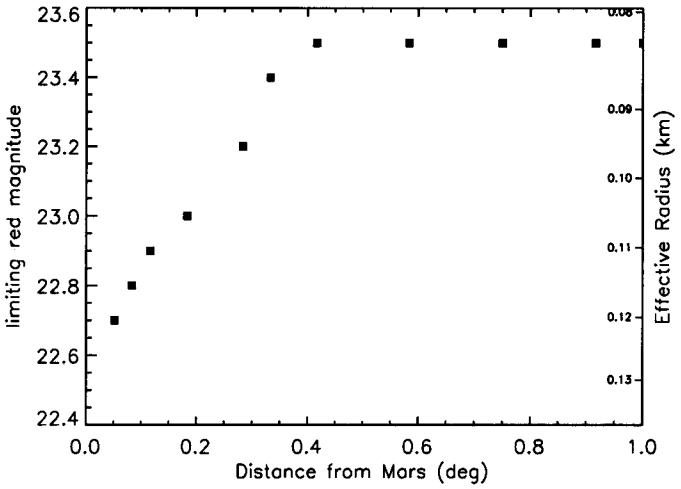

Figure 10.4 50% efficiency detection red limiting magnitude of the survey versus distance from Mars. Scattered light is only significant starting at about 15 arcminutes from Mars. The calculation of the effective radius assumes an albedo of 0.07.

10.4 Results and Discussion

We found no new satellites of Mars to limiting apparent red magnitude of 23.5 mag (Figure 10.1). In order to determine the corresponding size limit we relate the apparent red magnitude of an object, m_R, to its radius, r, through

$$r = \left[\frac{2.25 \times 10^{16} R^2 \Delta^2}{p_R \phi(\alpha)}\right]^{1/2} 10^{0.2(m_\odot - m_R)} \tag{10.2}$$

in which r is in km, R is the heliocentric distance in AU, Δ is the geocentric distance in AU, $m_\odot$ is the apparent red magnitude of the sun (-27.1), p_R is the geometric red albedo, and $\phi(\alpha)$ is the phase function in which the phase angle $\alpha = 0$ deg at opposition. For linear phase functions we use the notation $\phi(\alpha) = 10^{-0.4\beta\alpha}$, where β is the "linear" phase coefficient. If we use data from Table 10.1, a phase coefficient of $\beta = 0.05$ mags per degree and assume the albedo is 0.07 we find that an apparent magnitude of 23.5 corresponds to

objects that are about 0.09 km in radius at Mars' distance. With this kind of sensitivity we would have easily detected any Phobos ($r \sim 11$ km) or Deimos ($r \sim 6$ km) sized satellites in our fields. The survey covered 99.5% of Mars' Hill sphere. Only about the inner 3 arcminutes ($\leq 0.07 r_H$) near Mars was not covered in our survey due to scattered light from the planet.

Mars' lack of outer satellites compared to the giant planets is shown in Figure 10.5 and Table 10.2. By comparing its Hill sphere to the outer planets we would expect to find outer irregular satellites much more distant than Phobos and Deimos. Why are there no known irregular satellites around the terrestrial planets? Previous authors have found that the inner terrestrial planets Mercury and Venus probably have no satellites because of the consequence of strong Solar tides which would make them unstable (Counselman (1973); Ward & Reid (1973); Burns (1973)). The Earth and Mars are spared extreme solar tides. The Earth might have lost small outer satellites due to the presence of the large Moon (Callegari & Yokoyama (2001)).

There are two basic reasons for why Mars may have no irregular satellites. Either such objects are dynamically unstable on timescales comparable to or less than the age of the Solar System or Mars lacked any mechanism to capture irregular satellites in the first place. The proximity of Mars to the asteroid belt and Jupiter may limit distant stable orbits about Mars. The role of these perturbations on long timescales and as a function of location within Mars' Hill sphere is still yet to be fully explored. Analysis of main-belt asteroid satellite stability shows that the Sun is the dominant perturber for asteroids in the mid to inner main belt while Jovian perturbations become dominant in the outer main-belt (Chauvineau & Mignard (1990)). Extrapolation to Mars suggests that satellites may be stable for a significant portion of the Hill sphere for the age of the Solar System.

Alternatively, the deficiency of irregular satellites around Mars may arise from the difference in the formation process of Mars compared to the giant planets. Irregular satellite capture for the giant planets probably occurred towards the end of the planet's formation

Table 10.2. Irregular Satellites of the Planets

Planet	Irr[a] (#)	Groups[b] (#)	Size[c] limit (km)	Hill[d] Radii (deg)	Hill[e] Area (deg)
Mars	0	0	0.09	0.7	1.6
Jupiter	53	~ 6	1.5	4.7	70
Saturn	14	$\sim 4-5$	4	3.0	28
Uranus	9	$\sim 2-3$	8	1.4	6
Neptune	7	~ 4	17	1.5	7

[a]Number of known irregular satellites.

[b]Apparent number of dynamical groupings.

[c]Approximate limiting radii of satellite searches to date.

[d]The apparent angular Hill Sphere radius of the planet at opposition.

[e]The Hill Sphere area of a planet when at opposition.

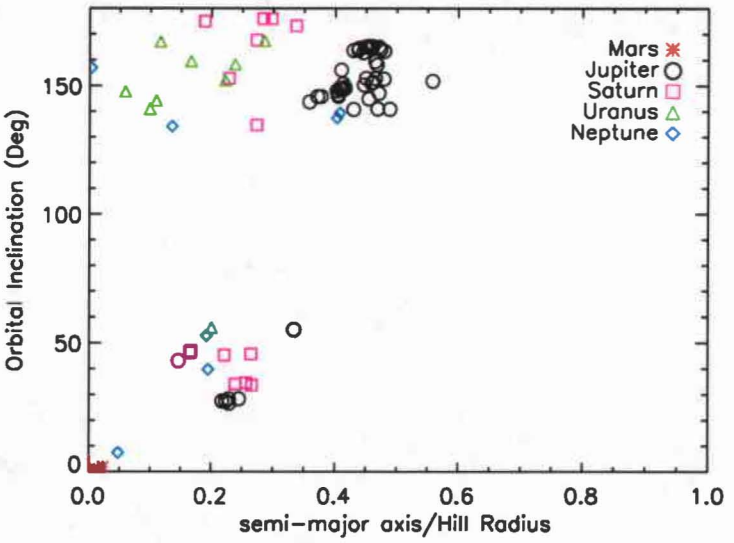

Figure 10.5 A comparison of the known irregular satellites of the giant planets with Mars' two known satellites. The horizontal axis is the ratio of the satellites semi-major axis to the respective planet's Hill radius. The vertical axis is the inclination of the satellite to the equator of its planet. Only Nereid of Neptune is close to the position of the known Martian satellites in this parameter space.

epoch where the energy dissipation needed for capture could be caused by gas drag from an extended atmosphere, the enlargement of the Hill sphere caused by the planet's mass growth and/or higher collision probabilities with nearby small bodies (Kuiper (1956); Colombo & Franklin (1971); Heppenheimer & Porco (1977); Pollack et al. (1979)). Unlike the giant planets, Mars is not expected to have gone through a significant Hill sphere enlargement from a large mass accretion event or to have had a dense extended atmosphere during formation.

10.5 Conclusions

No outer satellites of Mars larger than about 0.09 km in radius were detected in our survey which covered 99.5% of Mars' Hill sphere (from 3′ to over 0.7 degrees from the planet). The absence of outer satellites around Mars may indicate it did not have the right conditions for irregular satellite capture as did the giant planets during their formation or may show that such objects are dynamically unstable, or both.

Acknowledgments

The Canada-France-Hawaii telescope is operated by the National Research Council of Canada, Le Centre National de la Recherche Scientifique de France, and the University of Hawaii. We thank Jing Li for help on IDL contour plotting. This work was supported by a grant to DJ from NASA.

Chapter 11

Ultra Deep Survey for Small Irregular Satellites of Uranus: Limits to Completeness

11.1 Abstract

We present a deep survey of Uranus' Hill sphere for small satellites. Two new satellites of Uranus were discovered and all previously known outer satellites of the planet were detected as well as the two inner satellites Titania and Oberon. One of the newly discovered satellites (S/2003 U3) is the first known irregular prograde of the planet. Our survey covered about 3.5 square degrees and had a 50% detection efficiency at a limiting red magnitude of 26.1 mags. This magnitude corresponds to objects that are about 7 km in radius if assuming an albedo of 0.04. Though the ice giant Uranus is tilted about 98 degrees to the ecliptic, its irregular satellite population, size distribution and orbital parameters are remarkably similar to the more massive gas giant Jupiter. Both have shallow size distributions of about $q \sim 2$ for satellites with radii > 7 km with no correlations between the sizes of the satellites and their orbital parameters. Unlike Jupiter, Uranus' irregular satellites do not appear to be in distinct dynamical groups in semi-major axis and inclination phase space, though Uranus may have groupings in semi-major axis and eccentricity phase space.

11.2 Introduction

A planetary satellite system is restricted to the space in which the planet's gravitational force dominates over the sun's. This region is known as the Hill sphere where the radius, r_H, depends on the planet's mass and distance from the sun as

$$r_H = a_p \left[\frac{m_p}{3M_\odot} \right]^{1/3} \tag{11.1}$$

where a_p and m_p are the semi-major axis and mass of the planet and $M_\odot$ is the mass of the sun. Table 11.1 lists the Hill radii and areas for each of the giant planets.

The giant planets have been found to have two major types of satellite (Peale 1999). The regular satellites, are found within about $0.05r_H$ of their planet. They have nearly circular, prograde orbits with low inclinations. The regular satellites likely formed within a circumplanetary disk of gas and dust around the giant planets during the planetary formation process itself. The irregular satellites are found up to $0.65r_H$ from their host planets and have moderate to high eccentricities and inclinations with prograde or retrograde orbits. The irregular satellites can not have formed in their present orbits and are likely products of early capture from heliocentric orbit (Kuiper (1956); Pollack, Burns & Tauber (1979)). Table 11.1 shows the currently known populations of irregular satellites for each giant planet.

Orbital characteristics displaying strong capture signatures instead of in situ formation around the planet is often used to define an irregular satellite. Burns (1986) defined irregular satellites as those satellites which are far enough from their parent planet that the precession of their orbital plane is primarily controlled by the sun instead of the planet's oblateness. In other words, the satellite's inclination is fixed relative to the planet's orbit plane instead of the planet's equator. In this interpretation, any satellite with a semi-major axis more distant than the critical semi-major axis (Burns 1986), $a_{\text{crit}} \sim (2J_2 r_p^2 a_p^3 m_p / M_\odot)^{1/5}$, is an irregular satellite (Table 11.1). Here J_2 is the planet's second gravitational harmonic coefficient and r_p is the planet's equatorial radius.

Because of the reversibility of Newton's equations of motion some sort of energy dissipation is required for permanent satellite capture. The giant planets currently have no efficient mechanism of energy dissipation for satellite capture. During the planet formation epoch several mechanisms may have operated to efficiently capture satellites: 1) Gas drag from a extended primordial planetary atmosphere (Pollack, Burns & Tauber (1979)) 2) Pull-down capture from the mass growth of the planet (Heppenheimer & Porco (1977)) and 3) Collisional dissipation between asteroids and/or satellites passing near the planet (Colombo & Franklin (1971); Tsui (2000)). Study of the irregular satellites is important for insight into the planet formation process.

Current giant planet formation models from core accretion or disk instabilities have trouble forming Uranus and Neptune within the age of the solar system (Pollack et al. (1996); Boss (2001)). The massive hydrogen and helium gas giants Jupiter and Saturn likely formed quickly in the protoplanetary disk ($\leq 10^6$ years). The less massive, deficient in hydrogen and helium, more distant ice giants Uranus and Neptune appear to have taken much longer or an altogether different route of formation (Thommes et al. 2002; Boss 2002). Preliminary comparisons of the number of irregular satellites around each giant planet show they have similar irregular satellite systems (Sheppard & Jewitt 2003; Jewitt & Sheppard 2004). Any formation and evolution theories for the gas and ice giants should take into account their similar irregular satellite systems.

Uranus is unusual in the sense that its obliquity is 98 degrees. This is significantly larger than any of the other planets which have obliquities < 30 degrees. The likely cause is that near the end of Uranus' formation its core of several Earth masses collided with another protoplanet of about one Earth mass (Korycansky et al. (1990); Slattery et al. (1992)). Greenberg (1974) argued that the current regular satellites must have formed after Uranus' obliquity reached 98 degrees because their low inclination prograde orbits would not have tilted to their current configurations with Uranus. Recently Brunini et al. (2002) suggested that if Uranus' tilt was created by a giant impact any satellites beyond about 2×10^6 km (all known irregular satellites of Uranus) would have likely been lost from the orbital impulse

Table 11.1. Irregular Satellites of the Planets

Planet	Irr[a] (#)	Groups[b] (#)	$r_{\min}$[c] limit (km)	a_{crit}[d]	Hill[e] Radii (deg)	Hill[f] Area (deg)
Jupiter	53	~ 6	1.5	0.044	4.7	70
Saturn	14	$\sim 4-5$	4	0.038	3.0	28
Uranus	9	$\sim 2-3$	7	0.019	1.4	6
Neptune	7	$\sim 3-4$	16	0.025	1.5	7

[a]Number of known irregular satellites.

[b]Apparent number of dynamical groupings.

[c]Limiting radii of satellite searches to date.

[d]Critical semi-major axis in Hill radii. Satellites with semi-major axes larger than this are defined as irregular because their orbits are significantly perturbed by the Sun (Burns 1986).

[e]The apparent angular Hill Sphere radius of the planet at opposition.

[f]The Hill Sphere area of the planet when at opposition.

imparted to Uranus from the impactor. In addition, Beaugé et al. (2002) show that any significant migration by Uranus through a residual planetary disk would have caused its satellites to become unstable. Gladman et al. (1998) discovered the first distant irregular satellites of Uranus.

We wish to determine if the ice giant Uranus has a similar population of small irregular satellites as the gas giant Jupiter. Because of its proximity (Figure 11.1) Jupiter has the best studied irregular satellite system (Sheppard and Jewitt 2003). We observed the majority of Uranus' Hill sphere to very faint magnitudes to explore the very faint, small irregular satellites around Uranus. Our primary goal was to cover the dynamically stable inner Hill sphere of the planet ($\sim 0.7 r_H$ see Hamilton & Krivov (1997)).

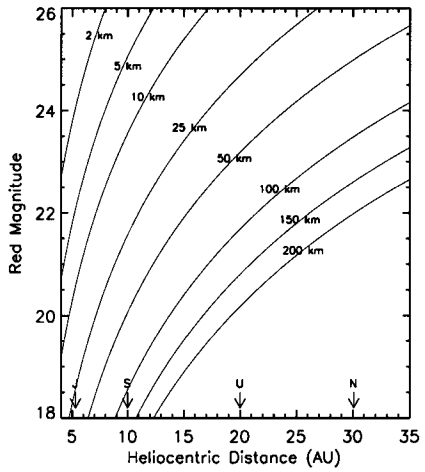

Figure 11.1 The distances of the planets versus the observable small body population diameter for a given red magnitude assuming a low albedo.

11.3 Observations

The geometry of Uranus during the survey is indicated in Table 11.2. We observed the space around Uranus for faint satellites near new moon on UT August 29 and 30, 2003 with the Subaru 8.2 meter diameter telescope atop Mauna Kea. The Suprime-Cam imager has 10 MIT/LL 2048×4096 CCDs arranged in a 5×2 pattern (Miyazaki et al. (2002)). The 15μm pixels give a scale of $0.''20$ pixel^{-1} at prime focus. The field-of-view is about $34' \times 27'$ with the North-South direction aligned with the long axis. Gaps between the chips are about $16''$ in the North-South direction and only $3''$ in the East-West direction.

Images were obtained with a Kron-Cousins R-band filter. The images were bias subtracted and then flat-fielded with dome flats. During exposures the telescope was autoguided sidereally on field stars. Seeing during the two nights varied between $0.''4$ and $0.''6$. Integration times were between 400 and 420 seconds. Both nights were photometric and Landolt (1992) standards were used for calibration.

The area searched around Uranus for satellites is shown in Figure 11.2. Fourteen fields were imaged 3 times each on one night and 2 times each on the second night for a total of 5 images per field or 70 images for the survey. On a given night, images of the same field were separated by about 31 minutes between exposures. The fields on the second night were the same distance from Uranus as the first night, but the background star fields were slightly different on the two nights because of Uranus' movement between the two nights. Approximately 3.5 square degrees around Uranus were observed not accounting for chip gaps and bright stars. We covered $\sim 90\%$ of the theoretically stable Hill sphere ($\sim 0.7 r_H$) for retrogrades and near 100% for the stable Hill sphere ($\sim 0.5 r_H$) for prograde satellites (Hamilton & Krivov 1997).

Satellite confirmation astrometry over the next few months was obtained with the Gemini Multi-Object Spectrograph (GMOS) in imaging mode on the Gemini North 8.1 meter Telescope atop Mauna Kea (Hook et al. 2002). GMOS has a $5.'5$ field of view and pixel scale of $0.''0727$ pixel^{-1}. Recoveries were obtained with an r' filter based on the

Sloan Digital Sky Survey (SDSS) filter set. Images were bias subtracted and flat-fielded using dome flats. Observations were obtained by a staff astronomer at Gemini in queue scheduling mode.

11.4 Analysis

The Subaru survey observations were obtained when Uranus was near opposition. At opposition, the apparent movement of a distant solar system object is dominated by parallactic motion. Thus the apparent motion of an object is simply related to its heliocentric distance. Objects at the heliocentric distance of Uranus, $R \sim 20$ AU, will have an apparent motion of about $\sim 6''$ hr^{-1} (~ 30 pixels per hour). At this rate objects would have trailed about the FWHM of the seeing during the 400 second exposures.

The data was analyzed to find outer solar system small bodies in two complementary ways. First a computer algorithm was used to detect objects which appeared in all three images of one night and had a motion consistent with being beyond the orbit of Jupiter (motion of 18 to 1 arcsecond per hour). Second, all the fields were examined by visually blinking them on a computer display screen for moving objects again with motions indicative of distances beyond Jupiter.

We determined the limiting magnitude of the survey when no scattered light from Uranus was present by placing artificial objects in the fields matched to the point spread function of the images with motions mimicking that of Uranus. Results are shown in Figure 11.3 for both the visual blinking and computer algorithm. Both techniques had similar results, though the visual blinking was slightly more efficient in detection. The 50% detection efficiency of the Uranus satellite survey occurred at an R-band limiting magnitude of about 26.1 magnitudes which we take as the limiting magnitude of this survey. Scattered light from Uranus was only significant within 3.5 arcminutes of the planet. Figure 11.4 shows the 50% R-band limiting magnitude efficiency as a function of distance from Uranus in

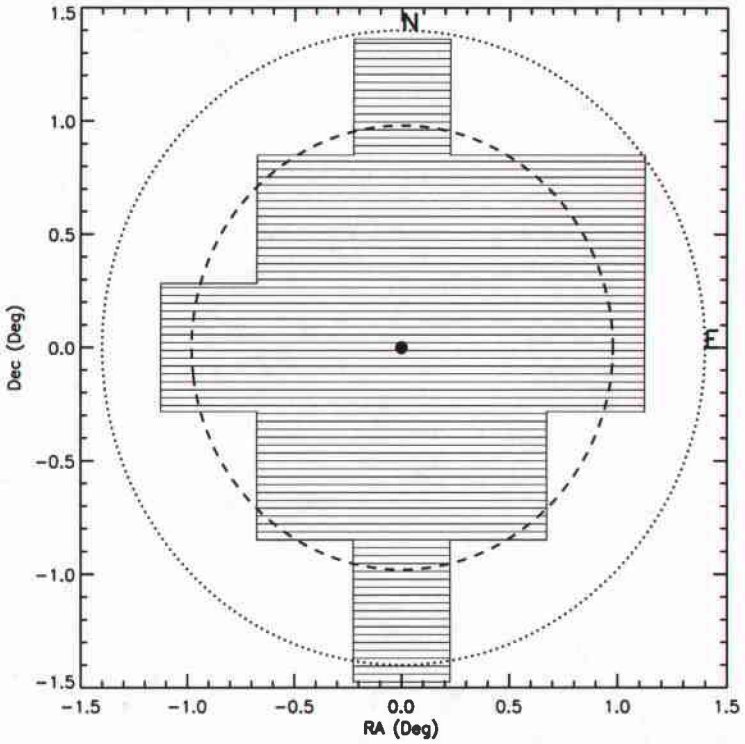

Figure 11.2 The area searched around Uranus for satellites using the 8.2m Subaru telescope. Fourteen fields were imaged 5 separate times over two nights (UT August 29 and 30, 2003) for a total of 70 images covering about 3.5 square degrees. The black dot at the center represents Uranus' position. Uranus was placed in a gap in the mosaic of CCD chips to prevent saturation. The dotted circle shows the Hill sphere of Uranus while the dashed circle shows the theoretical outer limits of stability for any Uranus satellites ($r_H \sim 0.7$).

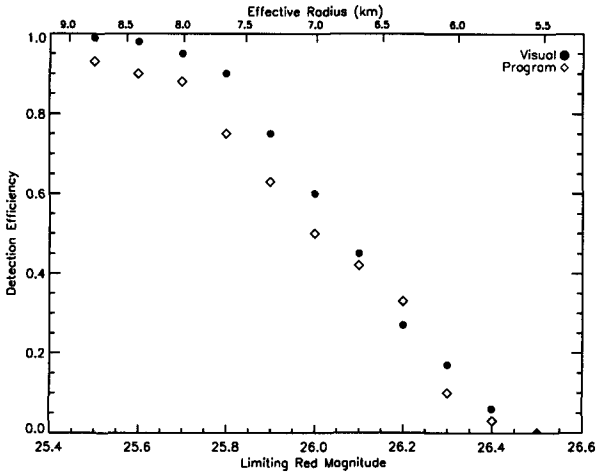

Figure 11.3 Detection efficiency of the Uranus survey versus the apparent red magnitude. The 50% detection efficiency is at about 26.1 mags from visual blinking and 26.0 mags from a computer program. All fields were searched with both techniques. The efficiency was determined by placing artificial objects matched to the Point Spread Function (PSF) of the images with motions similar to Uranus in the survey fields. Effective radii were calculated assuming the object had an albedo of 0.04. The efficiency does not account for objects which would have been undetected because of the chip gaps.

our survey. The scattered light results were determined the same as the nonscattered light technique described above.

11.5 Results and Discussion

In the survey we discovered the two new Uranus satellites S/2003 U3 and S/2001 U2 (Sheppard et al. 2003; Holman et al. 2003). We also detected, without prior knowledge of their positions, all of the then-known six irregular satellites of Uranus as well as the two outer-most regular satellites Titania and Oberon. S/2001 U2 has a 2001 designation because it was detected but not confirmed as a Uranus satellite in 2001. S/2001 U3 was confirmed as an Uranus irregular satellite after our survey (Marsden et al. 2003). The satellite was undetected in our Subaru data because it fell in a chip gap. In addition, six

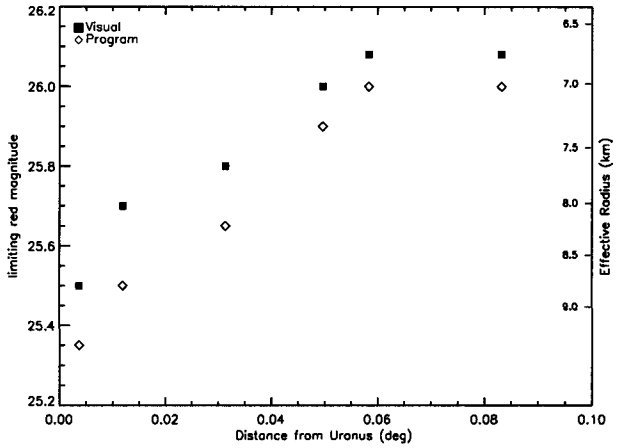

Figure 11.4 50% efficiency detection red limiting magnitude of the survey versus distance from Uranus. Scattered light is only significant starting at about 3.5 arcminutes from Uranus. The calculation of the effective radius assumes an albedo of 0.04.

other objects near Uranus which turned out to be Centaurs, as well as hundreds of Kuiper Belt objects, were discovered. A detailed report about the discovery of these other objects will be given in a future paper.

To determine the size limit of satellites detectable by the survey and the approximate sizes of the new satellites we relate the apparent red magnitude of an object, m_R, to its radius, r, through

$$r = \left[\frac{2.25 \times 10^{16} R^2 \Delta^2}{p_R \phi(\alpha)}\right]^{1/2} 10^{0.2(m_\odot - m_R)} \tag{11.2}$$

in which r is in km, R is the heliocentric distance in AU, Δ is the geocentric distance in AU, $m_\odot$ is the apparent red magnitude of the sun (-27.1), p_R is the geometric red albedo, and $\phi(\alpha)$ is the phase function in which the phase angle $\alpha = 0$ deg at opposition. For linear phase functions we use the notation $\phi(\alpha) = 10^{-0.4\beta\alpha}$, where β is the "linear" phase coefficient. Using data from Table 11.2 and an albedo of 0.04 we find that 26.1 magnitudes corresponds to a satellite with radius of about 7 km.

Table 11.2. Geometrical Circumstances

UT Date	R (AU)	Δ (AU)	α (deg)	RA[a] ($''/hr$)	Dec[b] ($''/hr$)
2003 Aug 29	20.031	19.024	0.25	-5.7	-2.1
2003 Aug 30	20.031	19.026	0.30	-5.7	-2.1

[a]The apparent Right Ascension motion of Uranus.

[b]The apparent Declination motion of Uranus.

11.5.1 Orbital Element Distribution

Table 11.3 shows some of the properties of the known irregular satellites of Uranus. Figures 11.5 and 11.6 compare the semi-major axes with inclinations and eccentricities, respectively, of Uranus' irregular satellites with other irregular satellites of the giant planets. The semi-major axes of Uranus' irregular satellites expressed in Hill radii range from about $0.05r_H$ to $0.3r_H$. They have apoapses up to $0.38r_H$ while their periapses are well outside that of the regular satellite region. The one known prograde, S/2003 U3, has a semi-major axis at about the average distance of the retrograde irregulars. Uranus has the closest known "normal" irregular satellites in terms of Hill radii (Neptune has the unusually large Triton and eccentric Nereid which are closer but Triton may have severely disrupted this system and thus we do not consider it "normal" (Goldreich et al. 1989). In addition, Triton is not an irregular satellite and Nereid is a borderline case under the definition of Burns (1986) which we discussed in the introduction (Table 11.1).). A possible explanation is because Uranus' regular satellite system is much less massive and does not extend as far from the planet as those of the other giant planets. Thus the perturbations from Uranus' regular satellites on the irregular satellites are decreased compared to other giant planets because of their smaller masses and further distance from the irregulars. This may allow the irregulars to be more stable closer to the planet. We also note that Uranus has the smallest a_{crit} of any of the giant planets (Table 11.1).

Table 11.3. Physical and Orbital Properties of Uranus' Irregular Satellites*

Name	a[a] (10^3 km)	i[b] (deg)	e[c]	Peri[d] (deg)	Node[e] (deg)	M[f] (deg)	Period[g] (days)	mag.[h] (m_R)	r[i] (km)	Year[j]
Low a & e										
S/2001U3	4276	145	0.15	125	93	91	266	25.0	11	2002
Caliban	7231	141	0.16	343	164	163	579	22.4	36	1997
Stephano	8004	144	0.23	19	188	82	677	24.1	16	1999
Trinculo	8504	167	0.22	160	195	22	759	25.4	9	2001
High a & e										
Sycorax	12179	159	0.52	20	260	170	1288	20.8	75	1997
Prospero	16256	152	0.45	176	317	181	1977	23.2	25	1999
Setebos	17418	158	0.59	1.5	248	126	2234	23.3	24	1999
S/2001U2	20901	170	0.37	160	216	235	2823	25.1	10	2003
Prograde										
S/2003U3	14345	57	0.66	89	3.5	322	1694	25.2	10	2003

*Orbital data are from Robert Jacobson at JPL (*http : //ssd.jpl.nasa.gov/sat_elem.html*). Fits are over a 1000 year time span.

[a]Mean semi-major axis with respect to Uranus.

[b]Mean inclination of orbit with respect to the ecliptic.

[c]Mean eccentricity.

[d]The argument of Periapsis.

[e]The longitude of the ascending node.

[f]The mean anomaly.

[g]Orbital period of satellite around Uranus.

[h]Apparent red (0.65 μm wavelength) magnitude.

[i]Radius of satellite assuming a geometric albedo of 0.04.

[j]Year in which observations determined that the object was a satellite.

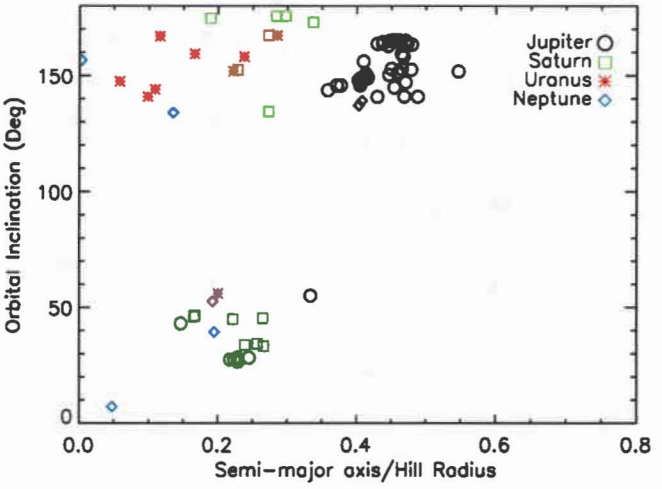

Figure 11.5 A mean inclination comparison between the known irregular satellites of the giant planets. The horizontal axis is the ratio of the satellite's mean semi-major axis to its respective planet's Hill radius. The vertical axis is the mean inclination of the satellite to the ecliptic. All giant planets independent of their mass or formation appear to have similar irregular satellite systems. Except for Neptune's "unusual" Triton and Nereid, Uranus appears to have the closest irregular satellites in terms of Hill radii of the giant planets.

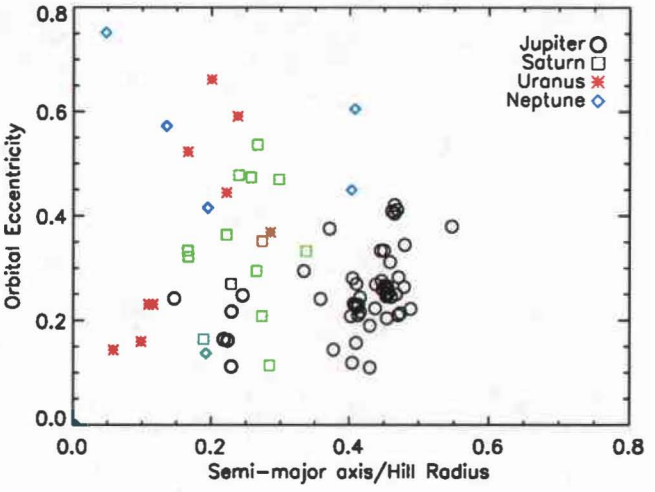

Figure 11.6 Same as Figure 11.5 except here mean eccentricity is used instead of inclination for the vertical axis.

It is interesting to note that the four irregular satellites close to Uranus appear to have similar orbital characteristics. In Figure 11.6 there may to be two possible groupings of Uranus' irregular satellites in semi-major axis and eccentricity phase space. The four irregular satellites closest to Uranus ($< 0.15 r_H$) have moderate eccentricities of around 0.2. The five irregular satellites of Uranus with $> 0.15 r_H$ have high eccentricities of around 0.5. The most likely reason for higher eccentricities more distant from the planet is that the closer satellites would be unstable to perturbations by the much larger regular satellites of Uranus if they had large eccentricities. As mentioned above, the four satellites with small eccentricity are significantly closer to their host planet than other known irregular satellites of the giant planets (except Neptune's "unusual" irregular satellites Triton and Nereid).

To determine the significance of the possible two semi-major axis eccentricity groups several statistical tests were performed. The low eccentricity, low semi-major axis group has a mean eccentricity of 0.19 ± 0.02 and mean semi-major axis of $7003 \pm 946 \times 10^3$ km while the high semi-major axis and eccentricity group has 0.52 ± 0.05 and $16688 \pm 1798 \times 10^3$

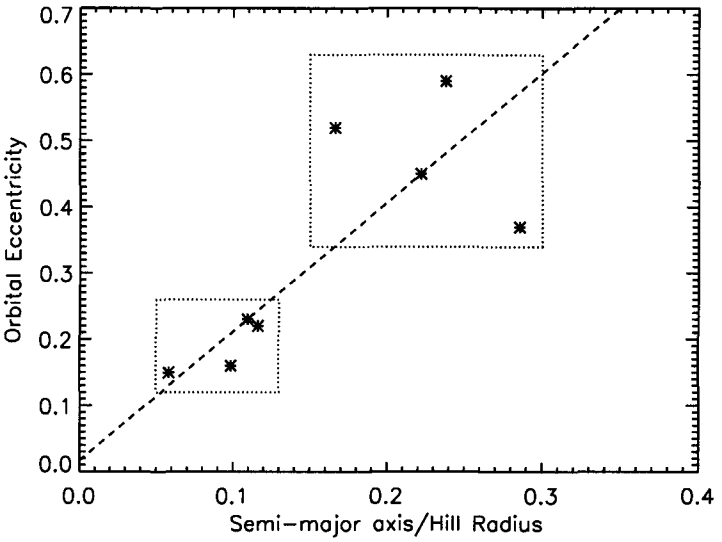

Figure 11.7 The orbital eccentricity versus the satellite's mean semi-major axis to its respective planet's Hill radius for retrograde Uranus irregulars only. There is a trend for satellites to have a larger eccentricity if they are more distant from Uranus. A linear fit gives a slope of 2.0 ± 0.7 and a y-intercept at 0.0 ± 0.1. The Pearson correlation coefficient is 0.76. Boxes show the two possible groupings discussed in the text.

km, respectively. A student's t-test (with 7 degrees of freedom) gave a t-statistic of 6.0 with a significance of 0.0016 for the difference in their mean eccentricities and a t-statistic of 4.8 with a significance of 0.0064 for the difference in their mean semi-major axes. Since the student's t-test gave a result which was greater than 3 σ we next performed more stringent nonparametric statistical tests. The Wilcoxon-Mann-Whitney U-test, the robust rank-order test and a permutation test (see Siegel & Castellan 1988) all found that the groupings of the eccentricity were statistically significant to at least 3σ. Figure 11.7 shows a linear fit of the retrograde satellites semi-major axes and eccentricities which gives a slope of 2.0 ± 0.7 and a y-intercept at 0.0 ± 0.1. The Pearson correlation coefficient is 0.76 or is significant to about the 97% level.

Except for the distinct prograde irregular S/2003 U3 with an orbital inclination of 57 degrees to the ecliptic compared to the eight irregulars between 140 and 170 degrees there are no other obvious groupings in semi-major axis and inclination phase space (Figure 11.5). The inclination region $60 < i < 140$ degrees is void of known satellites similar to other known irregular satellite systems and consistent with instabilities caused by the Kozai instability (Kozai 1962; Carruba et al. 2002; Nesvorny et al. 2003). Objects with high inclinations are strongly influenced by solar perturbations at their apoapse. These perturbations cause the satellites at high inclinations to acquire large eccentricities which eventually cause the satellite to collide with the planet, a regular satellite or be lost from the Hill sphere in $10^7 - 10^9$ years (Carruba et al. 2002; Nesvorny et al. 2003).

There does not appear to be any size versus semi-major axis, inclination or eccentricity correlation for Uranus' irregular satellites. In the gas drag capture model it would be expected that larger objects would have small periapses since the magnitude of the gas drag would be higher near the planet. In addition, any small satellites would have their orbital elements evolve faster to smaller inclinations and eccentricities and may spiral into the planet if the gas drag is not eventually removed. Of the two largest irregular satellites around Uranus one of each is in the two possible eccentricity groups. Caliban is relatively close to the planet with a low eccentricity while Sycorax is with the distant, higher eccentricity irregular satellites (Table 11.3).

The escape velocity for an object is $V_e = (2m_sG/r)^{1/2}$ where m_s is the mass of the satellite, G is the gravitational constant and r is the object's radius. For Uranus' known irregular satellites the escape velocity would be about 80 m/s for the largest Sycorax and 10 m/s for the smallest if assuming they are spherical and have densities of about 2000 kg m^3. The orbital velocities of the irregular satellites around Uranus range from 300 to 1100 m/s (Kessler 1981). Three of the low eccentricity satellites, Caliban, Stephano and Trinculo, have relative velocities comparable to Caliban's escape velocity around 40 m/s. The higher eccentricity objects have relative velocities of about 50 m/s to each other with the lowest being Prospero and Setebos at around 20 m/s. These velocities are lower than

that of Sycorax's escape velocity. For comparison, Jupiter's irregular satellites were found to be grouped in semi-major axis and inclination phase space with their relative velocities within a group about 30 m/s while relative group velocities to each other was over 200 m/s (Sheppard & Jewitt 2003). Similar to Jupiter, Uranus' possible two retrograde groups have relative velocities of over 100 m/s while members within a group have velocities comparable to the largest members escape velocity.

The possible groupings may have formed from parent objects which were fragmented through collisions. A simple particle in a box calculation shows that collisional timescales between the currently known or predicted (see next section) outer satellite population of Uranus would happen at a rate much longer than the age of the solar system ($\sim 10^{10}$ years). Fragmentation could have occurred from collisions with objects in heliocentric orbits (principally comets around the heavy bombardment period (Sheppard & Jewitt 2003)) or other now defunct satellites of the planet (Nesvorny et al. 2004). Jupiter's irregular satellite orbital velocities are much greater than Uranus' (> 2200 m/s) and thus any collisional processing would have been much more violent compared to collisions around Uranus.

11.5.2 Size and Population Distribution

The Cumulative Luminosity Function (CLF) describes the sky-plane number density of objects brighter than a given magnitude. The CLF is modeled by

$$\log[\Sigma(m_R)] = \alpha(m_R - m_o) \tag{11.3}$$

where $\Sigma(m_R)$ is the number of objects brighter than m_R, m_o is the magnitude at which $\Sigma = 1$, and 10^{α} describes the slope of the luminosity function. The CLF for Uranus' irregular satellites is shown in Figure 11.8. We believe outer satellites of Uranus are probably complete to near 26 mags ($r > 7$ km) as found in our survey. For Uranus we find the best fit to the CLF for $m_R < 26$ mags is $\alpha = 0.20 \pm 0.04$ and $m_o = 20.73 \pm 0.2$ (Figure 11.8).

The CLF represents the combined effects of the albedos, heliocentric distances and size distributions of the objects. If we assume all Uranus satellites are at the same heliocentric distance and their albedos are similar, the CLF simply represents the size distribution of the satellites. The objects appear to follow a single power-law size distribution for $r > 7$ km (Figure 11.10). In order to model the irregular satellite size distribution we use a differential power-law radius distribution of the form $n(r)dr = \Gamma r^{-q} dr$, where Γ and q are constants, r is the radius of the satellite, and $n(r)dr$ is the number of satellites with radii in the range r to $r + dr$. The slope of the CLF (α) and exponent of the size distribution (q) are simply related as $q = 5\alpha + 1$ when assuming similar heliocentric distance and albedos for all satellites (Irwin et al. (1995)). Using $\alpha = 0.20$ for Uranus' irregular satellites we find $q \sim 2.0$.

In comparison asteroid families have been found to usually have $q \geq 4$ (Tanga et al. 1999), collisional equilbrium is $q \sim 3.5$ (Dohnanyi 1969), nonfamily small asteroids have $q \sim 2.0$ to 2.5 (Cellino et al. 1991), while the Kuiper Belt Objects (KBOs) have $q = 4.2 \pm 0.5$, $\alpha = 0.64 \pm 0.1$, $m_o = 23.23 \pm 0.15$ (Trujillo et al. 2001) and Centaurs have a similar slope as the KBOs with $m_o = 24.6 \pm 0.3$ (Sheppard et al. 2000). If $q > 3$, most of the collisional cross section is in the smallest objects while $q > 4$ means most of the mass is in small bodies. Uranus' irregular satellite size distribution of $q \sim 2$ means the mass and cross section is dominated by the few large objects and is most similar to nonfamily small asteroids.

11.5.3 Comparison of Uranus' and Jupiter's Irregular Satellites

We compare Uranus' irregular satellite's size and population distribution to the most well determined irregular satellite system, that of Jupiter (Sheppard & Jewitt 2003). Both Jupiter's and Uranus' CLF and size distributions are shown in Figures 11.8 and 11.10, respectively. The optical flux scattered from an spherical atmosphereless body goes as $\sim p_R r^2 / R^4$. Thus similar sized objects at Jupiter ($R \sim 5$ AU) and Uranus ($R \sim 20$ AU) will be about 6 magnitudes fainter at the more distant Uranus if they have similar albedos (Figure 11.1).

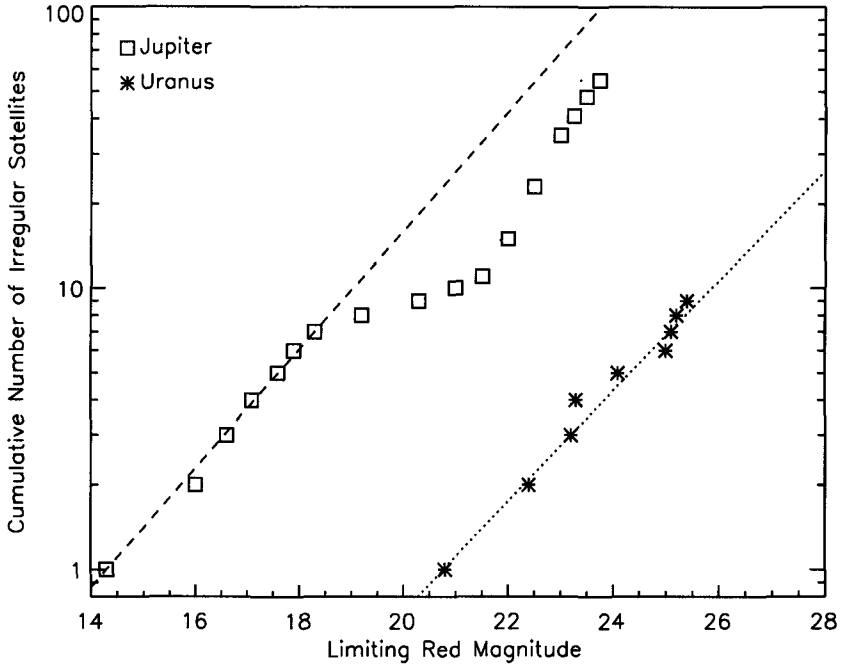

Figure 11.8 The cumulative luminosity function (CLF) for the irregular satellites of Uranus and Jupiter. The slope for both planets is very similar but because of Uranus' further distance it is shifted about 6 magnitudes to the right. The dashed line is the slope of the CLF for Jupiter's irregular satellites with $r \geq 10$ km ($\alpha = 0.21 \pm 0.03$) and the dotted line is for Uranus' irregular satellites with the same size range ($\alpha = 0.20 \pm 0.04$).

Jupiter's irregular satellites are not modeled well by a single power law (Figure 11.8) but two separate power laws (Sheppard & Jewitt 2003). For large objects ($m_R < 19$ or $r > 10$ km) a shallow power law is found ($q \approx 2.05$) while for smaller objects ($m_R > 21.5$ or $r < 4$ km) a steep power law is found ($q \geq 3.5$) with strong flattening for $4 < r < 10$ km ($q \sim 0$).

The points in a CLF are heavily correlated with one another in which the bright end of the distribution obtains more weight. The Differential Luminosity Function (DLF) has independent individual points. We plot the DLF of both Uranus and Jupiter using a bin size of 2 mags for all of Uranus' and Jupiter's irregular satellites in Figure 11.9. The DLF and CLF slopes should be similar. We find the DLF for Uranus' irregular satellites is $\alpha = 0.16 \pm 0.05$ with $m_o = 21.0 \pm 0.4$ and for Jupiter's irregular satellites with the same size range $\alpha = 0.18 \pm 0.05$ with $m_o = 14.0 \pm 0.4$. The slopes of the DLF like the CLF for both planets are very similar and within their statistical uncertainties. Bin sizes of 1 mag and 1.5 mag give similar fits as the 2 mag bin size. Uncertainties of the fits for the 2 mag bin size are determined from the fits of these other bin sizes. A deficiency of satellites around Jupiter with radii just less than 10 km is clearly seen as described in Sheppard & Jewitt (2003).

Jupiter's irregular satellites completeness limit is at least $r = 3$ km (Sheppard & Jewitt 2003). Our survey for Uranus satellites is complete to about $r \sim 7$ km (see above) and thus may be directly compared to Jupiter's irregular satellite population for $r > 7$ km. Like Jupiter's irregular satellites it appears that there is an absence of satellites with radii just below 10 km at Uranus. It may be that Uranus like Jupiter has a steep increase of smaller satellites ($r < 4$ km), but these satellites would have avoided detection to date since their magnitudes would be fainter than about 27.2 mags.

If we naively assume the known CLF for Uranus' larger irregular satellites extends down to radii of about 1 km, we would expect about 75 ± 30 irregular satellites of this size or larger around Uranus (Figure 11.10). This is very similar to what is predicted around Jupiter down to this size (Sheppard & Jewitt 2003).

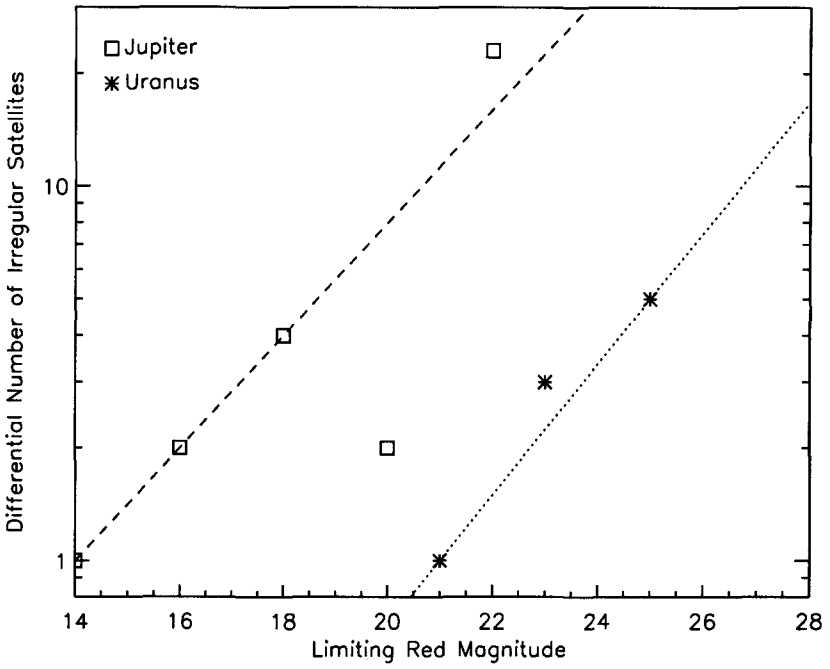

Figure 11.9 The differential luminosity function (DLF) for the irregular satellites of Uranus and Jupiter. The slope for both planets is very similar but because of Uranus' further distance it is shifted about 6 magnitudes to the right. The dashed line is the slope of the DLF for Jupiter's irregular satellites with $r \geq 10$ km ($\alpha = 0.18 \pm 0.05$) and the dotted line is for Uranus' irregular satellites with the same size range ($\alpha = 0.16 \pm 0.05$). A deficiency of satellites around Jupiter with radii just less than 10 km is clearly seen as described in Sheppard & Jewitt (2003).

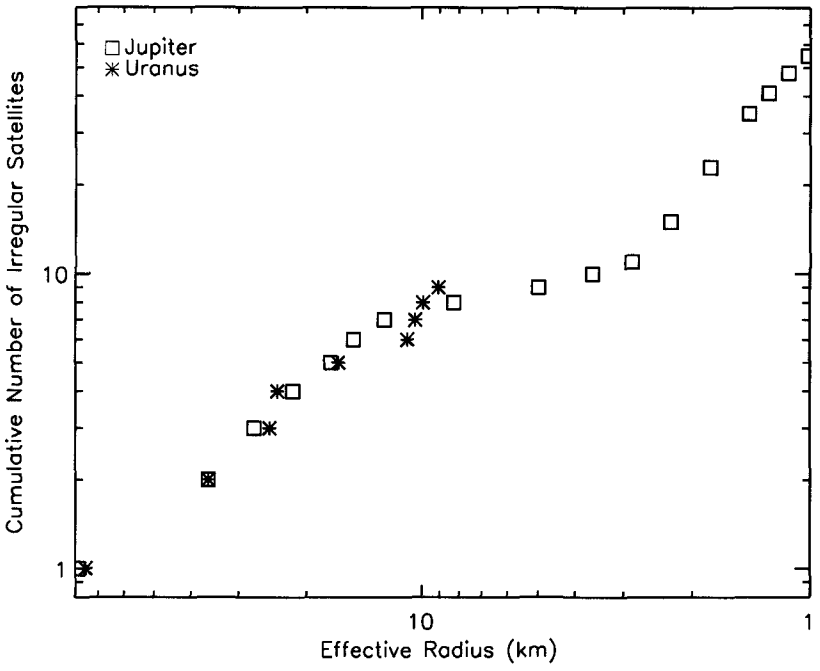

Figure 11.10 The cumulative radius function for the irregular satellites of Uranus and Jupiter. This figure directly compares the sizes of the satellites of the two planets assuming both satellite populations have albedos of about 0.04. Both planets appear to have very similar size distributions of irregular satellites.

We would expect any gas drag effects to change the size distribution at the small end since these objects should be fewer because of spiraling into the planet. Its possible that Jupiter's irregular satellites show this by the flattening of the power-law size distribution at $r \sim 10$ km. In this interpretation, the increase of smaller objects with $r < 4$ km are just the collisional fragments created after a significant amount of time from capture in which any significant gas drag would have dissipated. Uranus may show the same situation since no satellites were found between 25.5 and 26 magnitudes ($7 \leq r \leq 9$ km) though 2.6 ± 1.6 satellites would be expected if extending the size distribution power-law to smaller sizes.

11.6 Summary

Two new distant satellites of Uranus were discovered including Uranus' first and only known irregular prograde satellite. All known outer satellites of Uranus were detected in the survey with no prior knowledge of their locations. The survey covered about 100% of the prograde stability region around Uranus and about 90% of the retrograde stability region to a 50% detection efficiency at a red limiting magnitude of 26.1 mags. This corresponds to objects of about 7 km in radius if assuming a low albedo. Some results of the survey are:

1) When comparing Uranus' irregular satellites size and population distribution to Jupiter we find the two systems to be remarkably similar. Jupiter's size distribution is virtually the same as Uranus' for objects with radii > 10 km. Both planets have an apparent lack of satellites just below the 10 km radius region, though fainter searches ($m_R \sim 27$) are required around Uranus to statistically determine this.

2) The size distribution of the Uranus irregular satellites with radii > 7 km approximates a power law with an exponent $q \sim 2$. The irregular satellites cross-section and mass are dominated by the largest few members, similar to what has been found for the nonfamily small asteroids in the main belt.

3) There is no correlation between orbital parameters and the sizes of the satellites as may be expected from gas drag capture.

4) Except for the one prograde and eight retrograde irregulars, there does not appear to be any grouping in semi-major axis and inclination phase space as has been found for Jupiter's irregular satellites.

5) We tentatively define two groups of irregular satellites in semi-major axis and eccentricity phase space. Four retrograde irregular satellites are less than about 0.15 Hill radii from the planet and have moderate eccentricities (~ 0.2) while four retrograde satellites have larger semi-major axes with high eccentricities (~ 0.5). The four irregular satellites with semi-major axes less than 0.15 Hill radii are the closest irregular satellites of any of the known irregulars around the giant planets (except for the very eccentric Nereid around Neptune).

6) The large tilt of Uranus does not appear to have disrupted the irregular satellite system of the planet as it is similar to the other giant planet's known irregular satellite systems. The formation of Uranus as an ice giant must be reconciled with the formation of Jupiter as a gas giant, yet both have a statistically similar population densities and size distributions of irregular satellites.

Acknowledgments

This work was supported by a grant from NASA to DJ. We thank Richard Wainscoat for confirming coordinates for Gemini and the Gemini staff for their professionalism in running the queue servicing mode with GMOS. We are grateful to B. Marsden and R. Jacobson for orbital calculations of the satellites.

Chapter 12

Satellite Summary and Future

12.1 Summary

Wide-field surveys around Mars, Jupiter and Uranus covered the vast majority of these planets Hill Spheres for satellites. Through the surveys we discovered 46 new Jupiter satellites and 2 new Uranus satellites.

Both the gas giant Jupiter and ice giant Uranus have statistically similar irregular satellite populations, size distributions and orbital characteristics independent of their mass or formation scenarios. The less will determined irregular satellite populations of the gas giant Saturn and ice giant Neptune also show similar irregular satellite characteristics.

The irregular satellites around each giant planet have similar shallow size distributions which means the few large satellites dominate the mass of the population. Jupiter's proximity allows us to probe the very small satellites, which shows satellites smaller than about 4 km in radius may have a steeper size distribution. Dynamical groupings may be explained through collisional fragmentation of parent satellites from either heliocentric objects or now defunct satellites from the early solar system. The orbital inclinations of all the irregular satellites avoid the Kozai instability region $55 < i < 130$ degrees. No size versus orbital characteristics are observed for any of the irregular satellites of the planets as would be expected if gas drag was a factor for capture or collisional breakup.

12.2 Future Work

Jupiter's Hill sphere has been searched up to 24th magnitude ($r \sim 1$ km) for satellites. Current technology with wide-field imagers on 8-10 meter class telescopes allows for efficient searches which could reach to over 25th magnitude ($r \sim 0.5$ km) for satellites around Jupiter. Covering the whole Hill sphere to this limit and acquiring followup time to reliably determine orbits would require an unreasonable number of nights of 8-10 meter time. A mini survey to 26th mag. of a few small portions of Jupiter's Hill sphere (a few degrees) would be useful to determine if the size distribution found for the larger satellites extends down to the very small satellites. If gas drag was a factor in the capture process it would be expected that there should be some minimum size for the satellites around Jupiter.

Saturn's Hill sphere is currently the least searched to date. We searched only a very small portion of the Hill sphere (~ 1 square degree) to just over 24th magnitude ($r \sim 4$ km) with Subaru and found one new satellite (S/2003 S1) in February 2003. These few images were obtained when Saturn was not at a favorable position in the sky. Saturn was near the galactic planet and was well away from opposition. There was considerable confusion with moving foreground main belt asteroids and the high density of background stars and galaxies. Thus this mini survey is not very worthwhile to examine in detail. We obtained Subaru telescope time to search the Saturn Hill sphere to 26th magnitude ($r \sim 2$ km) in January 2004 but were wiped out by weather. We currently have time in December 2004 to try the Saturn search again.

Saturn is the second closest giant planet to the Earth and thus is second only to Jupiter in our ability to characterize the small irregular satellite population. The most recent published survey of the planet by Gladman et al. (1998) claim that they searched the majority of the inner Hill sphere to about 23rd magnitude. As shown in previous chapters of this thesis Saturn's irregular satellites show very similar orbital characteristics as well as size distribution to the other giant planets. A deep search of Saturn's Hill sphere will be

very beneficial to statistically determining how similar the small population of the irregular satellite system is to the other giant planets.

Uranus' Hill sphere has now been searched to the limits of current efficient direct imaging techniques. Deeper searches can be made if special shift and add techniques are used to remove the trailing losses experienced by a moving object in a single long exposure. This requires multiple exposures of one field. The individual images can then be shifted and stacked at the rate of the planet's motion to detect very faint satellites. This requires a high amount of large telescope time since one field is observed for long periods of time.

Neptune's Hill sphere was searched by us while we waited for Uranus to rise during that survey. We discovered one new Neptune satellite (S/2003 N1) and recovered several others for there first opposition. This survey only covered a portion of Neptune's Hill sphere but shows that Neptune has a similar population of irregular satellites as the other giant planets. Further searches of this planet would be beneficial to determine its large satellite population. Because Neptune is so distant only the largest satellites may be detected efficiently to date. The "unusual" irregular satellites Triton and Nereid appear to just be anomalies in which 5 "normal" irregular satellites are now known. Initial results show the ice giant Neptune has, like Uranus, a satellite population similar to the gas giant Jupiter. Further surveys are required of Neptune to better determine its overall satellite population.

Finally, the inner terrestrial planets Mercury and Venus have not been searched for new satellites with current efficient CCD detectors. As explained in the Mars chapter, solar tides are expected to destabilize any satellites around these planets, but observations would still be worthwhile to confirm this.

References

Allen, R. L., Bernstein, G. M., & Malhotra, R. 2002, AJ, 124, 2949

Altenhoff, W. J., Bertoldi, F., & Menten, K. M. 2004, A&A, 415, 771

Asher, D. J. & Steel, D. I. 1993, MNRAS, 263, 179

Asphaug, E. & Benz, W. 1996, Icarus, 121, 225

Aumann, H. H., Beichman, C. A., Gillett, F. C., de Jong, T., Houck, J. R., Low, F. J., Neugebauer, G., Walker, R. G., & Wesselius, P. R. 1984, ApJ, 278, L23

Beaugé, C., Roig, F., & Nesvorný, D. 2002, Icarus, 158, 483

Belskaya, I. N. & Shevchenko, V. G. 2000, Icarus, 147, 94

Binzel, R. P., Farinella, P., Zappala, V., & Cellino, A. 1989, in Asteroids II, 416–441

Boss, A. P. 2001, ApJ, 563, 367

Boss, A. P., Wetherill, G. W., & Haghighipour, N. 2002, Icarus, 156, 291

Boulade, O., Charlot, X., Abbon, P., Aune, S., Borgeaud, P., Carton, P., Carty, M., Da Costa, J., Deschamps, H., Desforge, D., Eppellé, D., Gallais, P., Gosset, L., Granelli, R., Gros, M., de Kat, J., Loiseau, D., Ritou, J.-., Roussé, J. Y., Starzynski, P., Vignal, N., & Vigroux, L. G. 2003, in Instrument Design and Performance for Optical/Infrared Ground-based Telescopes. Edited by Iye, Masanori; Moorwood, Alan F. M. Proceedings of the SPIE, Volume 4841, pp. 72-81 (2003)., 72–81

Bowell, E., Hapke, B., Domingue, D., Lumme, K., Peltoniemi, J., & Harris, A. W. 1989, in Asteroids II, 524–556

Brown, R. H., Cruikshank, D. P., & Pendleton, Y. 1999, ApJ, 519, L101

Brunini, A., Parisi, M. G., & Tancredi, G. 2002, Icarus, 159, 166

Buie, M. W., Tholen, D. J., & Wasserman, L. H. 1997, Icarus, 125, 233

Burns, J. A. 1973, Nature Physical Science, 242, 23

Burns, J. A. 1986a, in IAU Colloq. 77: Some Background about Satellites, 1–38

Burns, J. A. 1986b, in IAU Colloq. 77: Some Background about Satellites, 117–158

Burns, J. A. 1992, in Mars, 1283–1301

Burns, J. A. & Safronov, V. S. 1973, MNRAS, 165, 403

Callegari, N. & Yokoyama, T. 2001, Planet. Space Sci., 49, 35

Capaccioni, F., Cerroni, P., Coradini, M., Farinella, P., Flamini, E., Martelli, G., Paolicchi, P., Smith, P. N., & Zappala, V. 1984, Nature, 308, 832

Carruba, V., Burns, J. A., Nicholson, P. D., & Gladman, B. J. 2002, Icarus, 158, 434

Carter, B. D., Ashley, M. C. B., Sun, Y.-S., & Storey, J. W. V. 1992, Proceedings of the Astronomical Society of Australia, 10, 74

Catullo, V., Zappala, V., Farinella, P., & Paolicchi, P. 1984, A&A, 138, 464

Cellino, A., Pannunzio, R., Zappala, V., Farinella, P., & Paolicchi, P. 1985, A&A, 144, 355

Cellino, A., Zappala, V., & Farinella, P. 1991, MNRAS, 253, 561

Chandrasekhar, S. 1987, Ellipsoidal figures of equilibrium (New York : Dover, 1987.)

Chauvineau, B. & Mignard, F. 1990, Icarus, 87, 377

Colombo, G. & Franklin, F. A. 1971, Icarus, 15, 186

Cook, A. F. & Franklin, F. A. 1970, Icarus, 13, 282

Counselman, C. C. 1973, ApJ, 180, 307

Cruikshank, D. P. 1977, Icarus, 30, 224

Davis, D. R. & Farinella, P. 1997, Icarus, 125, 50

de Angelis, G. 1995, Planet. Space Sci., 43, 649

Degewij, J., Tedesco, E. F., & Zellner, B. 1979, Icarus, 40, 364

Dohnanyi, J. W. 1969, J. Geophys. Res., 74, 2531

Dones, L., Gladman, B., Melosh, H. J., Tonks, W. B., Levison, H. F., & Duncan, M. 1999, Icarus, 142, 509

Doressoundiram, A., Peixinho, N., de Bergh, C., Fornasier, S., Thébault, P., Barucci, M. A., & Veillet, C. 2002, AJ, 124, 2279

Drummond, J. D., Weidenschilling, S. J., Chapman, C. R., & Davis, D. R. 1991, Icarus, 89, 44

Duncan, M., Quinn, T., & Tremaine, S. 1988, ApJ, 328, L69

Duncan, M. J., Levison, H. F., & Budd, S. M. 1995, AJ, 110, 3073

Dunlap, J. L. & Gehrels, T. 1969, AJ, 74, 796

Durda, D. D. & Stern, S. A. 2000, Icarus, 145, 220

Duxbury, T. C. & Ocampo, A. C. 1988, Icarus, 76, 160

Dworetsky, M. M. 1983, MNRAS, 203, 917

Edgeworth, K. E. 1949, MNRAS, 109, 600

Elliot, J. L. & Osip, D. J. 2001, in International Astronomical Union Circular, 7765

Everhart, E. 1972, Astrophys. Lett., 10, 131

Farinella, P. & Davis, D. R. 1996, Science, 273, 938

Farinella, P., Paolicchi, P., Tedesco, E. F., & Zappala, V. 1981, Icarus, 46, 114

Farinella, P., Paolicchi, P., & Zappala, V. 1982, Icarus, 52, 409

Farinella, P. & Zappalà, V. 1997, Advances in Space Research, 19, 181

Farnham, T. L. 2001, in International Astronomical Union Circular, 7583

Fernandez, J. A. 1980, MNRAS, 192, 481

Fleming, H. J. & Hamilton, D. P. 2000, Icarus, 148, 479

Fujiwara, A., Kamimoto, G., & Tsukamoto, A. 1978, Nature, 272, 602

Gehrels, T. 1977, in IAU Colloq. 39: Comets, Asteroids, Meteorites: Interrelations, Evolution and Origins, 323–325

Gehrels, T., Roemer, E., Taylor, R. C., & Zellner, B. H. 1970, AJ, 75, 186

Gladman, B., Holman, M., Grav, T., Kavelaars, J., Nicholson, P., Aksnes, K., & Petit, J.-M. 2002, Icarus, 157, 269

Gladman, B., Kavelaars, J., Holman, M., Petit, J.-M., Scholl, H., Nicholson, P., & Burns, J. A. 2000, Icarus, 147, 320

Gladman, B., Kavelaars, J. J., Holman, M., Nicholson, P. D., Burns, J. A., Hergenrother, C. W., Petit, J., Marsden, B. G., Jacobson, R., Gray, W., & Grav, T. 2001, Nature, 412, 163

Gladman, B., Kavelaars, J. J., Nicholson, P. D., Loredo, T. J., & Burns, J. A. 1998, AJ, 116, 2042

Goldreich, P., Lithwick, Y., & Sari, R. 2002, Nature, 420, 643

Gomes, R. S. 2003, Icarus, 161, 404

Green, S. F., McBride, N., O Ceallaigh, D. P., Fitzsimmons, A., Williams, I. P., & Irwin, M. J. 1997, MNRAS, 290, 186

Greenberg, R. 1974, Icarus, 23, 51

Hahn, G. & Bailey, M. E. 1990, Nature, 348, 132

Hahn, J. M. & Malhotra, R. 1999, AJ, 117, 3041

Hainaut, O. R., Delahodde, C. E., Boehnhardt, H., Dotto, E., Barucci, M. A., Meech, K. J., Bauer, J. M., West, R. M., & Doressoundiram, A. 2000, A&A, 356, 1076

Hainaut, O. R. & Delsanti, A. C. 2002, A&A, 389, 641

Hall, A. 1878, Astronomische Nachrichten, 92, 47

Hamilton, D. P. & Krivov, A. V. 1997, Icarus, 128, 241

Harris, A. W. 1994, Icarus, 107, 209

Hartmann, W. K. & Cruikshank, D. P. 1978, Icarus, 36, 353

Hartmann, W. K., Ryder, G., Dones, L., & Grinspoon, D. 2000, The Time-Dependent Intense Bombardment of the Primordial Earth/Moon System (Origin of the earth and moon, edited by R.M. Canup and K. Righter and 69 collaborating authors. Tucson: University of Arizona Press., p.493-512), 493–512

Heppenheimer, T. A. & Porco, C. 1977, Icarus, 30, 385

Hestroffer, D., Marchis, F., Fusco, T., & Berthier, J. 2002, A&A, 394, 339

Hilton, J. L. 1997, AJ, 114, 402

Holman, M., Kavelaars, J., Grav, T., Fraser, W., Milisavljevic, D., Gladman, B., Petit, J.-M., Mousis, O., Rousselot, P., Nicholson, P., Carruba, V., & Marsden, B. G. 2003, in International Astronomical Union Circular, 8047

Holman, M. J. & Wisdom, J. 1993, AJ, 105, 1987

Howell, S. B., Everett, M. E., Tonry, J. L., Pickles, A., & Dain, C. 2003, PASP, 115, 1340

Ida, S., Larwood, J., & Burkert, A. 2000, ApJ, 528, 351

Irwin, M., Tremaine, S., & Zytkow, A. N. 1995, AJ, 110, 3082

Jedicke, R. & Herron, J. D. 1997, Icarus, 127, 494

Jewitt, D., Aussel, H., & Evans, A. 2001, Nature, 411, 446

Jewitt, D. & Luu, J. 1993, Nature, 362, 730

Jewitt, D., Luu, J., & Chen, J. 1996, AJ, 112, 1225

Jewitt, D., Luu, J., & Trujillo, C. 1998, AJ, 115, 2125

Jewitt, D. C. & Luu, J. X. 1995, AJ, 109, 1867

—. 2000, Protostars and Planets IV, 1201

—. 2001, AJ, 122, 2099

Jewitt, D. C. & Sheppard, S. S. 2002, AJ, 123, 2110

Joss, P. C. 1973, A&A, 25, 271

Kenyon, S. J. & Luu, J. X. 1999, ApJ, 526, 465

Kessler, D. J. 1981, Icarus, 48, 39

Korycansky, D. G., Bodenheimer, P., Cassen, P., & Pollack, J. B. 1990, Icarus, 84, 528

Kowal, C. T. 1978, Sciences, 18, 12

—. 1989, Icarus, 77, 118

Kuiper, G. P. 1951, in Proceedings of a topical symposium, commemorating the 50th anniversary of the Yerkes Observatory and half a century of progress in astrophysics, New York: McGraw-Hill, 1951, edited by Hynek, J.A., p.357, 357–+

Kuiper, G. P. 1956, Vistas in Astronomy, 2, 1631

Kuiper, G. P. 1961, in Planets and Satellites, 575–+

Lagerkvist, C.-I., Harris, A. W., & Zappala, V. 1989, in Asteroids II, 1162–1179

Landolt, A. U. 1992, AJ, 104, 340

Larsen, J. A., Gleason, A. E., Danzl, N. M., Descour, A. S., McMillan, R. S., Gehrels, T., Jedicke, R., Montani, J. L., & Scotti, J. V. 2001, AJ, 121, 562

Lazzarin, M., Barucci, M. A., Boehnhardt, H., Tozzi, G. P., de Bergh, C., & Dotto, E. 2003, AJ, 125, 1554

Leinhardt, Z. M., Richardson, D. C., & Quinn, T. 2000, Icarus, 146, 133

Leonard, F. C. 1930, Leaflet of the Astronical Society of the Pacific, 1, 121

Leone, G., Paolicchi, P., Farinella, P., & Zappala, V. 1984, A&A, 140, 265

Levison, H. F. & Duncan, M. J. 1997, Icarus, 127, 13

Lupo, M. J. & Lewis, J. S. 1979, Icarus, 40, 157

Luu, J. & Jewitt, D. 1996, AJ, 112, 2310

Luu, J., Jewitt, D., Trujillo, C. A., Hergenrother, C. W., Chen, J., & Offutt, W. B. 1997, Nature, 387, 573

Malhotra, R. 1995, AJ, 110, 420

Margot, J. 2002, Nature, 416, 694

Marzari, F. & Scholl, H. 1998, A&A, 339, 278

McKinnon, W. B. 1989, ApJ, 344, L41

McMillan, R. S., Larsen, J. A., & Marsden, B. G. 2000, Minor Planet Circulars, 2

Melosh, H. J. 1989, Impact cratering: A geologic process (Research supported by NASA. New York, Oxford University Press (Oxford Monographs on Geology and Geophysics, No. 11), 1989, 253 p.), 45–+

Merline, W. J., Close, L. M., Dumas, C., Chapman, C. R., Roddier, F., Menard, F., Slater, D. C., Duvert, G., Shelton, C., & Morgan, T. 1999, Nature, 401, 565

Millis, R. L. 1977, Icarus, 31, 81

Millis, R. L., Buie, M. W., Wasserman, L. H., Elliot, J. L., Kern, S. D., & Wagner, R. M. 2002, AJ, 123, 2083

Miyazaki, S., Komiyama, Y., Sekiguchi, M., Okamura, S., Doi, M., Furusawa, H., Hamabe, M., Imi, K., Kimura, M., Nakata, F., Okada, N., Ouchi, M., Shimasaku, K., Yagi, M., & Yasuda, N. 2002, PASJ, 54, 833

Morbidelli, A. & Levison, H. F. 2003, Nature, 422, 30

Morbidelli, A. & Valsecchi, G. B. 1997, Icarus, 128, 464

Nakamura, T. & Yoshikawa, M. 1995, Icarus, 116, 113

Noll, K. S., Stephens, D. C., Grundy, W. M., Millis, R. L., Spencer, J., Buie, M. W., Tegler, S. C., Romanishin, W., & Cruikshank, D. P. 2002, AJ, 124, 3424

Oke, J. B., Cohen, J. G., Carr, M., Cromer, J., Dingizian, A., Harris, F. H., Labrecque, S., Lucinio, R., Schaal, W., Epps, H., & Miller, J. 1995, PASP, 107, 375

Oort, J. H. 1950, Bull. Astron. Inst. Netherlands, 11, 91

Ortiz, J. L., Gutiérrez, P. J., Casanova, V., & Sota, A. 2003, A&A, 407, 1149

Ostro, S. J., Hudson, R. S., Nolan, M. C., Margot, J., Scheeres, D. J., Campbell, D. B., Magri, C., Giorgini, J. D., & Yeomans, D. K. 2000, Science, 288, 836

Peale, S. J. 1999, ARA&A, 37, 533

Peixinho, N., Doressoundiram, A., Delsanti, A., Boehnhardt, H., Barucci, M. A., & Belskaya, I. 2003, A&A, 410, L29

Pollack, J. B., Burns, J. A., & Tauber, M. E. 1979, Icarus, 37, 587

Pollack, J. B., Hubickyj, O., Bodenheimer, P., Lissauer, J. J., Podolak, M., & Greenzweig, Y. 1996, Icarus, 124, 62

Quinn, T., Tremaine, S., & Duncan, M. 1990, ApJ, 355, 667

Rettig, T. W., Walsh, K., & Consolmagno, G. 2001, Icarus, 154, 313

Rickman, H. 1989, Advances in Space Research, 9, 59

Romanishin, W. & Tegler, S. C. 1999, Nature, 398, 129

Russell, H. N. 1906, ApJ, 24, 1

Ryan, E. V., Davis, D. R., & Giblin, I. 1999, Icarus, 142, 56

Sagdeev, R. Z., Elyasberg, P. E., & Moroz, V. I. 1988, Nature, 331, 240

Saha, P. & Tremaine, S. 1993, Icarus, 106, 549

Schaefer, B. E. & Rabinowitz, D. L. 2002, Icarus, 160, 52

Sekiguchi, T., Boehnhardt, H., Hainaut, O. R., & Delahodde, C. E. 2002, A&A, 385, 281

Sheppard, S. S. & Jewitt, D. C. 2002, AJ, 124, 1757

—. 2003, Nature, 423, 261

Sheppard, S. S., Jewitt, D. C., Fernandez, Y. R., Magnier, G., Marsden, B. G., Dahm, S., & Evans, A. 2001, in International Astronomical Union Circular, 7555

Sheppard, S. S., Jewitt, D. C., Kleyna, J., Fernandez, Y. R., Hsieh, H. H., & Marsden, B. G. 2003a, in International Astronomical Union Circular, 8087

Sheppard, S. S., Jewitt, D. C., Kleyna, J., Marsden, B. G., Holman, M., Kavelaars, J., Grav, T., & Fraser, W. 2003b, in International Astronomical Union Circular, 8193

Sheppard, S. S., Jewitt, D. C., Kleyna, J., Marsden, B. G., & Jacobson, R. 2002, in International Astronomical Union Circular, 7900

Sheppard, S. S., Jewitt, D. C., Trujillo, C. A., Brown, M. J. I., & Ashley, M. C. B. 2000, AJ, 120, 2687

Showalter, M. R., Hamilton, D. P., & Nicholson, P. D. 2001, Bulletin of the American Astronomical Society, 33, 1095

Singer, S. F. 1975, Icarus, 25, 484

Slattery, W. L., Benz, W., & Cameron, A. G. W. 1992, Icarus, 99, 167

Smith, B. A., Soderblom, L., Batson, R., Bridges, P., Inge, J., Masursky, H., Shoemaker, E., Beebe, R., Boyce, J., Briggs, G., Bunker, A., Collins, S. A., Hansen, C. J., Johnson, T. V., Mitchell, J. L., Terrile, R. J., Cook, A. F., Cuzzi, J., Pollack, J. B., Danielson, G. E., Ingersoll, A., Davies, M. E., Hunt, G. E., Morrison, D., Owen, T., Sagan, C., Veverka, J., Strom, R., & Suomi, V. E. 1982, Science, 215, 505

Smith, B. A., Soderblom, L. A., Beebe, R., Bliss, D., Brown, R. H., Collins, S. A., Boyce, J. M., Briggs, G. A., Brahic, A., Cuzzi, J. N., & Morrison, D. 1986, Science, 233, 43

Smith, B. A. & Terrile, R. J. 1984, Science, 226, 1421

Soter, S. L. 1971, Ph.D. Thesis

Stellingwerf, R. F. 1978, ApJ, 224, 953

Stern, S. A. 1996a, AJ, 112, 1203

—. 1996b, A&A, 310, 999

—. 2002, AJ, 124, 2300

Tanga, P., Cellino, A., Michel, P., Zappalà, V., Paolicchi, P., & dell'Oro, A. 1999, Icarus, 141, 65

Tedesco, E. F. 1989, in Asteroids II, 1090–1138

Tedesco, E. F., Williams, J. G., Matson, D. L., Weeder, G. J., Gradie, J. C., & Lebofsky, L. A. 1989, AJ, 97, 580

Tegler, S. C. & Romanishin, W. 1998, Nature, 392, 49

—. 2000, Nature, 407, 979

—. 2003, Icarus, 161, 181

Tegler, S. C., Romanishin, W., & Consolmagno, S. J. 2003, ApJ, 599, L49

Tholen, D. J. & Buie, M. W. 1997, Icarus, 125, 245

Tholen, D. J. & Tedesco, E. F. 1994, Icarus, 108, 200

Thomas, P. C., Binzel, R. P., Gaffey, M. J., Storrs, A. D., Wells, E. N., & Zellner, B. H. 1997, Science, 277, 1492

Thommes, E. W., Duncan, M. J., & Levison, H. F. 2002, AJ, 123, 2862

Tiscareno, M. S. & Malhotra, R. 2003, AJ, 126, 3122

Tonry, J., Burke, B. E., & Schechter, P. L. 1997, PASP, 109, 1154

Trujillo, C. A. & Brown, M. E. 2002, ApJ, 566, L125

Trujillo, C. A., Jewitt, D. C., & Luu, J. X. 2000, ApJ, 529, L103

—. 2001, AJ, 122, 457

Tsui, K. H. 2000, Icarus, 148, 139

Veillet, C., Parker, J. W., Griffin, I., Marsden, B., Doressoundiram, A., Buie, M., Tholen, D. J., Connelley, M., & Holman, M. J. 2002, Nature, 416, 711

Viateau, B. 2000, A&A, 354, 725

Ward, W. R. & Reid, M. J. 1973, MNRAS, 164, 21

Washabaugh, P. D. & Scheeres, D. J. 2002, Icarus, 159, 314

Weidenschilling, S. J. 1980, Icarus, 44, 807

—. 2002, Icarus, 160, 212

Weissman, P. R. 1984, Science, 224, 987

Whipple, F. L. 1950, ApJ, 111, 375

Yeomans, D. K., Barriot, J.-P., Dunham, D. W., Farquhar, R. W., Giorgini, J. D., Helfrich, C. E., Konopliv, A. S., McAdams, J. V., Miller, J. K., Owen, W. M., Scheeres, D. J., Synnott, S. P., & Williams, B. G. 1997, Science, 278, 2106

Young, E. F., Binzel, R. P., & Crane, K. 2001, AJ, 121, 552

Zappala, V. 1980, Moon and Planets, 23, 345